Dissertation

Submitted to the
Combined Faculties of the Natural Sciences and Mathematics
of Ruperto-Carola-University of Heidelberg, Germany,
for the degree of
Doctor of Natural Sciences

Put forward by

Gigi Ying Chi Leung
Born in: Hong Kong

Oral examination: July 16, 2019

Page left intentionally blank.

Constraining the nature of dark matter in galaxies with multi-tracer dynamical models

A dissertation presented

by

Gigi Ying Chi Leung

to

The Combined Faculties of the Natural Sciences and Mathematics

for the degree of

Doctor of Natural Sciences

The Ruperto-Carola-University of Heidelberg

Heidelberg, Germany

May 2019

Referees: Glenn van de Ven, Rainer Spurzem Gigi Ying Chi Leung

Constraining the nature of dark matter in galaxies with multi-tracer dynamical models

Abstract

The detailed mass distribution in galaxies provides important constraints on the nature of dark matter (DM), especially in relation to the baryonic content and feedback efficiency of a galaxy. In this thesis I use multiple kinematic tracers and a diverse set of dynamical models to simultaneously constrain DM density profiles, halo shapes and the evolutionary history of galaxies. I first show that the most common and advanced stellar dynamical models can reproduce the circular velocities (as traced independently by molecular gas rotation curves), to within ∼10% accuracy. I further use high resolution observations to understand the sources (gravitational, feedback driven) of high velocity dispersion ionised gas. By incorporating realistic birth conditions for globular clusters (GCs) and flexible, self-consistent velocity distribution functions for the Fornax dSph, I am able to understand the survival of its five GCs. The comprehensive evolutionary model suggests that Fornax has a large DM core ($\gtrsim$1.5 kpc) and has undergone a past merger of mass ratio ∼1:2 to 1:5. Finally, by combining stellar and gas kinematic tracers together in a single dynamical model, I provide evidence that the isolated dwarf irregular galaxy WLM has a DM halo that has both an inner density core ($\gamma \sim 0.3 \pm 0.1$), and a prolate axis ratio of 2:1. The recovered orbit structure (tangential anisotropic) is very similar to nearby dSph galaxies - suggesting that internal processes rather than tidal origin may lead to this dynamical configuration. The DM halo profile is consistent with the ΛCDM cosmological picture when baryonic feedback is included. The prolate geometry is difficult for MOND and at the same time challenges self-interacting DM (SIDM) theories to create a thermalised DM core of the observed size, without sphericalising the halo. From both the dynamical models on WLM and Fornax, I am able to provide constraints on the particle mass of Bose-Einstein condensate DM models to $1.1 - 1.3 \times 10^{-22}\,\mathrm{eV/c^2}$, and interaction cross section for (velocity independent) SIDM particles of $0.8 \lesssim \sigma/m_{\mathrm{SIDM}} \lesssim 3.1\,\mathrm{cm^2/g}$ - though it remains to be seen that these can produce the proper core size and shape in the DM halos we find. Application of these new techniques and models to more galaxies will provide even tighter constraints on dark matter particle models.

Zusammenhang

Die detaillierte Massenverteilung in Galaxien liefert wichtige Einschränkungen für die Natur der Dunklen Materie (DM), insbesondere in Bezug auf den Baryongehalt und die Rückkopplungseffizienz einer Galaxie. In dieser Dissertation verwende ich mehrere kinematische Tracer und verschiedene dynamische Modelle, um gleichzeitig DM-Dichteprofile, Halo-Geometrie und die Evolutionsgeschichte von Galaxien einzuschränken. Ich zeige zunächst, dass die gängigsten und fortschrittlichsten stellaren dynamischen Modelle die Kreisgeschwindigkeiten (unabhängig verfolgt von molekularen Gasrotationskurven) mit einer Genauigkeit innerhalb von $\sim$10% reproduzieren können. Ich verwende auch hochauflösende Beobachtungen, um die Quellen (gravitationsbezogen, rückkopplungsgesteuert) von ionisiertem Gas mit hoher Geschwindigkeitsdispersion zu verstehen. Durch die Einbeziehung realistischer Geburtsbedingungen für Kugelsternhaufen (GCs) und flexibler, selbstkonsistenter Geschwindigkeitsverteilungsfunktionen für den Fornax dSph kann ich das Überleben seiner fünf GCs verstehen. Das umfassende Evolutionsmodell lässt darauf schließen, dass Fornax einen großen DM-Kern ($\gtrsim$1,5 kpc) hat und zuvor eine Verschmelzung des Massenverhältnisses $\sim$1:2 bis 1:5 durchlaufen hat. Schließlich gebe ich durch die Kombination von Stern- und Gas-Kinematitracern in einem einzigen dynamischen Modell den Beweis, dass der DM-halo der isolierte unregelmäßige Zwerggalaxie WLM einen inneren Kern ($\gamma \sim 0.3 \pm 0.1$) und ein verlängerte Achsenverhältnis von 2:1 hat. Die abgeleitete Orbitstruktur (tangential Anisotropie) ist sehr ähnlich zu nahe gelegenen dSph-Galaxien - was darauf hindeutet, dass interne Prozesse anstelle des Gezeitenursprungs zu dieser dynamischen Konfiguration führen können. Das DM-Halo-Profil stimmt mit dem ΛCDM kosmologischen Bild überein, wenn baryonisches Feedback enthalten ist. Die verlängerte Geometrie ist für MOND schwierig und fordert gleichzeitig selbst interagierende DM (SIDM)-Theorien heraus, einen thermisierten DM-Kern der beobachteten Größe zu erzeugen, ohne den Halo zu kugeln. Bei beiden dynamischen Modellen von WLM und Fornax kann ich die Teilchenmasse von Bose-Einstein-Kondensat-DM-Modellen auf $1,1-1,3\times10^{-22}\,\mathrm{eV/c^2}$ und die Interaktionswirkungsquerschnitt für (geschwindigkeitsunabhängige) SIDM-Partikel von $0,8 \lesssim \sigma/m_{\mathrm{SIDM}} \lesssim 3.1\,\mathrm{cm^2/g}$ beschränken - obwohl es bleibt abzuwarten, ob diese die richtige DM-Kerngröße und Halo-Geometrie gleichzeitig produzieren können, die wir finden. Die Anwendung dieser neuen Techniken und Modelle auf mehr Galaxien werden noch stärkeren Einschränkungen für Modelle der dunklen Materie führen.

Contents

List of Figures

List of Tables

Acknowledgments

This thesis is made possible through the support from many others. I would like to thank my supervisors, Glenn van de Ven and Ryan Leaman, for providing interesting science questions to ponder upon, as well as both the temporal and intellectual space for doing so. I am most grateful for the trust and freedom they have granted to me for conducting my own research. The scientific and non-scientific discussions with them have always given me both intellectual stimulation and heart felt encouragements. Collaboration and conferences, which have from time to time provided much appreciated fresh perspectives, were made possible by Glenn's generosity. I feel incredibly fortunate, to have encountered Ryan's patience, guidance and attentiveness, all of which played a crucial role in the completion of this thesis.

I am grateful also to my supportive scientific collaborators, who have provided valuable insights. In particular I would like to thank the CALIFA and EDGE team, for helpful discussions and providing the essential data for my work. I would also like to thank Ling Zhu for providing her Schwarzschild models on CALIFA galaxies, as well as her detailed explanation of the models. I am grateful likewise to Giuseppina Battaglia, for her careful review and feedback to my work.

I am in debt to my loved ones and their indispensable emotional support throughout this journey. Lastly, I would like to thank IMPRS for the many comrades it has introduced to me along this path and for its financial support.

To my younger self.

Chapter 1

Introduction

1.1 Galaxies: overview

Less than a hundred years ago, distances to 'clouds' in the night sky that can be seen with our naked eyes were first determined. Starting with M31, then known as the 'Andromeda nebula', Opik (1922) estimated a distance of 450 kpc, establishing the fact that it resides outside of the Milky Way galaxy that we live in. With the then new 100 inch Mt. Wilson telescope, Hubble (1929) was able to resolve the outer region of M31 into 'swarms of faint stars', confirming its nature as a stellar system. Many more nebulae were found to be extra-galactic stellar systems during those years (e.g. M87, M33; Hubble 1923, 1926a). Baffling to the human minds, these systems are gravitationally bound system that contain more than millions of stars, as well as interstellar dust and gas, much like our own Milky Way. They are galaxies outside of our own Galaxy.

These galaxies are found to come in various shape and forms, for which Hubble (1926b) established a classification known as the Hubble sequence. It classifies galaxies into two main groups based on their morphologies: the ellipticals (E) that are spherical or ellipsoidal featureless blobs and the spirals (S) that contains spiral arms; these classes are often referred to as early and late type galaxies respectively. The ellipticals are then further labelled based on their observed ellipticity: $10\times(1\text{-}b/a)$ where b and a are lengths of the short and long axes respectively, such that an E0 galaxy would be observed as spherical and an E6 galaxy would be observed as more elliptical. Since such an apparent ellipticity can be the result from pure projection effects, Kormendy & Bender (1996) revised the classification of ellipticals to include the boxy-distortion (b) and the disky-distortion (d) as illustrated in Figure 1.1.

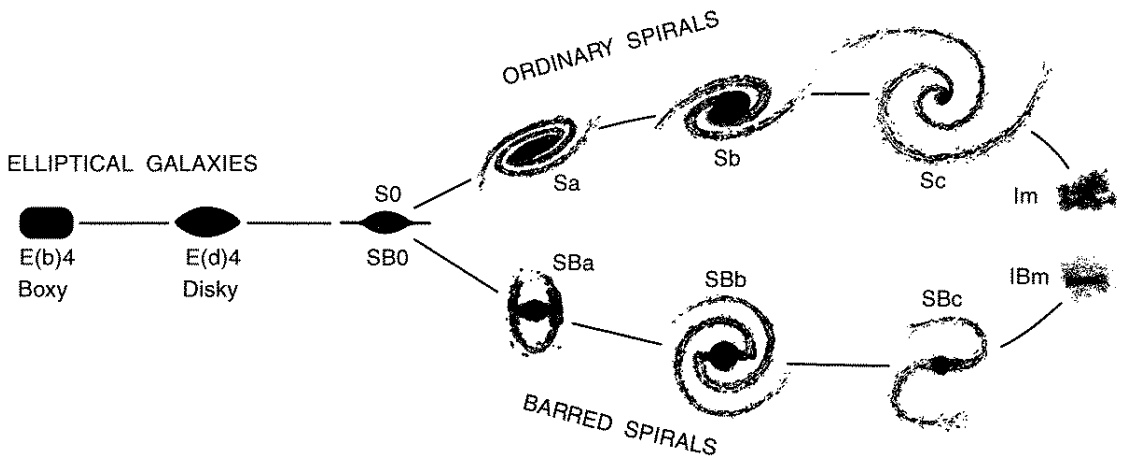

Figure 1.1: A representation of the revised Hubble sequence by Kormendy & Bender (1996).

On the other hand, spirals are separated into two groups: the barred (SB) and the unbarred spirals (S), with the barred galaxies consisting of a central bar-shaped structure composed of stars. Other than bars, common features of spirals include an extended flat stellar disk and a central round structure primarily composed of old stars known as the bulge. The spirals are further classified by the tightness of their spiral arms. Spirals with tightly wounded spiral arms are known as Sa or SBa and those with open spiral arms are known as Sc or SBc. Connecting the ellipticals and the spirals are the lenticular galaxies S0. Similar to spirals, lenticulars contain stellar disks and bulges, giving them lens-like shapes when viewed edge on. Unlike spirals however, lenticulars do not show signs of spiral arms.

The Hubble sequence is still in use today not only for historical reasons, but also as various physical parameters are found to be tightly correlated with galaxy morphologies. The most characteristic ones include: mass or luminosity, colour, metallicities and age. We shall dive deeper into discussion of the correlations between galaxy morphologies and other physical parameters in §1.2.1.

1.1.1 Galaxy formation in the ΛCDM framework

Galaxies are thought to form hierarchically in an Universe that can be described by the Λ Cold Dark Matter (ΛCDM) model. Multiple lines of evidence suggest that the Universe began with the big-bang and a subsequent rapid inflation, and that the universe has been expanding in all directions ever since. The expansion is thought to be driven by a dark energy with constant energy density Λ. At the present-day, such dark energy contributes up to $\sim 70\%$ of the total energy density in the Universe (with $\Omega_\Lambda = 0.6889 \pm 0.0056$, Planck Collaboration et al. 2018). The remaining energy density is thought to be composed of baryonic matter ($\sim$5%), cold dark matter ($\sim$26%) and neutrinos ($<$0.3%). The 'cold' in cold dark matter implies that dark matter has negligible streaming velocities when structure formation is considered. Standard models for CDM particles also do not interact through any means other than gravitational forces. Proposed candidates for CDM particles include for example Weakly Interacting Massive Particles (WIMPs), pressure-less axions and Massive Compact Halo Objects (MACHOs) such as free floating black holes.

As the universe is expanding, the overdensities in dark matter (DM) quantum fluctuations grow through gravitational accretion to form sheets, filaments and haloes. These DM haloes at first grow through diffuse accretion of dark matter and gas from the cosmic web (of filaments). The size of a DM halo first grows with the expansion of the universe until the halo has accreted enough mass to go through gravitational collapse. The point at which a DM halo reaches its maximum size is known as 'turn-around'.

The number density of DM haloes with respect to halo mass is known as the mass function ($n(M_{\rm halo})\mathrm{d}M_{\rm halo}$), which is found to be decreasing monotonically with halo mass, as shown on the left panel of Figure 1.2 (Jenkins et al. 2001). This means that there are more low-mass haloes than high-mass haloes and this can be reproduced analytically with the extended Press-Schechter formalism[1] (Bond et al. 1991; Lacey & Cole 1993). These haloes are then the locations where galaxies can

[1]The original Press-Schechter formalism relates the halo mass function to the volume density of the initial density field fluctuation of above some density threshold (Press & Schechter 1974). While successful in predicting the form of the halo mass function, its prediction is discrepant with simulated values by a factor of two. Such discrepancy is caused by 'cloud-in-cloud' problem; when underdense regions are enclosed within overdense regions, they and the surrounding patches of overdense regions can be counted as parts of one larger collapsed object. The extended Press-Schechter formalism applies excursion set theory on the Press-Schechter formalism, allowing mass assignments to virialised objects on various spatial scales.

form.

In the standard picture of gas accretion, infalling gas onto the haloes is shock-heated to the haloes' virial temperature and mixed within the halo until its virialisation, this is known as the 'hot-accretion phase'. As the gas cools down, it then falls onto the centre of the halo and and can contribute to the formation of the galaxy's stellar component. High resolution cosmological simulations have however shown that such virialisation happens only for high mass haloes (e.g. Kereš et al. 2005; Brooks et al. 2009). Haloes of $M_{\rm halo} \lesssim 10^{11}\,M_{\odot}$ are shown to be dominated at most redshifts by gas accreted through 'cold-flows' that stay well-below the virial temperature. Even for high mass haloes at particular redshifts, filaments can develop within the dense haloes to allow cold flow accretion towards the halo centres, providing high-angular momentum materials for earlier growth of galaxies.

DM haloes and galaxies also grow hierarchically through halo mergers. While mergers between two DM haloes can happen at all mass ratios, it is seen in simulations that most of the mass growth through mergers come from mergers of mass ratio $0.02 \lesssim M_{\rm sat}/M_{\rm halo} \lesssim 0.3$ (e.g. Boylan-Kolchin et al. 2008). This is because minor mergers ($M_{\rm sat}/M_{\rm halo} \lesssim 0.3$) happen more often than major mergers ($M_{\rm sat}/M_{\rm halo} \gtrsim 0.3$), a direct result from the monotonically decreasing power-law halo mass function.

After infall, the satellites can survive as substructures in the host. In which case they serve as useful probes to the accretion history of the halo, providing information on parameters such as the infall time and orbit types of the satellites. The survival timescale and subsequent evolution of satellites are influenced by tides and ram pressure stripping exerted by the host halo, and therefore in turn allow us to probe the underlying gravitational potential of the host.

1.1.2 DM haloes in pure ΛCDM cosmological simulations

Density profile

The hierarchical assembly of DM haloes implies self-similarity of structure and substructure across a wide range of halo masses in a pure DM picture. In particular, the density profile $\rho(r)$ of DM haloes of all masses are found, in cosmological N-body simulations, to ubiquitously follow a Navarro-Frenk-White (NFW) profile (Navarro et al. 1996):

$$\rho_{\rm NFW}(r) = \rho_0 \Big(\frac{r}{r_{\rm s}}\Big)^{-1} \Big(1 + \frac{r}{r_{\rm s}}\Big)^{-2}, \tag{1.1}$$

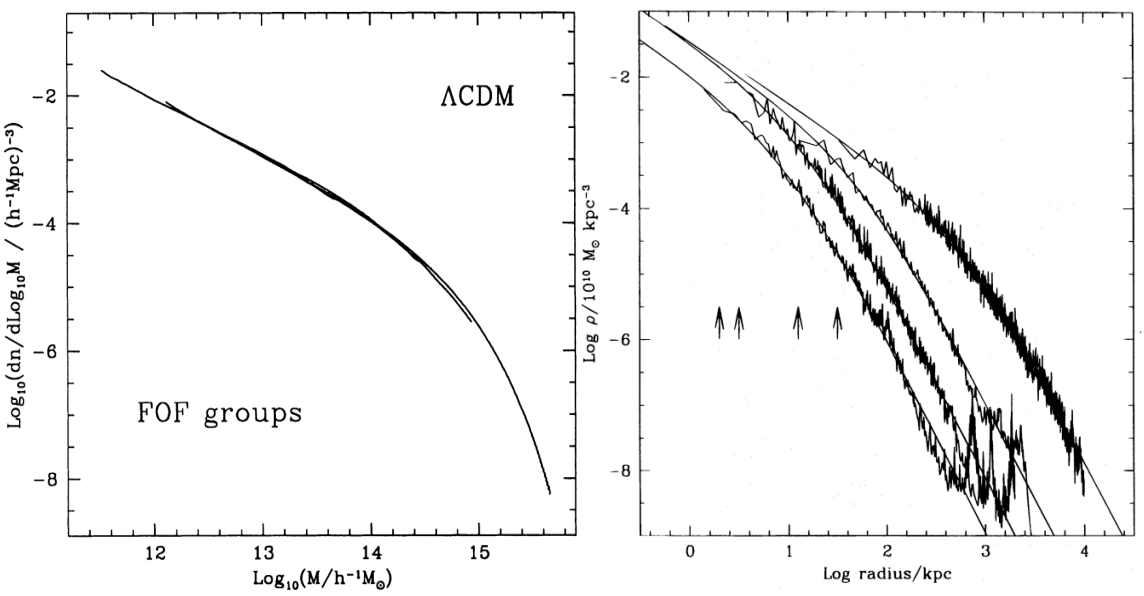

Figure 1.2: *Left:* Simulated halo mass function under ΛCDM cosmology by Jenkins et al. (2001). *Right:* Density profile of simulated DM haloes of different masses under the ΛCDM cosmology. The curves through the simulated data are best fitted NFW profiles from (Navarro et al. 1996).

which is characterised by only two parameters: the scale radius r_s and the characteristic density ρ_0. The characteristic of the NFW profile is a central cusp with logarithmic slope of $\partial \ln \rho / \partial \ln r \sim -1$ and an outer slope of $\sim -3.$, as shown on the right panel of Figure 1.2. (Modifications to the inner or outer slopes can occur due to the impact of baryons, more on this in §1.5.2.)

Not only is the density profile of halos of a wide range of masses self-similar in terms of their density profiles, but ρ_0 and r_s are further found to be correlated such that DM haloes in the universe can be described completely with just one parameter. Such correlation can be expressed as a mass-concentration ($M - c$) relation, where the mass of a DM halo is characterised by the virial mass $M_{\rm vir}$, i.e. the spherically enclosed mass of the halo within virial radius $r_{\rm vir}$; and the concentration c is defined for NFW haloes as the ratio between $r_{\rm s}$ and $r_{\rm vir}$: $c \equiv r_{\rm vir}/r_{\rm s}$. The virial radius $r_{\rm vir}$ itself is often defined as the radius within which the average density of the halo drops to $\Delta_{\rm c}\rho_{\rm c}$, where $\Delta_{\rm c}$ is known as the overdensity constant and $\rho_{\rm c}$ is the critical density of the Universe[2]. With a suite of N-body simulations using cosmological parameters

[2]While $\Delta_{\rm c}$ is formally defined through the density parameter $\Omega \equiv \rho/\rho_{\rm c}$, the ratio between the actual observed density of the universe ρ relative to the critical density $\rho_{\rm c}$, and hence is cosmological

(e.g., Ω_Λ, Ω_m, σ_8) derived from the Planck satellite, Dutton & Macciò (2014) found the $M - c$ relation to be:

$$\log_{10} c = 1.025 - 0.07 \log_{10}(M_{\rm vir}/[10^{12} h^{-1} M_\odot]). \tag{1.2}$$

This self-similarity is rather remarkable, as together with the NFW profile, one can completely describe the density profile of a DM halo through its $M_{\rm vir}$.

Halo shape

DM haloes under the ΛCDM cosmology are found through analytical models of Gaussian random fields as well as pure DM N-body simulations (e.g. Bardeen et al. 1986; Dubinski 1994) to be triaxial in geometry, and closer to being prolate than oblate. Given three orthogonal axes: $a \geq b \geq c$ as the long, intermediate and short axes, a prolate halo is characterised by two short axes and one long axis ($a > b = c$), as opposed to an oblate geometry, which is characterised by two long axes and one short axis ($a = b > c$).

While the angular momentum is generally found to be perpendicular to the short axis c, the shape of the DM haloes are found not to be rotationally supported (e.g. Warren et al. 1992; Tormen 1997). Instead, it is proposed that the shapes of DM haloes are supported by anisotropic velocity dispersion. By following satellite accretion events through time in their cosmological simulation, Allgood et al. (2006) suggested that the source of the anisotropic distribution of velocity dispersion is directional accretion and large scale cosmological torques.

Spin parameter

Another characterisation of a DM halo is its spin, characterised by the dimensionless spin parameter λ as

$$\lambda \equiv \frac{|\mathbf{J}| E^{1/2}}{G M^{5/2}}, \tag{1.3}$$

where G is the gravitational constant, $\mathbf{J}$ is the angular momentum, E and M are the total energy and mass of the halo (Peebles 1969). The spin parameters of DM haloes in ΛCDM cosmological simulations have been found to be halo mass- and environment-independent, with a log-normal distribution that peaks at $\lambda_{\rm mean} \sim 0.042$ Bullock et al. (2001), acquired through tidal interactions with neighbours (e.g.

model dependent, $\Delta_{\rm c} = 200$ is typically adopted as a common definition. In which case the virial radius and the virial mass are also labelled as r_{200} and M_{200}.

Doroshkevich 1970; White 1984) and mass accretion during mergers (Hetznecker & Burkert 2006).

The spin acquired by a DM halo is intimately related to the spin of the galaxy formed within the halo. Shock-heated accreted gas in particular is expected to have the same angular momentum as the DM halo, setting the available angular momentum for the formation of rotationally supported disks as well as disk parameters such as their size and rotation velocities (Mo et al. 1998). Additional components that come into play include the aforementioned cold flow accretion which can add pristine high angular momentum material that support larger disks (Brooks et al. 2009), as well as angular momentum transfer between disks and DM haloes caused by asymmetric features such as bars and/or triaxial haloes.

1.2 Understanding galaxies through dynamics

1.2.1 Scaling relations in galaxies: relationships between dynamical, spatial and chemical properties

While galaxies exist over a broad range of sizes, masses and morphologies, as well as chemical and dynamical properties, their distribution throughout the vast parameter space is not uniform. Instead, physical laws apply such that the various parameters of galaxies end up being correlated with one another. Such correlations are known as scaling relations of galaxies and are useful in understanding the evolutionary processes that alter galaxies in their lifetime.

The Fundamental Plane

The basic observable global structural parameters of a galaxy are its luminosity L, apparent size $R_\star$ and the rotation velocity V. For disk galaxies, these three properties are found to lie mostly on a specific plane within the 3-dimensional $(L, R_\star, V)$ space such that $R_\star \propto L^{1/3}$, $V \propto R_\star$ and $L \propto V^3$. Such a plane is known as the Fundamental Plane (FP) and the latter of the three correlations is also known as the Tully-Fisher Relation (TFR, Tully & Fisher 1977)[3]. We show in Figure 1.3

[3]The more fundamental formation of the TFR is known as the baryonic-TFR (BTFR), which relates the total baryonic masses M_b to the velocities of galaxies. Lelli et al. (2019) show that depending on the chosen representative velocity, the power index can range from 3 to 4, with the tightest relation given by the velocities of the flat part of the rotation curve v_f as $M_b \propto v_f^{3.85\pm0.09}$.

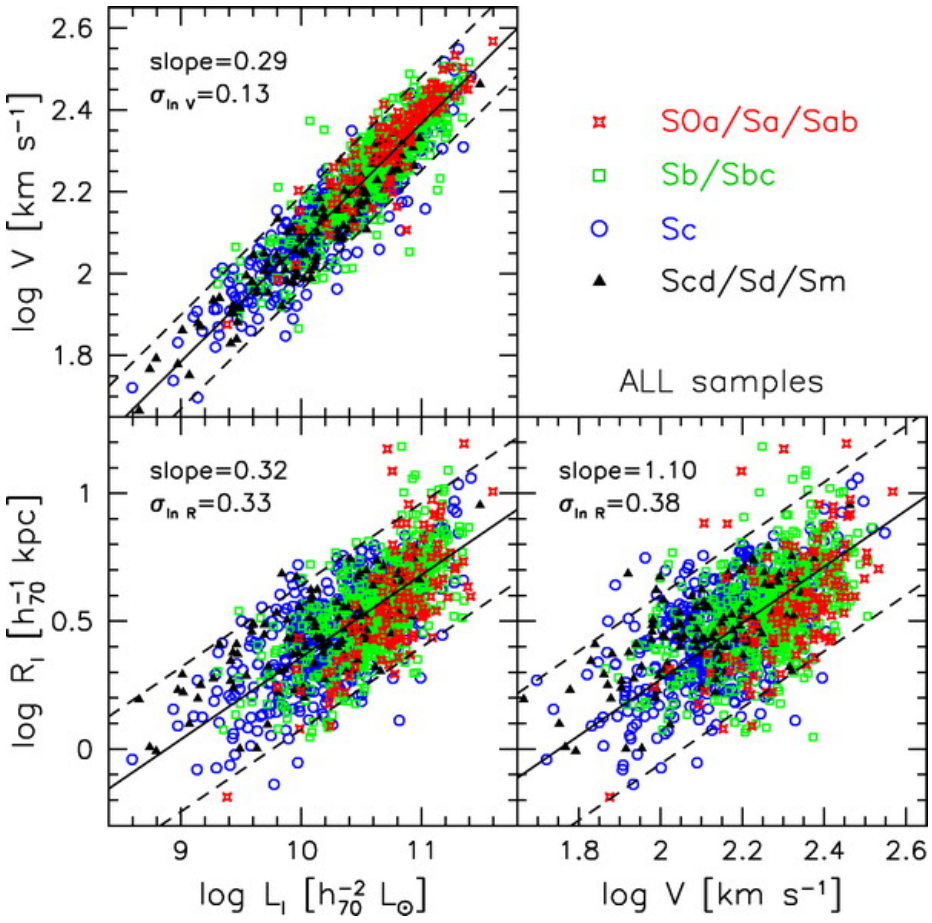

Figure 1.3: The projections of the Fundamental Plane of disk galaxies (Courteau et al. 2007). The different colours correspond to different morphologies, the black straight line is the best-fit to the scaling relations with the dashed lines indicating the $2\,\sigma$ scatter.

the 2D projection of the FP assembled by Courteau et al. (2007) using 1300 field and cluster spiral galaxies, where they have parametrised L_I as the total luminosities in I-band images, R_I as the disk scale lengths from I-band images and V as the maximum velocities reached in HI rotation curves.

The FP of disk galaxies is an observed dynamical phenomenon and can be rewritten with the more fundamental parameters: stellar mass $M_\star$ and stellar specific angular momentum $j_\star$, where $j_\star \equiv |\mathbf{J}_\star|/M_\star$ and $\mathbf{J}_\star$ is the total stellar angular momentum. A correlation between the two: $j_\star \propto M_\star^{2/3}$, was first observed by Fall (1983) with 44 spiral and 44 elliptical galaxies, and extended to larger samples by Romanowsky & Fall (2012). We show the $j_\star - M_\star$ they found on the left panel of Figure 1.4. Since $j_\star \propto R_\star V$ by definition and assuming that mass follow light $L \propto M_\star$, one can rewrite $j_\star \propto M_\star^{2/3}$ as $L^{2/3} \propto R_\star V$. Under the crude assumption

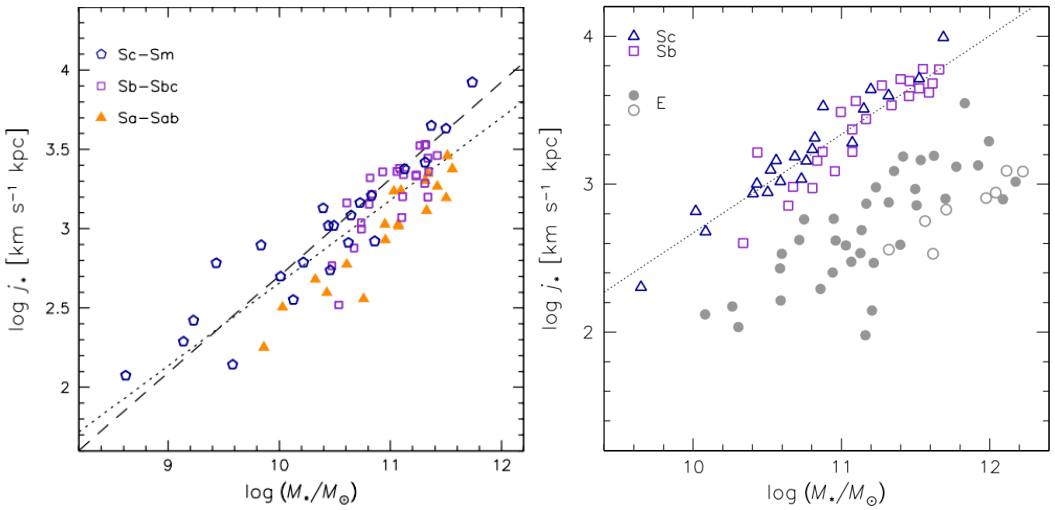

Figure 1.4: The $j_\star - M_\star$ scaling relation from Romanowsky & Fall (2012). *Left:* The $j_\star - M_\star$ relation in disk galaxies. *Right:* Grey points are elliptical galaxies, they have lower angular momentum given the same $M_\star$ and therefore lie below the $j_\star - M_\star$ relation of disk galaxies.

of spherical symmetry $V \propto M^{1/3}$ and by assuming that $M_\star/M = const$, one can recover the FP relations between $(L, R_\star, V)$.

This correlation may be expected when one considers a stellar analog to the halo spin parameter described in §1.1.2:

$$\lambda_\star \equiv \frac{|\mathbf{J}_\star| E^{1/2}}{G M_\star^{5/2}}. \tag{1.4}$$

By rearranging the terms, the specific angular momentum can be expressed as $j_\star \propto \lambda_\star M_\star^{2/3}$. A $j_\star \propto M_\star^{2/3}$ relation hence implies a stellar mass-independence of $\lambda_\star$.

In other words, the fundamental parameters of a disk galaxy: mass, size and angular momentum, are all interlinked as a result of the mass independence of $\lambda_\star$. The occurrence of such elegance may be understood in two steps. First, as described in §1.1.2, DM haloes across the wide range of virial masses have the same distribution of spin $\lambda_{\rm halo}$. Second, the spin from the DM halo λ, would have to be imparted onto the disk, $\lambda_\star$ in similar fractions across galaxy masses in order to preserve the mass independence of the latter. By constructing mass models for a large sample of disk galaxies of virial masses $\log_{10}(M_{\rm vir}/M_\odot) = 11.3 - 12.7$, Dutton & van den Bosch (2012) reconfirmed that $\lambda_\star/\lambda \sim 0.6$ needs to be constant across halo masses, in order to reproduce observed scaling relations.

Possible causes for the difference of $\sim 40\%$ could be loss of angular momentum due to dynamical friction during galaxy formation or feedback processes (e.g. Governato et al. 2010). Given the mass-dependent nature of dynamical friction and feedback processes, the reason behind the required constancy in the spin loss is not straightforward to understand. More study into the underlying physical mechanism is needed to understand such phenomena. For example, the inside-out cooling of gas during the hot-accretion phase is likely to cause the more massive galaxies to lose more angular momentum. Dutton & van den Bosch (2012) suggested that the constancy in $\lambda_\star$ may then be regulated by disk instabilities, which prevent high-mass systems with too low angular momentum to form disks.

Such a regulation could mean that the mass independence of $\lambda_\star$ should relax as we examine galaxies that are not purely disk-like. When closely examining the left panel of Figure 1.4, the galaxies with a higher bulge fraction such as the Sa-Sab galaxies seem to be shifted in the $j_\star - M_\star$ plane from the thin disks Sc-Sm. The shift is even more obvious when we compare Sb and Sc galaxies with elliptical galaxies, as shown as grey points in the right panel of Figure 1.4.

The FP also exists for elliptical galaxies. Due to their relatively low rotation, gravitational support is provided by random motion instead the amount of which is characterised by the velocity dispersion. The dynamical parameter used for the ellipticals' FP is therefore the central velocity dispersion σ_0, instead of the rotation velocity V. Specifically, a relationship between the luminosity and velocity dispersions in ellipticals is first found by Faber & Jackson (1976) and is known as the Faber-Jackson relation $L \propto \sigma^4$. The FP for ellipticals are first introduced by Bender et al. (1992) as $R_e \propto \sigma_0^{1.4} \langle I_e \rangle^{-0.85}$ for the ellipticals in the Virgo cluster, where R_e is the effective radius and $\langle I_e \rangle$ is the mean surface brightness within R_e. As such the proportionality constants are different from the ones in the FP of disk galaxies.

Stellar ages, metallicities and their relationship with dynamics

Scaling relations also exist in between the structural and chemical properties of galaxies. While there is a general trend in which massive galaxies tend to also be redder, galaxies are known to lie mostly in two areas within the colour-mass plane. Using >25000 galaxies from the combined data of SDSS, GALEX and Galaxy Zoo, Schawinski et al. (2014) demonstrate this bimodality in the $(u-r) - M_\star$ space as shown in Figure 1.5. Separated by two green lines on the top left panel are the two populations of galaxies, with the ones above the green lines known as the 'red sequence' and the ones below known as the 'blue cloud'. Schawinski et al. (2014) also show that the early-type galaxies lie mostly in the red sequence and the late-type

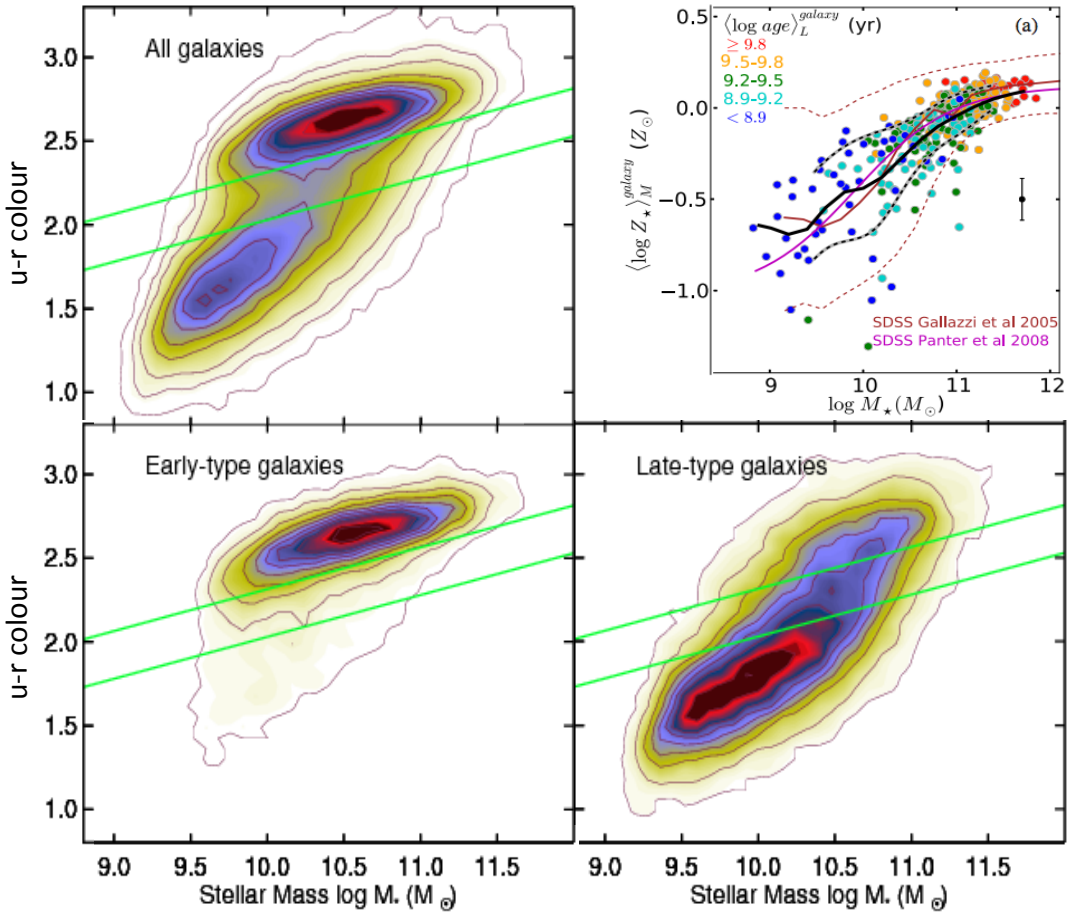

Figure 1.5: *Top right:* The mass metallicity relation of galaxies observed from the CALIFA survey from González Delgado et al. (2014). *Other panels:* $u-r$ colour versus $M_\star$ contour plots from Schawinski et al. (2014) illustrating the bimodality between the early and late type galaxies from the SDSS survey.

galaxies lie mostly in the blue cloud, as demonstrated by the left and right panels on the bottom row of Figure 1.5 respectively.

The difference in colours can be caused by a difference in stellar ages and/or metallicities. Less massive late-type spiral galaxies may therefore be younger and/or more metal-rich while the more massive early-type ellipticals may be older and/or more metal-poor. The correlation between mass with both colours and ages have been seen with >175000 SDSS galaxies by Gallazzi et al. (2005). González Delgado et al. (2014) reconfirm the correlations using spectroscopic data of 300 galaxies from the CALIFA IFU survey, as shown in the top right panel of Figure 1.5.

Other than correlations with overall structure parameters such as stellar mass

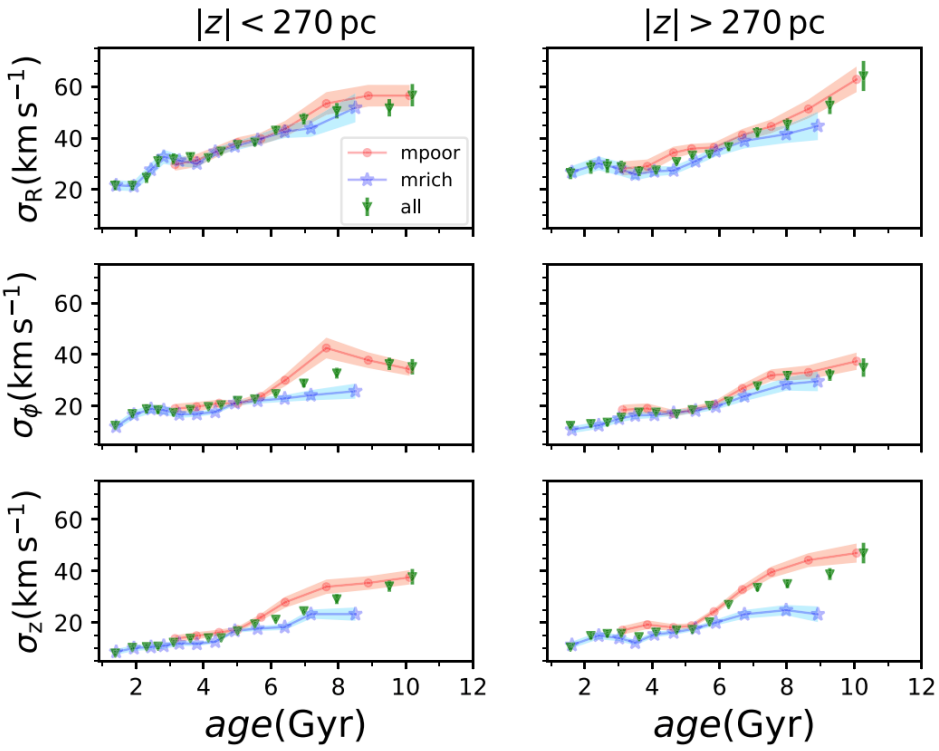

Figure 1.6: Age-velocity relation in the Solar neighbourhood observed by GAIA survey from Yu & Liu (2018). Here (R, ϕ, z) denote the cylindrical coordinates along the radial, azimuthal and vertical directions. The stellar velocity dispersion σ along all three directions increases with stellar age. Such relation holds at both low ($|z| < 270\,\mathrm{pc}$) and high ($|z| > 270\,\mathrm{pc}$) disk heights, as well as for both the metal poor (orange) and metal rich (purple) stars.

and morphology, chemical properties of galaxies also have correlations with internal dynamical properties. Within the Milky Way, stellar ages are further found to be correlated with velocity dispersions such that older stars tend to have a larger velocity dispersion while younger stars tend to have a smaller velocity dispersion. This is known as the age-velocity dispersion relation (AVR) and was already known decades ago from studying stars in the solar neighbourhood (e.g. Strömberg 1946; Wielen 1977). With recent advancement from GAIA, Yu & Liu (2018) found that not only does the AVR hold for both metal-rich and metal-poor stars, with the AVR of the metal-rich stars being steeper, the AVR also holds for all three dispersion components (z, ϕ, R in cylindrical coordinates, as shown in Figure 1.6).

The AVR can be interpreted as a result of disk heating processes or as a consequence of stars being born out of more turbulent molecular gas at higher

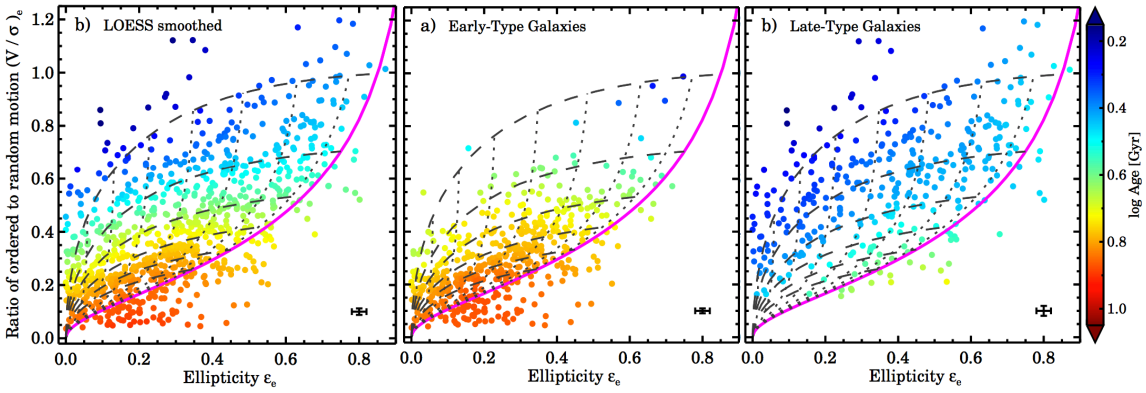

Figure 1.7: A diagram relating galaxy morphology to dynamics obtained from the SAMI IFU survey by van de Sande et al. (2018), where the morphology is parametrised through ellipticity ϵ and the galaxy's dynamical state is parametrised through the ratio of ordered to random motion V/σ.

redshifts. Martig et al. (2014) showed in their simulations that σ can increase smoothly with time through disk growth as well as processes like minor mergers, vertical bending waves and overdensities like spiral arms and bars. By fitting power-laws to their derived AVR for the Milky Way along the three axes separately, Yu & Liu (2018) find that the in-plane velocity dispersions σ_ϕ and σ_R have similar power-law indices (~ 0.3) with respect to stellar age, consistent with the theoretical expectation from epicyclic approximation where the in-plane velocity dispersions are coupled (Binney & Tremaine 1987). On the other hand, the vertical velocity dispersion σ_z has a higher power-law index (~ 0.5), meaning that the vertical heating rate is higher. The authors suggest that a combination of spiral arms (provide in-plane heating) and giant molecular clouds (which alone would render a too high vertical-to-in-plane velocity dispersion ratio, Lacey 1984) heating could be responsible for such differences.

1.2.2 Dissecting galaxies with their dynamics: structure correspondences between orbits and shapes

We previously discussed the relationship between angular momentum and mass in galaxies, the latter of which is also correlated with morphologies, stellar metallicities and ages. We showed then that ages and metallicities are correlated with the amount of random motion in stellar orbits. As such, one would expect that these correlations

should come back in a full circle, such that the angular momentum of stellar orbits should be correlated with the mass and morphologies of galaxies. Such a correlation might also be expected, at least in terms of the motion along the z direction, from looking at images of disk and elliptical galaxies alone. With less stars populating the space away from the disk plane, stars in disk galaxies clearly have less kinematic randomness along the z direction than stars in an elliptical galaxies.

The relative contribution of coherent streaming motions, to random dispersion supported motions of stellar orbits is often quantified using V/σ, the ratio between the rotational motions and the random motions. Using 843 galaxies from the SAMI IFU survey, van de Sande et al. (2018) found that V/σ indeed correlates with the ellipticity of galaxies ϵ, such that galaxies with more ordered stellar motion (higher V/σ) are flatter (high ϵ) while galaxies with more random stellar motion (lower V/σ) are rounder (lower ϵ). They also found that such $V/\sigma - \epsilon$ relation has however an extra dependence on the galaxy age.

While substructures of galaxies such as thin disks, thick disks, bulges and bars had been separated through photometry, these substructures should be better decomposed through dynamics because they are comprised of different types of stellar orbits, allowing us to better understand the timescales and mechanisms which build up these parts of the galaxies. For example, Soubiran et al. (2003) found that the Milky Way thin disk has a faster net rotation and lower velocity dispersion compared to the thick disk. In general, flatter structures such as disks should be composed of stars with more ordered orbits of higher angular momentum $\mathbf{J}_\star$, while rounder structures such as bulges should be composed of stars with more randomised orbits of lower angular momentum. While directly measuring $\mathbf{J}_\star$ of individual stars of galaxies outside of the Local Group is still a challenge, such decomposition methods have been applied onto simulated galaxies successfully (e.g. Abadi et al. 2003; Obreja et al. 2016). Dynamical modelling techniques also exist which model galaxies as composition of various stellar orbits and hence allow such decomposition for nearby galaxies, which will be discussed in more detail in §1.3.

1.2.3 Velocity anisotropies

Another way of quantifying the dynamical structure of galaxies is with its stellar velocity ellipsoid. The stellar velocity ellipsoid is defined at each spatial point of the galaxy and is an ellipsoid with axis ratios defined by the amount of velocity dispersion in each of the three orthogonal direction. In a spherical coordinate system, such an ellipsoid would be spanned by the velocity dispersions σ_r, σ_ϕ, σ_θ. In a cylindrical coordinate system, such ellipsoid would be spanned by σ_R, σ_z and σ_ϕ.

The shape of the stellar velocity ellipsoid can be parametrised by velocity anisotropies, which quantify the various ratios between the velocity dispersions[4] along different directions. Various anisotropy parameters have been defined in the literature and the relevant ones in this thesis are $\beta_r \equiv 1 - (\sigma_\phi^2 + \sigma_\theta^2)/\sigma_r^2$ defined in the spherical coordinates and $\beta_z \equiv 1 - \sigma_z^2/\sigma_R^2$ defined in the cylindrical coordinates. In particular β_r characterises the relative motion in the tangential versus the radial direction and β_z characterises the relative motion perpendicular and parallel to the plane along the radial direction. $\beta_r > 0$, $\beta_r = 0$ and $\beta_r < 0$ are also known as radial, isotropic and tangential anisotropy respectively.

While β_z is more sensitive to the overall structure of the gravitational potential and can be related to hydrostatic equilibrium of the disk self-gravity, β_r is more sensitive to the orbital structure of the stellar system. In particular, the relative contribution of random motions along tangential and radial direction can shed light on how the stellar system reaches its current dynamical state, as various processes can impart random motions along different directions. For example, in-plane processes like spiral arms are unlikely to contribute to out-of-plane random motions, while disk heating processes like bar-buckling can increase σ_z (e.g. Mayer et al. 2006; Łokas et al. 2010). On the other hand, three-dimensional processes such as merger may isotropise the velocity ellipsoid (see also §1.2.1). In addition, processes like tidal stripping are thought to be more effective on radial than tangential orbits and hence should leave behind a tangentially-biased remnant (e.g. Takahashi & Lee 2000; Baumgardt & Makino 2003).

1.3 Modelling galaxy dynamics

Galaxy dynamics is hence not only useful for tracing the mass distribution in galaxies, but also for understanding how the various orbital structures in galaxies come about. The cornerstone of modelling galaxy dynamics lies in two equations: the Poisson equation and the Boltzmann equation. The Poisson equation states that the gravitational potential of a system of particles at any spatial location can be specified through its total mass density at that location:

$$\nabla^2\Phi = 4\pi G\rho, \tag{1.5}$$

where ∇^2 is the Laplacian operator, Φ is the gravitational potential, G is the gravitational constant and ρ is the mass density. In cylindrical coordinates (R, ϕ, z),

[4]Or formally the second velocity moments (e.g. $\langle v_R^2 \rangle$, $\langle v_z^2 \rangle$ and $\langle v_\phi^2 \rangle$ in the cylindrical coordinates), which equal to the velocity dispersions when streaming motions are negligible.

the Poisson equation can also be written as

$$\frac{1}{R}\frac{\partial}{\partial R}\Big(R\frac{\partial \Phi}{\partial R}\Big) + \frac{1}{R^2}\frac{\partial^2 \Phi}{\partial \phi^2} + \frac{\partial^2 \Phi}{\partial z^2} = 4\pi G\rho(R, \phi, z). \tag{1.6}$$

In a spherically symmetric system, the Poisson Equation (Eq. 1.5) can be rewritten as:

$$\frac{1}{r}\frac{\mathrm{d}}{\mathrm{d}r}\Big(r\frac{\mathrm{d}\Phi(r)}{\mathrm{d}r}\Big) = 4\pi G\rho(r), \tag{1.7}$$

for a test particle moving in a circular orbit subjected to the gravitational potential Φ. Multiplying both sides with $r\mathrm{d}r$ and integrating gives

$$\frac{GM_{enc}(r)}{r} = r\frac{\mathrm{d}\Phi(r)}{\mathrm{d}r} \equiv v_c^2, \tag{1.8}$$

where v_c is defined as the circular velocity. In cylindrical coordinates the circular velocity can be similarly defined as $v_c^2 \equiv R(\mathrm{d}\Phi/\mathrm{d}R)$.

The Boltzmann equation describes statistically the thermodynamical behaviour of a system of particles, and in this case the kinematic tracer. The distribution function $f(\mathbf{r}, \mathbf{p}, t)$ is defined as $\mathrm{d}N = f\mathrm{d}\mathbf{r}^3\mathrm{d}\mathbf{p}^3$, where N is the number of particle in a phase space element $\mathrm{d}\mathbf{r}^3\mathrm{d}\mathbf{p}^3$, a product of the volume in physical space $\mathrm{d}\mathbf{r}^3$ and momentum space $\mathrm{d}\mathbf{p}^3$. The Boltzmann equation states that:

$$\frac{\partial f}{\partial t} + \frac{\mathbf{p}}{m}\cdot\nabla f + \mathbf{F}\cdot\frac{\partial f}{\partial \mathbf{p}} = \Big(\frac{\partial f}{\partial t}\Big)_{\mathrm{coll}}, \tag{1.9}$$

where m is the mass of the particles, $\mathbf{F}$ is the force field that the particles are subjected to and $(\partial f/\partial t)_{\mathrm{coll}}$ is the change in the distribution function caused by collision. In a collisionless system $(\partial f/\partial t)_{\mathrm{coll}} = 0$.

1.3.1 Gas as kinematic tracers

The interstellar medium (ISM) consist of gases of different phases, including atomic, molecular and ionised gas. The different ISM phases not only have different thermodynamical properties such as temperatures, densities and pressures, they also have different spatial distribution and dynamical properties. Gas as a collisional fluid, dominated by elastic collisions, implies that (1) kinetic energy can be exchanged through collisions and hence a particular gas phase should achieve kinetic equilibrium with velocity distribution function approximating a Maxwellian distribution, (2) other than having velocity dispersions acting as gravitational support, smaller-scale turbulence, magnetic or thermal pressures could be another source of velocity dispersion and (3) such velocity dispersions can decay through dissipation, shocks and turbulent cascades.

Whether or not a particular ISM phase is supported by random or ordered motion depends on its source/how it is transformed into that state, and the respective timescales of dynamical cooling and the lifetime of the gas. Cold gas accreted from the cosmic web can be heated through various means, such as by stellar radiation or supernova. Hot gas often has more support from random motions than cold gas. Thermal broadening from the higher temperature contributes to a higher velocity dispersion, however in addition kinetic energy can be injected in the form of random motion due to the heating source itself (e.g. stellar feedback).

Extracting rotation curves from dynamically cold gas

We describe gas that follows near circular, rotationally supported orbits on a thin disk as dynamically cold gas. Dynamically cold gas should therefore have rotation velocities that closely follow v_c and through Eq. 1.8, allow us to probe the gravitational potential Φ directly.

Examples of dynamically cold gas in the ISM include atomic or molecular gases that has settled in the galaxy disk but not yet turned into stars, such as HI or CO gas. These gas also have low effective temperatures of $\lesssim$20 K. HI can be observed through the hyperfine emission line at 21 cm and CO can be observed through emissions from its various rotational transitions at $\sim$mm wavelengths. Galaxies that have their rotation inclined with respect to our line of sight would be redshifted (shifted to longer wavelength) on one side and blueshifted (shifted to shorter wavelength) on the other. Such shifts in the observed wavelengths of a particular emission line would us to trace the rotation velocities $V_{\rm rot}$ of a particular tracer in the galaxy.

The long radio wavelength of the cold gas emission implies that single-dish radio telescope observations would have typically low spatial resolution. In the first radio observations when the velocity gradient across the galaxy could not be spatially resolved, the redshifted and blueshifted emission would be seen as broad integrated spectral line, from which the line width was interpreted to correspond to two times the maximum rotational velocity - thus providing a good estimate to the total enclosed mass. As an example, we show an HI spectrum obtained by Tully & Fisher (1977) using single dish, as part of the sample forming the famous Tully-Fischer relation on the left panel of Figure 1.8. In order to measure the spatial variation of the rotational velocity and to better trace the underlying mass distribution, interferometers are now commonly used. While not recovering the total flux, interferometry allows the combination of data observed from multiple single dish telescopes with the distances between them acting as baselines to increase the

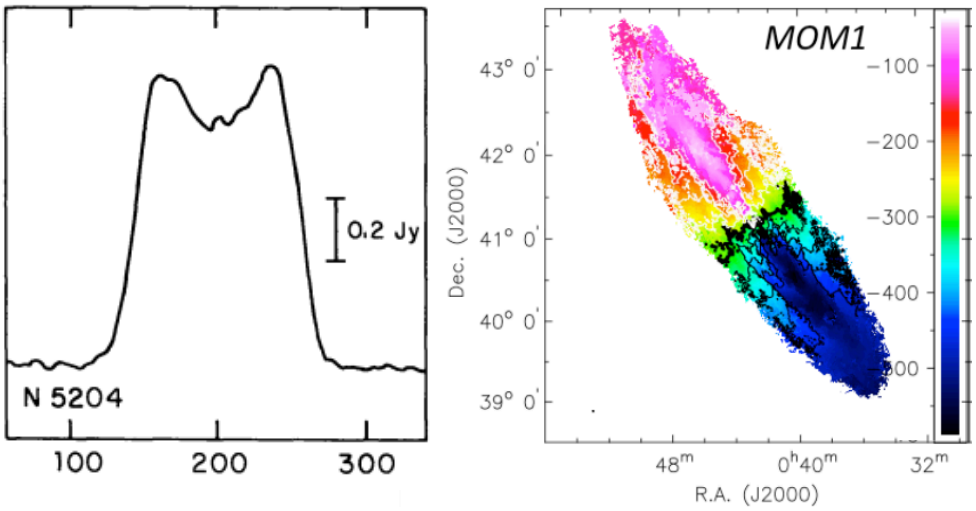

Figure 1.8: *Left:* HI spectrum of NGC5204 measured using a single-dish telescope from Tully & Fisher (1977). *Right:* HI velocity map of NGC224 obtained using interferometer from Ponomareva et al. (2016), where a spectrum is obtained at each spatial location, from which the velocity shift (colour-coded) can be mapped.

spatial resolution. With the improved spatial resolution, the rotational velocities of a galaxie's gas can be plotted as a two-dimensional map. On the right panel of Figure 1.8 we show such a map from Ponomareva et al. (2016). Interferometric data provide a much higher spatial resolution and more information in comparison to the single dish spectra on the left, and allows the derivation of the rotation velocity as a function of radius $V_{\rm rot}(R)$, i.e. the rotation curve.

Dynamically warm/hot gas

There also exist in galaxies ISM phases that have considerable velocity dispersion, and are considered dynamically warm/hot. Examples of dynamically warm gas includes ionised gas such as Hα, which is heated by a combination of the ionising photons from young O and B stars, as well as shocks or collisional ionisation. Hα has an effective Temperature of $\sim 10^5$ K and emits at the optical wavelengths. Integral Field Spectroscopy Units (IFUs) are now commonly used to measure the two dimensional distribution of Hα kinematics and flux across galaxies disks. These spectrographs pass light from every spatial element through a dispersing element, forming a spectrum at each position on the galaxy.

With cold gas transitions being redshifted out of the wavelength range of most

radio interferometers, and with stellar absorption lines (see §1.3.2) lying below the sensitivity of present-day instruments, Hα is often used as a kinematic tracer for high redshift galaxies. A problem, however, lies in the simultaneous dynamically warm and collisional nature of the Hα gas. Being dynamically warm means that one must take into account the random motion of the gas when deriving the underlying gravitational potential. Being collisional means however that not all the velocity dispersion $\sigma_{\mathrm{H}\alpha}$ goes into gravitational support, i.e. part of it comes from smaller scale turbulence, and including all of the velocity dispersion can lead to an overestimation of the enclosed mass. Additionally, $\sigma_{\mathrm{H}\alpha}$ is typically below the spectral resolution of most instruments. Nonetheless, parametrisation such as $S_{0.5} = \sqrt{0.5V_{\mathrm{rot}}^2 + \sigma_{\mathrm{H}\alpha}^2}$ or $v_c^2 = V_{\mathrm{rot}}^2 + 2\sigma_{\mathrm{H}\alpha}^2(R/R_d)$, where V_{rot} is the Hα rotational velocity and R_d is the disk scale length, have been used when characterising the gravitational potential from Hα(e.g. Weiner et al. 2006; Kassin et al. 2012; Übler et al. 2017). We shall attempt to put observational constraint on the role of $\sigma_{\mathrm{H}\alpha}$ in using Hα kinematics for mass estimation in Chapter 5.

1.3.2 Stellar dynamical models

Given the average distances between stars in galaxies, the stellar systems of galaxies can be effectively considered as a collisionless system, which are supported against gravity by both rotation and velocity dispersion. While this means that we cannot derive the circular velocity directly from the observed rotational velocities of stars (as has been done from cold gas), the derivation of Φ from stellar kinematics is still possible with other methods. Moreover, stellar kinematics allow us to probe galactic structures, such as disks and bulges, dynamically.

Just like Hα, two dimensional stellar kinematic maps can be obtained through IFU. Unlike Hα, stellar kinematics are recovered through spectral absorption lines instead of emission lines. In unresolved integrated light observations of galaxies, the wavelength shift of the lines directly gives the mean velocity at each spatial location. The width of a stellar absorption line is however a combination not only of the instrumental resolution and velocity dispersion, but is also affected by chemical properties such as metallicities and ages of the stars. Stellar kinematics of unresolved galaxies studied in integrated light are therefore not obtained through analysing one spectral line, but instead by fitting the whole spectrum. From this fit, properties such as the shape of the continuum and relative strengths of different absorption lines provide handles on the stellar age and metallicity of the galaxy, in addition to information on velocity dispersion from the line width.

The Boltzmann Equation, Eq. 1.9 can also be rewritten as the collisionless

Boltzmann Equation or the continuity equation:

$$\mathbf{v} \cdot \nabla f + \nabla \Phi \cdot \frac{\partial f}{\partial \mathbf{v}} = \frac{\partial f}{\partial t}. \tag{1.10}$$

For systems in dynamical equilibrium i.e. $\partial f/\partial t = 0$, rewriting Eq. 1.10 in the cylindrical coordinates with axis-symmetry ($\partial\Phi/\partial\phi = \partial f/\partial\phi = 0$) gives:

$$v_R \frac{\partial f}{\partial R} + \Big(\frac{v_\phi^2}{R} - \frac{\partial \Phi}{\partial R}\Big)\frac{\partial f}{\partial v_R} + v_z \frac{\partial f}{\partial z} - \frac{\partial \Phi}{\partial z}\frac{\partial f}{\partial v_z} - \frac{v_R v_\phi}{R}\frac{\partial f}{\partial v_\phi} = 0. \tag{1.11}$$

Since the distribution function f is not observable, one would rewrite Eq. 1.11 in terms of only the gravitational potential Φ and the observables: velocity moments and luminosity density ν, by first multiplying the equation by v_R and v_z and then integrating over all velocities:

$$\begin{aligned} \frac{-\nu\overline{v_\phi^2}}{R} + \frac{\partial(\nu\overline{v_R^2})}{\partial R} + \frac{\partial(\nu\overline{v_R v_z})}{\partial z} &= -\nu\frac{\partial \Phi}{\partial R} \\ \frac{\nu\overline{v_R v_z}}{R} + \frac{\partial(\nu\overline{v_z^2})}{\partial z} + \frac{\partial \nu\overline{v_R v_z}}{\partial R} &= -\nu\frac{\partial \Phi}{\partial z}. \end{aligned} \tag{1.12}$$

These two equations are known as the Jeans Equations.

Unlike cold gas that lies on a thin disk plane with the rotation velocity v_ϕ being its primary support against the gravitational potential, the second order velocity moments describing random motions: $\overline{v_R^2}$, $\overline{v_z^2}$ and $\overline{v_z^2}$, as well as the cross term $\overline{v_R v_z}$ are non negligible for stars. For each specific ν and Φ in the axisymmetric case described using the cylindrical coordinates, there are four unknowns in the two Jeans Equations.

Various approaches in closing the Jeans Equations can be found in the literature, all done through various level of assumptions in the underlying geometry of the system or the stellar velocity ellipsoid. We shall return to validating these methods, as well as presenting their limitations in Chapter 2. In Chapter 3, we shall present how these models can benefit from independent constraints on the circular velocities from cold molecular gas kinematics. Below we provide an overview of these models.

Asymmetric Drift Correction

The simplest of which is the Asymmetric Drift Correction (ADC). ADC assumes that even though the stars are not following circular orbits, they lie on a thin disk. The Jeans Equations are then solved on the $z = 0$ plane. The ADC equation can then be written as (rearranged from Eq. A3 of Weijmans et al. 2008):

$$v_c^2(R) = \overline{v_\phi}^2 + \sigma_R^2\Big[\frac{\partial \ln(\nu\sigma_R^2)}{\partial \ln R} + (\frac{\sigma_\phi^2}{\sigma_R^2} - 1) - \frac{R}{\sigma_R^2}\frac{\partial \overline{v_R v_z}}{\partial z}\Big], \tag{1.13}$$

where $\overline{v_\phi^2} = \overline{v_\phi}^2 + \sigma_\phi^2$. v_ϕ and ν are the rotation velocities and surface brightness densities, both of which are observables. The individual σ components along different direction can also be related to the observed line-of-sight velocity dispersion σ_{los} through a free parameter: velocity anisotropy. The last term in 2.6 specifies the alignment of the velocity ellipsoid with respect to the cylindrical coordinate system and can be parametrised through a free parameter κ, where:

$$\overline{v_R v_z} = \kappa(\sigma_R^2 - \sigma_z^2)\frac{z/R}{1-(z/R)^2}, \tag{1.14}$$

$0 \leq \kappa \leq 1$, with $\kappa = 0$ parametrising a completely cylindrical coordinates-aligned velocity ellipsoid and $\kappa = 1$ parametrising a spherical coordinates-aligned one. Even with the geometry of the velocity ellipsoid assumed to follow certain observed value (e.g. 0.5 for disk galaxies, Kent & de Zeeuw 1991), the dynamical mass (specified through the circular velocity v_c) is still degenerate with the velocity anisotropy. This is known as the mass-anisotropy degeneracy, which is often suppressed through certain parametrisation of the shape of the underlying mass and/or the velocity dispersion profile.

Jeans models

Jeans models on the other hand, allow the stellar distribution to be described three-dimensionally with axis ratios that can be constrained through observations. For comparison with the observed velocity moments, Jeans models perform line-of-sight integration to obtain the modelled ones from the Jeans Equations. Assumptions such as $\overline{v_R v_z} = 0$ are often applied. Under spherical symmetry assumption, the Jeans model up to the second order moments can be written in the spherical coordinates as:

$$\sigma_r^2(r) = \frac{1}{\rho(r)}\int_r^\infty \rho(r)\frac{d\Phi}{dr'}dr', \tag{1.15}$$

the modelled radial velocity dispersion $\sigma_r(r)$ can then be projected and integrated along the line of sight (Merrifield & Kent 1990):

$$\sigma_{\rm los}^2(r) = \frac{2}{\mu(r)}\int_r^\infty \nu(r')\Big(1-\beta_r\frac{r^2}{r'^2}\Big)\sigma_r(r)^2\frac{r'}{(r'^2-r^2)^{1/2}}{\rm d}r', \tag{1.16}$$

where β_r is the velocity anisotropy and

$$\mu(r) = 2\int_r^\infty \nu(r')\frac{r'}{(r'^2-r^2)^{1/2}}{\rm d}r'. \tag{1.17}$$

Jeans models hence still suffer from mass-anisotropy degeneracy. While in general such degeneracy persists at any one particular spatial point of a galaxy even

when we generalise to axisymmetric Jeans models applied on two-dimensional stellar kinematics maps, the often assumed constancy of β_r with respect to radius at a given inclination and stellar surface density distribution helps constrain the shape of the velocity dispersion map and hence greatly reduces the mass-anisotropy degeneracy (Cappellari 2008).

Orbit-based dynamical models

The above approaches using the Jeans Equations model the stellar system as a statistical system of particles. This can recover the observed kinematics reasonably well, and provide limited information on the orbit structure, through the anisotropy parameter. However it provides no further insights into the orbital composition of the galaxy, as the system is parametrised only in terms of statistical moments (surface density, velocity, velocity dispersion etc.).

An alternative approach is orbit-based dynamical models. Instead of building the models with moments, one can represent the stellar system as a superposition of orbits (Schwarzschild 1979). Conceptually speaking, for every potential, one can first build a library of possible orbits in that potential and assign a weight to each orbit. Together the weighted orbits can be integrated and projected to create moment maps. The weights of the orbits can then be adjusted to fit the observed moments. The projected moments from the best-fitted orbit weight of each potential can then be again fitted against the observed moments to obtain the best-fitted potential. The Schwarzschild model allows therefore not only the modelling of the total gravitational potential, but also the composition of the stellar system in the orbital space.

In practice, not all possible orbits in a potential can be included when building the orbit library for computational reason. Sampling of orbits can be done, for example on separable potentials[5], with a grid in the space of energy-momentum (E, L) or integrals of motion (E, I_2, I_3) (e.g. Richstone & Tremaine 1984; Rix et al. 1997) or when the potential is not separable, on the space of initial conditions of (E, θ, ϕ) (e.g. Schwarzschild 1993; van den Bosch et al. 2008). Techniques such as dithering can then be applied to smoothen the orbit sampling and hence the modelled moment maps.

Zhu et al. (2018b) applied the Schwarzschild model on a homogenous

[5]A separable potential can be written as a product of three functions, each dependent only on one of the three dimensional coordinates. All orbits are regular in separable potentials and conserve three integrals of motions.

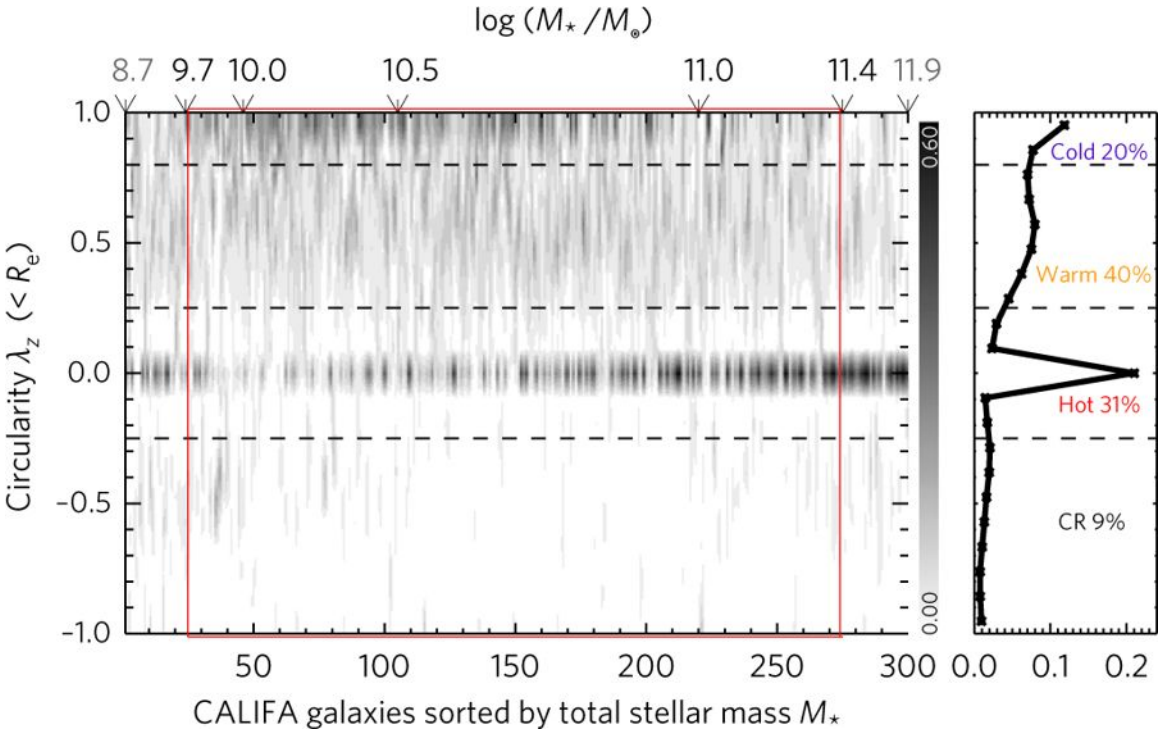

Figure 1.9: Orbital density distribution (grey scale) of 300 CALIFA galaxies over a wide range of masses and morphological types, obtained by applying the Schwarzschild orbit-based dynamical model on IFU data (Zhu et al. 2018b); black indicates high densities and white indicates low densities. It is evident that high-mass early-type ellipticals are dominated by hot random orbits of low circularity ($\lambda_z \sim 0$), while cold ordered disk-like orbits of high circularity ($\lambda_z \sim 1$) begin to dominate in lower-mass late-type galaxies. $\lambda_z < 0$ indicates counter-rotation. Red box indicates the mass range in which the CALIFA sample is statistically representative.

set of 300 nearby galaxies from the CALIFA IFU survey, covering early-type ellipticals to late-type disk galaxies, volume-complete in the stellar mass range of $9.7 < \log(M_\star/M_\odot) < 11.4$. The derived orbital density distribution is plotted against stellar masses in Figure 1.9. A clear trend of the increasing ratio of hot-to-cold orbits from lower-mass late-type galaxies to high-mass early-type galaxies was demonstrated for the first time. In addition, distinct bulge-like components of low circularities ($\lambda_z \sim 0$) can be identified, suggesting that orbit-based dynamical models can act as an effective alternative to photometric decomposition when identifying galaxy components.

1.3.3 Discrete massive objects as kinematic tracers

Discrete massive objects such as globular clusters (GCs) trace the gravitational potential not only through their orbits, their survival allows us to probe the underlying tidal field which in turns puts constraints on the gravitational potential. Furthermore, unlike stars, star clusters or satellite galaxies can be subjected to effects of dynamical friction, which should be taken into account when modelling their orbits. The fact that both dissipation and dynamical friction can cause the destruction of GCs means that their mere survival at some distances away from the centre of the galaxy provides some constraints on the underlying gravitational potential.

Dissipation in a tidal field

The tidal radius of a satellite (r_t) of mass M_s is given by (King 1962; Binney & Tremaine 1987):

$$r_t = \frac{GM_s}{\Omega^2(r) - \mathrm{d}^2\Phi/\mathrm{d}r^2}, \tag{1.18}$$

where $\Omega(r)$ is the rotational velocity of the satellite and is given by $\Omega^2(r) = (\mathrm{d}\Phi/\mathrm{d}r)/r$. The tidal radius is also known as the Jacobi radius and defines for an entity, the radius within which it is self-gravitating. in other words, beyond r_t, the background gravitational potential dominates and a satellite can experience substantial mass loss through tidal stripping.

With the mass and radius of a satellite as measurable quantities, knowing its location r would allow constraints on the shape of the gravitational potential Φ. While the projected galactocentric distance is easily observable, the line-of-sight distances can be obtained in some cases through RR Lyrae stars, or when the satellite is close enough, through constraints on the satellite orbit through proper motion measurements. The inferred location r then allows one to calculate the tidal radius of the satellite in any gravitational potential Φ through Eq. 1.18. By requiring the size of a satellite to be smaller than the tidal radius, certain mass profiles can be ruled out. For example, Amorisco (2017) suggested that the DM halo density profile is likely to have a shallow central slope in the galaxies Eridanus II and Andromeda XXV, by requiring their clusters to have $2r_h < r_t$, where r_h is the half-light radius of the satellite.

Dynamical Friction

The sea of background particles in a galaxy, including stars and dark matter, provide a drag onto more massive orbiting objects, reducing their velocities and causing them to sink towards the centre of the potential well. Such a drag is known as dynamical friction. Energy partition provides another intuitive way of understanding dynamical friction, where massive particles sink towards the centre of the potential well through losing kinetic energies to less massive particles. It has therefore been suggested that given enough time, star clusters could infall into the galactic centre to form a nuclear star cluster (e.g. Tremaine 1976; Hernandez & Gilmore 1998).

For an isotropic and homogenous distribution of background particles, Chandrasekhar (1943) has analytically described dynamical friction as:

$$\frac{\mathrm{d}\vec{v_s}}{\mathrm{d}t} = -4\pi G^2 M_s \rho_\bullet \ln(\Lambda) f(v_\bullet < v_s) \frac{\vec{v_s}}{v_s^3}, \tag{1.19}$$

where v_s is the velocity of the infalling satellite, $\rho_\bullet$ and $v_\bullet$ are the density and velocity of the background particles, $\ln(\Lambda)$ is the Coulomb logarithm (given by the ratio between the maximum ($b_{\max}$) and minimum ($b_{\min}$) impact parameters: $\ln(\Lambda) = \ln(b_{\max}/b_{\min})$) and $f(v_\bullet < v_\mathrm{s})$ is the fraction of background particle that has a velocity slower the v_s.

It is evident already from Eq. 4.11 that the dynamical friction experienced by a satellite is tightly correlated with the underlying mass distribution of the galaxy. However, one would need to relate $\mathrm{d}\vec{v_s}/\mathrm{d}t$ to observables in order to constrain the gravitational potential using arguments from dynamical friction. One common approach is to required the age of a star cluster outside the galactic centre to be smaller than the timescale of the infall, also known as the dynamical friction timescale t_{df} (e.g. Angus & Diaferio 2009). Under the assumption of an isothermal spherical host and a Maxwellian velocity distribution function for the background particles, t_{df} can be written as (Binney & Tremaine 1987):

$$t_{\mathrm{df}} = 1.17 \frac{M_{\mathrm{vir}}}{M_\mathrm{s}} \frac{\tau_{\mathrm{dyn}}}{\ln(\Lambda)}, \tag{1.20}$$

where $\tau_{\mathrm{dyn}} = R_{\mathrm{vir}}/M_{\mathrm{vir}}$ is the dynamical timescale of the galaxy.

This approach in principle asserts only that the present-day galactocentric distance of the satellite d_s is >0, one can however put a tighter constraint of $d_s > d_p$, where d_p is the observed projected distance. While the orbital evolution of the infalling satellite through its lifetime can be calculated through Eq. 4.11, one would need to have a handle on the starting galactocentric distance at its time of formation

in order to calculate its present day location. Moreover, N-body simulations have shown that Eq. 4.11 presents too simplistic a picture and fails to reproduce the infall trajectories under certain DM halo profiles (e.g. Goerdt et al. 2006; Cole et al. 2012; Petts et al. 2015). We shall return building a comprehensive analytic model of dynamical friction for GCs in Chapter 4.

1.4 Dwarf galaxies

Under the ΛCDM hierarchical framework, dwarf galaxies are expected to exist in the highest numbers compared to other galaxy types. With typical stellar masses of less than a few $10^8\,M_\odot$, dwarf galaxies are typically less luminous than $M_V \sim -16$ (McConnachie 2012). Just like larger galaxies, dwarf galaxies come in various shapes, chemistry and dynamics. They can be found as satellites around larger galaxies and are considered to be the building blocks of larger galaxies under the ΛCDM hierarchical cosmological framework. Due to their low metallicities, understanding their evolution is therefore not only important for explaining the varieties in their observed properties, but also aids in understanding star formation in low-metallicity environments. Their shallow gravitational potential also means that they are more susceptible to, and hence a good candidate for studying baryonic feedback effects. From abundance matching, dwarf galaxies are also expected to be the most dark matter dominated objects of the universe and hence serve as excellent testbeds of the nature of dark matter. Given the low luminosities of dwarf galaxies in general, the ones lying in the neighbourhood of Milky Way and M31, classically considered to be within the 'Local Group', are therefore the best objects for studying the formation and evolution of dwarf galaxies.

1.4.1 Dwarf spheroidals and dwarf irregulars

It has been long known that the dwarf galaxies within the Local Group can be generally classified into two types based on their morphologies. Dwarf spheroidals (dSph) and dwarf irregulars can be seen as analogous to elliptical and disk galaxies of higher masses, with the former being thicker and having a rather featureless smooth luminosity distribution while the latter tend to be thinner with irregular overdensities of young stars. In Figure 1.10 we show a few examples of images of dSphs and dIrrs to illustrate their morphological differences. We shall in the following delve into other chemical and dynamical differences between the two classes of dwarfs. The readers should however keep in mind that there also exist a class of

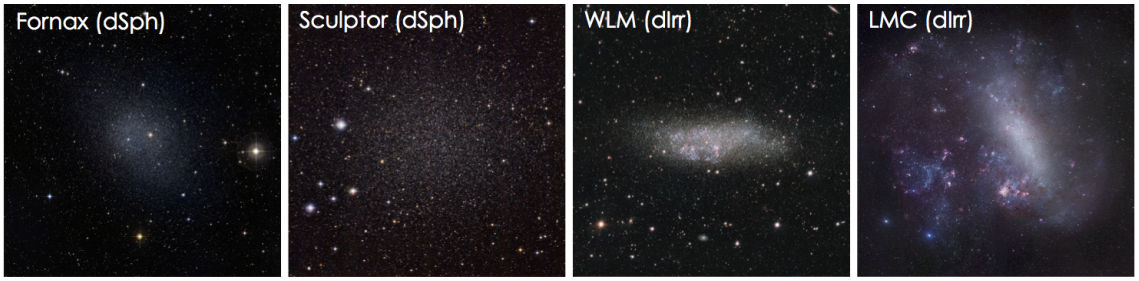

Figure 1.10: Examples of dwarf spheroidals (dSph) and dwarf irregulars (dIrr).[6]

transition dwarfs (dTrans). This class of dwarfs exhibit properties lying between the dSphs and dIrrs, indicating that dSphs and dIrrs do not present a dichotomy in dwarf properties, but instead as two ends of a spectrum.

Chemical Properties

Other than just the morphologies, the analogue between dSphs and dIrrs with ellipticals and disk galaxies can also be extended to their respective gas contents: dSphs tend to be gas-poor while dIrrs tend to be richer in gas. And just like the higher-mass counterparts, one can expect that the difference in gas content should correspond to differences in star formation histories (SFH) and therefore also metallicities. In the case of dwarfs in the local group, the ages and metallicities of stars are often obtained through photometry, from which colour-magnitude diagrams (CMD) are constructed and isochrones of stellar population models are fitted.

Indeed, Weisz et al. (2014) found that in the early universe (>10-12 Gyrs ago), the SFHs of dIrrs tend to drop quicker than the SFHs on dSphs. After 10 Gyrs however, the SFHs of dIrrs tend to plateau while those of dSphs continue to drop with the same rate. This also means, while dSphs have already formed most of their stars 10 Gyrs ago, dIrrs formed only $\sim 30\%$ of their stellar mass by that time and form stars with an increasing star-formation rate (SFR) until the present time. Such difference in the sustainability of star formation can be naively expected from the fact that dIrrs retain gas until the present day while dSphs do not. Interestingly, such a difference in star formation between the dSphs and dIrrs shows also a radial

[6]Fornax: By ESO/Digitized Sky Survey 2; Carina: By ESO/G. Bono & CTIO - `http://www.eso.org/public/images/potw1126a/`; WLM: By ESO: VST/Omegacam Local Group Survey - The WLM galaxy on the edge of the Local Group; LMC: Robert Gendler `http://www.robgendlerastropics.com`

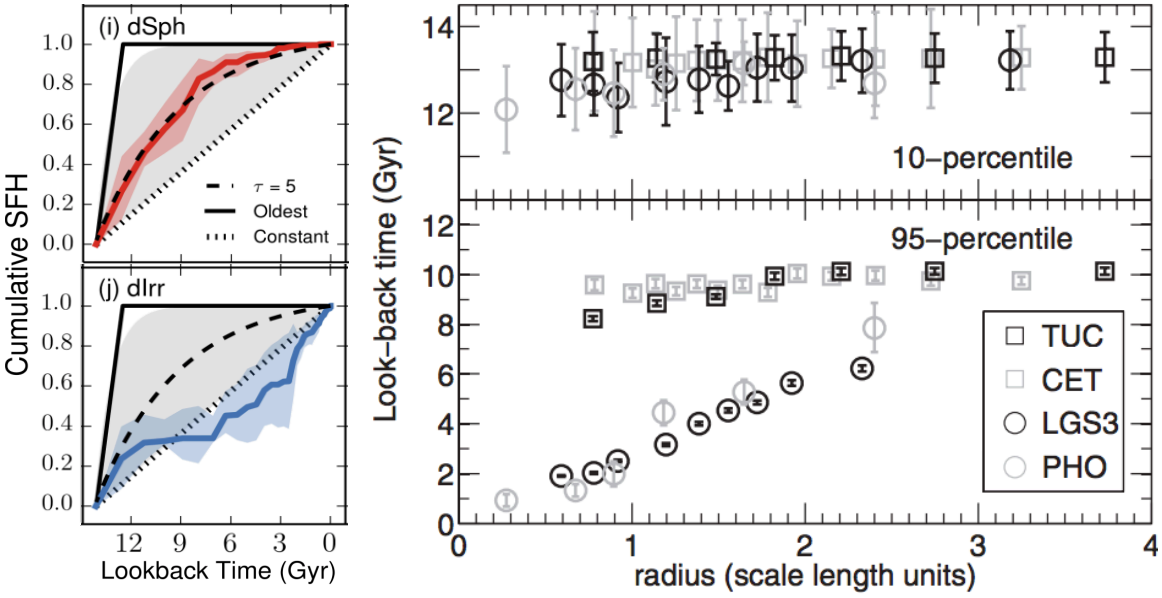

Figure 1.11: *Left:* Red and blue show the unweighted average of the star formation history (SFH) of dSphs and dIrrs from Weisz et al. (2014). The SFHs are compared with various star formation models plotted in black lines; dotted: constant star formation rate (SFR), dashed: exponentially declining SFR with a timescale $\tau = 5\,\mathrm{Gyr}$. (the grey shaded area represent exponentially declining SFR with $\tau = 0.1 - 100\,\mathrm{Gyr}$) and solid: a single old population of stars formed $> 12\,\mathrm{Gyrs}$ ago. *Right:* Top and bottom are the look-back time at which 10th and 95th percentile of the stars formed plotted with respect to the scale radius, plotted in squares are two dSphs and plotted in circles are two dIrrs (Hidalgo 2011).

dependence. While dIrrs tend to have younger stars at all radii when compared to dSphs, and that both the dSphs and dIrrs tend to have younger stars toward the centre of the galaxies, the differences in the stellar ages between the dSphs and dIrrs at a specific radius increases drastically towards the galactic centers. Hidalgo (2011) have characterised this dependence using $\int_0^T \psi(t)dt$, where $\psi(t)$ is the normalised SFR as a function of look-back time. The right panels of Figure 1.11 (Fig. 3 of Hidalgo (2011)) shows the 10th (top) and 95th (bottom) percentile of the function, with the two examples of dSphs (Tucana and Cetus) plotted in squares and the examples of dIrrs (LGS3 and Phoenix) plotted in circles. It is evident from the plot of the 95th percentile that the age gradient is much steeper in dIrrs.

The difference in the SFHs of the two classes of dwarfs implies a difference in their respectively chemical enrichment histories which might lead to different metallicity distributions. In particular, the metallicity gradients in the two classes

of dwarfs can be well distinguished. Using RGB spectroscopic data of nine LG dwarfs, Leaman et al. (2013) found that dSphs tend to have steeper metallicity gradients as dIrrs. They found that while dSphs typically have a metallicity gradient $-0.1 \lesssim d[\mathrm{Fe/H}]/dr_c \lesssim -0.2$ (where r_c is the core radii of each galaxy), dIrrs have a much milder gradient of $d[\mathrm{Fe/H}]/dr_c \sim -0.04$. While such dichotomy can possibly be due to the difference in the total mass (dIrrs tend to be more massive than dSphs), it can also be hinting at the effects from various internal and external processes. For example, radial migration of stars can be caused by disk instabilities and transient spiral structures which are more likely to be found in dIrrs than dSphs. Also, star formation driven fountain is another mechanism that allows redistribution of chemically enriched material within the galaxy. On the other hand, ram pressure or tidal stripping at early times could have preferentially stripped star-forming gas from the outskirts of the galaxies and hence confine the star-forming region to the inner part of the galaxies, rendering a preferential chemical enrichment in the inner parts of the galaxies. Additionally, a wall in [Fe/H] at the metal-rich end is seen in the metallicity distribution function (MDF) of the most luminous dSphs, which is not seen in any of the dIrrs, further supporting the scenario of ram pressure stripping (Kirby et al. 2013).

Dynamical properties

Another possible pathway to the dichotomy between the two morphological classes of dwarfs lie in their dynamics. It has been shown that the stars in dSphs have little or no rotation, and are supported with random motions ($V_{\mathrm{rot}}/\sigma \lesssim 0.5$) with a flat velocity dispersion profile (e.g. Muñoz et al. 2005; Walker et al. 2007). On the other hand, rotation signatures have been found in gaseous dIrrs, displaying a slightly higher V_{rot}/σ of $\sim 1 - 1.5$ (e.g. Harris & Zaritsky 2006; Leaman et al. 2013). Many dIrrs have also been demonstrated to have a dynamically cold gas disk, from which HI rotation velocities, that trace closely the circular velocities, can be extracted (e.g. Swaters et al. 2009; Iorio et al. 2017).

Related to the above discussion on chemical properties, Schroyen et al. (2011a) showed with N-body/SPH simulations that angular momentum is an efficient eraser of metallicity gradients. They showed that rotation can give rise to a centrifugal barrier that slow down the infall of gas towards the galactic center, rendering star formation and thereby chemical enrichment to be less centrally concentrated.

Indeed the differences seen in the metallicity gradients may be mirrored by a dichotomy of V/σ between the dSphs and the dIrrs. We show on the right panel of Figure 1.12 (Fig. 11 of Leaman et al. 2013) the metallicity gradient of various

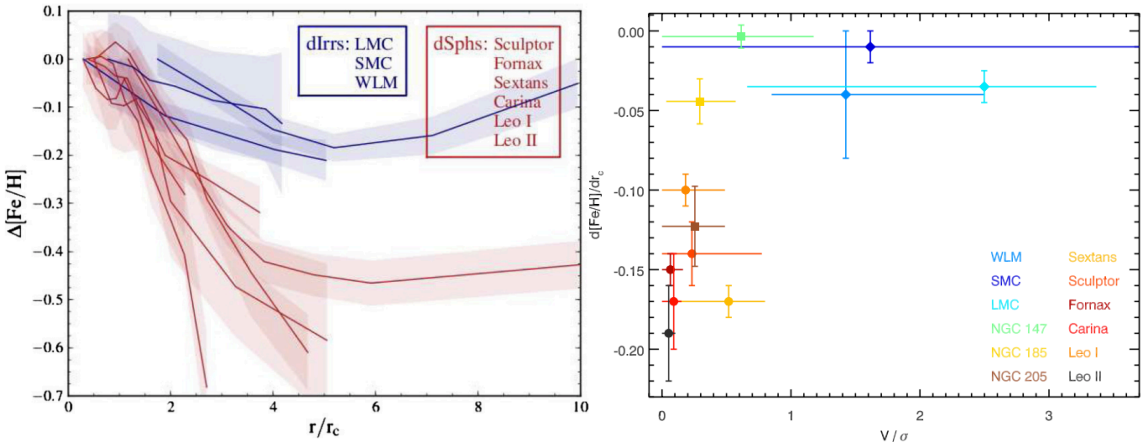

Figure 1.12: *Left:* Metallicity gradient plotted against radius in terms of the core radii of dIrrs in blue and dSphs in red of the Local Group (Leaman et al. 2013). *Right:*Dichotomy in the metallicity gradient-V/σ space between dIrrs (blue) and dSphs (red, orange, yellow and black) (Leaman et al. 2013).

dwarfs plotted against V/σ. It is suggested that the dSphs with steep metallicity gradients are predominantly dispersion supported ($V/\sigma < 1$) while the dIrrs with mild metallicity gradients are predominantly rotationally supported ($V/\sigma > 1$). However, it is yet unclear if there is a causal link between the two, as the parameter space is degenerate also with star formation history, gas content, environment and mass (Zhuang et al. 2019). Just like the SFHs, such a difference in V/σ may be seen as a natural consequence of the difference in gas content between the two classes of dwarfs, as explained for galaxies of larger masses in §1.2.2.

In terms of velocity anisotropies, while to date there is no measurements of such for dIrrs, a wealth of measurements for dSphs had been made using Jeans or Schwarzschild models. Evidences pointing to an increasingly tangential velocity anisotropy towards the outskirts of dSphs (e.g. Zhu et al. (2016) for Sculptor, Kowalczyk et al. (2018) for Fornax) could and have been interpreted a result of tidal stripping. We shall provide the first measurement for stellar velocity anisotropy in a dIrr in Chapter 3.

Dwarf galaxy evolution/formation pathways

Other than the above-mentioned differences in morphologies and chemodynamical properties, another clear differentiation between the two classes of dwarfs is their relative distances with respect to the host galaxies Milky Way and M31. Figure 1.13

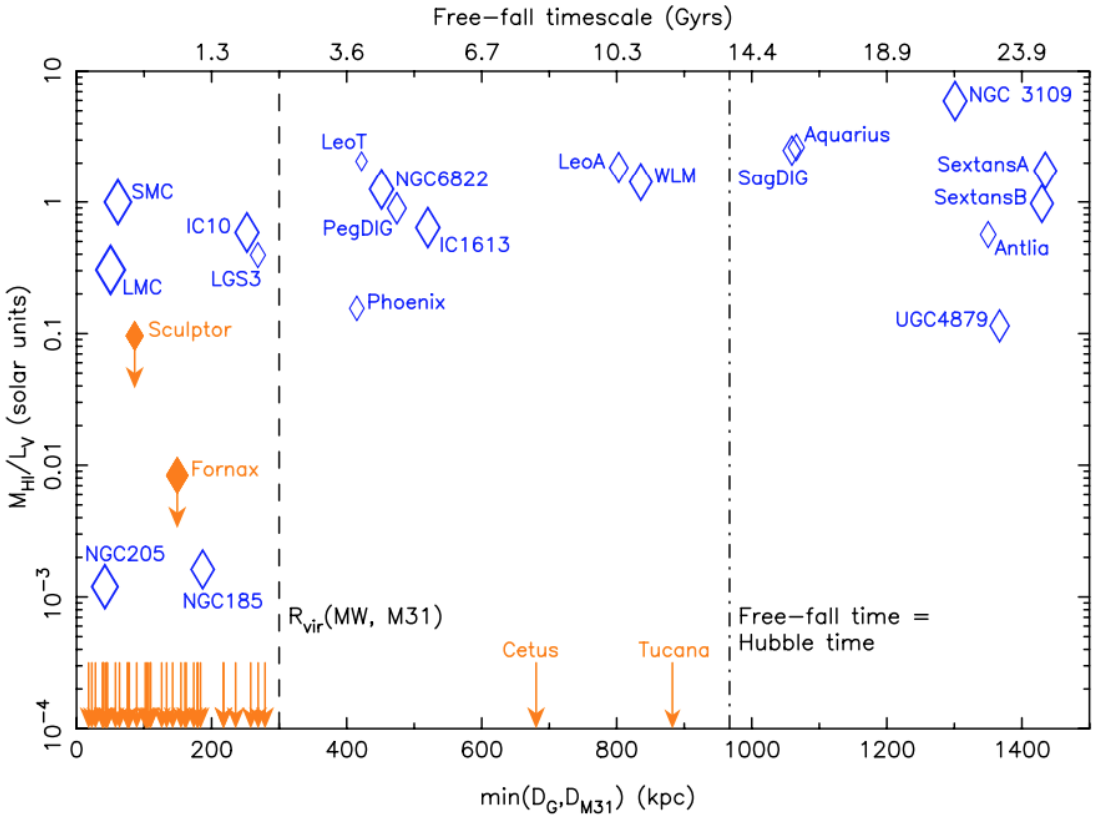

Figure 1.13: Gas fraction, expressed in terms of the ratio between total mass of HI gas and V-band luminosities ($M_{\rm HI}/L_V$), of dwarf galaxies in the LG plotted as a function of the minimum distance to one of the host galaxies: the Milky Way or M31, min(D_G, D_{M31}) (McConnachie 2012). DSphs are marked with orange solid diamonds with orange arrows indicating upper limits. DIrrs are plotted in blue open diamonds.

from McConnachie (2012) shows the gas fraction, expressed in terms of the ratio between the total mass of HI gas and V-band luminosities ($M_{\rm HI}/L_V$), of each of the dwarf galaxies in the Local Group with respect to the lesser of the distances to the Milky Way ($D_{\rm G}$) and M31 (D_{M31}). Galaxies with low gas fractions are typically dSphs, as marked with orange diamonds or arrows indicating an upper limit, while those with high gas fractions are typically dIrrs, as marked with blue open diamonds. It is evident that gas-poor dSphs tend to lie closer to either of the host galaxies while the gas-rich dIrrs tend to lie more to the outskirt of the LG. The correlation between environment and morphology leads to the questions: whether the difference in gas contents and hence morphologies of these two classes are a purely environmental effect? Are these two classes born differently or do they transform from one to another? What are some possible internal/external transformation pathways?

While we still do not have a complete understanding on whether or not dSphs and dIrrs are evolutionarily connected, the correlation between the distances to the host galaxies and gas fraction may suggest that interaction between the dwarf galaxies and the host galaxies strip away the gas from infalling dIrrs and turn them into gas-poor dSphs. Possible processes are tidal and ram-pressure stripping. In addition to gas stripping, tidal effects from the host can also heat up the stellar component to become more dynamically hot and spheroidal in shape (e.g. Mayer et al. 2006; Mayer 2010). The observed tangential anisotropies in some dSphs (e.g. Zhu et al. 2016; Kowalczyk et al. 2018) have also been interpreted as remnants of system that has gone through tidal interactions, as radial orbits tend to be more easily tidally stripped. Tidal streams from the Sagittarius dSph have also been found in the Milky Way halo, traced through its well-defined Age-Metallicity Relation and chemical signatures (e.g. Majewski et al. 2004; Hasselquist et al. 2019). While it has been shown in simulations to be an effective mechanism in removing gas from and thereby quenching star formation in dwarf galaxies (e.g. Mayer et al. 2006; Simpson et al. 2018), especially during the first infall towards the host galaxy when the velocity is high, evidence of ram-pressure stripping in the LG remains is scarce. Ram-pressure stripping occurs when the ram pressure that a dwarf experiences, as it moves through a dense intra-cluster medium, is stronger than the gravitational force that holds the gas onto the dwarf itself. An example of ram-pressure stripping in act is demonstrated by McConnachie et al. (2007). They show that the distribution of the HI gas in the dwarf Pegasus is evidently different from its regular elliptical stellar distribution; the HI gas shows a comet-like distribution characteristic of ram-pressure stripping.

Additionally, dwarf-dwarf mergers maybe a possible pathway for the transformation of gas-poor dSphs from gas-rich dwarf irregulars in cosmological simulations (e.g. Wetzel et al. 2015). Satellites can merge with one another within the halo of the host galaxies (e.g. Angulo et al. 2009; Wetzel et al. 2009), or they could have merged through group pre-processing before infalling onto the halo of the host galaxy (which includes, other than mergers, also other environmental effects such as tidal and ram stripping, that dwarfs can experience in a group or cluster before the group as a whole infalls to the current host). Furthermore, Benítez-Llambay et al. (2016) showed with cosmological simulations that mergers can form dSphs that have metallicity gradients resembling the ones observed in local group dSphs, with multiple distinct stellar populations of which the older and metal-poorer component is the most spatially extended - suggesting that mergers are a viable pathway for dSph formation.

On the other hand, internal processes such as stellar feedback and/or photo-

evaporation may also expel gas from dwarfs. While the shallow gravitational wells of dwarfs suggest that gas in dwarfs are more easily driven out by feedback mechanisms in comparison to more massive galaxies, their relatively lower star-formation rate also means that less feedback energy is available. In particular, Gatto et al. (2013) show in their simulation for the dwarf Sextans that by turning on supernova feedback, the dwarf galaxy lose all its cold gas in <1 Gyr as compared to only losing 40% of the cold gas within the same timescale through external agents (e.g. tidal and ram-pressure stripping) only. However, as suggested by Geha et al. (2012), the lack of evidence of isolated quenched dwarf galaxies may indicate that external processes are necessary to remove gas from dwarfs completely.

1.4.2 Scaling relations in the Local Group

To further understand the inter-relation between the chemical and dynamical evolution of dwarf galaxies and to place dwarf galaxies into the framework of other galaxy types, we explore here the various scaling relations observed within the Local Group.

The stellar mass-metallicity relation (MZR) in galaxies as we have seen in §1.2.1 extends to the low-mass dwarf galaxies. Kirby et al. (2013) have found, using 35 local group dwarf galaxies with spectroscopic stellar abundances, that the MZR for dwarf galaxies is tightly defined as $\langle[\mathrm{Fe/H}]\rangle \propto M_\star^{0.30\pm0.02}$ and that such relation holds for dwarfs across morphologies and with different metallicity distributions. We show this MZR in Figure 1.14. The MZR can be partly understood through the process of baryonic feedback. More massive galaxies have a steeper potential well and therefore can better retain metals that are produced in stars but then driven away by stellar winds or supernova ejecta. Indeed Kirby et al. (2011) showed that most dSphs of the Milky Way may have lost upwards of 96% of their total metals produced in outflows.

Another interesting scaling relation between the chemical and dynamical properties of dwarf galaxies is the age-velocity relation (AVR). Nearby dwarf galaxies allow us to study the AVR with spectroscopic data of individual stars. Due to their low masses and low gas densities, dwarfs are more susceptible to heating by feedback mechanisms such as supernovae, than more massive galaxies. Unlike their more massive counterparts, the AVR in dwarfs are more likely to reflect tidally driven changes in the gravitational potential, therefore allowing us not just to study the internal but also the external processes throughout the galactic evolution. Leaman et al. (2017) found that while dIrrs show similar increase in velocity dispersion as a function of age as found in more massive galaxies such as the Milky Way and M31, dSphs lack such an evolution, as shown on the left panel of Figure 1.15. By modelling

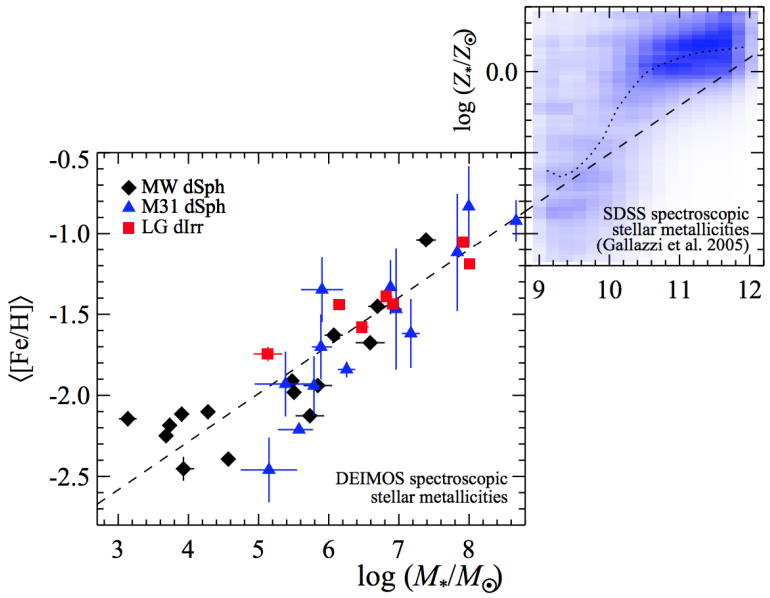

Figure 1.14: *Bottom left:* Mass-metallicity relation (MZR) of dwarfs in the Local Group (Kirby et al. 2013). *Top right*: The MZR for more massive galaxies derived from the SSDS survey by Gallazzi et al. (2005) for comparison.

the cooling of ISM and the scattering of stars caused by disks overdensities, they are able to reproduce the time evolution of velocity dispersions in dIrrs. To explain the flat AVR of dSphs on the other hand, may require a better understanding of the environmental effects such as tidal heating and ram pressure stripping, as well as internal effects such as stellar feedback.

Within individual dwarf galaxy, the stars also follow a tight age-metallicity relation (AMR), we show in the right column of Figure 1.15the AMR of a few LG dwarfs (taken from (Leaman et al. 2013). While younger stars also tend to be more metal-rich as a general rule, the exact shape of the AMR in each galaxy depends on its history of gas content and its particular SFH.

1.5 Bigger than just galaxies: galaxy dynamics and the nature of dark matter

Galaxies dynamics is an important avenue for studying the nature of dark matter. Through probing the mass distribution of galaxies, one can infer quantities like the relative ratio of stellar mass $M_\star$ and DM halo mass $M_{\rm halo}$ as a function of $M_\star$, as

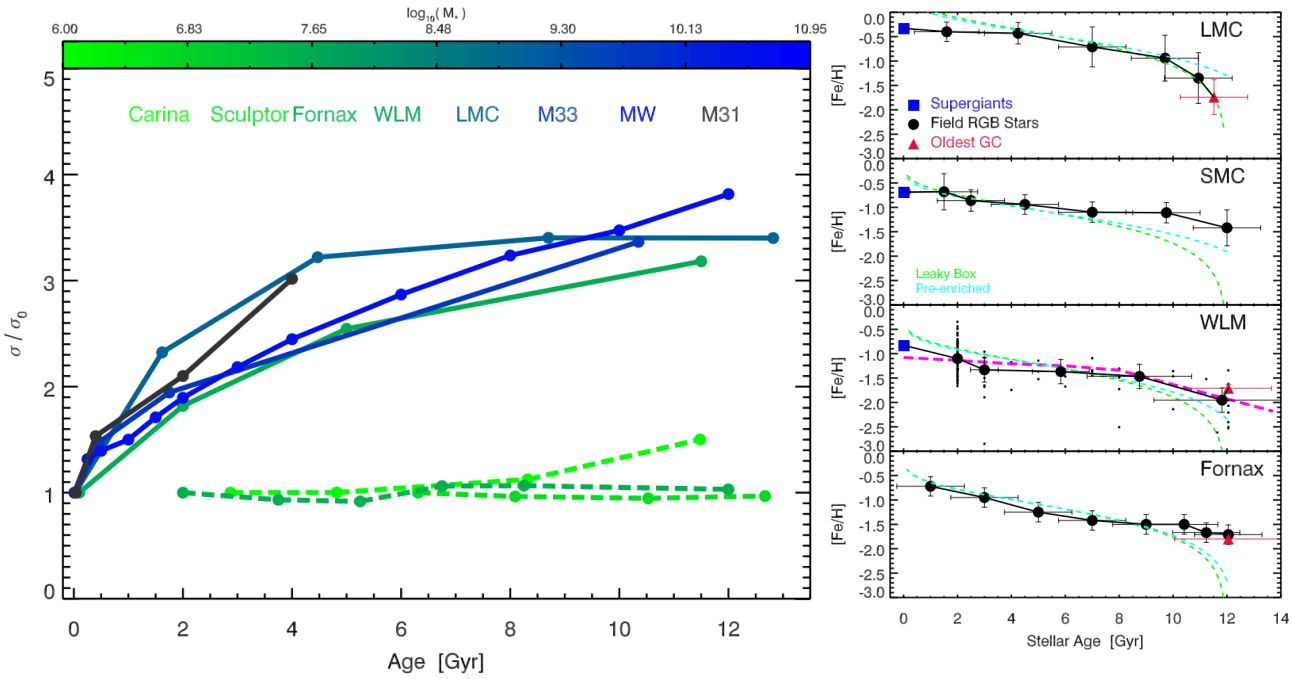

Figure 1.15: *Left:* Age-velocity relation (AVR) of the Local Group dwarfs show a dichotomy, where dIrrs (WLM, LMC in solid ilnes) show similar AVRs as more massive star forming galaxies like the Milky Way (in dark blue) and M31 (in black) while dSphs (in dashed green lines) show no age dependence in the velocity dispersion (Leaman et al. 2017). *Right:* Age-metallicity relation in individual dwarfs plotted in black, the best-fitted 'Leaky-Box' and 'Pre-enriched' chemical enrichment models are shown in green and blue dashed lines Leaman et al. (2013).

well as the density profile and geometrical shape of DM haloes, all of which have been precisely predicted from cosmological and galactic simulations under ΛCDM or alternate models of dark matter.

1.5.1 $M_\star - M_{\rm halo}$ relation

While it might be a natural expectation that more massive DM haloes contain also a more massive stellar component, the relative ratio between the two $M_\star/M_{\rm halo}$ is tightly related to the physics behind star formation and feedback processes. By matching the galaxy stellar mass function $n(M_\star)\mathrm{d}M_\star$ from Sloan Digital Sky Survey Data Release 3 (SDSS DR3; with $n(M_\star)\mathrm{d}M_\star$ derived by Panter et al. 2007) and the halo mass function $n(M_{\rm halo})\mathrm{d}M_{\rm halo}$ from their own DM only simulation, Moster et al.

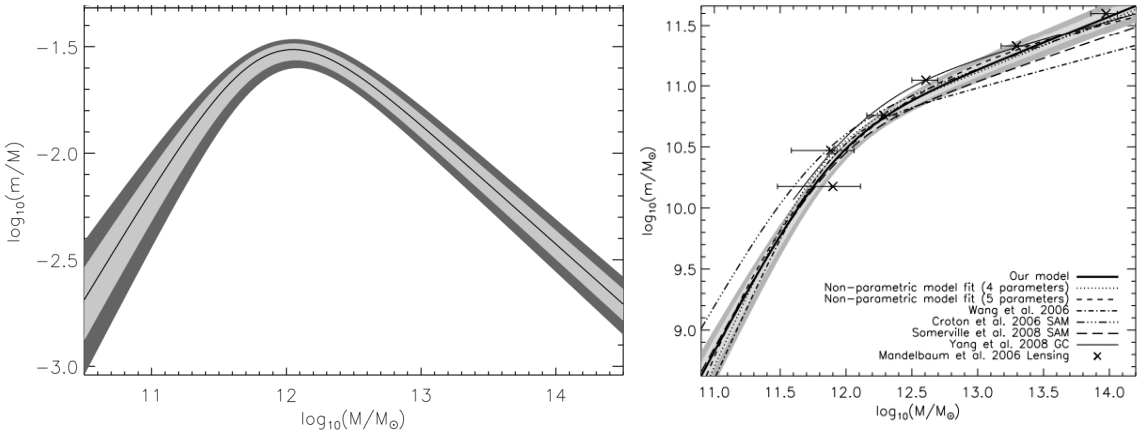

Figure 1.16: *Left:* The best-fitt stellar-to-halo-mass ratio plotted against halo mass from Moster et al. (2010) in black line, the light and dark grey shaded areas represent the $1\,\sigma$ and $2\,\sigma$ uncertainties. *Right:* The same relation but now plotted in the stellar mass vs. halo mass space. Overlaid in curves on top are models from other authors, and in crosses are the observed values from galaxy-galaxy lensing.

(2010) show that the $M_\star/M_{\rm halo}$ is a function of $M_{\rm halo}$ that can be written as:

$$\frac{M_\star}{M_{\rm halo}}(M_{\rm halo}) = 2\Big(\frac{M_\star}{M_{\rm halo}}\Big)_0\Big[\Big(\frac{M_\star}{M_{\rm halo,1}}\Big)^{-\beta} + \Big(\frac{M_\star}{M_{\rm halo,1}}\Big)^{\gamma}\Big]^{-1}, \tag{1.21}$$

where $(M_\star/M_{\rm halo})_0 = 0.02820^{+0.00061}_{-0.00053}$, $\log_{10}(M_{\rm halo,1}/M_\odot) = 11.884^{+0.030}_{-0.023}$, $\beta = 1.057^{+0.054}_{-0.046}$ and $\gamma = 0.556^{+0.010}_{-0.004}$ are the best-fit values. The form of the function is shown on the left panel of Figure 1.16. To validate their derived $M_\star - M_{\rm halo}$ relation, Moster et al. (2010) have also overplotted the observationally derived $M_\star$ and $M_{\rm halo}$ values derived from galaxy-galaxy lensing (right panel of Figure 1.16).

Galaxies therefore have a highest efficiency in forming stars at $\log_{10}(M_{\rm halo}/M_\odot) \sim 12$, at which $M_\star/M_{\rm halo}$ peaks. The decline in star formation efficiency towards the low-mass end and towards the high-mass end is often interpreted as effects from stellar and AGN feedbacks respectively. Gas in galaxies with shallower potential well (lower mass) are more susceptible to being blown away or heated by stellar feedback while the probability of harbouring an AGN is higher in massive galaxies; the depletion of cold gas then implies the depletion for material for star formation, and the galaxies end up with proportionally less stars than dark matter.

1.5.2 Dark matter density profiles: cusp vs. core?

Being the most dark-matter dominated objects in the universe, dwarf galaxies act as prime laboratories for testing the impact of baryonic feedback and the nature of dark matter. Various techniques have been adopted to infer the relative contribution of stellar and dark components in low mass galaxies. For example, decomposition of rotation curves obtained from HI kinematics has been used to study the fractional amount of dark matter in low mass galaxies (e.g. Lelli et al. 2010; Swaters et al. 2011; Adams et al. 2014; Katz et al. 2017). These results typically found that despite the uncertainties in stellar mass-to-light ratios, the baryonic mass was a small fraction of that necessary to reproduce the circular velocity profiles. These objects thus can provide a stringent test also on the nature of dark matter and/or non-Newtonian dynamics (e.g. Lelli et al. 2010; McGaugh & Milgrom 2013; Vogelsberger et al. 2014).

Various modelling techniques, as described in §1.3, have been adopted to infer the density profile of galaxy DM haloes. Many of the studies concerning the decomposition of HI rotation curves, as mentioned above, found inner slopes of DM haloes to be shallower than the cosmologically predicted cuspy NFW profile (e.g. Oh et al. 2011; Adams et al. 2014; Brook 2015). This discrepancy comes to be known as the cusp-core problem.

For Local Group low mass dwarfs, the dark matter density profiles can be recovered from stellar kinematics either through the virial mass estimates (Walker & Peñarrubia 2011), the Jeans equations (e.g. Łokas 2009; Zhu et al. 2016) or Schwarzschild models (e.g. Breddels et al. 2013; Kowalczyk et al. 2018). Measuring the mass profile from stellar kinematics suffers from uncertainties associated with the unknown velocity anisotropy, known as the mass-anisotropy degeneracy. To break the mass-anisotropy degeneracy, Łokas (2009) have utilised the higher order moment (kurtosis). And as such degeneracy is found to have a spatial dependence and is minimal at the half-light radius (Wolf 2010), other authors have separated stellar kinematics into populations of different chemistry with different spatial and kinematical distributions to serve as a lever arm to understand the host potential (Walker & Peñarrubia 2011; Zhu et al. 2016).

The constraints on the inner slopes of the dark matter density profiles by stellar kinematics alone is difficult however. For example, while Walker & Peñarrubia (2011) show that there is a large central dark matter core in Fornax, this is only true under the spherical symmetry assumption. Even with a discrete Jeans model on two chemically distinct population, Zhu et al. (2016) could only constrain the inner slope of the dark matter halo of Sculptor to be within $\gamma = 0.5 \pm 0.3$ (where γ parametrises the inner slope of a generalised NFW profile, with $\gamma = 0$ corresponding to a cored

profile and $\gamma = 1$ an NFW profile). In another study Kowalczyk et al. (2018) showed that while a cored profile is preferred by their models for Fornax, cuspy NFW and Einasto profiles fall within the 1σ uncertainties.

Modifications to the dark matter density profile have been shown to occur as stellar feedback can rapidly eject large quantities of gas and causes a non-adiabatic expansion of the dark matter and stellar orbits in the centres of low mass dwarf galaxies (e.g Governato et al. 2012; Di Cintio et al. 2014). This process has been seen in hydrodynamic simulations including baryonic feedback, and its efficiency may depend on sub-grid prescriptions for star formation and energy injection. There are predictions from these simulations that the effect of the feedback driven core creation will leave some imprint on the surviving stellar populations. For example, Read et al. (2016) showed, with hydrodynamical simulations of individual dwarf galaxies, that the size of the DM core is proportional to the half-light radius of the stellar disk and that the inner slope itself depends on the star-forming time of the galaxy. With the hydrodynamical cosmological simulation suite NIHAO, Di Cintio et al. (2014) showed that the coring of DM haloes by baryonic feedback which changes the inner slopes of DM haloes, is correlated with the stellar-mass-to-halo-mass fraction $M_\star/M_{\rm halo}$:

$$\gamma = -0.06 + \log_{10}[(10^{X+2.56})^{-0.68} + (10^{X+2.56})], \tag{1.22}$$

where $X = \log_{10}(M_\star/M_{\rm halo})$, meaning that DM haloes in galaxies at the low- and high-end of $M_\star/M_{\rm halo}$ are easily cored by baryonic feedback. Such a nonlinear relation suggests that there is an interplay between the amount of feedback energy produced by a galaxy's star formation, and the depth of its total potential well.

1.5.3 Predictions for halo geometry

While in purely ΛCDM simulations DM haloes are predicted to have prolate geometries regardless of their halo masses, Butsky et al. (2016) showed with the NIHAO simulations that such constancy is weakened when baryonic matter is taken into account. Especially for the inner regions ($\lesssim 0.5\, r_{vir}$) of the haloes, baryonic feedback from massive galaxies can sphericalise the halo. In DM only simulations, haloes typically have a short-to-long axis ratio of ~ 0.4 in the inner region ($\lesssim 0.12\, r_{vir}$) regardless of their mass. When baryonic effects are taken into account, the c/a of a Milky Way like galaxy would rise to $c/a \sim 0.8$ while that of dwarf galaxies are mostly unaffected.

Inferring the three-dimensional mass distribution of the unseen DM halos is difficult, however some attempts have been made in individual galaxies. For

example, the geometry of DM haloes can be constrained through the flaring of the cold disk, given the gaseous velocity ellipsoid. Such methodology is applicable to edge-on disk galaxies and was first proposed by Olling (1995). Olling (1996) and Banerjee & Jog (2008) applied this to constrain the DM halo shape of the Scd galaxy NGC4244 and M31 and found them both to be highly flattened, axis ratios $c/a \sim 0.2$ and ~ 0.4 respectively. Alternatively, the geometry of a DM halo can also be probed through its stellar dynamics. While again shape and velocity anisotropy are degenerate in moment-based stellar dynamical models, observations of proper motions in the future will allow the breaking of such degeneracy.

1.5.4 Alternative DM theories

While the cusp-core problem could be reconciled by baryonic feedback altering the DM density profile in the CDM paradigm, it could also be viewed as an evidence to alternative DM theories. In addition to the cusp-core problem, another famous inconsistency between the pure dark matter ΛCDM cosmological universe and observations is the missing satellite problem. This refers to the discrepancy between the simulated dark matter halo power spectrum at the low-mass end and the observed number of small satellite galaxies. For example, a simulated Milky Way-like halo is seen in CDM simulations to host 100-1000 subhaloes that are massive enough to form galaxies, while we do not observe such a large number of satellites around our own Galaxy (e.g. Moore et al. 1999; Klypin et al. 1999). Similar under-abundance of satellites is also found in other nearby galaxies (e.g. Zavala et al. 2009; Zwaan et al. 2010). While the missing satellite problem is not directly tested through dynamics, it provides a further motivation to study alternative DM theories through galaxy dynamics.

While CDM models typically interpret the dark matter particle as non-interacting (e.g., a WIMP), however other options may be possible. Below I discuss three classes of alternative DM theories (Warm, Wave and Self-Interaction DM), which successfully predict large scale structures while allowing the small-scale problems of CDM to be solved without invoking baryonic effects. In contrast to CDM, which interacts only through gravitational forces, these alternative DM achieve a central core by being heated up through interaction from other forces and do not require energy input from baryonic effects. The dependence of the DM geometry, inner slope and core size with respect to $M_\star/M_{\rm halo}$ or the spatial distribution of stellar mass as predicted in the CDM paradigm would be expected to be non-existent or at least different in such alternative models, and this can be tested.

Warm Dark Matter (WDM)

Warm dark matter, for example thermal relic particle theories, relativistically decouple from overdensities and act to suppress aspects of the matter power spectrum on small scales. These particle theories could effectively prevent formation of cusps in DM halos without needing baryonic effects. A high streaming velocity can be achieved if DM particles have lower masses ($m_{\rm WDM} \sim$keV; in contrast to $m_{\rm CDM} \sim$100-1000 GeV for CDM), allowing them to decouple from the hot plasma of the early universe when it is still relativistic. Other than suppressing density cusps in DM haloes, the higher streaming velocities of WFM would at the same time suppress structure formation below the free-streaming length. Allowable free-streaming lengths can hence be constrained through observation of large-scale structure. For example, Viel et al. (2013) use observations of the high redshift Lyman-α forest[7] that $m_{\rm WDM} \gtrsim 3.3\,$keV. Bozek et al. (2019) showed with hydrodynamical cosmological simulations that in an universe with WDM, DM haloes and hence stars are formed later and the stellar distributions are less centrally dense than CDM haloes, offering a young population of ultra-faint dwarfs (which have not yet been found observationally and also are not seen in their CDM simulations) as a testable prediction.

On the other hand, even though WDM allows the formation of cores in DM haloes, such cores would be rather small given the allowed $m_{\rm WDM}$ constrained from large-scale structures. Villaescusa-Navarro & Dalal (2011) showed numerically that the core radii is of the order of $\lesssim 0.1\%$ of the virial radii, in contrast to the observed ratio $\sim 5\%$ in some Low Surface Brightness galaxies (LSB). While this might serve as a counter argument to WDM, they arrived at this conclusion by assuming that no haloes can form below the cut-off scale, such an assumption has however, as the authors pointed out, not been verified with N-body simulations due to numerical difficulties in simulating a truncated power spectra.

Wave Dark Matter (ψDM)

Another popular candidate of alternative DM is made up of ultra-light axions ($m_{\psi\rm DM} \sim 10^{-22}\,$eV), known in the literature also as the Bose-Einstein Condensate DM, scalar-field DM or Fuzzy DM. ψDM is so light that the de Broglie wavelength is on the order of ∼kpc, meaning that quantum effects act on galactic scale and support

[7]Lyman-α forest are absorption lines caused by neutral Hydrogen in the intergalactic medium along the line-of-sight to distant quasars and allows us to trace the large-scale structure/mass power spectrum at high redshift.

a DM core in the centre of galaxies. Schive et al. (2014a) performed cosmological simulation with ψDM and find that such DM cores have the form of a soliton, manifested as a stationary and lowest-energy solution to the Schrödinger–Poisson equation and is surrounded by a CDM-like envelope. The density profile of the soliton in ψDM halo can be written as:

$$\rho_{\psi\mathrm{DM}}(r) = \frac{1.9(m_{\psi\mathrm{DM}}/10^{-23})^{-2}(r_\mathrm{c}/\mathrm{kpc})^{-4}}{[1+9.1\times10^{-2}(r/r_\mathrm{c})^2]^8}; r < r_\mathrm{a}, \tag{1.23}$$

where r_c is known as the core radius and beyond r_a, the density profile of the ψDM halo can be described by an NFW profile. From their simulations, they find $r_\mathrm{a} \sim 3r_\mathrm{c}$ typically.

Just like WDM, ψDM also suppress small-scale structure formation. The Lyman-α forest hence provides again a constraint on the mass of the DM particle. It is found that that the Lyman-$\alpha forest constrains \mathrm{m}_{\psi\mathrm{DM}} = 0.26 - 2.5\times10^{-22}$ (e.g. Bozek et al. 2015; Sarkar et al. 2016). Alternatively, $m_{\psi\mathrm{DM}}$ can also be constrained through the core size of DM haloes. As shown in Eq. 1.23, for a soliton of a particular r_c, the normalisation of the density profile of the DM core is set by $m_{\psi\mathrm{DM}}$. The shape of the DM density profile can be obtained through dynamical means. For example, using the Jeans Eq. and the stellar kinematics of the Fornax dSph, Schive et al. (2014a) constrained $m_{\psi\mathrm{DM}}$ to $0.8 \pm 0.2 \times 10^{-22}\,\mathrm{eV}$.

Self-interacting Dark Matter (SIDM)

SIDM particles are a class of particles interact with each other through $2 \rightarrow 2$ elastic scattering (the case of inelastic scattering was explored in Vogelsberger et al. 2019). Such self-interactions transfer energy from the dynamically hotter outer region to the dynamically colder inner region of a DM halo and hence allow a formation of an inner DM halo core. This kinetic thermalisation also drives the DM halo to become isothermal, with radially uniform velocity dispersion of DM particles and Maxwell-Boltzmann velocity distribution function (Vogelsberger & Zavala 2013). Also, the collision between the DM particles, depending on the exact cross-section, can lead to sphericalisation, erasing the triaxiallity seen in CDM haloes and predicting spherical DM haloes (e.g. Vogelsberger et al. 2012; Peter et al. 2013).

While it has been suggested that the scattering cross-section constraints from lensing of galaxy clusters ($\sigma/m \lesssim 0.02\,\mathrm{cm}^2\,\mathrm{g}^{-1}$, Miralda-Escudé 2002) is too small to exert any effect on DM halo structure to resolve small scale problems of CDM in dwarf galaxies (e.g. an inner core), a new class of SIDM particles with velocity-dependent scattering cross-section circumvent this issue. This is also known

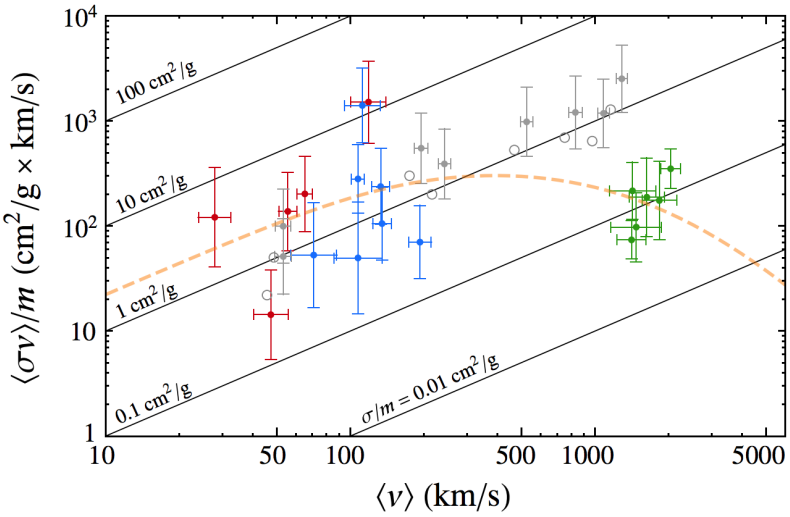

Figure 1.17: The derived velocity-dependent scattering cross section of SIDM plotted in orange dashed curve, with constraints from dwarf galaxies (red), LSB galaxies (blue) and galaxy clusters (green)(Kaplinghat et al. 2016).

as the dark photon model, where the self-interaction between SIDM particles is described by a Yukawa potential: $V(r) = \alpha_{\rm SIDM} e^{-\mu r}/r$, where $\alpha_{\rm SIDM}$ is in analog with the EM fine structure constant ($\alpha_{\rm EM} \sim 1/137$) and μ is the dark photon (mediator) mass. With a combination of lensing data from galaxy clusters and Jeans models of dwarf and LSB galaxies, Kaplinghat et al. (2016) constrained μ to be tied to the mass of SIDM particle ($m_{\rm SIDM}$) itself and $\mu \sim 10^{-3} m_{\rm SIDM}$, with 60 MeV$< m_{\rm SIDM} <$30 GeV and $10^{-6} < \alpha_{\rm SIDM} < 10^{-1}$. We show their fit of SIDM scattering cross section over objects of wide range of masses in Figure 1.17.

Another compelling advantage of SIDM is that it allows for the observed wide variety of rotative curve profiles. For models such as WDM and ψDM, one would expect all dwarfs to have cores in their DM haloes, contrary to the observed diversity. CDM models predict self-similar haloes such that any halo of a given mass have remarkably similar structures, it has hence been pointed out that such a diversity cannot be reproduced through baryonic feedback in the CDM scenario (Oman et al. 2015). Recently however, Santos-Santos et al. (2018) were able to reproduce the diversity of observed $V_{\rm rot}$ in terms of the ratio between the $V_{\rm rot}$ at 2 kpc and the outermost measured value, using the NIHAO cosmological hydrodynamical simulations. They suggest that the diversity in rotation curves enter in the CDM model through a dependence between $M_\star/M_{\rm halo}$ and the size of the DM core formed by baryonic feedback. In the case of SIDM, DM density profiles are altered by thermalisation caused by self-interaction, meaning that the distribution of baryonic

matter can play an important role when a galaxy is baryon-dominated in the inner region. In such a case, the isothermal solution would largely determined by the baryonic density distribution. On the other hand, for DM-dominated systems such as dwarf galaxies, (Robles et al. 2017) have shown that the inclusion of baryons in SIDM simulations only induces negligible changes to the DM density profile. By simply applying isothermal solutions to the Jeans Eq. and inputing the observed baryonic distribution, Kamada et al. (2017) were able to reproduce the diversity of the rotation curves of 30 dwarf galaxies with remarkable success.

Chapter 2

Validating stellar dynamical mass models with molecular gas kinematics

Abstract[1]

Deriving circular velocities of galaxies from stellar kinematics can provide an estimate of their total dynamical mass, provided a contribution from the velocity dispersion of the stars is taken into account. Molecular gas (e.g., CO) on the other hand, is a dynamically cold tracer and hence acts as an independent circular velocity estimate without needing such a correction. In this work we test the underlying assumptions of three commonly used dynamical models, deriving circular velocities from stellar kinematics of 54 galaxies (S0-Sd) that have observations of both stellar kinematics from the CALIFA survey, and CO kinematics from the EDGE survey. We test the Asymmetric Drift Correction (ADC) method, as well as Jeans, and Schwarzschild stellar dynamical models. The three methods each reproduce the CO circular velocity at $1R_{\rm e}$ to within 10%. All three methods show larger scatter (up to 20%) in the inner regions ($R < 0.4R_{\rm e}$) which may be due to an increasingly spherical mass distribution (which is not captured by the thin disk assumption in ADC), or non-constant stellar M/L ratios (for both the JAM and Schwarzschild models). This homogeneous analysis of stellar and gaseous kinematics provides one of the first empirical validation that all three models can recover $M_{\rm dyn}$ at $1R_{\rm e}$ to

[1]This chapter originally appeared in the literature as Leung et al. (2018). I hereby affirm that I have conducted all the research presented here myself.

better than 20%, but users should be mindful of scatter in the inner regions where some assumptions may break down.

2.1 Introduction

The kinematics of stars or gas in galaxies allows one to trace its underlying gravitational potential and hence the enclosed mass within a particular radius. In particular, the circular velocity, $V_{\rm c}$, defined as $V_{\rm c}^2(R) \equiv -R(\partial\Phi/\partial R)$, is an optimal tracer of a galaxy's potential. The mass profile of galaxies provides insight into, for example: understanding how baryons and dark matter co-habitate in galaxies, how the galaxies assemble, and how galaxy evolution proceeds across the Hubble sequence in a variety of environments (e.g. see reviews: Courteau et al. 2014; Cappellari 2016, and references therein).

Typical kinematic tracers for galaxies include atomic, molecular or ionised gas, and stars. While observations of stellar kinematics can be done at high spatial resolution, the high velocity dispersion intrinsic to the stellar component renders their dynamical analysis non-trivial. Luminous ionised gas can be similarly complicated due to turbulent shocks surrounding star formation (of which it is associated). Molecular gas, such as the CO, which is often used as a tracer of H_2, typically is dynamically cold with an intrinsic dispersion of $\lesssim 10\,{\rm km\,s^{-1}}$ at low redshift (Mogotsi et al. 2016). This means that the molecular gas rotation curves closely follow the circular velocities and therefore is an optimal tracer of the gravitational potential. However, molecular gas is found in the disk plane and can often show kinematic features due to perturbations occurring in the disk by a bar or spiral arms (e.g. Laine et al. 1999; Shetty et al. 2007). A method for removing these perturbation, for example by fitting tilted rings or by harmonic decomposition (e.g. Begeman 1987; Wong et al. 2004), is therefore necessary in order to extract a smooth rotation curve from molecular gas.

As stars are collisionless, their orbits can cross and stars born from the cold molecular gas eventually dynamically evolve to have large random motions at present day (Leaman et al. 2017), resulting in velocity dispersions up to a hundred $\rm km\,s^{-1}$ at a typical $L_\star$ mass galaxy's effective radius and as high as a few hundreds $\rm km\,s^{-1}$ in the galactic bulge. Hence when estimating the circular velocity (and dynamical mass) of a galaxy from stellar kinematics, we must take into account both the rotation velocity and the velocity dispersion - especially when they are of comparable magnitude.

There are various methods to recover V_c from stellar kinematics, typically either by solving the Jeans equations (e.g Jeans 1922; Binney et al. 1990; Emsellem et al. 1994), by using orbit-based models such as the Schwarzschild model (e.g. Schwarzschild 1979; van der Marel et al. 1998; Thomas et al. 2004; Valluri et al. 2004), or by particle-based models such as the Made-to-measure method (e.g. de Lorenzi et al. 2007; Long & Mao 2010; Syer & Tremaine 1996; Zhu et al. 2014). Having only the line-of-sight information of the velocity field (e.g., the projected components of the rotation and dispersion) implies that some assumptions must be made. The Jeans models often make assumptions on, for example, the geometry of the underlying potential, the mass-to-light ratio and the velocity anisotropy profile of the galaxies. Schwarzschild or made-to-measure models, on the other hand, do not make assumption on the velocity anisotropy, but may still require assumptions on the geometry of the gravitational potential and the mass-to-light ratio.

This work aims to verify commonly used models for deriving circular velocities and hence dynamical masses, from stellar kinematics, and calibrate how well each model works in different regimes (e.g. over different radii or galactic properties). We do so by comparing the circular velocities derived from stellar kinematics to those extracted from the molecular gas as traced by CO. As the molecular gas and the stars in a galaxy orbit in the same gravitational potential, the V_c inferred from their kinematics should match each other. We test three commonly used stellar dynamical models in this study: (1) the asymmetric drift correction (ADC) (e.g. §4.8 Binney & Tremaine 1987; Weijmans et al. 2008), (2) the Axisymmetric Jeans Anisotropic Multi-gaussian expansion (JAM) model (Cappellari 2008), and (3) the orbit-based Schwarzschild model (Schwarzschild 1979; van den Bosch et al. 2008). Both ADC and JAM derive V_c by solving the Jeans equations.

Among the three, ADC is the most simplistic model and assumes that stars lie on a thin disk with either a constant or a parametrised form of velocity anisotropy. JAM removes the thin-disk assumption and takes into account the full line-of-sight integration of the stellar kinematics, but still makes assumptions about the velocity anisotropy and the shape of the velocity ellipsoid. The triaxial Schwarzschild models we utilise in this work are the state of the art in stellar dynamical modelling. The Schwarzschild method is an orbit-based model which does not require any assumption on the shape of velocity ellipsoid, but is expensive in terms of computational power. By comparing the V_c derived from these three models with that from CO kinematics, we aim to show if and how the relaxation in assumptions allowed by improved computational power in stellar dynamical modelling leads to better constraints in circular velocities. In the remainder of this work we shall refer to the circular velocities derived from CO, ADC, JAM and Schwarzschild models as $V_{\rm CO}$, $V_{\rm ADC}$,

$V_{\rm JAM}$ and $V_{\rm SCH}$ respectively.

Gas and stellar kinematics have been compared in some individual cases, or for particular applications (e.g. Weijmans et al. 2008; Leaman et al. 2012; Bassett et al. 2014; Pizzella et al. 2004; Johnson et al. 2012; Hunter et al. 2002). In particular, Davis et al. (2013) show, for a sample of 16 early type galaxies (ETG) from the ATLAS^{3D} survey, the agreement of CO and stellar kinematics. Over the late type galaxies, however, a large scale homogeneous test of stellar dynamical models with *cold* gas circular velocity curves is still needed.

The EDGE (Bolatto et al. 2017) and CALIFA IFU surveys (Sánchez et al. 2016) respectively provide CO and stellar kinematics over an overlapping sample of nearby galaxies, allowing us to compare the CO rotation curves and stellar circular velocities over a large and homogeneous sample for the first time. Moreover, our sample includes 54 galaxies from type S0 to Scd, allowing us to look for systematic differences in the kinematic tracers as a function of galaxy morphological type. The CALIFA survey also provides Hα kinematics; for a comparison between $V_{\rm CO}$ and the rotation curves extracted from Hα kinematics please refer to Levy et al. (2018).

Readers interested in the data sample may refer to section 2.2. In section 2.3, we describe the extraction of rotation curves from the CO velocity field. In section 2.4, we describe the methods and the underlying assumptions of the three stellar dynamical models (ADC, JAM and Schwarzschild) and compare the circular velocities extracted from stars using different models in section 2.4. In section 2.5, we compare the circular velocities extracted using gaseous and stellar kinematics and we characterise the comparisons as functions of radii, local stellar $V/\sigma_\star$ values and galactic parameters. In section 2.6, we discuss the plausible causes for the differences we see. We summarise in section 2.7.

2.2 Data

The CARMA Extragalactic Database for Galaxy Evolution (EDGE) survey consist of interferometric observations of 126 galaxies, all of which are included in the Calar Alto Legacy Integral Field Area (CALIFA) survey. The data were obtained using the Combined Array for Research in Millimeter-wave Astronomy (CARMA) at Owens Valley Radio Observatory. These 126 galaxies were mapped in ^{12}CO($J = 1 - 0$) using the D and E array configuration. Each galaxy typically had 4.3 hours of observation, and all galaxies were observed in the period from December 2014 to April 2015. The velocity resolution of the observations was $20\,{\rm km\,s^{-1}}$, and the typical

beam has $\mathrm{FWHM_{beam}}$ of $\sim 3-5$". In this work, we utilise the integrated intensities, mean velocities and velocity dispersion maps. The kinematic maps are obtained by fitting a gaussian to the spectrum observed at each pixel, with the peak of the fitted gaussian and the standard deviation representing the mean velocity and the velocity dispersion respectively. Complete details of the observations and reduction for the survey, as well as all the CO moment maps, can be found in Bolatto et al. (2017)[2].

The measured stellar kinematics come from integral field spectroscopic observations of the CALIFA survey. The observations have a spatial resolution with a FWHM of ~ 2.7". The stellar kinematics come from the V1200 data set (Falcón-Barroso et al. 2017)[3], with a velocity resolution of $\sigma \sim 70\,\mathrm{km\,s^{-1}}$. While the optical and radio community often follow different velocity conventions when extracting kinematics from the observed spectra, both the CO and stellar kinematical maps presented in this work are converted to: $V \equiv c\Delta \ln \lambda$, where V is the extracted velocities, c is the speed of light and $\Delta\lambda$ is the difference between the observed wavelength and the rest wavelength of any particular lines. This is done to avoid any systematic differences due to the different conventions when comparing the circular velocities extracted from CO and stellar kinematics.

Out of the 126 overlapping galaxies, we select 54 galaxies that provide sufficient signal to noise in CO for us to trace the galaxy kinematics. We select only the galaxies from which we can extract at least three rotation velocity measurements (more on selection criterion in Section 2.3.3). We also exclude merging galaxies as identified for the CALIFA sample in Barrera-Ballesteros et al. (2015), of which the interaction may complicate the differences between gaseous and stellar kinematics. The 54 galaxies of our sample and their parameters as adopted in the CALIFA survey, including the total stellar mass ($M_\star$), distance, inclination (i) and photometric position angle (PA_{morph}) are listed in Table 2.1.

[2]the publicly available data can be downloaded from http://www.astro.umd.edu/EDGE/

[3]the stellar kinematics can be found in http://califa.caha.es

Galaxy	Type[a]	Dist (Mpc)[a]	Incl (°)[a]	log $M_\star/M_\odot$ [a]	$PA_{\rm morph}$ (°)[a]	$PA_{\rm kin}$ (°)[b]	$R_{\rm e}$ ($''$) [a]	$\sigma_\star(R=R_{\rm e})$[a]	$V_{\rm sys}$ (km s^{-1})[b]
IC0480	Sc	65.2	76.7	10.15	167.9	−12.1	24.16	90.27	4541.97
IC0944	Sab	100.0	69.5	11.26	105.7	−74.3	19.01	195.23	6845.50
IC1199	Sb	60.7	64.5	10.60	157.3	157.3	20.99	146.53	4666.25
IC1683*	Sb	69.3	50.5	10.59	15.6	−161.3	13.07	114.72	4773.18
IC2247	Sab	61.8	77.8	10.51	148.5	148.5	21.38	111.76	4215.30
IC2487	Sc	62.2	78.0	10.40	162.9	162.9	25.34	116.64	4278.08
IC4566	Sb	79.7	53.9	10.95	161.0	−19.0	15.84	144.33	5515.33
NGC0477	Sbc	83.8	60.5	10.48	128.4	−51.6	21.78	104.86	5731.99
NGC0496	Scd	85.9	57.0	10.41	32.7	−147.3	19.01	77.23	5908.02
NGC0551	Sbc	74.3	64.2	10.64	137.5	137.5	19.80	115.83	5094.57
NGC2253	Sbc	51.2	48.3	10.52	109.7	109.7	15.44	103.49	3516.41
NGC2347	Sbc	63.6	50.7	10.94	9.1	9.1	18.61	175.43	4359.36
NGC2410*	Sb	66.8	71.6	10.88	34.6	54.6	21.38	175.55	4600.08
NGC2639	Sa	46.5	50.2	11.17	130.3	130.3	17.42	203.92	3149.31
NGC2906	Sbc	30.6	55.7	10.39	82.6	82.6	19.40	117.05	2120.89
NGC3815	Sbc	53.0	60.4	10.35	67.8	−112.2	14.26	115.52	3660.81
NGC3994	Sbc	44.1	59.9	10.42	8.1	8.1	9.50	164.85	3085.49
NGC4047	Sbc	49.2	42.9	10.69	97.6	−82.4	16.63	109.69	3405.28
NGC4149	Sa	44.0	66.2	10.36	85.4	−94.6	18.61	137.22	3062.19
NGC4210	Sb	38.8	41.8	10.29	97.7	97.7	21.38	83.34	2701.64
NGC4644	Sb	70.5	72.9	10.45	57.0	−123.0	12.60	115.77	4870.88
NGC4711	Sbc	58.2	58.5	10.31	41.4	41.4	17.82	86.55	4019.40
NGC4961	Scd	36.6	47.4	9.68	100.6	−79.4	15.05	66.73	2539.42
NGC5016	Sbc	37.3	40.9	10.24	57.4	−122.6	17.82	87.83	2595.19
NGC5056	Sc	79.4	55.7	10.48	3.4	3.4	15.84	120.70	5494.81

Galaxy	Type[a]	Dist (Mpc)[a]	Incl (°)[a]	log $M_\star/M_\odot$ [a]	$PA_{\rm morph}$ (°)[a]	$PA_{\rm kin}$ (°)[b]	$R_{\rm e}$ ($''$) [a]	$\sigma_\star(R=R_{\rm e})$[a]	$V_{\rm sys}$ (km s^{-1})[b]
NGC5218	Sab	41.4	31.7	10.65	101.4	101.4	18.61	152.12	2878.92
NGC5480*	Scd	27.0	36.2	10.14	41.9	−2.0	25.74	62.98	1887.88
NGC5520	Sbc	26.8	59.4	9.86	63.1	63.1	12.28	99.89	1877.19
NGC5633	Sbc	33.2	42.8	10.26	16.9	−163.1	13.86	90.54	2322.21
NGC5784*	S0	77.6	36.4	11.22	19.2	−110.0	13.46	203.65	5353.01
NGC5908*	Sa	47.8	50.7	11.22	154.0	−27.1	34.45	198.41	3298.51
NGC5980	Sbc	58.4	66.2	10.72	11.7	−168.3	17.42	150.54	4044.62
NGC6060	Sb	64.5	64.3	10.93	102.0	−78	28.51	143.28	4395.10
NGC6168	Sc	36.8	76.7	9.86	110.2	110.2	26.93	66.35	2523.05
NGC6186	Sb	42.1	40.5	10.57	49.6	−110.2	20.20	90.26	2946.99
NGC6301	Sbc	119.7	52.8	11.02	108.5	108.5	24.55	147.97	8134.66
NGC6394	Sbc	121.7	68.9	10.90	42.6	42.6	14.65	143.59	8324.46
NGC6478	Sc	97.1	68.4	11.01	34.2	−145.8	23.36	180.19	6637.44
UGC00809	Scd	60.0	79.0	9.69	23.6	−156.4	20.20	93.37	4146.13
UGC03539	Sc	47.2	72.1	9.85	117.9	117.9	20.99	NaN	3263.57
UGC03969	Sb	117.8	77.4	10.68	134.3	−45.7	15.05	130.62	7926.60
UGC04029	Sc	63.5	77.7	10.33	63.5	−116.5	26.14	108.85	4350.80
UGC04132	Sbc	74.4	72.0	10.77	27.6	27.6	22.97	160.56	5092.49
UGC05108	Sb	116.1	66.1	10.89	138.1	−41.9	9.50	194.46	7935.95
UGC05598	Sb	80.3	74.8	10.23	35.6	35.6	15.84	85.51	5522.98
UGC08107	Sa	118.6	71.4	11.07	53.2	53.2	16.63	207.94	8086.28
UGC09067	Sbc	112.1	62.5	10.58	12.6	−167.4	14.65	139.51	7649.28
UGC09537	Sb	126.1	78.0	11.22	140.7	−39.3	20.20	210.31	8545.50
UGC09542	Sc	78.4	72.7	10.32	34.3	34.3	21.38	99.09	5372.05
UGC09665	Sb	36.5	74.1	10.00	138.2	−41.8	18.61	74.93	2568.17

Galaxy	Type[a]	Dist (Mpc)[a]	Incl (°)[a]	log $M_\star/M_\odot$ [a]	$PA_{\rm morph}$ (°)[a]	$PA_{\rm kin}$ (°)[b]	$R_{\rm e}$ ($''$) [a]	$\sigma_\star(R=R_{\rm e})$[a]	$V_{\rm sys}$ (km s^{-1})[b]
UGC09892	Sbc	81.1	72.2	10.30	101.0	−79.0	16.63	73.22	5564.49
UGC10123	Sab	53.8	77.1	10.52	53.6	53.6	18.22	122.92	3729.22
UGC10384	Sb	70.7	74.3	10.27	92.8	92.8	11.88	112.19	4894.88
UGC10710	Sb	119.7	69.6	10.99	147.2	147.2	20.20	168.86	8144.29

[a] Refer to the CALIFA survey (Sánchez et al. 2016) for the derivation of these values.

[b] From fitting the CO kinematics in this work. $PA_{\rm kin}$ denotes the receding side.

[*] $PA_{\rm kin}$ as a free parameter when fitting for $V_{\rm CO}$ (i.e. $PA_{\rm kin} \neq PA_{\rm morph}$).

Table 2.1:: Galaxy sample and their galactic parameters.

2.3 Extraction of the CO Rotation Velocities and Dispersion Profiles

2.3.1 Beam-smearing correction on CO mean velocity and velocity dispersion fields

Interferometric observations have a characteristic spatial resolution which depends on the configuration of antennae and receiver response - known as the primary beam. This finite spatial resolution can result in blending of velocities from different areas of the galaxy, depending on how quickly the velocity fields vary and the spatial scale of the galaxy with respect to the beam. This is known as beam-smearing.

Before extracting the rotation curves and dispersion profiles, we first applied a beam-smearing correction to both the CO mean velocity and velocity dispersion maps. The observed mean velocity field (especially in the inner region) as well as the velocity dispersion field are affected by beam smearing effect as the observations have an average beam size of $\sim$4.5″ ($\sim$1/5 of the typical effective radii of our sample of galaxies). To recover the intrinsic V_ϕ and $\sigma_{\rm CO}$ (and hence the most precise dynamical mass to serve as a reference), we need to estimate and remove the effect of beam smearing on dispersion. This is done in two steps: (1) recover the pre-beam-smeared mean velocity map and (2) calculate the velocity dispersion caused by the beam around each pixel from the pre-beam-smeared velocity field.

To recover the pre-beam-smeared mean velocity field, we assume the molecular gas in the galaxy is a thin disk such that the mean velocity equals the line-of-sight velocity. We first create a perturbed velocity field V' by varying the velocity at each pixel, within the range $V_{\rm obs} \pm \sigma_{\rm obs}$ (observed velocity dispersion). From V' we calculate a modelled velocity field $V_{\rm mod}$ from the beam weighted average of the velocities within the two FWHM of the beam around each pixel. This is illustrated in Figure 2.1, where the black pixel labelled as pixel i is the pixel at which we want to evaluate the beam-smearing corrected mean velocity, grey ellipse indicates two FWHM of the beam and the grey pixels indicate the pixels with which we compute the beam weighed average.

We iterate on this procedure until a V' field is found such that its model velocity $V_{\rm mod}$, reproduces the original, beam-smeared observed velocity field, $V_{\rm obs}$. This V' is then taken as the intrinsic beam-smearing corrected mean velocity field, $V_{\rm int}$, and is

related to the observed velocity field as:

$$V_{\rm obs,i} = \frac{\sum_{j \in X_i} w_{\rm ij} V_{\rm int,j}}{\sum_{j \in X_i} w_{\rm ij}}, \tag{2.1}$$

with $X_{\rm i}$ is the set of pixels within a full beam around pixel i (i.e. the grey pixels in Figure 2.1 and $w_{\rm ij}$ being the weight of the beam of pixel i (a 2D gaussian) at the jth pixel. This relation holds simultaneously for all pixels.

From $V_{\rm int}$ we can then compute $\sigma_{\rm mod}$, the amount of dispersion contributed from beam-smearing. First we take $\sigma_{\rm mod}$ at a certain pixel as the beam-weighted standard deviation of $V_{\rm int}$ within a full beam size around the pixel:

$$\sigma_{\rm mod,i} = \sqrt{\frac{\sum_{j \in X_i} w_{\rm ij} (V_{\rm int,j} - \overline{V_{\rm int,j}})^2}{\sum_{j \in X_i} w_{\rm ij}}}. \tag{2.2}$$

Finally, we obtain the intrinsic dispersion, $\sigma_{\rm int}$ by performing a quadrature subtraction of the modelled dispersion, $\sigma_{\rm mod}$, from the observed dispersion, $\sigma_{\rm obs}$:

$$\sigma_{\rm int} = \sqrt{\sigma^2_{\rm obs} - \sigma^2_{\rm mod}}. \tag{2.3}$$

In Figure 2.2, we show as an example the pre- and post- beam-smearing corrected mean velocity maps, velocity dispersion maps, the observed and beam-smearing corrected rotation curve $V_{\rm CO}$ (see §2.3.2) and the $V/\sigma_{\rm CO}$ ratio of UGC04132. The corresponding plots for all 54 galaxies in our sample in Figure A.5 in Appendix A.4.

In Figure 2.3, we show the differences between the rotation curves extracted from the CO kinematics before and after beam-smearing correction. After beam-smearing correction, the rotation curves show a larger value, the differences may be negligible in the outer radii but become significant in the inner region where the gradient in the velocity field is larger. The modelled beam-smearing contribution to the dispersion field as well as the beam-smearing corrected dispersion field obtained using the method described above make it evident that most of the observed velocity dispersion comes from beam-smearing.

While this method serves as a good estimation of the beam-smearing effect, a few minor effects may lead to us not fully capturing the beam-smearing effect: including the simplifying assumption of an uniform gas distribution, and the fact that instead of applying beam-smearing correction to each and every channel, we utilise only the mean velocity map. We therefore utilise still only the CO $V_{\rm c}$ beyond $3\sigma_{\rm beam}$ for testing the stellar dynamical models, where the effect of beam smearing on the CO rotation curve is insignificant. Nevertheless, we can see that for most of the

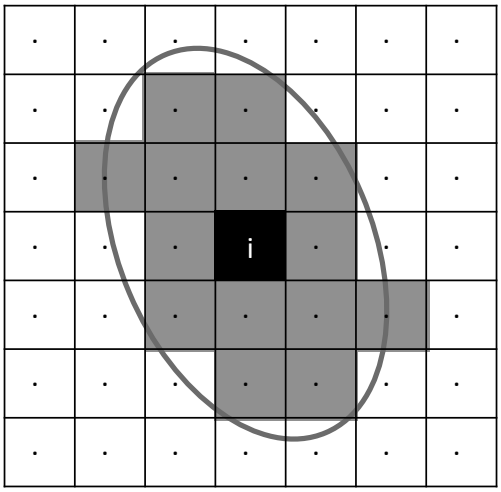

Figure 2.1: Illustration of selected pixel set X_i (in grey) around pixel i (in black). The grey ellipse denotes two FWHM of the beam.

observed dispersion field, the patterns that are caused by the beam-smearing effect can be reproduced in the modelled dispersion field, and hence be subtracted. Such a correction to the CO velocity dispersion map is however of particular importance in assuring that CO acts as a dynamically cold tracer for our galaxy sample (see Section 2.3.4).

2.3.2 Rotation curves

We extract the rotation curves from the CO mean velocity map of each galaxy by first fitting ellipses to the mean velocity map, stepping outwards along the semi-major axes, each time determining the kinematic centre and systemic velocity ($V_{\rm sys}$) of the ellipses. The ellipses are extracted with a minimum of 20 pixels per annulus, and a minimum step size of half $\rm FWHM_{beam}$ along the semi-major axis. The inclinations were based on estimates from the ellipses characterising the outer isophotes and global ellipticity respectively of the r-band photometry from the CALIFA survey and are the same as the ones adopted in the stellar dynamical models (section 2.4). For most cases, we fix the kinematic position angle ($PA_{\rm kin}$) to be the same as $PA_{\rm morph}$ (as fitted from the outer isophotes of the r-band photometry). In the few cases where an adjustment of $PA_{\rm kin}$ is needed, we allow it to be a free parameter in the extraction of ellipses. Galaxies with adjusted $PA_{\rm kin}$ are marked (with *) in Table 2.1.

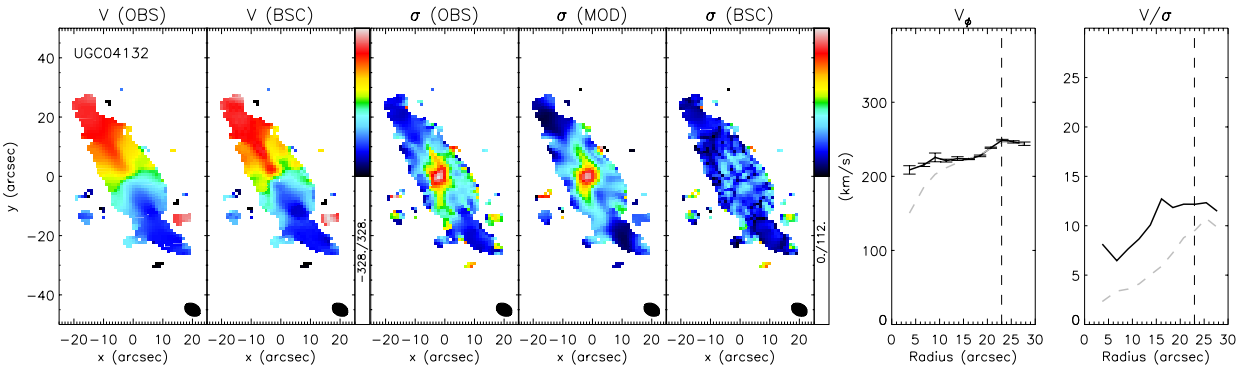

Figure 2.2: Kinematic maps for UGC04132 from the EDGE CO survey. The coloured maps from left to right are: observed mean velocity map, beam-smearing corrected mean velocity map, observed dispersion map, modelled dispersion map and beam-smearing corrected dispersion map. The two plots on the right are the extracted rotation curve and V/σ ratio, with the grey dashed line indicating the observed value and black solid line indicate the beam-smearing corrected value which we adopt in our analysis. The black dashed lines mark the effective radius $R_{\rm e}$.

The ellipse parameters and rotation velocity of each ellipse are found by fitting a velocity field of the form:

$$V_{\rm mod} = V_{\rm sys} + V_{\rm rot}\cos(\phi)\sin(i), \tag{2.4}$$

to the observed mean velocity map. Here $V_{\rm mod}$, $V_{\rm sys}$ and $V_{\rm rot}$ are the modelled, systemic and rotation velocities respectively, ϕ and i are the azimuthal angle (measured from the major axis) and the inclination respectively. To determine the global kinematic centre, $PA_{\rm kin}$ and $V_{\rm sys}$ of each galaxy, we compute the mean of these parameters over all ellipses. The extracted $PA_{\rm kin}$ and $V_{\rm sys}$ are listed in Table 2.1.

To remove any non-circular kinematic perturbations that may come from a bar or spiral arms and could affect our measurement of the rotation curve, we use the method of harmonic decomposition (e.g. Krajnović et al. 2006; van de Ven & Fathi 2010). We model the velocity fields up to their 3rd order harmonics:

$$\begin{aligned} V_{\rm mod} = {} & V_{\rm sys} + c_1\cos(\phi) + s_1\sin(\phi) + c_2\cos(2\phi) \\ & + s_2\sin(2\phi) + c_3\cos(3\phi) + s_3\sin(2\phi), \end{aligned} \tag{2.5}$$

The obtained value $c_1/\sin(i)$ gives us the CO circular velocity (labelled as $V_{\rm CO}$ from hereon), largely removing effects from high order perturbations such as for example spiral arms and bars. Whereas the other terms such as s_1 (radial flow) and the higher

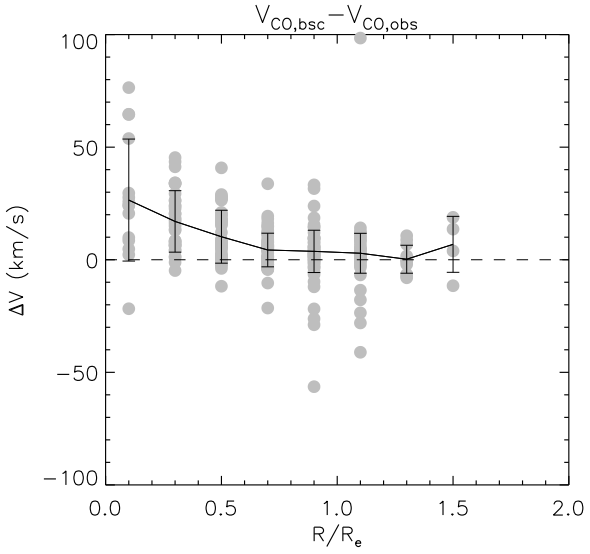

Figure 2.3: We show the differences between the CO rotation curves before and after beam-semaring correction of all the 54 galaxies in grey dots. The black curve and error bars indicate the error-weighted mean and standard deviation of the differences in each bin. As shown in the plot, beam-smearing correction increases the rotation curve and the differences between the two increases inwards.

order terms are not directly related to the rotation curve, they provide an estimate on the small remaining effects from high order perturbation on c_1. The relevant higher order terms c_1, c_3 and s_1 are $\lesssim 10\%$ of our extracted $V_{\rm CO}$. In Appendix A.1, we estimate the upper limit of the effect of the higher order perturbations in our $V_{\rm CO}$ and demonstrate that such perturbations are not correlated with any differences we see between the CO and stellar $V_{\rm c}$.

2.3.3 Uncertainty estimates and selection criteria

To estimate the uncertainties in the extracted CO rotation curves, we performed Monte Carlo perturbations of each pixel with a perturbation randomly sampled from a gaussian with width corresponding to the mean velocity error in the corresponding velocity error map. We perform 200 perturbed runs, each time repeating the steps in Section 2.3.2. As our final CO rotation curve, we take the mean of the rotation curves extracted from the 200 runs and use that to compare with the CALIFA stellar circular velocities. The standard deviation of the 200 rotation curves is taken as the uncertainty of the rotation curves δV. We then remove any rotation velocity measurements with $V/\delta V < 3$. Finally, we remove the rotation velocity

measurements that come from patchy areas in the map as we find that an uneven sampling of line-of-sight velocities along the annuli can render a rotation velocity measurement with large errors (as reflected by a deviation from a smooth rotation curve) that cannot be captured with our estimation of uncertainties. We quantify the patchiness of each annuli by the parameter $P_{\rm patch} = \sigma(n_\phi)/\overline{n_\phi}$, where n_ϕ is the number of pixels with a velocity measurement per degree in ϕ of a particular annuli, $\sigma(n_\phi)$ and $\overline{n_\phi}$ are the standard deviation and mean of n_ϕ. Rotation velocity measurements from annuli with $P_{\rm patch} > 1.5$ are removed. After cleaning our sample with the two criteria mentioned above, the average δV of our galaxy sample is $\sim$10 km s^{-1}. The extracted $V_{\rm CO}$ of UGC04132 are shown in Figure 2.2 as an example.

2.3.4 CO as a kinematically cold tracer

Here, we demonstrate that the CO gas is not pressure supported (i.e. by random motions) and hence our derived rotation curve is a good measure of the circular velocity. Despite being a dynamically cold gas, the CO gas in our sample of galaxies can show a velocity dispersion of up to $\sim$50 km s^{-1} in the inner region. At regions with high velocity dispersion, just like the stellar velocity field, the tangential velocities (V_ϕ) can deviate from the true circular velocity ($V_{\rm c}$). To estimate this deviation, we applied asymmetric drift corrections (ADC) on the CO rotation curve, which solves the first Jeans equation in the equatorial plane (z=0) such that (rearranged from Eq. A3 of Weijmans et al. 2008):

$$V_{\rm c}^2(R) = \overline{V_\phi}^2 + \sigma_R^2\Big[\frac{\partial \ln(\nu\sigma_R^2)}{\partial \ln R} + (\frac{\sigma_\phi^2}{\sigma_R^2} - 1) - \frac{R}{\sigma_R^2}\frac{\partial \overline{V_R V_{\rm z}}}{\partial z}\Big], \tag{2.6}$$

where ν is the intrinsic luminosity density, as deprojected from the integrated intensity map of CO, (V_R, V_z, V_ϕ) and $(\sigma_R, \sigma_z, \sigma_\phi)$ are the velocity and velocity dispersion components in the three dimensions of the cylindrical coordinates (R, z, ϕ). The last term of equation 2.6 vanish if we assume the velocity ellipsoid is aligned with the cylindrical coordinate system. Since we do not know how the velocity dispersion is distributed among turbulent, thermal and gravitational dispersions, we take into account the full beam-smeared corrected (see Appendix 2.3.1) velocity dispersion to obtain an upper limit of any possible deviation of the CO V_ϕ to $V_{\rm c}$ due to support from random motions. We tested the two limiting cases in which the CO gas is isotropic (i.e. $\sigma_\phi^2/\sigma_R^2 = 1$) and radially anisotropic (i.e. $\sigma_\phi^2/\sigma_R^2 = 0$). In both cases we assume that the CO gas lies on a thin disk with $\sigma_z = 0$ when deprojecting the velocity dispersion map, such that: $\sigma_{los}^2 = \sigma_R^2 \sin\phi^2 \sin i^2 + \sigma_\phi^2 \cos\phi^2 \sin i^2$.

In Figure 2.4, we show for all the galaxies in our sample, the difference between the CO rotation curves before and after ADC correction in red for the isotropic case

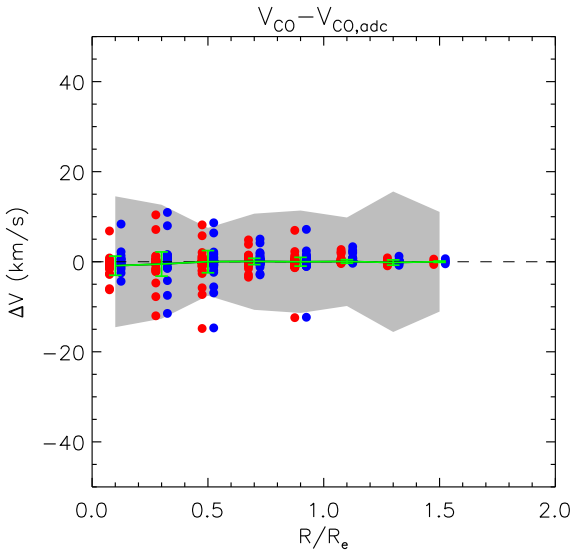

Figure 2.4: We show the differences between the CO rotation curves before and after ADC correction of all the 54 galaxies. Each red/blue dot represents one galaxy in that specific radial bin. The grey slab indicates the average 2σ value of the error of all galaxies in our sample in each radius bin. The green curve and error bars indicate the mean and standard deviation of the differences in each bin. As shown in the plot, even in the inner region, the ADC corrections are in fact mostly lying within the uncertainties.

and in blue for the radially anisotropic case, with each dot corresponding to a galaxy at that particular radial bin. We find that the correction to the CO rotation curve is insignificant in either cases, mostly lying even within the error of the rotation curve itself. This suggests that CO is a dynamically cold tracer in our sample of galaxies and the extracted rotation velocity V_ϕ is a good representation of V_c.

2.4 Modelling V_c from stellar kinematics

We consider three commonly used stellar dynamical models, namely: (1) Asymmetric Drift Correction (ADC), (2) Jeans Anisotropic Models (JAM) and (3) Schwarzschild models (SCH). As mentioned in the Introduction, out of these three models, ADC is the most easily implemented and requires the largest amount of assumptions. SCH, on the other hand, require the fewest assumptions but is the most computationally expensive method. Below we outline the methods and assumptions behind each of the models, which we summarise in Table 2.2.

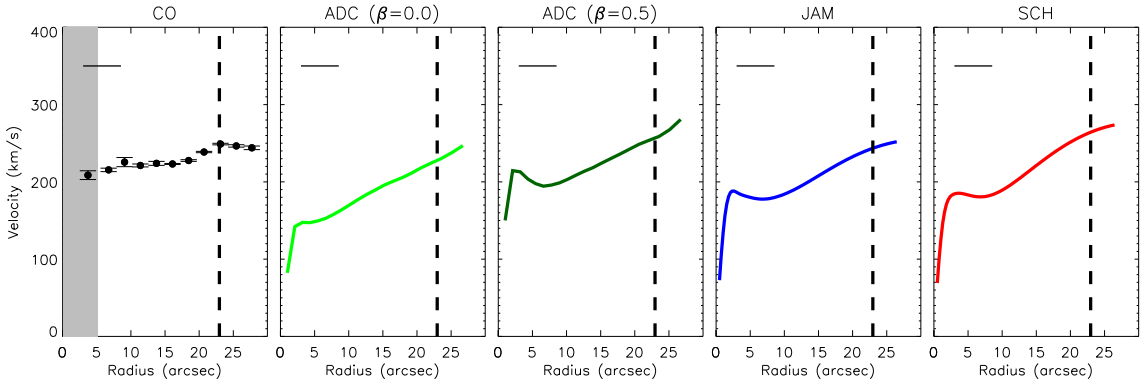

Figure 2.5: We show V_c of UGC04132 using different kinematic tracers and models. From left to right, the tracer used is: CO gas (black dots, with error bars), and stellar kinematics with the ADC model (green), stellar kinematics with the JAM model (blue) and stellar kinematics with the Schwarzschild model (red). The grey region indicates $3\sigma_{\rm beam}$ of the CO observations. The horizontal line on the top left of each panel indicates the scale of 2 kpc. The vertical dashed line marks the effective radius. These V_c from different tracers are stacked on top of each other in Figure 2.8 for easier comparison for each galaxy.

2.4.1 Asymmetric Drift Correction (ADC)

As described in section 2.3.4, ADC solve the Jeans equations utilising the line-of-sight mean velocity and velocity dispersion maps, adopting a thin disk assumption by solving the Jeans equation only in the $z = 0$ plane (i.e. equation 2.6), and in addition assumes an axisymmetric gravitational potential. In solving equation 2.6, we assume that the velocity ellipsoid aligns with cylindrical coordinates and that the velocity anisotropy is constant. We derive $V_{\rm ADC}$ for all the galaxies in our sample with two commonly assumed values of the velocity anisotropy $\beta = 1 - \sigma_\phi^2/\sigma_r^2$: $\beta = 0.0$ (isotropic) and $\beta = 0.5$ (radially anisotropic) (e.g. Hinz et al. 2001; Leaman et al. 2012). To derive smooth surface brightness profiles ν, we fitted Multi Gaussian Expansions (MGEs; Emsellem et al. 1994) to SDSS r-band images. We also fitted a power law to the extracted V_ϕ and an exponential profile to σ_R to ensure a smooth V_c. The functional form of the fittings are:

$$\begin{aligned} V_\phi &= V_0 \frac{R}{(R_c^2 + R^2)^{0.5+0.25\alpha}} \\ \sigma_R &= \sigma_0 e^{-R/R_s} + \sigma_\infty, \end{aligned} \tag{2.7}$$

where (V_0, R_c, α) and $(\sigma_0, R_s, \sigma_\infty)$ are the free parameters in the fitting of V_ϕ and σ_R respectively. The fitted MGEs, the extracted and fitted V_ϕ and σ_R (for the case of $\beta = 0.5$) of all the galaxies in our sample can be found in Appendix A.3, those

Method	ADC	JAM	Schwarzschild
	Solving Jeans Equations		Orbit-based
Geometric Assumption	Axisymmetric Thin Disk	Axisymmetric 3D	Triaxial
Constant M/L	X	Luminous matter	
Dark matter halo	X	Spherical NFW	
Velocity Ellipsoid	$\beta = 0.0$ or $\beta = 0.5$	Constant Anisotropy	No Assumption
	Aligned with cylindrical coord.		

Table 2.2:: Properties and assumptions of the three stellar dynamical models: ADC, JAM and Schwarzschild models. "X" indicates that the respective parameter is not incorporated in that specific model.

of UGC04132 are shown here in Figure 2.7 as an example. The circular velocities extracted using ADC are labelled as $V_{\rm ADC}$ in the rest of this work, the two specific cases with $\beta = 0.0$ and $\beta = 0.5$ are labelled as $V_{\rm ADC,\beta=0.0}$ and $V_{\rm ADC,\beta=0.5}$. In Figure 2.5, we show $V_{\rm ADC,\beta=0.0}$ and $V_{\rm ADC,\beta=0.5}$ for UGC04132 in light and dark green curves respectively.

2.4.2 Axisymmetric Jeans Anisotropic Multi-Gaussian Expansion Models (JAM)

JAM also solves the Jeans equations utilising the line-of-sight mean velocity and velocity dispersion maps, but under different assumptions. Just like with ADC, JAM assumes an axisymmetric gravitational potential and a velocity ellipsoid aligned with the cylindrical coordinate system. Unlike ADC however, JAM takes into account a full line-of-sight integration when modelling the observed velocity moments. It involves two of the Jeans equations (all the terms in the third Jeans equation vanish due to the axisymmetric assumption):

$$\begin{aligned} &\frac{\partial(R\nu\overline{V_R^2})}{\partial R} + R\frac{\partial(\nu\overline{V_R V_z})}{\partial z} - \nu\overline{V_\phi^2} + R\nu\frac{\partial\Phi}{\partial R} = 0, \\ &\frac{\partial(R\nu\overline{V_R V_z})}{\partial R} + R\frac{\partial(\nu\overline{V_z^2})}{\partial z} + R\nu\frac{\partial\Phi}{\partial z} = 0, \end{aligned} \tag{2.8}$$

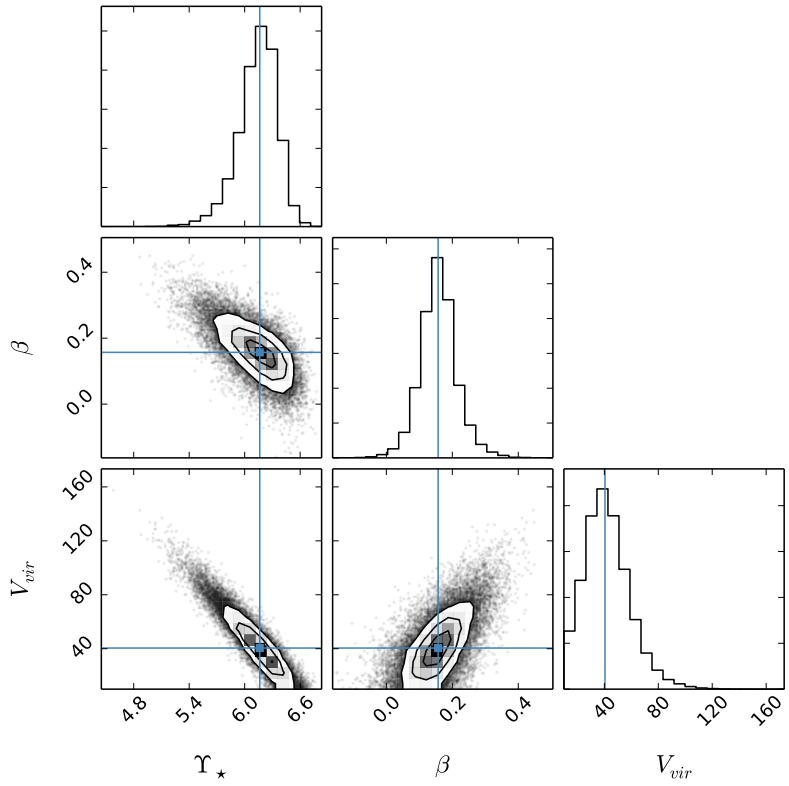

Figure 2.6: Posterior and covariance distributions return from our MCMC analysis for parameters in the JAM model of UGC04132. Contours show the 1, 2 and 3σ constrains on each parameter.

where $\nu(R, z)$ is the intrinsic luminosity density and $\Phi(R, z)$ is the axisymmetric gravitational potential. Again, (V_R, V_z, V_ϕ) are the velocity components in the three dimensions of the cylindrical coordinates (R, z, ϕ). We use the JAM code developed by Cappellari (2008)[4] to construct the modelled kinematics. In our models, the gravitational potential is composed of two components: a luminous component and a dark matter halo. For the luminous component, we follow the commonly adopted mass-follow-light assumption. We again describe the light distribution $\nu(R, z)$ with the same MGEs as used in our ADC, and multiply that with a constant stellar mass-to-light ratio $\Upsilon_\star$ to obtain the mass distribution of the luminous matter, which we assume to be axisymmetric. A spherical NFW (Navarro et al. 1996) dark matter halo is then added to the potential, with the concentration fixed to be related to the

[4]we use the python version of code which can be downloaded from http://www-astro.physics.ox.ac.uk/∼mxc/software

virial mass M_{200} (Dutton & Macciò 2014), defined as the enclosed mass within r_{200}. In addition, we assume a constant velocity anisotropy $\beta_z = 1 - \sigma_z^2/\sigma_r^2$ in our JAM models. There are hence in total three free parameters in the fitting of the models: the stellar mass-to-light ratio $\Upsilon_\star$, the virial velocity of the dark matter halo $V_{\rm vir}$, and the velocity anisotropy β_z. The modelled kinematics are then fitted to the observed kinematics via the term $V_{\rm rms} = \sqrt{V_{\rm los}^2 + \sigma_{\rm los}^2}$, where $V_{\rm los}$ is the line-of-sight mean velocity and $\sigma_{\rm los}$ is the line-of-sight projected velocity dispersion.

We constrain the fitting of the kinematics by the Markov-Chain Monte-Carlo method (MCMC), implemented with the publicly available software `emcee`[5] (Foreman-Mackey et al. 2013). We employ 100 walkers and 500 steps when modelling each of the galaxies, with a burn-in phase of 50 steps. We apply uniform priors of $0.5 < \Upsilon_\star < 10$, $0\,{\rm km/s} < V_{\rm vir} < 400\,{\rm km/s}$ and $-2 < \beta_z < 1$. We assume that the observation errors are gaussian and adopt $L = \exp\big(-\frac{\chi^2}{2}\big)$ as our likelihood function. For most galaxies, the free parameters converge well within our imposed priors. We show in Figure 2.6, the posterior distribution of the parameter space for galaxy UGC04132 as a representative example. The observed and modelled $V_{\rm rms}$ of this particular galaxy is shown in Figure 2.7. The MGE and $V_{\rm rms}$ fittings for the rest of the galaxies in our sample are shown in Appendix A.3. We label the circular velocities extracted using JAM as $V_{\rm JAM}$ from hereon. $V_{\rm JAM}$ of UGC04132 is shown in blue in Figure 2.5.

[5]the software can be found on https://github.com/dfm/emcee

Galaxy	$\Upsilon_\star$	β_z	$V_{\rm vir}$ (km/s)	reduced χ^2
IC0480	5.66	0.73	59.19	2.86
IC0944	5.90	0.43	181.17	3.19
IC1199	5.54	0.54	132.25	1.53
IC1683	3.39	-1.41	223.03	1.45
IC2247	5.15	0.67	98.38	1.87
IC2487	7.52	0.07	48.88	1.17
IC4566	5.04	-0.73	57.20	2.39
NGC0477†	4.99	-1.95	44.88	1.50
NGC0496	2.43	0.40	67.53	0.94
NGC0551	4.32	0.23	34.36	1.98
NGC2253†	2.32	-1.97	98.41	1.26
NGC2347‡	3.89	-0.74	109.52	2.24
NGC2410	5.68	0.23	18.25	1.28
NGC2639‡	3.64	0.82	111.16	4.22
NGC2906	4.49	0.13	193.42	0.91
NGC3815	3.57	0.55	122.62	1.74
NGC3994	3.49	0.47	14.53	3.46
NGC4047†	2.58	-1.94	190.30	0.73
NGC4149	5.40	0.44	24.23	8.28
NGC4210†	4.11	-1.94	32.17	2.52
NGC4644†	4.50	-1.90	96.82	2.29
NGC4711	3.66	-0.15	47.95	0.83
NGC4961‡	2.92	0.40	78.35	1.75
NGC5016	3.15	-0.57	131.73	0.58
NGC5056†	4.09	-1.97	19.85	2.57
NGC5218‡	7.20	0.61	104.53	1.81
NGC5480†	2.44	-1.90	19.39	1.32
NGC5520	3.74	-0.01	351.46	1.39
NGC5633	3.24	0.47	50.70	1.57
NGC5784‡	3.84	-0.54	121.16	7.51
NGC5908‡	5.57	0.51	111.33	10.29
NGC5980	4.50	0.56	15.65	5.45
NGC6060	4.97	0.31	32.34	0.40
NGC6168	2.76	0.88	113.70	0.74
NGC6186	3.53	0.61	14.40	5.36
NGC6301	4.92	-0.86	106.80	3.98
NGC6394	5.14	-0.02	114.90	4.74

NGC6478	4.48	0.10	94.09	4.82
UGC00809	8.37	0.54	90.07	2.33
UGC03539	5.02	0.89	255.40	1.88
UGC03969	6.36	0.77	71.45	1.98
UGC04029	6.14	0.65	61.95	7.50
UGC04132	6.16	0.16	40.48	2.40
UGC05108	5.89	-0.52	288.76	1.89
UGC05598	4.02	0.73	75.32	1.16
UGC08107	9.91	0.41	175.84	1.80
UGC09067	4.52	0.32	33.67	1.78
UGC09537‡	6.28	0.10	134.90	5.64
UGC09542	4.05	0.79	83.43	1.87
UGC09665	2.74	0.82	315.18	0.71
UGC09892	3.40	0.12	48.85	0.66
UGC10123	5.19	0.65	340.85	2.25
UGC10384	3.82	0.81	255.11	1.94
UGC10710	4.80	0.47	148.44	2.86

Table 2.3:: Best fitted parameters and reduced χ^2 of our JAM models. † marks the galaxies which have best fitted $\beta_z < -1.5$, and ‡ marks the galaxies for which we impose an additional stellar-mass-halo-mass relation from Leauthaud et al. (2012).

The best fitted parameters for all the galaxies, and the reduced χ^2 of our best fit models are listed in Table 2.3. We note that for 7 galaxies in our sample, β_z is driven to the lower limit of our imposed prior, as marked with † in Table 2.3. Such behaviours persist even if we allow the inclination to vary, as we show in Appendix A.2, suggesting the behaviours are intrinsic to the JAM models for these galaxies and do not arise from incorrect assumptions of inclinations. Additionally, for 7 galaxies in our sample, $V_{\rm vir}$ is driven to the upper limit of our imposed prior, as marked with ‡ in Table 2.3. To improve the fits for these galaxies, we further impose constraints from studies of abundance matching in simulations and empirical stellar-halo mass relations. We adopt the function form outlined in Leauthaud et al. (2012):

$$\log(M_h) = \log(M_1) + \beta \log\left(\frac{M_s}{M_0}\right) + \frac{(\frac{M_s}{M_0})^{\delta}}{1 + (\frac{M_s}{M_0})^{-\gamma}} - 0.5, \tag{2.9}$$

where M_h is the halo virial mass and M_s is the total stellar mass, which is the integrated mass from the MGEs multiplied by $\Upsilon_\star$. We adopt the parameters $\beta = 0.456$, $\delta = 0.583$, $\gamma = 1.48$, $\log(M_0) = 10.917$ and $\log(M_1) = 12.518$ from Leauthaud et al. (2012). We further discuss both issues and how they might affect our results in Appendix A.2.

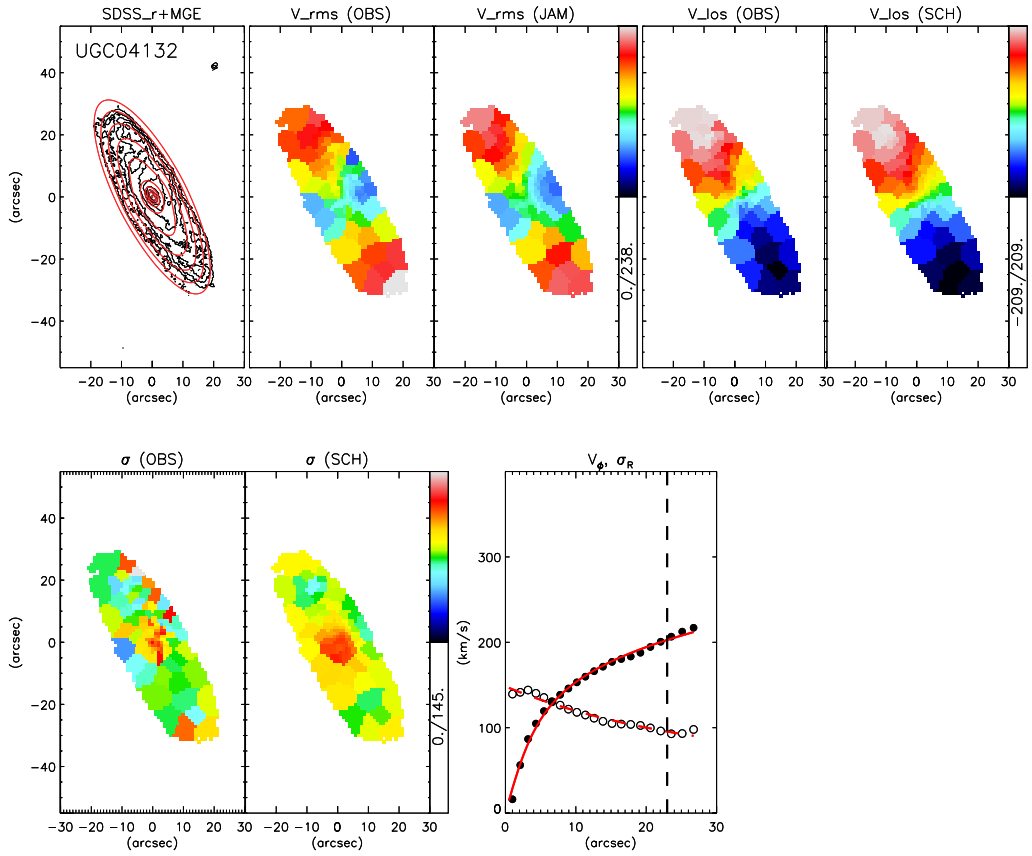

Figure 2.7: Observables and best fit models of stellar dynamical models of UGC04132. *Top from left to right:* (1) r-band image from SDSS plotted in black contours with the fitted MGEs are over-plotted with red contours, (2) observed $V_{\rm rms}$ from the CALIFA survey, (3) best fitted JAM modelled $V_{\rm rms}$, (4)$V_{\rm los}$ from the CALIFA survey, (5) $V_{\rm los}$ from the Schwarzschild model; *Bottom from left to right:* (6) observed $\sigma_{\rm los}$, (7) modelled $\sigma_{\rm los}$, (8) extracted V_ϕ and σ_R (for the case of $\beta = 0.5$) values in solid and open circles, and the fitted functional forms in solid and dashed red lines respectively.

2.4.3 Schwarzschild Models (SCH)

The Schwarzschild models adopt a different approach. Instead of solving the Jeans equations, the Schwarzschild models compute the orbits in a gravitational potential to recover the observed kinematics. A complete description to the methodology of our Schwarzschild models can be found in Zhu et al. (2018a) and the resulting orbital distribution derived for the CALIFA galaxies and their fitted parameters as adopted here can be found in Zhu et al. (2018b). Here we give a brief overview of our Schwarzschild models for completeness. First, a set of mock triaxial gravitational potentials are created. Each of the gravitational potentials is described by two components: mass from luminous matter and mass from dark matter. The stellar mass-to-light ratio is assumed to be constant: $\Upsilon_\star$, with the light distribution again

modelled with MGEs. Unlike in JAM however, the luminous mass distributions in our Schwarzschild models are allowed to be triaxial. The triaxial luminous mass distributions are characterised by the two parameters p and q, which are the ratio between the intermediate axis and short axis with the long axis respectively. Again, the dark matter component is assumed to follow a spherical NFW profile, with the same mass-concentration relation as adopted in JAM. The free parameters here therefore include only the stellar mass-to-light ratio $\Upsilon_\star$, the virial mass M_{200} and the triaxial parameters (p, q). For each of the mock potentials, an orbit library is computed. The orbits in the library are then weighted and used to create mock line-of-sight mean velocity and velocity dispersion maps. The mock kinematic maps (both $V_{\rm los}$ and $\sigma_{\rm los}$) are then fitted to the observed kinematic maps to constrain the weight of each orbit. The gravitational potential with which its best-fitted orbital weights provide the best fit to the observed map is chosen as the best estimate of the true gravitational potential. Finally, the circular velocity is calculated from this best-fit gravitational potential. The Schwarzschild model therefore does not put assumptions on the velocity ellipsoid but still assumes a constant stellar mass-to-light ratio and an NFW profile for the dark matter halo. To allow the readers an assessment to how well the Schwarzschild models are fitted to the kinematics, we include the observed and best fitted Schwarzschild model kinematics of our full sample of galaxies in Appendix A.3 and show here in Figure 2.7, those of UGC04132 as an example. We label the circular velocities extracted from the Schwarzschild models as $V_{\rm SCH}$. $V_{\rm SCH}$ of UGC04132 is shown in red in Figure 2.5.

2.5 Differences of $V_{\rm c}$ extracted from CO and stellar kinematics

In this section we describe the comparison of V_c extracted using different kinematic tracers: dynamically cold molecular tracer CO and dynamically hot stellar kinematics, including those derived from the Asymmetric Drift Correction (ADC), Jeans (JAM) and Schwarzschild (SCH) models. All the V_c for our sample of 54 galaxies extracted with the aforementioned kinematic tracers are presented in Figure 2.8. We first compare the different stellar dynamical models with CO in the following order: ADC vs. CO, JAM vs. CO and SCH vs. CO. For each model, we begin by comparing the stellar and CO $V_{\rm c}$ at one effective radius, and then we characterise the variation of the differences with respect to galactic radii, stellar $V_\phi/\sigma_{R\star}$ values and galactic properties. We then also examine how the three stellar dynamical models perform when compared against each other.

2.5.1 ADC vs. CO

In Figure 2.9(a), we plot in solid circles the values of $V_{\rm ADC}$ versus $V_{\rm CO}$ at the effective radii $R_{\rm e}$ for the 47 galaxies in our sample in which $V_{\rm CO}$ reaches $1\,R_{\rm e}$. For galaxies where the observed CO kinematics reaches $1\,R_e$ while the observed stellar kinematics do not, we extrapolate $V_{\rm ADC}$ with the MGEs, the fitted power-law for V_ϕ and the fitted exponential law for σ_R. The extrapolated $V_{\rm ADC}$ are shown as dashed lines in Figure 2.8. In open circles, we plot $V_{\rm ADC}$ versus $V_{\rm CO}$ at the maximum observed radius ($R_{\rm max}$) for the remaining 9 galaxies for references. We do not extrapolate $V_{\rm CO}$.

Light green circles denote $V_{{\rm ADC},\beta=0.0}$ and dark green circles denote $V_{{\rm ADC},\beta=0.5}$. This plot indicates visually that $V_{{\rm ADC},\beta=0.0}$ is smaller than $V_{\rm CO}$ at $R_{\rm e}$ in general. On the other hand, $V_{{\rm ADC},\beta=0.5}$ mostly agree well with $V_{\rm CO}$, with the exception of the few highest mass galaxies with $V_{\rm CO} \gtrsim 280\,{\rm km\,s^{-1}}$. $V_{{\rm ADC},\beta=0.5}$ tend to overestimate $V_{\rm c}$ on the high-mass end at $R_{\rm e}$. To quantify any biases or agreements, we compute the relative difference $Q_{\rm ADC} = (1 - \frac{V_{\rm ADC}}{V_{\rm CO}})_{R_{\rm e}}$. The histogram of $Q_{\rm ADC}$ is shown in Figure 2.9(b) in solid lines for galaxies with $R_{\rm max} > R_{\rm e}$, and in dashed line we show the histogram for all galaxies, with Q being computed at $R = R_{\rm max}$ for galaxies which have $R_{\rm max} < R_{\rm e}$. Considering only the galaxies which are observed beyond $1\,R_{\rm e}$, the mean and standard deviation of $Q_{{\rm ADC},\beta=0.0}$ are 11% and 6% respectively, confirming $V_{{\rm ADC},\beta=0.0}$ is smaller than $V_{\rm CO}$ on average. $V_{{\rm ADC},\beta=0.5}$ shows a better agreement with $V_{\rm CO}$, with the mean and standard deviation of $Q_{{\rm ADC},\beta=0.5}$ being -5% and 8% respectively.

We next investigate how the difference $\Delta V_{\rm ADC}$ ($= V_{\rm CO} - V_{\rm ADC}$) varies with galactic radii. In Figure 2.10(a) and (b), we show the relative difference $\Delta V_{\rm ADC}/V_{\rm CO}$ for $\beta = 0.0$ and $\beta = 0.5$ respectively, plotted against normalised radii $R/R_{\rm e}$. Circular velocities of each galaxy are first binned into radial bins as listed in Table 2.4. Then we compute a value for $\Delta V_{\rm ADC}/V_{\rm CO}$ for each bin in each galaxy, corresponding to a grey point in Figure 2.10(a). Then for each radial bin, we compute the average and standard deviation over all galaxies, shown as the black curve and error bars in Figure 2.10(a), with values listed in Table 2.4. We shall restrict our discussion to bins that are outside 3σ of the radio beam ($\sigma_{\rm beam}$); even though we already performed a beam smearing correction, an uneven distribution of CO gas within the beam can still affect the resulting $V_{\rm CO}$. We still show the bins within $3\sigma_{\rm beam}$ for reference in Figure 2.10 with open circles.

Figure 2.10(a) shows an increasing trend in mean $\Delta V_{{\rm ADC},\beta=0.0}/V_{\rm CO}$ towards the center, indicating that the isotropic ADC increasingly underestimate $V_{\rm c}$ towards the central regions of galaxies. Within $1R_{\rm e}$, $V_{{\rm ADC},\beta=0.0}$ underestimate $V_{\rm c}$ by $\sim$13%

on average, with the scatter of $\Delta V_{\rm ADC,\beta=0.0}/V_{\rm CO}$ increasing towards the center to $\sim$12%. On the other hand, $V_{\rm ADC,\beta=0.5}$ perform better than $V_{\rm ADC,\beta=0.0}$ in all radial bins with $R < R_{\rm e}$, as shown in Figure 2.10(b). At $R < R_{\rm e}$, $V_{\rm ADC,\beta=0.5}$ and $V_{\rm CO}$ agree to within $1\,\sigma$. Just like the case with $\beta = 0.0$, the scatter in $\Delta V_{\rm ADC,\beta=0.5}/V_{\rm CO}$ increases towards the inner region to $\sim$16%.

We show a similar plot of $\Delta V_{\rm ADC}/V_{\rm CO}$, but against $V_\phi/\sigma_{R\star}$, in Figure 2.11(a) for $\beta = 0.0$ and in Figure 2.11(b) for $\beta = 0.5$. $V_\phi/\sigma_{R\star}$ represents the amount of ordered rotation in stellar kinematics and is abbreviated as $V/\sigma_\star$ from hereon. The average and standard deviation of $\Delta V_{\rm ADC}/V_{\rm CO}$ in each $V/\sigma_\star$ bin are listed in Table 2.5. In $0.5 < V/\sigma_\star < 3$, $V_{\rm ADC,\beta=0.0}$ underestimate $V_{\rm c}$ by up to to $\sim$18% in a bin, with both an increasing $\Delta V_{\rm ADC}/V_{\rm CO}$ and an increasing scatter towards the low $V/\sigma_\star$ regime. $V_{\rm ADC,\beta=0.5}$ agrees better with $V_{\rm CO}$ in all the $V/\sigma_\star > 1.0$ bins, with a difference averaging to < 4% in this regime. For $V/\sigma_\star < 1.0$, however, $V_{\rm ADC,\beta=0.5}$ overestimate $V_{\rm c}$ by 14%. The scatter in $\Delta V_{\rm ADC}/V_{\rm CO}$ for the case of $\beta = 0.5$ also increases towards the low $V/\sigma_\star$ regime.

To discern any systematics in the difference between $V_{\rm ADC}$ and $V_{\rm CO}$ with galactic properties, we show plots of $\Delta V_{\rm ADC}/V_{\rm CO}$ against stellar mass and morphological types for $\beta = 0.0$ in Figure 2.13(a) and 2.13(e), and for $\beta = 0.5$ in Figure 2.13(b) and 2.13(f). Each circle correspond to one grey circle in Figure 2.11, colour coded here with the respective $V/\sigma_\star$ bin value, with the lowest $V/\sigma_\star$ bin $(0 - 0.5)$ coloured red and the highest $V/\sigma_\star$ bin $(3.5 - 4.0)$ coloured grey. We do not find any trends in $\Delta V_{\rm ADC}/V_{\rm CO}$ with respect to these galactic properties.

2.5.2 JAM vs. CO

The values of $V_{\rm JAM}$ are plotted against that of $V_{\rm CO}$ in Figure 2.9(c), and show good agreement with $V_{\rm CO}$ at $R = R_{\rm e}$. Again, we extrapolate $V_{\rm JAM}$ to $1\,R_{\rm e}$ using the MGEs and show in open circles $V_{\rm c}$ at $R_{\rm max}$ for galaxies which have $R_{\rm max} < R_{\rm e}$. The corresponding histogram of $Q_{\rm JAM} = (1 - \frac{V_{\rm JAM}}{V_{\rm CO}})_{R_{\rm e}}$ is shown in Figure 2.9(d). The mean and standard deviation of $Q_{\rm JAM}$ are -0.3% and 8% respectively, indicating a good agreement between $V_{\rm JAM}$ with $V_{\rm CO}$ at 1 $R_{\rm e}$, with no preferential bias (of either being smaller or larger than $V_{\rm CO}$). Already, this tells us that without the thin disk assumption, JAM can well recover $V_{\rm c}$.

Again we show the relative difference $\Delta V_{\rm JAM}/V_{\rm CO}$ against $R/R_{\rm e}$ in Figure 2.10(c). The average and standard deviation in each radial bin are listed in Table 2.4. On average, $V_{\rm JAM}$ agrees with $V_{\rm CO}$ to within 1σ at all radii, the scatter in $\Delta V_{\rm JAM}/V_{\rm CO}$ increases towards the centre to up to 17% for $R < 0.4R_{\rm e}$. Plotting

$\Delta V_{\rm JAM}/V_{\rm CO}$ against $V/\sigma_\star$ in Figure 2.11(c) shows similar features, $\Delta V_{\rm JAM}/V_{\rm CO}$ agrees to within 1σ at all bins, with an increasing scatter towards the low $V/\sigma_\star$ regime. No specific trend is seen in $\Delta V_{\rm JAM}/V_{\rm CO}$ with respect to $V/\sigma_\star$.

Despite $\Delta V_{\rm JAM}/V_{\rm CO}$ agrees to within 1σ at all radial and $V/\sigma_\star$ bins, we see a large scatter in $\Delta V_{\rm JAM}/V_{\rm CO}$. In particular towards the inner and low $V/\sigma_\star$ region. Again, to better understand this scatter, we investigate how $\Delta V_{\rm JAM}/V_{\rm CO}$ changes with various galactic properties. In Figure 2.13(c) and Figure 2.13(g), we plot $\Delta V_{\rm JAM}/V_{\rm CO}$ against the total stellar mass and morphological type of each galaxy respectively. No systematic trend can be found with respect to these galactic properties.

2.5.3 SCH vs. CO

$V_{\rm SCH}$ show good agreement with $V_{\rm CO}$ at $1R_{\rm e}$, as shown in the one-to-one plot of $V_{\rm SCH}$ against $V_{\rm CO}$ in Figure 2.9(e). The corresponding $Q_{\rm SCH} = (1 - \frac{V_{\rm SCH}}{V_{\rm CO}})_{R_{\rm e}}$ is shown in Figure 2.9(f). $Q_{\rm SCH}$ has a mean and a standard deviation of -0.2% and 9% respectively, again showing no preferential bias towards being positive or negative.

We plot the relative difference $\Delta V_{\rm SCH}/V_{\rm CO}$ against $R/R_{\rm e}$ in Figure 2.10(d), and then against $V/\sigma_\star$ in Figure 2.11(d). The average and standard deviation in each radial and $V/\sigma_\star$ bins are listed in Table 2.4 and Table 2.5. On average, $\Delta V_{\rm SCH}/V_{\rm CO}$ agrees to within 1σ at all radial bins. Just like JAM, the scatter in $\Delta V_{\rm SCH}/V_{\rm CO}$ also increases towards the centre up to 17% for $R < R_{\rm e}$. Also, no systemic trend is seen with respect to $V/\sigma_\star$ values. We investigate how $\Delta V_{\rm SCH}/V_{\rm CO}$ varies with respect to total stellar mass in Figure 2.13(d) and morphological type in Figure 2.13(h) but once again find no systematic trend.

2.5.4 Comparison between the three stellar dynamical models

In Figure 2.12, we show the differences between the circular velocity obtained using the three different methods using the same stellar kinematics. Each grey dot correspond to the velocity difference measured at a certain $V/\sigma_\star$ bin of a galaxy. With the black curve and corresponding error bars we show the average and standard deviations of the differences in stellar $V/\sigma_\star$ bins, we list the corresponding values in Table 2.6.

Comparing the two models that derive $V_{\rm c}$ by solving the Jeans equation, ADC

and JAM (Figure 2.12(a) and 2.12(b)), shows that $V_{\mathrm{ADC},\beta=0.0}$ in general are smaller than V_{JAM}. Moreover, the difference between the two increases with decreasing $V/\sigma_\star$, the same trend had been found with SAURON late-type spiral galaxies in Kalinova et al. (2017). Especially at the regime $V/\sigma_\star < 1$, where the random motion dominate over the ordered rotation, the difference between ADC and JAM reaches an average of $\sim$36 km s^{-1}. $V_{\mathrm{ADC},\beta=0.5}$, on the other hand, agrees with V_{JAM} to within $1\,\sigma$ at all $V/\sigma_\star$ bins > 0.5. In the lowest $V/\sigma_\star$ bin of $V/\sigma_\star < 0.5$, however, $V_{\mathrm{ADC},\beta=0.5}$ is larger than V_{JAM} on average by $\sim$21 km s^{-1}.

We next compare V_{SCH} and V_{ADC} in Figure 2.12(c) and 2.12(d). Just like when compared with V_{JAM}, $V_{\mathrm{ADC},\beta=0.0}$ is smaller than V_{SCH}, with an increasing difference towards lower $V/\sigma_\star$ to on average by $\sim$33 km s^{-1} at $V/\sigma_\star < 1$. $V_{\mathrm{ADC},\beta=0.5}$, on the other hand, agrees with V_{SCH} to within $1\,\sigma$ on average except for the $V/\sigma_\star < 0.5$ bin. There, $V_{\mathrm{ADC},\beta=0.5}$ is larger than V_{SCH} by $\sim$22 km s^{-1} on average.

Both the Jeans and Schwarzschild methods take into account the full line-of-sight integration when modelling the observed mean velocity and velocity dispersion map. The two models show good agreement to within 4% bins on average, with scatters of $\sim$8-23%.

The biggest difference is shown when comparing the two V_{c} derived from ADC, with $\beta = 0.0$ and $\beta = 0.5$, as shown in Figure 2.12(f). $V_{\mathrm{ADC},\beta=0.0}$ is always smaller than $V_{\mathrm{ADC},\beta=0.5}$, with the average difference increasing towards lower $V/\sigma_\star$ regimes up to $>$50 km s^{-1}.

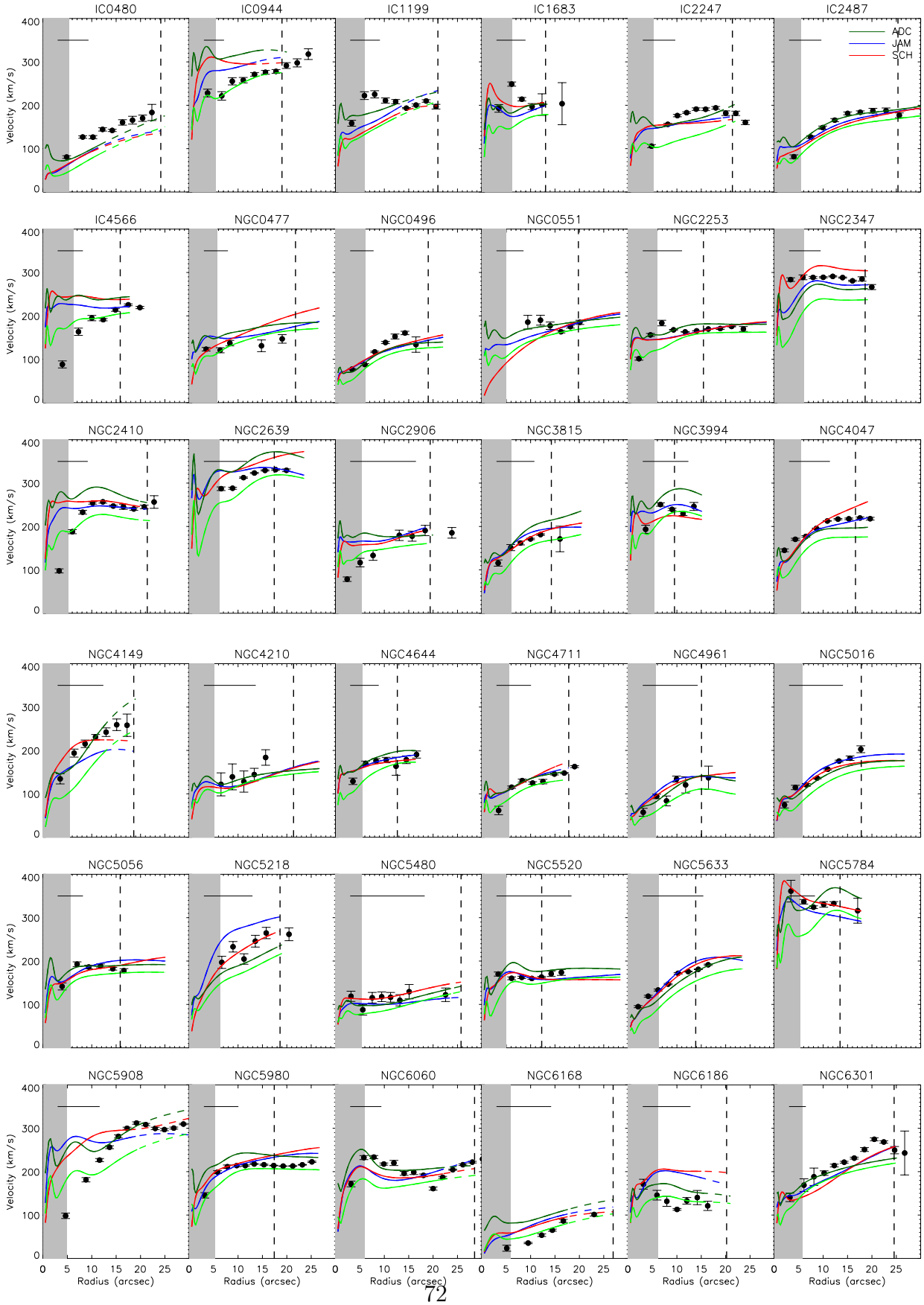
IC0480
IC0944
IC1199
IC1683
IC2247
IC2487
IC4566
NGC0477
NGC0496
NGC0551
NGC2253
NGC2347
NGC2410
NGC2639
NGC2906
NGC3815
NGC3994
NGC4047
NGC4149
NGC4210
NGC4644
NGC4711
NGC4961
NGC5016
NGC5056
NGC5218
NGC5480
NGC5520
NGC5633
NGC5784
NGC5908
NGC5980
NGC6060
NGC6168
NGC6186
NGC6301
ADC
JAM
SCH
Velocity (km/s)
Radius (arcsec)

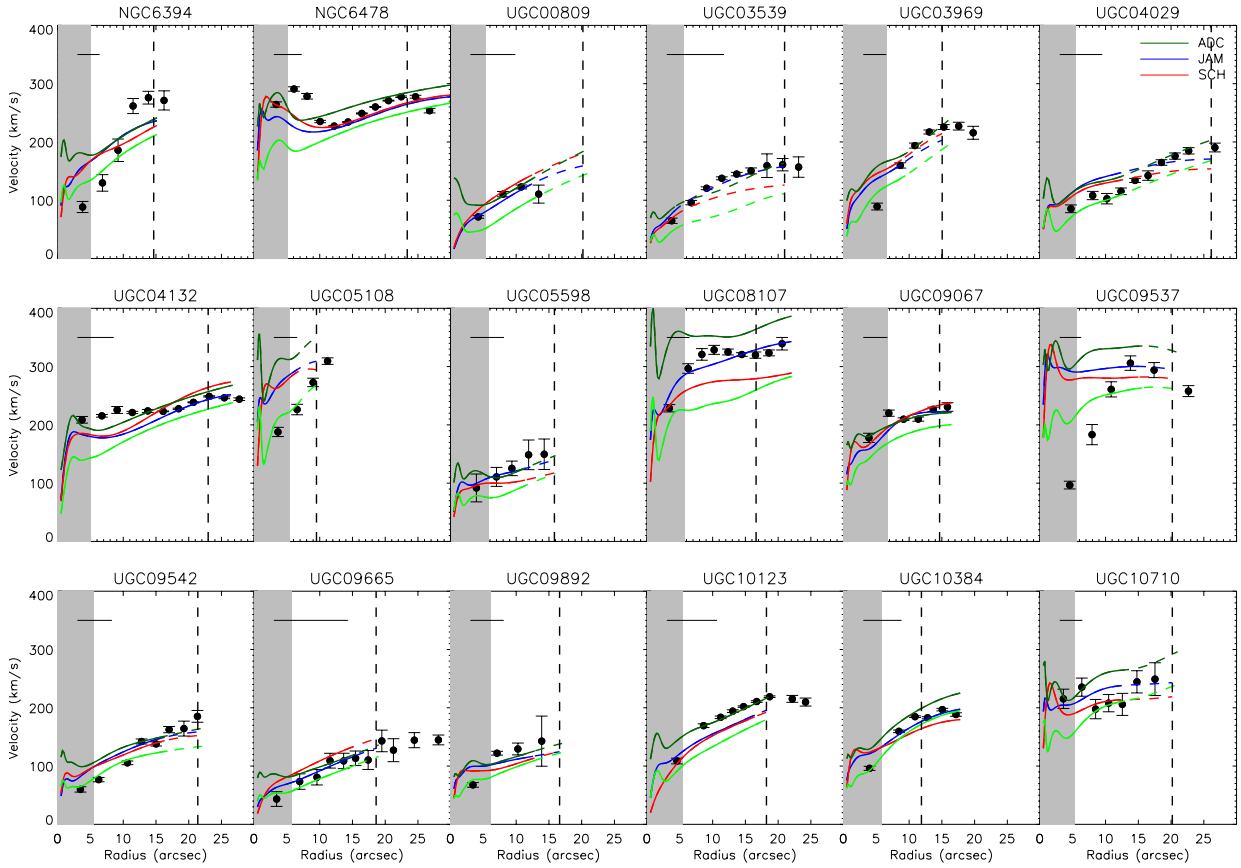

Figure 2.8: Circular velocities of the 54 galaxies. $V_{\rm CO}$ obtained in this work are plotted in black dots, with the error indicated by the error bars. $V_{{\rm ADC},\beta=0.0}$, $V_{{\rm ADC},\beta=0.5}$, $V_{\rm JAM}$ and $V_{\rm SCH}$ are plotted in light green, dark green, blue and red curves respectively. The horizontal line on the top left of each panel indicate the scale of 2 kpc. The vertical dashed line marks the effective radius. The grey region indicate $3\sigma_{\rm beam}$ of the CO observations.

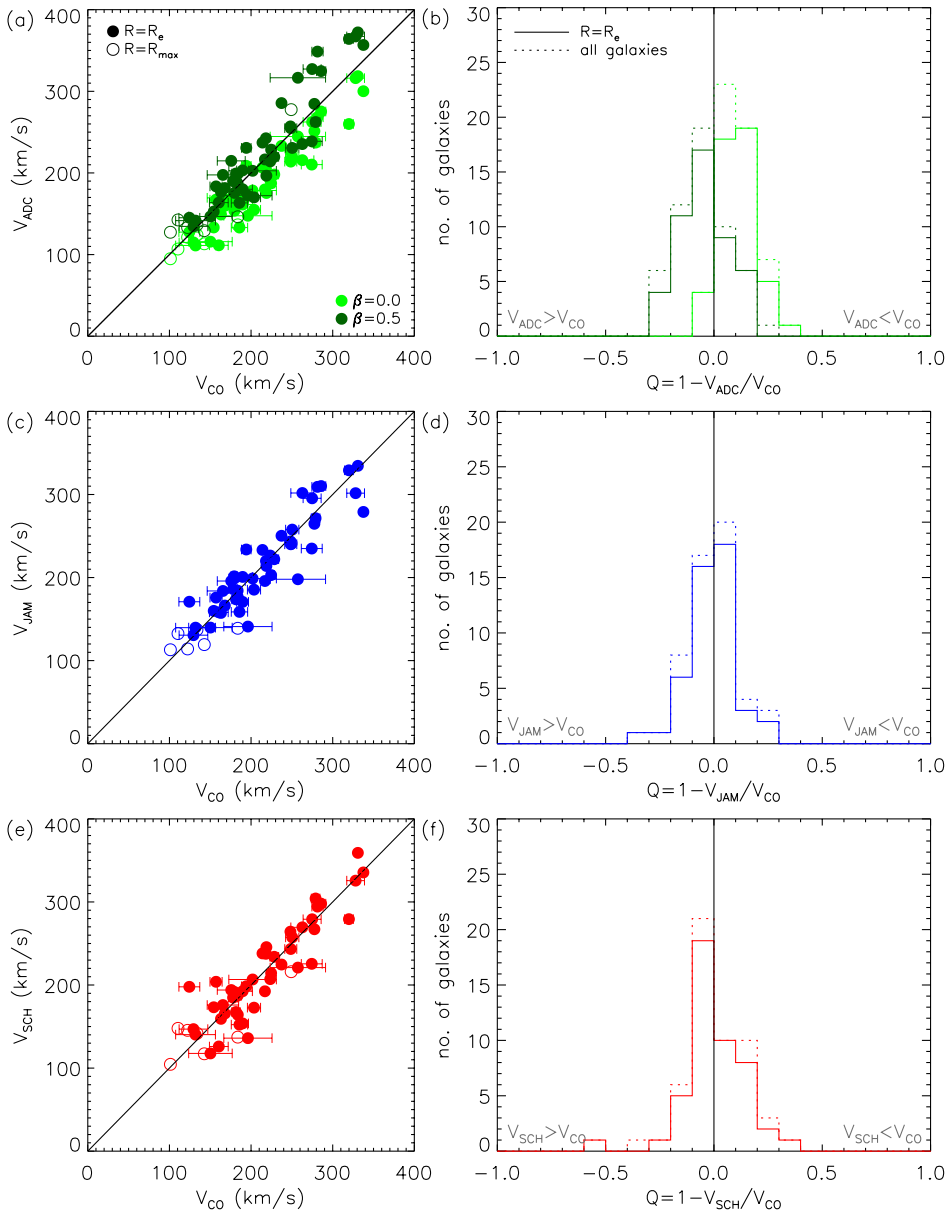

Figure 2.9: Comparison between the stellar and CO circular velocities at 1 $R_{\rm e}$. Panels (a), (c) and (e) show $V_{\rm CO}$ plotted against $V_{\rm ADC}$, $V_{\rm JAM}$ and $V_{\rm SCH}$ respectively, with the black line indicating the one-to-one line. It is shown here that $V_{\rm ADC}$ underestimate the circular velocity with $\beta = 0.0$, but agree well with $V_{\rm CO}$ with $\beta = 0.5$, except for high-mass galaxies. Also, both $V_{\rm JAM}$ and $V_{\rm SCH}$ agree well with $V_{\rm CO}$ at $R_{\rm e}$. Panels (b), (d) and (f) show the relative difference, Q_X, for ADC, JAM and SCH respectively. The black vertical lines indicate $Q = 0$, to the right of the black lines are galaxies from which the stellar $V_{\rm c}$ is smaller than $V_{\rm CO}$, again a bias is seen for $V_{{\rm ADC},\beta=0.0}$, but none in $V_{{\rm ADC},\beta=0.5}$, $V_{\rm JAM}$ and $V_{\rm SCH}$.

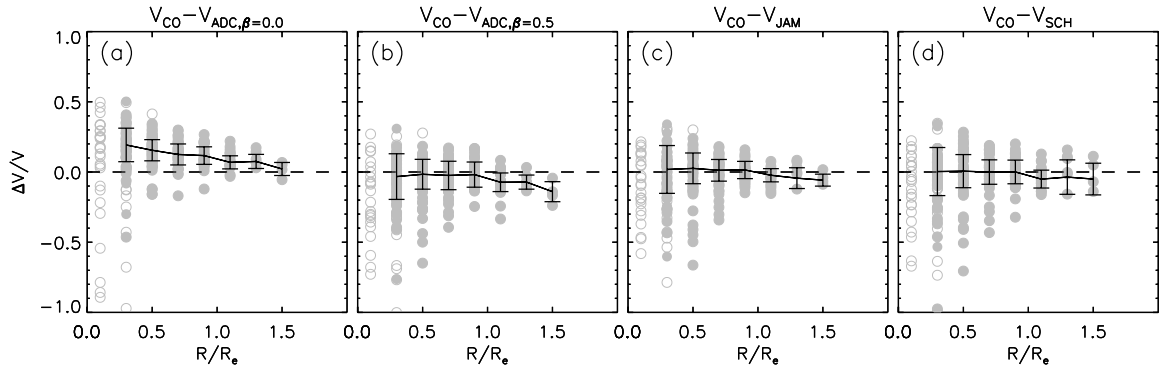

Figure 2.10: Velocity differences between the stellar and CO circular velocity curves in radial bins. Each grey dot represent a measurement from one galaxy at that specific radial bin. The error-weighted mean and standard deviation of each bin are shown in black curve and error bars respectively. $V_{\rm ADC,beta=0.0}$ underestimate $V_{\rm c}$ at all radii, with increasing disagreement with the intrinsic value towards the inner region. While on average, $V_{\rm ADC,beta=0.5}$, $V_{\rm JAM}$ and $V_{\rm SCH}$ agree with CO at all radii, a large scatter can be seen in the inner region. The open grey circles indicate measurements at $R < 3\sigma_{\rm beam}$, the corresponding mean and standard deviation are marked with dotted lines.

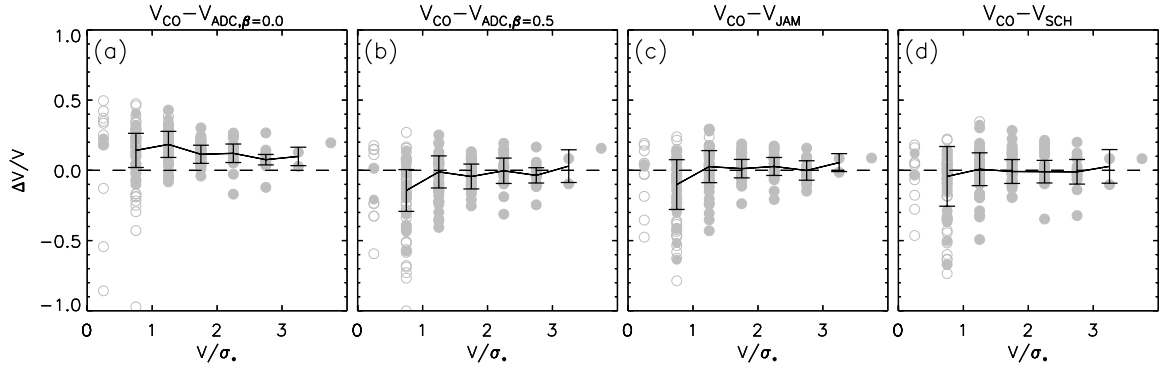

Figure 2.11: Velocity differences between the stellar and CO circular velocity curves in $V/\sigma_\star$ bins. Each grey dot represent a measurement from one galaxy at that specific $V/\sigma_\star$ bin. The error-weighted mean and standard deviation of each bin are shown in black curve and error bars respectively. Again, $V_{\rm ADC,beta=0.0}$ underestimate $V_{\rm c}$ at all $V/\sigma_\star$ bins. All $V_{\rm ADC,beta=0.5}$, $V_{\rm JAM}$ and $V_{\rm SCH}$ agree well with CO on average in all $V/\sigma_\star$ bins. A large scatter can be seen towards the low $V/\sigma_\star$ regime. The open grey circles indicate measurements at $R < 3\sigma_{\rm beam}$.

$R/R_{\rm e}$	$\overline{\Delta V_{\rm ADC}/V}$ $\beta = 0.0$	$\sigma_{\Delta{\rm V/V,ADC}}$ $\beta = 0.0$	$\overline{\Delta V_{\rm ADC}/V}$ $\beta = 0.5$	$\sigma_{\Delta{\rm V/V,ADC}}$ $\beta = 0.5$	$\overline{\Delta V_{\rm JAM}/V}$	$\sigma_{\Delta{\rm V/V,JAM}}$	$\overline{\Delta V_{\rm SCH}/V}$	$\sigma_{\Delta{\rm V/v,SCH}}$
0.2-0.4	0.19	0.12	−0.03	0.16	0.02	0.17	0.00	0.17
0.4-0.6	0.16	0.08	−0.02	0.11	0.03	0.11	0.01	0.12
0.6-0.8	0.13	0.07	−0.02	0.10	0.01	0.08	0.00	0.09
0.8-1.0	0.12	0.06	−0.02	0.09	0.01	0.06	0.00	0.08
1.0-1.2	0.07	0.05	−0.07	0.07	−0.02	0.05	−0.05	0.06
1.2-1.4	0.08	0.05	−0.07	0.05	−0.04	0.07	−0.04	0.12
1.4-1.6	0.02	0.05	−0.14	0.07	−0.06	0.04	−0.05	0.11

Table 2.4:: Discrepancies in derived circular velocities between CO and stellar kinematics, listed in bins of $R/R_{\rm e}$. $\overline{\Delta V}$ is the error-weighted average of stellar and gaseous velocity difference in each bin, $\sigma_{\Delta{\rm V}}$ is the corresponding standard deviation. All velocities are listed in the unit of $\mathrm{km\,s^{-1}}$.

$V/\sigma_\star$	$\overline{\Delta V_{\rm ADC}/V}$ $\beta = 0.0$	$\sigma_{\Delta{\rm V/V,ADC}}$ $\beta = 0.0$	$\overline{\Delta V_{\rm ADC}/V}$ $\beta = 0.5$	$\sigma_{\Delta{\rm V/V,ADC}}$ $\beta = 0.5$	$\overline{\Delta V_{\rm JAM}/V}$	$\sigma_{\Delta{\rm V/V,JAM}}$	$\overline{\Delta V_{\rm SCH}/V}$	$\sigma_{\Delta{\rm V/V,SCH}}$
0.5-1.0	0.14	0.12	−0.14	0.15	−0.10	0.18	−0.04	0.21
1.0-1.5	0.18	0.09	−0.01	0.11	0.03	0.11	0.00	0.12
1.5-2.0	0.11	0.06	−0.04	0.09	0.01	0.07	−0.01	0.09
2.0-2.5	0.12	0.07	0.00	0.09	0.03	0.06	−0.01	0.08
2.5-3.0	0.08	0.04	−0.04	0.05	0.00	0.07	−0.01	0.09
3.0-3.5	0.19	0.07	0.03	0.12	0.06	0.06	0.03	0.12

Table 2.5:: Discrepancies in derived circular velocities between CO and stellar kinematics, listed in bins of stellar velocity dispersion, $V/\sigma_\star$. $\overline{\Delta V}$ is the error-weighted average of stellar and gaseous velocity difference in each bin, $\sigma_{\Delta{\rm V}}$ is the corresponding standard deviation. All velocities are listed in the unit of $\mathrm{km\,s^{-1}}$.

$V/\sigma_\star$	$V_{\rm SCH-ADC,\beta=0.0}$		$V_{\rm SCH-ADC,\beta=0.5}$		$V_{\rm JAM-ADC,\beta=0.0}$		$V_{\rm JAM-ADC,\beta=0.5}$		$V_{\rm SCH-JAM}$		$V_{\rm ADC,\beta=0.0-\beta=0.5}$	
	$\overline{\Delta V}$	$\sigma_{\Delta V}$	$\overline{\Delta V}$	$\sigma_{\Delta V}$	$\overline{\Delta V}$	$\sigma_{\Delta V}$	$\overline{\Delta V}$	$\sigma_{\Delta V}$	$\overline{\Delta V}$	$\sigma_{\Delta V}$	$\overline{\Delta V}$	$\sigma_{\Delta V}$
0.0-0.5	31.1	19.4	−22.0	21.6	32.3	17.2	−20.8	17.5	−1.18	15.1	−53.1	20.6
0.5-1.0	40.2	26.2	−9.67	28.3	44.3	24.2	−5.59	28.2	−4.08	23.1	−49.9	24.7
1.0-1.5	31.2	16.1	−6.08	18.0	27.9	11.7	−9.43	16.2	3.35	11.9	−37.4	13.2
1.5-2.0	23.8	17.6	−6.71	20.1	20.4	10.5	−10.2	14.4	3.46	13.3	−30.4	14.8
2.0-2.5	15.8	8.96	−9.59	10.7	19.2	7.44	−6.11	8.97	−3.47	7.97	−25.0	7.31
2.5-3.0	15.4	13.1	−6.31	11.9	13.7	10.5	−8.03	9.46	1.72	9.49	−21.5	8.57
3.5-4.0	14.3	15.1	−10.9	16.4	16.1	5.76	−9.11	7.53	−1.81	15.0	−20.6	6.56

Table 2.6:: Discrepancies in derived circular velocities with different models using stellar kinematics, listed in bins of stellar velocity dispersion, $V/\sigma_\star$. $\overline{\Delta V_{\rm JAM-ADC}}$, $\overline{\Delta V_{\rm SCH-JAM}}$ and $\overline{\Delta V_{\rm SCH-ADC}}$ are the error-weighted average of stellar and gaseous velocity difference in each bin, $\sigma_{\rm JAM-ADC}$, $\sigma_{\rm SCH-JAM}$ and $\sigma_{\rm SCH-ADC}$ are the corresponding standard deviation. All velocities are listed in the unit of $\mathrm{km\,s^{-1}}$.

2.6 Discussion

In this section, we discuss the possible reasons for the disagreements we see between the V_c obtained from different stellar dynamical models and CO, as well as their respective trends with radius and galactic properties. To recap, we find that: (1) $V_{ADC,\beta=0.0}$ underestimate V_c by ∼8-20%, showing a trend of increasing relative difference $\Delta V/V$ with respect to the V_{CO}, as well as scatter in $\Delta V/V$, towards the inner region. (2) On average, $V_{ADC,\beta=0.5}$, V_{JAM} and V_{SCH} agree with CO to within 1σ over all radii. (3) Towards the inner region ($R < 0.4R_e$) and low $V/\sigma_\star (< 1)$ regime, we find a large scatter among our galaxy sample of 15%, 18% and 21% in $\Delta V/V$, for $V_{ADC,\beta=0.5}$, V_{JAM} and V_{SCH} respectively. (4) Within the large scatter, we do not find any systematic trend with respect to galactic properties such as stellar mass and morphological type. All of these comparisons are done with data outside of $3\sigma_{beam}$ of the CO observations. One should keep in mind that part of the scatter arises from the noise in both the CO and the stellar kinematics (∼5% in the innermost region). Comparing the V_c obtained from the 3 stellar dynamical models directly with each other gives three main results: (1) $V_{ADC,\beta=0.0}$ is smaller than $V_{ADC,\beta=0.5}$, V_{JAM} and V_{SCH}, with differences increasing towards lower $V/\sigma_\star$, (2) while $V_{ADC,\beta=0.5}$ agree with both V_{JAM} and V_{SCH} at $V/\sigma_\star > 0.5$ to within $1\,\sigma$, it is on average larger than both by $\sim 20\,\mathrm{km\,s^{-1}}$ at $V/\sigma_\star < 0.5$, and (3) that V_{JAM} and V_{SCH} are in excellent agreement with each other.

2.6.1 Effects of model assumptions on derived V_c

The ADC models assume a thin disk distribution of stars and therefore cannot account for masses distributed away from the $z = 0$ plane. This is the case for $V_{ADC,\beta=0.0}$, which underestimate V_c at all radii. The trend of velocity discrepancies with radius can also be explained by the fact that thick disks and/or bulges in galaxies tend to be more prominent in the inner region, both of which imply masses distributed away from the disk plane and hence reduces the accuracy of the ADC model. We show however, that by adopting $\beta = 0.5$, the ADC models can reproduce accurate V_c. Such agreement is not surprising when one consider that the light-weight kinematic measurements are mostly dominated by young bright stars which lie close to the disk plane. We should emphasis here that the agreement between $V_{ADC,\beta=0.5}$ with V_{CO} does not suggest that the intrinsic value of β is 0.5, but rather, under the incomplete (thin disk) assumption of ADC, $\beta = 0.5$ can empirically provide a good estimate of the true V_c except for the high mass galaxies (with $V_c \gtrsim 280\,\mathrm{km\,s^{-1}}$). Similar overestimation of V_c can be seen in at low $V/\sigma_\star$ (<1)

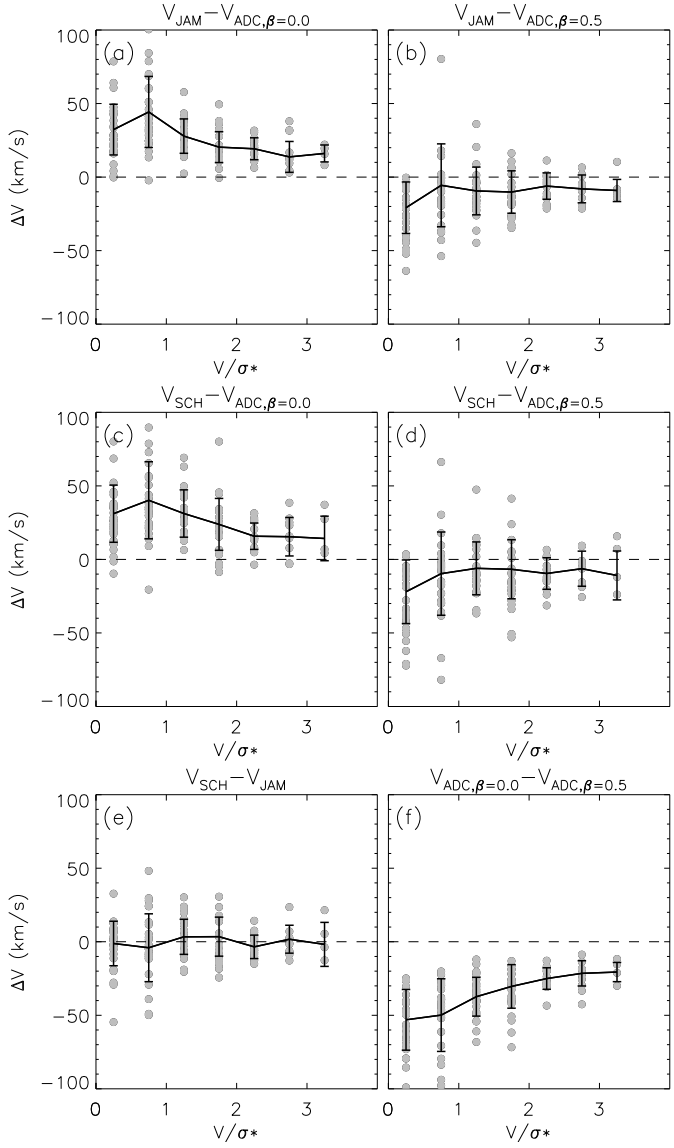

Figure 2.12: Comparison between V_c extracted from stellar kinematics using JAM, ADC and SCH at different $V/\sigma_\star$. Each grey dots represent a measurement from one galaxy at that specific $V/\sigma_\star$ bin. The black curve show the mean and the error bars show the standard deviation of each bin. ADC shows a smaller V_c when compared to either JAM or SCH, and the differences increases towards lower $V/\sigma_\star$. Comparing JAM and SCH also shows a slight trend: in the low $V/\sigma_\star$ regime, JAM tends to produce V_c that are higher than SCH while in the high $V/\sigma_\star$ regime, JAM tends to produce V_c that are lower than SCH.

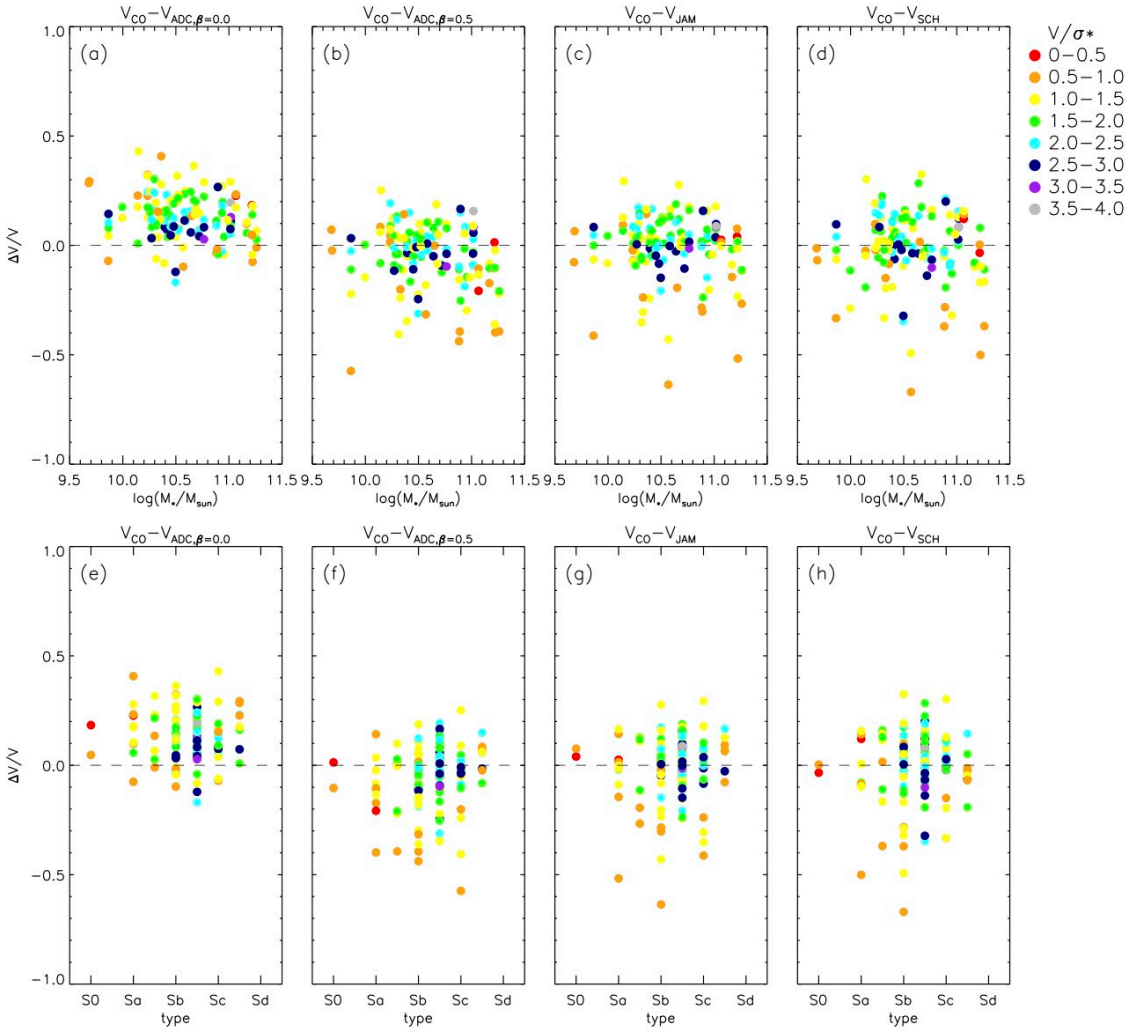

Figure 2.13: Velocity differences between the stellar and gaseous circular velocity curves plotted against the total stellar mass (top row) and morphological types (bottom row) of the galaxies. Each dot here correspond to a grey dot in Figure 2.11(a), (b) for ADC, Figure 2.11(c) for JAM and Figure 2.11(d) for SCH. Only points with $R > 3\sigma_{\rm beam}$ are included in these plots. The points are colour-coded with their respective $V/\sigma_\star$ value. No systematic trends can be found in $\Delta V/V$ with respect to galactic properties.

by $V_{\rm ADC,\beta=0.5}$. This might indicate that in rounder and hotter systems such as early type high-mass galaxies or the inner region of disk galaxies, assuming $\beta = 0.5$ is an overkill even when adopting the thin-disk assumption, as such systems are likely to be more isotropic. The similar differences in the derived $V_{\rm c}$ at $V/\sigma_\star < 0.5$ seen when $V_{\rm ADC,\beta=0.5}$ is compared with $V_{\rm JAM}$ and $V_{\rm SCH}$ are likely caused by the same reason.

Since both the Jeans and Schwarzschild models take into account the full line-of-sight integration of the stellar kinematics, masses distributed away from the disk plane can also be taken into account in these models. The good agreement between $V_{\rm JAM}$ and $V_{\rm SCH}$ with $V_{\rm CO}$ at $R > 0.5R_{\rm e}$ suggests that both models are reliable in recovering the dynamical masses of galaxies at larger radii. For the inner region, the large scatter between $V_{\rm JAM}$ or $V_{\rm SCH}$ and $V_{\rm CO}$ suggests, however, that one should be aware of the possible discrepancies when interpreting the result from the models in these regimes.

Below we suggest the possible reasons causing the $\sim$20% scatter in both the Jeans and Schwarzschild models when being compared with CO in the innermost region. The stellar mass-to-light ratio is still assumed to be constant in both models. Stellar mass-to-light ratio tends to increase toward the inner region due to the increasing stellar age. How the two models compensate for the incorrectly estimated stellar mass with the dark matter component would affect the resultant total mass-to-light ratio. In addition, the assumed shape of the underlying mass distribution can also affect the resulting $V_{\rm c}$. In particular, we assume a spherical dark matter halo and that the stellar mass distribution follows the shape of light distribution. If the mass distribution assumed is flatter than the true distribution, one would overestimate the $V_{\rm c}$ and vice versa (Binney & Tremaine 1987). In galaxies, the older stars that are scattered higher above the disk plane would have a higher M/L ratio than the younger stars in the disk plane, leading to a less flattened distribution in mass compared to light. Although both effects should be more prominent in the inner region of the older galaxies and rounder systems such as the earlier type galaxies, the opposite effects can wash out any systematic trend in the discrepancies with galaxy types.

We would like to warn our readers that even though JAM reproduces $V_{\rm c}$ in good agreement with CO (at $R \gtrsim R_{\rm e}$ and high $V/\sigma_\star$ regimes) or the Schwarzschild models, the other extracted parameters such as $\beta_{\rm z}$ or mass ratio between dark matter and luminous matter are not necessarily correct or physical. This has been reflected by the few galaxies with which $\beta_{\rm z}$ and $V_{\rm vir}$ reach the boundaries of the parameter space to unphysical values. In both cases, Schwarzschild models provide well constrained $\beta_{\rm z}$ and $V_{\rm vir}$. The inability of JAM in recovering $\beta_{\rm z}$ and $V_{\rm vir}$ in certain galaxies is likely caused by the fact that these galaxies do not satisfy additional assumptions in JAM

models, such as having velocity ellipsoids aligned with the cylindrical coordinate system.

2.6.2 Implications on high redshift Tully-Fisher relation

The evolution of the Tully-Fisher relation towards high redshift, z, is a subject of debate. While some authors find no significant evolutions (e.g. Miller et al. 2011; Molina et al. 2017; Pelliccia et al. 2017), others find an evolution towards a lower zero-point (in stellar mass) at high-z (e.g. Cresci et al. 2009; Tiley et al. 2016; Price et al. 2016). When obtaining the rotation velocity from high-redshift galaxies, emission lines from ionised gas are often used as the kinematic tracer. Such high-z ionised gas kinematics show similar V/σ values as the local stellar kinematics in our sample ($\sim 0.5 - 4$ at $z \sim 2$, Wisnioski et al. 2015). Various authors took different approaches in dealing with the high dispersion of the ionised gas kinematics at high-z, namely, either by disregarding the galaxy with low V/σ in their sample, or by taking an approximated form of $V_{\rm c}$ such as $V_{\rm rms} = \sqrt{V^2 + \sigma^2}$. Our results suggest that ADC or JAM may be taken to recover $V_{\rm c}$ from the high-dispersion ionised gas kinematics at high-z, we shall provide a calibration to such application using Hα kinematics from nearby galaxies (from the EDGE-CALIFA survey) in Chapter 4.

2.7 Summary

Stars are present in all galaxies and can serve as a kinematic tracer for the underlying dynamical masses. The collisionless nature of stellar orbits, however, renders such task non-trivial and various dynamical models have been developed to solve the problem. In this work, we test the validity of three commonly used stellar dynamical models in recovering the underlying total mass in galaxies by comparing the circular velocities ($V_{\rm c}$) obtained from IFU stellar kinematics to that extracted from cold molecular gas kinematics over a large and homogeneous sample of 54 galaxies. Such comparison is for the first time enabled by two large surveys of nearby galaxies: the EDGE and the CALIFA survey. We extracted cold gas rotation curves from the CARMA EDGE survey CO($J = 1 - 0$) line emission. We applied harmonic decomposition to the mean velocity fields to remove perturbations from, for example, a bar or spiral arms. For the same galaxies, we show $V_{\rm c}$ obtained from stellar kinematics from the CALIFA survey, using the Asymmetric Drift Correction (ADC), Axisymmetric Jeans Anisotropic Multi-gaussian expansion Models (JAM) and Schwarzschild (SCH) models. For ADC, we tested the model with two commonly

adopted constant velocity anisotropy values: $\beta = 0.0$ (isotropic) and $\beta = 0.5$. For JAM, we assume a constant anisotropy, a constant stellar mass-to-light ratio and a spherical NFW dark matter halo, which are obtained from fitting the velocity moments. The Schwarzschild models adopt an orbit-based approach, with which we again model both the luminous (assuming a constant mass-to-light ratio) and dark matter masses (with an NFW halo), but with no assumption on the velocity anisotropy.

We compare the circular velocities obtained from kinematically cold molecular gas CO with that obtained from stellar kinematics. At the effective radii ($R_{\rm e}$), all the anisotropic ADC ($\beta = 0.5$), JAM and Schwarzschild models reproduce $V_{\rm CO}$ to within <5%, with scatter <10%. Specifically, $Q_{\rm ADC,\beta=0.5} = -5 \pm 11\%$, $Q_{JAM} = -0.3 \pm 11\%$ and $Q_{\rm SCH} = -0.2 \pm 14\%$ (where $Q_{\rm X} = 1 - \frac{V_{\rm x}}{V_{\rm CO}}$). In the inner regions ($R < 0.4R_{\rm e}$), the scatter increases to $\sim 20\%$ for all methods.

The excellent performance of even ADC, which has the strictest assumptions, is likely due to the luminosity weighted velocities in our IFU data - for which the brightest youngest stellar component will be predominantly the dynamically coldest and thinnest.

Possible reasons leading to such discrepancies between the stellar and CO $V_{\rm c}$ in the inner regions are as follows. ADC assumes stars to lie on a thin disk on the plane $z = 0$, therefore it cannot capture masses distributed away from this plane. In particular, in the inner region, the presence of a bulge or a thick disk would render the ADC models to underestimate the circular velocities even more, as reflected by the increasing discrepancies between the $V_{\rm ADC,\beta=0.0}$ and $V_{\rm CO}$ towards the inner region. By assuming $\beta = 0.5$, ADC can empirically recover $V_{\rm c}$ for galaxies with $V_{\rm c} < 280\,{\rm km\,s^{-1}}$.

Both the JAM and Schwarzschild models account for the 3 dimensional distribution of mass, however we suggest that the reasons for ∼20% scatter in the relative difference between both models and $V_{\rm CO}$ in the inner region to be: (1) the deviation of the fitted constant stellar mass-to-light ratio to the intrinsic radially varying value, and (2) the possibility that the underlying shape of the dark matter and stellar mass distribution differ from the assumed shape of spherical halo and light distribution respectively.

This work shows therefore that accurate dynamical masses for galaxies can be recovered from modelling the integrated stellar kinematics with these three methods. Since $V_{\rm ADC,\beta=0.0}$ underestimate $V_{\rm c}$ by ∼12-20% at $R < R_{\rm e}$, we advise that this method is least suitable -instead, the ADC method can still be applied using $\beta = 0.5$ which give a compatible estimate for $V_{\rm c}$ to within ∼10% at $R_{\rm e}$. Significant

deviations in the recovered values still possible locally due to non-constant baryonic and dark mass distributions, we hence advise readers to be aware of such possible discrepancies when interpreting the results from stellar dynamical models.

Acknowledgments

This study uses data provided by the Calar Alto Legacy Integral Field Area (CALIFA) survey (http://califa.caha.es/) and the CARMA Extragalactic Database for Galaxy Evolution (EDGE) survey (http://www.astro.umd.edu/EDGE/). We would like to thank the EDGE collaboration for useful discussions which helped improve this manuscript. This work was supported by Sonderforschungsbereich SFB 881 "The Milky Way System" (subproject A7 and A8) of the Deutsche Forschungsgemeinschaft (DFG). RL was supported by funding from the Natural Sciences and Engineering Research Council of Canada PDF award. RL, GvdV and JF-B. acknowledge support from grant AYA2016-77237-C3-1-P from the Spanish Ministry of Economy and Competitiveness (MINECO). ADB and RCL wish to acknowledge partial support from grants NSF-AST1412419 and NSF-AST1615960. LB and DU are supported by the National Science Foundation (NSF) under grants AST-1616924. This work was supported by the DAGAL network from the People Programme (Marie Curie Actions) of the European Union's Seventh Framework Programme FP7/2007- 2013/ under REA grant agreement number PITN-GA-2011-289313.

Chapter 3

Simultaneous dynamical modelling of stars and gas in dwarf galaxies

Abstract

We present multi-tracer dynamical models of the low mass ($M_* \sim 10^7$), isolated dwarf irregular galaxy WLM in order to simultaneously constrain the inner slope of the dark matter (DM) density profile (γ), halo flattening ($q_{\rm DM}$), and the stellar orbital anisotropy (β_z, β_r). For the first time, we show how jointly solving the Jeans' equations with both a gaseous kinematic tracer and discrete stellar kinematics leads to a factor of ~ 2 reduction in the uncertainties on γ and $M_{\rm vir}$. The mass-anisotropy degeneracy is partially broken by independently constraining the mass distribution from the HI gas rotation curve, leading to reductions of $\sim 25\%$ in the anisotropy uncertainties compared to models using the stellar kinematics alone. Our best fit values for the DM inner density slope, $\gamma = 0.3 \pm 0.1$ is robust to the halo shape, and in excellent agreement with predictions of stellar feedback driven DM core creation. The preferred models have a prolate DM halo with $q_{\rm DM} = 2 \pm 1$ consistent with ΛCDM simulations of dwarf galaxy halos, but which is problematic for MOND given the isolation and structure of WLM. While both velocity independent and dependent self-interacting DM models with $\sigma/m_X \sim 1$ can reproduce this cored DM profile, it is possible the interaction events may sphericalise the halos. The simultaneous cored and prolate DM halo found for this galaxy may therefore present a challenge for these frameworks. Finally we find that the radial profile of stellar anisotropy in WLM (β_r) follows a nearly identical trend of increasing tangential anisotropy to the classical dSphs, Fornax and Sculptor. Given WLM's extreme isolation, this result may call into question whether such anisotropy is a consequence of tidal stripping

and if it instead is a feature of the largely self-similar formation and evolutionary pathways for some dwarf galaxies.

3.1 Introduction

The shape and radial density profile of dark matter (DM) halos provides a window into the nature of dark matter, and the efficiency of baryonic feedback processes which influence the galaxies residing in these halos (e.g., Di Cintio et al. 2014). For instance, dark-matter only cosmological and N-body simulations have shown that, under the ΛCDM cosmological framework, the dark matter haloes around galaxies follow a cuspy density profile characterised by an NFW profile (e.g., Navarro et al. 1996; Dutton & Macciò 2014). With the addition of baryons, hydrodynamic simulations which incorporate energetic feedback from stars and AGN have shown that they can not only alter the star formation properties of the host baryonic disk, but also remove significant amounts of gas on short timescales; resulting in an expansion of the halo and reducing the central density cusp to a shallower profile (e.g., Peñarrubia et al. 2012; Pontzen & Governato 2012).

The DM halo properties may hence be correlated with the baryonic content of the galaxies. For example, Di Cintio et al. (2014) show that the inner slope of the dark matter haloes correlates with the stellar-mass-to-halo-mass ratio in their simulated galaxies, while Read et al. (2016) showed with hydrodynamical simulations that the core size of the dark matter haloes in dwarf galaxies generally correlates with the half-light radii of the stellar component. Significant variation in the predicted range of dark matter fractions is seen either directly from cosmological zoom-in simulations (Brook 2015), or from abundance matching predictions (e.g., Leauthaud et al. 2012; Sawala et al. 2013). Understanding this stochasticity is therefore crucial to gain a better understanding of the efficiency with which baryonic feedback can suppress star formation - and simultaneously alter the initial dark matter halo profiles.

As mentioned in the Introduction, dwarf galaxies are the most dark-matter dominated objects in the universe and therefore provide excellent laboratories to investigate the nature of dark matter. In particular, constraining the inner slope of the density profile of dark matter haloes in relation to the stellar-to-halo mass ratio can provide insights into whether any deviation from an NFW profile, predicted from pure dark matter ΛCDM cosmological simulations, arises from baryonic feedback - or alternative models for the particle/wave aspects of DM. HI kinematics have been used to derive circular velocities for gaseous dwarfs, which are then decomposed to

provide observational constraints on the inner slopes of DM haloes (Lelli et al. 2010; Adams et al. 2014; Katz et al. 2017). While DM inner slopes shallower than that of an NFW profile have been suggested from many of these studies, the fidelity of the results typically suffer from the uncertainties on the stellar mass-to-light ratio.

On the other hand, stellar dynamical models have been primarily applied to Local Group dwarf spheroidals due to their lack of gas and close proximity. As previously discussed, stellar dynamical models suffers from mass-anisotropy degeneracies which can contribute to the uncertainties in the derived DM density profile. While evidence of cored DM haloes have been suggested, these results are either inconclusive given the uncertainties (e.g., Zhu et al. 2016; Kowalczyk et al. 2018), or are geometry-dependent (Walker & Peñarrubia 2011). Given the difficulties in robustly inferring the profile shape through single or even multiple population stellar tracers, It is therefore desirable to study low mass dwarf galaxies with multiple kinematic tracers (e.g., gas and stars) with new analysis methods.

Combining a collisional gas tracer with discrete kinematic stellar tracers in principle should offer a more robust characterisation of the host potential. Despite their different orbit structure, the gas and the stellar kinematics should consistently trace the same potential when all sources of orbital energy are accounted for. Combining observations of stars and gas kinematics in the same galaxy then offers a way to break the mass anisotropy degeneracy and better characterise the dark matter halo properties. Observations of gas and stars in homogenous observations of a variety of galaxies were presented in Leung et al. (2018) (Chapter 2) and for $8.5 < \log L_\star < 9.5$ dwarf galaxies in Adams et al. (2014). However neither of these studies leveraged the tracers simultaneously to measure halo properties from the combined information of both tracers. Nevertheless there appears great promise in exploiting the simultaneous tracers for galaxies where both exist.

Apart from constraints on the underlying gravitational potential, proper modelling of the stellar kinematics can recover their orbit distribution in the galaxy. The shape of the velocity ellipsoid, often parameterised in terms of an anisotropy parameter such as $\beta_\phi = 1 - (\sigma_\phi/\sigma_R)^2$ provides an understanding of the relative amount of random motions in the tangential and radial directions. These quantities may be intimately tied to the formation and evolutionary pathways of the dwarf galaxies - either environmental or secular. Characterising the anisotropy profiles of dwarfs in the Local group is particularly helpful in understanding any evolutionary connection between dwarf irregulars (dIrr) and dwarf spheroidals (dSph) .

For example, predictions of simple dissipationless collapse result in an isotropic core surrounded by an envelope of more radial orbits (van Albada 1982). While

dwarfs with sufficiently radially anisotropic orbits may have undergone bar formation, which after subsequent buckling and excitation of bending modes, can result in significant morphological transformations (e.g., Mayer et al. 2006; Raha et al. 1991). Tidally stripped galaxies are thought to have strongly tangential anisotropy in their outer regions as the radial orbits with larger apocentres may be preferentially removed (Klimentowski et al. 2009).

The highly tangential velocity anisotropies found in dSphs (e.g., Zhu et al. 2016; Kowalczyk et al. 2018) may agree with some tidal transformation scenarios (e.g., Klimentowski et al. 2009), where dIrrs are tidally disturbed and lose their gas and form dSphs, leaving behind a tangential stellar anisotropy distribution for the resultant dSph. However there are no comparable estimates of anisotropy in isolated dwarf galaxies, which would serve as a crucial control sample, and help differentiate if this signature is caused by environmental effects, or rather something intrinsic to the formation of any low mass dwarf.

In addition, the recovery of the stellar anisotropy is not trivial and several degeneracies work to prevent accurate understanding of the stellar orbital, or dark matter halo properties. In addition to the aforementioned mass-anisotropy degeneracy, (e.g., Binney & Tremaine 1987) have shown that the derived anisotropy is highly degenerate with the DM halo geometry. This then means that another parameter, the halo flattening $q_{\rm DM}$, needs to be introduced in dynamical models in order to recover an unbiased estimate of β. For low mass nearby galaxies, incorporating variable DM profiles (γ, q_{DM}) and anisotropy simultaneously, has not been done as the constraints on parameters of interest get understandably poorer with the increasing (but necessary) model complexity. The necessity of understanding DM in low mass dwarfs, breaking anisotropy and halo property degeneracies, and testing the intrinsic orbit structure of *isolated* dwarf galaxies, clearly motivates the need for a new analysis techniques and observations.

In this work we demonstrate a promising way forward, by jointly modelling the stellar and gaseous kinematics in dwarf galaxies which have both resolved stellar kinematics, and well described HI gas rotation curves. With an alternate constraint on the galaxy's potential from the gas rotation curve, the stellar anisotropy estimate should be improved. A second necessary aspect of the modelling is to flexibly parameterise the DM halo's shape and inner density profile slope.

Often, the nature of the dwarf galaxies prevents observable stellar and gaseous tracers from co-existing, such as in the case of the nearby, quenched dSphs, or the low gas fraction transition dwarfs. Alternatively the observational cost of getting stellar kinematics in gas rich dwarf irregulars (which tend to be located at larger distances)

can be prohibitory. However in a few cases dwarfs with resolved stellar and gaseous kinematics have been studied (e.g., Leaman et al. 2012; Kirby et al. 2014), and the dynamical mass estimates from both tracers individually show agreement - provided contributions of non-circular motions are taken into account (e.g., Hinz et al. 2001).

One of the prime targets, which is near enough for obtaining sufficient stellar kinematics, and massive enough to have a well defined gaseous rotation curve, is the isolated dIrr Wolf-Lundmark-Melotte (WLM; Wolf (1910); Melotte (1926)). WLM lies at a distance of $\sim 1\,\mathrm{Mpc}$ from both the Milky Way and M31. The distance between WLM and its nearest neighbour, a low-mass dSph Cetus ($M_{\mathrm{dyn}} \sim 9 \times 10^7 M_\odot$; Walker et al. (2009)), is $\sim$250 kpc (Whiting et al. 1999). With a velocity of $v_{\mathrm{LG}} \sim -32\,\mathrm{km\,s^{-1}}$ towards the barycentre of the local group, Leaman et al. (2012) suggested that WLM has just passed its apocentre and would have at most one pericentre passage in its lifetime, which occurred at least 11 Gyrs ago. Constructing our proposed dynamical model of a dwarf galaxy in such extreme isolation would provide a null test on the effects external influences, such as tides and ram pressure, and provide one of the most detailed views of the DM halo and orbit structure of a low mass dwarf. Also, WLM's isolated location (together with its comprehensive constraints on thickness, stellar dispersion and circular velocity) renders it as an excellent test case for modified gravity, as external field effects cannot be invoked.

In the following, we first describe our HI and stellar data in Section 3.2. We then lay out the observational and model ingredients, including our construction of the dynamical model, the spatial distribution of the kinematic tracers, the baryonic and dark matter density profile, and the steps of our parameter estimation in Section 3.3. We present the obtained dark matter halo parameters and velocity anisotropies of WLM in Section 3.4. In Section 3.5, we discuss the cosmological implications of the derived dark matter halo profile and flattening, as well as the meaning of the derived orbital structure in terms of the evolution of dwarf galaxies. We conclude in Section 3.6.

3.2 Data

3.2.1 HI interferometric data

We have taken the HI integrated intensity map and the circular velocity V_{c} estimated using HI kinematics originally presented in Kepley et al. (2007) and re-analyzed by Iorio et al. (2017). The interferometric data is taken using the Very Large Array,

with a beam size of $\sim 10''$ and a velocity resolution of $\sim 2.6\,\mathrm{km\,s^{-1}}$. The integrated intensity map is shown as black contours on the left panel of Figure 3.1, the velocity map from which the circular velocities are derived from is shown on the right panel of Figure 3.1. From the velocity map, Iorio et al. (2017) have derived an inclination of i=74 and a position angle of ψ=174, which we would adopt throughout this work. Their derived V_c is shown in the left panel of Figure 3.2.

3.2.2 Photometric Data

The I band photometry was obtained using the INT Wide Field Camera and presented initially in McConnachie et al. (2005) and covers a $36' \times 36'$ field of view. We used the resolved radial stellar number density profiles constructed from this data and presented in Leaman et al. (2012) in both I band, and the JHK photometric observations of Tatton et al. (2011). We refer the reader to Leaman et al. (2012) for details of the profile construction.

In addition we utilise photometric observations in the I band taken with the MOSAIC-II imager formerly installed on the 4m Blanco telescope at CTIO. These observations were taken in excellent seeing conditions ($\sim 0.8"$) on September 11 -12, 2009 (PI: Leaman 2009B-0337). The CCD has a pixel scale of $0.27"$/pixel and the images were processed and co-added through the NOAO Science Archive pipelines. The co-added stacked image which was used to build the stellar contribution to the mass distribution, covers a field of view of 0.63×0.67 degrees. Further details of the observations and reductions will be presented in Hughes et al. (in prep.).

3.2.3 Resolved stellar spectroscopy

We utilise a discrete set of velocity measurements from 180 member giant branch stars obtained using FORS2 on VLT and DEIMOS on Keck. The typical uncertainties on velocity are $\delta V \sim 6 - 9\,\mathrm{km\ s^{-1}}$, and the reader is referred to Leaman et al. (2009, 2012, 2013) for details on the data reduction and observations. This sample has already been cleaned form non-member contaminants on the basis of radial velocity and position metrics. The position and line of sight velocities of the stellar kinematic members are plotted in Figure 3.1(e).

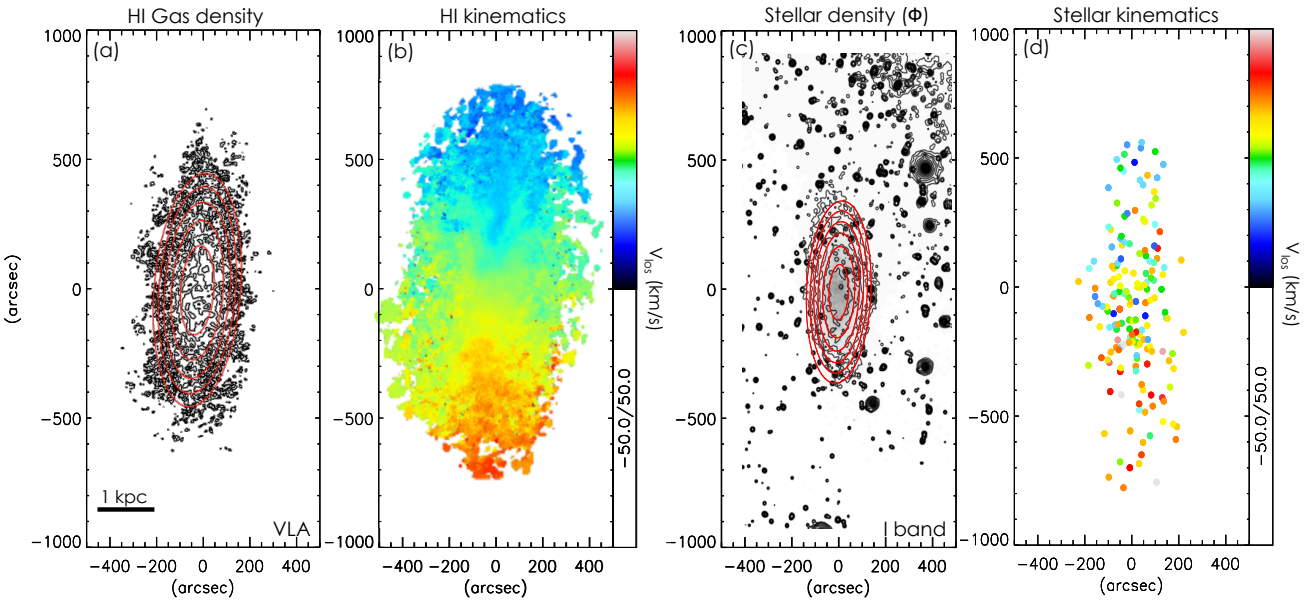

Figure 3.1: Photometric and kinematic data. (a) and (b): HI surface density and velocity maps (Iorio et al. 2017). (c): Greyscale and black contours are the smoothed I band image of WLM. The fitted MGEs are overlaid in red. (d) Discrete velocity measurements.

3.3 Discrete Jeans Model

Given a total gravitational potential Φ, a velocity anisotropy and an inclination, the Jeans equations (Jeans 1922) specify the projected second velocity moment $V^2_{\rm RMS} = V^2_{\rm mean} + \sigma^2$ of a kinematic tracer of known density, where $V_{\rm mean}$ and σ are the mean velocity and velocity dispersion. To begin, we assume axisymmetry for WLM and utilise Jeans Axisymmetric Models (JAM, Cappellari 2008) to solve for the predicted velocity moments. The Jeans equations, under the axisymmetric assumptions, can be written as:

$$
\begin{aligned}
&\frac{\partial(R\nu\overline{v_R^2})}{\partial R} + R\frac{\partial(\nu\overline{v_R v_z})}{\partial z} - \nu\overline{v_\phi^2} + R\nu\frac{\partial\Phi}{\partial R} = 0,\\
&\frac{\partial(R\nu\overline{v_R v_z})}{\partial R} + R\frac{\partial(\nu\overline{v_z^2})}{\partial z} + R\nu\frac{\partial\Phi}{\partial z} = 0,\\
&\nu\overline{v_\phi^2}(R,z) = \Big(1 - \frac{1}{\beta_z}\Big)\Big[R\frac{\partial}{\partial R}\Big(\int_z^\infty \nu\frac{\partial\Phi}{\partial z}dz\Big)\\
&+ \int_z^\infty \nu\frac{\partial\Phi}{\partial z}dz\Big] + R\nu\frac{\partial\Phi}{\partial R}
\end{aligned}
\tag{3.1}
$$

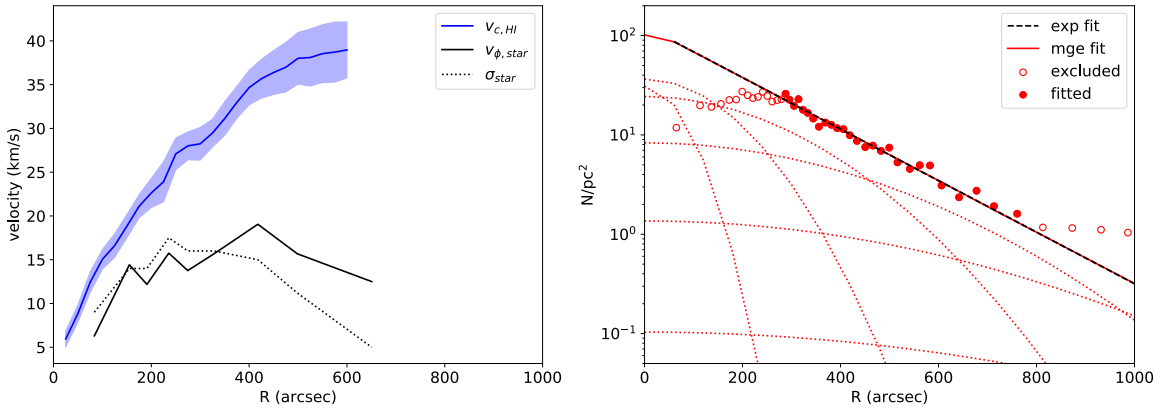

Figure 3.2: *Left:* Circular velocities derived by Iorio et al. (2017) with the velocity map shown in Figure 3.1(b) in blue, with uncertainties shown by the light blue band. The binned stellar mean velocity ($v_{\phi,\mathrm{star}}$) and velocity dispersion (σ_{star}) profiles are shown in solid and dotted black lines. *Right:* The RGB star counts are shown in red circles, with the open circles indicating points that are excluded due to crowding and background contamination in the fitting of exponential profile as adopted in Leaman et al. (2012), the fitted exponential profile is shown in the black dashed line. The individual MGEs fitted to the exponential profile are shown in red dotted lines and the total MGE is shown in a red solid line.

where $\nu(R,z)$ is the surface density of the kinematic tracer and $\Phi(R,z)$ is the axisymmetric gravitational potential. Again, (v_R, v_z, v_ϕ) are the velocity components in the three dimensions of the cylindrical coordinates (R,z,ϕ).

3.3.1 Constructing the potential

We construct the gravitational potential Φ with three components, namely, the gaseous component ($M_{\mathrm{gas,tot}} \sim 1.54 \times 10^8 M_\odot$), the stellar component ($M_{\star,\mathrm{tot}} \sim 1.1 \times 10^7 M_\odot$) and the dark matter component. Each of the components is parametrised by a set of Multi-Gaussian Expansions (MGEs) (Emsellem et al. 1994) as required for our Jeans model. Below we provide details on the distributions of the various components.

Gaseous component

We fit MGEs to the HI integrated intensity map using the python code provided by Cappellari (2008). When fitting the MGEs, we fixed the inclination to be 74,

$I_{0,\mathrm{gas}}$ ($M_\odot\,\mathrm{pc}^{-2}$)	σ_{gas} ($''$)	q_{gas}
3.775	40.58	0.28
1.854	91.71	0.30

Table 3.1:: Multi-Gaussian Expansions of the gaseous component obtained from HI surface brightness.

consistent with the derived inclination from the HI rotation by Iorio et al. (2017). Figure 3.1 shows the best-fitted MGEs in red contours overlaid on the HI gas density contours. We normalised the MGEs to the total neutral gas mass of WLM, $1.1 \times 10^8\,M_\odot$, which is taken from from the single dish observations of Hunter et al. (2011). We apply a correction factor of 1.4 to account for the presence of Helium. The resultant gaseous MGE parameters, the peak surface density $I_{0,\mathrm{gas}}$, the width σ_{gas} and flattening q_{gas}, of each of the constituent gaussians are presented in Table 3.1. The flattening paramete q is given by the ratio between the short and long axis of each gaussian.

Stellar component

To obtain a smooth stellar distribution, we utilise the I-band photometry which tracers evolved stars and avoids the irregular light density profiles of bluer bands. We first smooth the I-band image with a gaussian of width $5''$ in order to remove the stochasticity inherent in the nearby resolved systems, and then fit MGEs to the smoothed surface brightness. The MGEs are then normalised to a total stellar mass. The fitted MGEs are overlaid on top of the I band image in Figure 3.1(c). The resultant stellar MGEs parameters $I_{0,\star}$, $\sigma_\star$, and $q_\star$, as normalised to $M_\star = 1.1 \times 10^7 M_\odot$ (Jackson et al. 2007) are presented in Table 3.2. Despite the presence of some foreground stars in the image, we find that their presence does not change the MGE fits.

Dark matter component

To model the dark matter contribution to the potential of WLM, we utilise a generalised NFW (gNFW; Zhao 1996) profiles to describe our dark matter halo. This has a radial density profile of:

$$\rho(r) = \frac{\rho_{\mathrm{s}}}{(r/r_{\mathrm{s}})^{\gamma}(1 + r/r_{\mathrm{s}})^{3-\gamma}}, \tag{3.2}$$

$I_{0,\star}$ ($M_\odot\,pc^{-2}$)	$\sigma_\star$ ($''$)	$q_\star$
2.750	14.74	0.50
14.72	130.8	0.41
6.239	199.0	0.42

Table 3.2:: Multi-Gaussian Expansion of the smoothed I-band stellar surface brightness profiles used to constrain the stellar mass distribution, normalised to a total stellar mass of $M_\star = 1.1 \times 10^7\,M_\odot$.

with ρ_s, r_s and γ being the scale density, scale radius and slope of the dark matter profile respectively. To test the influence and degeneracy of non-spherical mass distributions, we also allow the dark matter halo to be axisymmetric with a flattening q_{DM} (with $q_{DM} = 1 - b/a$, where b and a are the short and long axis of the dark matter halo respectively). We normalise our DM haloes with the circular velocities at r_s ($V_c(r_s)$) such that dark matter haloes with the same (r_s, γ, ρ_s) but different q_{DM} would have the same $V_c(r_s)$. This normalisation is done so that the parameter q_{DM} is only sensitive to the shape of the dark matter halo but not the overall enclosed mass. A dark matter halo parametrised by a particular set of (r_s, γ, ρ_s and q_{DM}) can then be decomposed into MGEs - which together with the gaseous and stellar MGEs, provides a representation of the total gravitational potential of WLM.

3.3.2 Surface density of the kinematic tracer

To obtain the density profile of the kinematic tracer ν, we utilise the discrete giant branch star counts from Leaman et al. (2012). These star counts are constructed from photometric catalogues which have had a comparable colour and magnitude selection to the spectroscopic sample - thus providing the most representative density distribution for the kinematic tracer population. The stellar density profile for the kinematic tracers is shown in the right panel of Figure 3.2 in red circles. The inner flattened number count profile is potentially caused by crowding and we correct for it by fitting first an exponential profile to the star counts beyond the crowded region ($\gtrsim 300''$), as shown in the black line. We then fit MGEs to the black dashed line. The resultant MGE fit is shown by the red solid line and the MGE parameters are listed in Table 3.3. These MGEs are adopted as the surface density of the kinematic tracer in our models throughout the rest of this work. Readers interested in how robust our results are with respect to the choice of different profiles can refer to Appendix B.1, where we show the impact of this incompleteness correction on our final results.

$I_{0,\star}$ ($M_\odot\,\mathrm{pc}^{-2}$)	$\sigma_\star$ ($''$)	$q_\star$
1.601	64.769	0.422
1.882	135.675	0.422
1.259	232.891	0.422
0.430	348.873	0.422
7.029×10^{-2}	476.647	0.422
5.344×10^{-3}	611.309	0.422
1.893×10^{-4}	749.823	0.422
2.986×10^{-6}	893.630	0.422
1.233×10^{-8}	1057.583	0.422

Table 3.3:: Multi-Gaussian Expansion of the RGB star counts fitted by an exponential profile to measurements within 279$''$-813$''$to avoid bias caused by crowding, normalised to a total stellar mass of $M_\star = 1.1 \times 10^7\,M_\odot$.

parameter	distribution	range
$M_\star$	normal	$1.1 \pm 0.56 \times 10^7\,M_\odot$
$M_{\rm gas}$	normal	$1.54 \pm 0.77 \times 10^8\,M_\odot$
β_z	uniform	[-2.0, 1.0]
κ	uniform	[0.0, 1.5]
$q_{\rm DM}$	uniform/fixed	[0.1, 5.0]
$r_{\rm s}$	uniform	[500, 10000] pc
γ	uniform	[0.0, 1.0]
$\rho_{\rm s}$	uniform	$[0.001, 0.15]\,M_\odot\,\mathrm{pc}^{-3}$

Table 3.4:: The adopted priors on each of the model parameters.

3.3.3 Model parameters

The relevant velocity anisotropy for the JAM model is $\beta_{\rm z} = 1 - \langle v_z^2\rangle/\langle v_R^2\rangle$, where $\langle v_z^2\rangle$ and $\langle v_R^2\rangle$ are the second velocity moments along the z and R axes respectively of the cylindrical coordinate system.[1]

Typically the modelled $V_{\rm RMS}^{\rm mod}$ can be compared directly with the observed $V_{\rm RMS}^{\rm obs}$

[1]We note that under the assumptions of the JAM model, the vertical velocity dispersion is intrinsically coupled to the self-gravity of the disk plane, in a quasi-hydrostatic equilibrium, and thus β_z primarily reflects the vertical density distribution of the galaxy - however we show later the insight that other components of the velocity ellipsoid provide on the orbital structure of WLM

for spatially binned data. In the case of nearby dwarf galaxies, spherical Jeans models have often been applied on the observed $V_{\rm RMS}^{\rm obs}$ in spatial bins along the major axis of the galaxy (e.g., Battaglia et al. 2011). However for fully axisymmetric models, it is more flexible to fit to the discrete stellar kinematic data directly. To do this, we compare the observed line-of-sight velocity $V_{{\rm LOS},i}$ of each star $i \in N$, to the probability distribution function of the model line-of-sight velocity $V_{\rm LOS,mod}$ at their projected location on the sky-plane (x_i, y_i). The discrete data are by construction, only providing a single V_{LOS} value, while the relative contributions of $V_{\rm mean}^{\rm mod}$ and $\sigma^{\rm mod}$ to $V_{\rm RMS}^{\rm mod}$ are not constrained by the Jeans model itself. We therefore follow Satoh (1980) and Cappellari (2008) and introduce κ as another free parameter to characterize the amount of rotation the system has relative to an *isotropic rotator*, where $\kappa = \langle v_\phi \rangle / \sqrt{\langle v_\phi^2 \rangle - \langle v_{\rm R}^2 \rangle}$. As described in Cappellari (2008), $\kappa = 1$ is a rotating system with with an symmetric velocity ellipsoid in the $R - \phi$ plane (and spherically isotropic in cases where $\sigma_z = \sigma_R$, while κ approaches zero 0 when the system angular momentum drops, or the anisotropy increases. While not a direct analogue for angular momentum, the parameterisation allows for a flexible way to fit the discrete velocity field.

Assuming a gaussian velocity probability distribution function, the probability of $V_{\rm LOS,i}$ at the position of each star i can be written as:

$$\ln P(V_{\rm LOS,i}) = \ln \frac{1}{\sqrt{(\delta V_{\rm LOS,i})^2 + (\sigma^{\rm mod})^2}} - \frac{1}{2} \frac{(V_{\rm LOS} - V_{{\rm mean},i}^{\rm mod})^2}{(\delta V_{\rm LOS,i})^2 + (\sigma^{\rm mod})^2}, \tag{3.3}$$

where $\delta V_{\rm LOS,i}$ is the error of the observed $V_{\rm LOS,i}$.

With the inclination and the position angle fixed (i=74, PA=174), the inputs for calculating the likelihood $P(V_{\rm los,i})$ through the JAM model with Eq. 3.3 are: (1) the gravitational potential Φ specified by MGEs, (2) the tracer density distribution specified by the stellar MGEs, (3) the velocity anisotropy $\beta_{\rm z}$ and (4) the κ parameter. The free parameters in constructing Φ are the total stellar mass $M_{\star,\rm tot}$, $q_{\rm DM}$, $r_{\rm s}$, γ and $\rho_{\rm s}$. We assume that $\beta_{\rm z}$ and κ are constant with radius. We therefore have seven model parameters: $(M_{\star,\rm tot}, M_{\rm gas,tot}, \beta_{\rm z}, \kappa, q_{\rm DM}, r_{\rm s}, \gamma, \rho_{\rm s})$ (see Table 4).

3.3.4 MCMC sampling

To obtain marginalised distributions and covariances between the parameters of the most likely models, we sample the likelihood space using the affine-invariant MCMC ensemble sampler implemented in the python package `EMCEE` (Foreman-Mackey et al. 2013). We employ 200 walkers, each iterated through 300 steps; the burn-in phase is

100 steps for each walker.

We constrain $M_{\star,\mathrm{tot}}$ and $M_{\mathrm{gas,tot}}$ with their observed values, $1.1 \times 10^7\,M_\odot$ and $1 \times 10^8\,M_\odot$ respectively, through a prior with a normal distribution of width specifying the measurement error of 50%:

$$\begin{aligned}&\ln Pr_1(M_{\star,\mathrm{tot}}, M_{\mathrm{gas,tot}})\\ &= \ln \frac{1}{\sqrt{2\pi(0.5\times 1.1\times 10^7)^2}} - \frac{(M_{\star,\mathrm{tot}} - 1.1\times 10^7)^2}{2\times(0.3\times 1.1\times 10^7)^2}\\ &+ \ln \frac{1}{\sqrt{2\pi(0.5\times 1.54\times 10^8)^2}} - \frac{(M_{\mathrm{gas,tot}} - 1.54\times 10^8)^2}{2\times(0.3\times 1.54\times 10^8)^2}.\end{aligned} \tag{3.4}$$

For the other model parameters, we apply an uniform prior, the explored ranges of each of the parameters are listed in Table 3.4.

We run two sets of MCMC processes; one which only uses information from the stellar kinematics ('Stars only') and one with the observed HI V_c ($V_{\mathrm{c,HI}}$) as a constrain on the gravitational potential ('Stars + Gas'). In the case for which we include $V_{\mathrm{c,HI}}$ as a constrain on the gravitational potential, we introduce additionally a second prior term, which evaluate

$$\begin{aligned}&\ln Pr_2(M_{\star,\mathrm{tot}}, q_{\mathrm{DM}}, r_\mathrm{s}, \gamma, \rho_\mathrm{s}, R_j)\\ &= \ln \frac{1}{\sqrt{2\pi(\delta V_{\mathrm{c,HI}}(R_j))^2}} - \frac{(V_{\mathrm{c},\Phi}(R_j) - V_{\mathrm{c,HI}}(R_j))^2}{2\times\delta V_{\mathrm{c,HI}}(R_j)^2}.\end{aligned} \tag{3.5}$$

$\Phi = \Phi(M_{\star,\mathrm{tot}}, q_{\mathrm{DM}}, r_\mathrm{s}, \gamma, \rho_\mathrm{s})$ is computed through the MGEs, which gives us $V^2_{\mathrm{c},\Phi}(R) = -R(\partial\Phi/\partial R)$. $V_{\mathrm{c},\Phi}$ is then evaluated at $R = R_j$, where we have measurements of $V_{\mathrm{c,HI}}$ from the HI kinematics.

The total likelihood for the 180 stars can be written as a sum of the probability and the prior, i.e. $\ln L = \Sigma_i(\ln P(V_{\mathrm{LOS,i}})) + \ln Pr_1$ for the 'Stars only' case and $\ln L = \Sigma_{i,j}(\ln P(V_{\mathrm{LOS,i}})) + \ln Pr_1 + \ln Pr_2(R_j))$ for the 'Stars + Gas' case.

3.4 Results

The marginalised model parameters for the set of MCMC runs with free q_{DM} are shown in the corner plots in Figure 3.3. Black contours show the dark matter halo and stellar anisotropy parameters constrained from the 'Stars only' models, and red contours show the distributions recovered from the 'Stars + Gas' models. The corresponding best-fitted parameters and their 1-σ uncertainties are listed in Table 3.5.

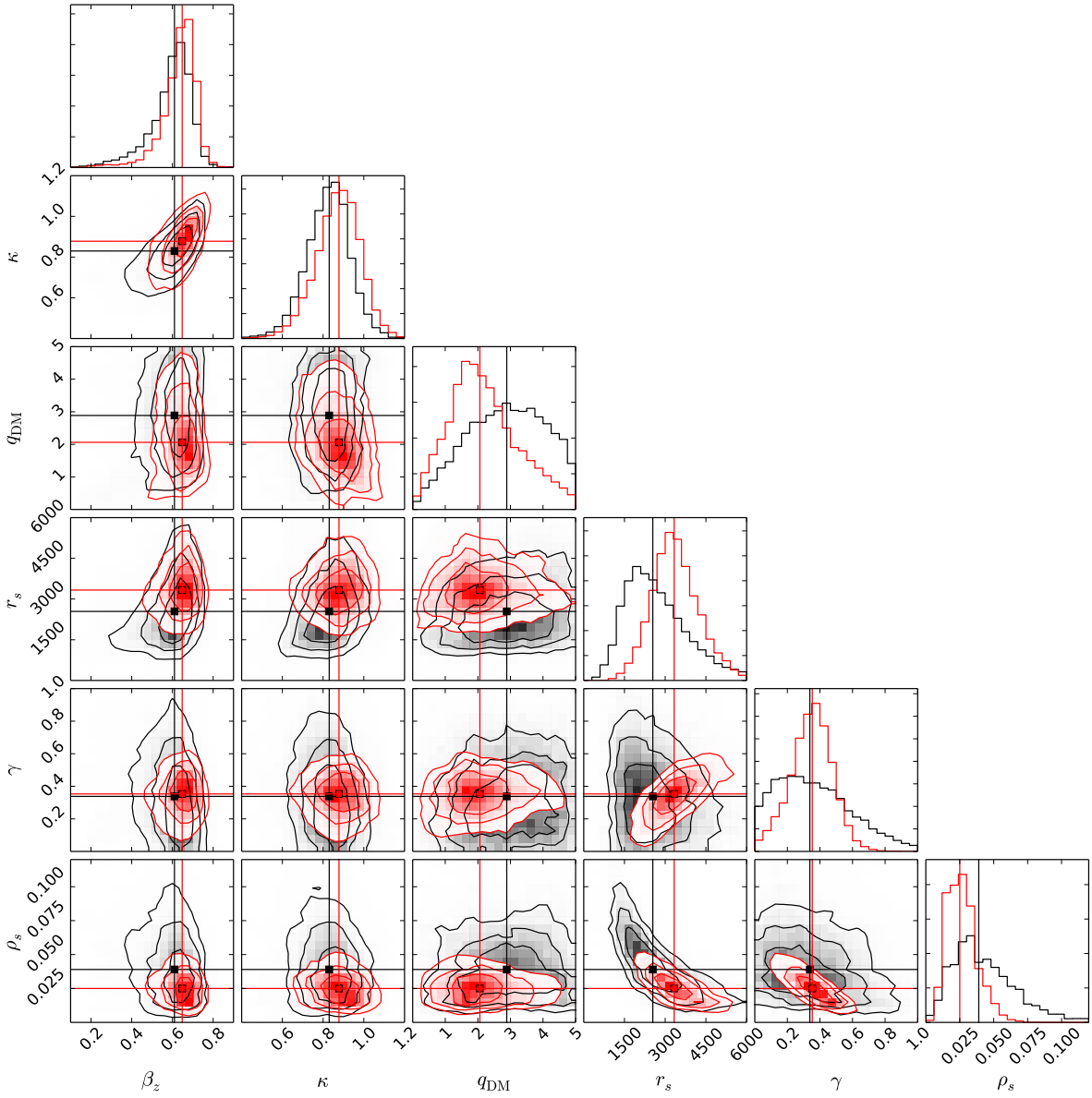

Figure 3.3: Marginalised parameters from the discrete Jeans models: stellar dynamical parameters $\beta_{\rm z}$, κ, and dark matter halo parameters $q_{\rm dm}$, $r_{\rm s}$, γ and $\rho_{\rm s}$. Black contours show the marginalised parameter values with the models using only stellar kinematics, with contour levels 1, 1.5 and $2\,\sigma$. Red contours show the models run using stellar kinematics and $V_{\rm c}$ derived from HI kinematics as a prior.

3.4.1 DM halo properties

Both the 'Stars only' and the 'Stars + Gas' models consistently prefer moderately cored DM profiles, with the posterior distributions showing $\gamma = 0.34^{+0.26}_{-0.21}$ and $\gamma = 0.34^{+0.12}_{-0.13}$ respectively. A prolate DM halo is preferred in both the the 'Stars only' and 'Stars + Gas' model, with the 'Stars + Gas' model indicating a best fit $q_{\rm DM} = 2.1^{+1.3}_{-0.9}$.

While the two models prefer parameters that agree with each other within the uncertainties, it is evident that the dark halo parameters ($r_{\rm s}$, γ, $\rho_{\rm s}$) are much better constrained in the 'Stars + Gas' models when the HI kinematics are used to jointly constrain the total potential. The uncertainties in the 'Stars + Gas' models in $r_{\rm s}$, γ, $\rho_{\rm s}$ are smaller than the 'Stars only' model by 29%, 48% and 54% respectively. The halo flattening also shows a 15% reduction in its uncertainty and drives towards more physical prolate values[2].

3.4.2 Stellar orbital properties

Within JAM, the stellar orbital properties are described by β_z and κ. β_z describes the velocity anisotropy and is the best fit models find $\beta_z = 0.61^{+0.07}_{-0.12}$ and $0.65^{+0.06}_{-0.09}$ respectively for the 'Stars only' and the 'Stars + Gas' models. The inclusion of gas kinematics allow a 24% improvement in the constraint of β_z. It is evident that such an improvement is enabled by breaking the degeneracy between β_z and several DM halo parameters such as $q_{\rm DM}$, $r_{\rm s}$ and γ. κ is constrained to $0.83^{+0.09}_{-0.11}$ and $0.88^{+0.10}_{-0.11}$ respectively for the 'Stars only' and the 'Stars + Gas' models. The uncertainties of κ in both models are similar due to the fact that κ is a property that is intrinsic to the stellar kinematical map itself and is not constrained by the Jeans model.

While the anisotropy is described in JAM by β_z, we can study the more informative link with tangential velocity dispersion by computing $\beta_r = 1 - (\sigma_\phi^2 + \sigma_\theta^2)/2\sigma_r^2$. From each of the JAM models we made in the MCMC process, one can compute the individual velocity dispersions in three dimensions: σ_ϕ, σ_R and $\sigma_{\rm z}$ in cylindrical coordinates, which can then be transformed into σ_ϕ, σ_θ and σ_r in spherical coordinates. Such a calculation can be made following Eqs. 19-23, 32 and 37 from Cappellari (2008) with input MGEs describing the gravitational potential $\Phi(R, z)$ and the density profile of the kinematic tracers $\nu(R, z)$, β_z and κ. Even

[2]Stability analysis for prolate, pressure supported collisionless systems has suggested that axis ratios greater than 5:2 will result in radial orbit instabilities which quickly increase the vertical velocity distribution and reduce the eccentricity (Merritt & Hernquist 1991)

though we have assumed a radially constant β_z and κ, the radially varying Φ and ν render a radially varying β_r.

Figure 3.4 shows the derived $\beta_r(R, z = 0)$, $\sigma_\phi(R, z = 0)$, $\sigma_r(R, z = 0)$ and $\sigma_\theta(R, z = 0)$ profiles derived from 5000 randomly selected individual MCMC steps in the 'Stars only' model in thin lines, with the best-fitted profile indicated by a thick black line and the 1-σ uncertainties by a black band. The corresponding profiles for the 'Stars + Gas' models are shown in red. The β_r profile transitions from a mildly radial central region to a tangentially anisotropic system in the outer regions. β_r goes from $0.32^{+0.03}_{-0.04}$ at $r = 0$ to $\beta_r = -0.35^{+0.57}_{-0.90}$ at two half light radius ($2r_\mathrm{h} \sim 3300\,\mathrm{pc}$) for the 'Stars + Gas' models. At $r = 2\,r_\mathrm{h}$, the constraint on β_r improves by 27% when incorporating gas kinematics in our model.

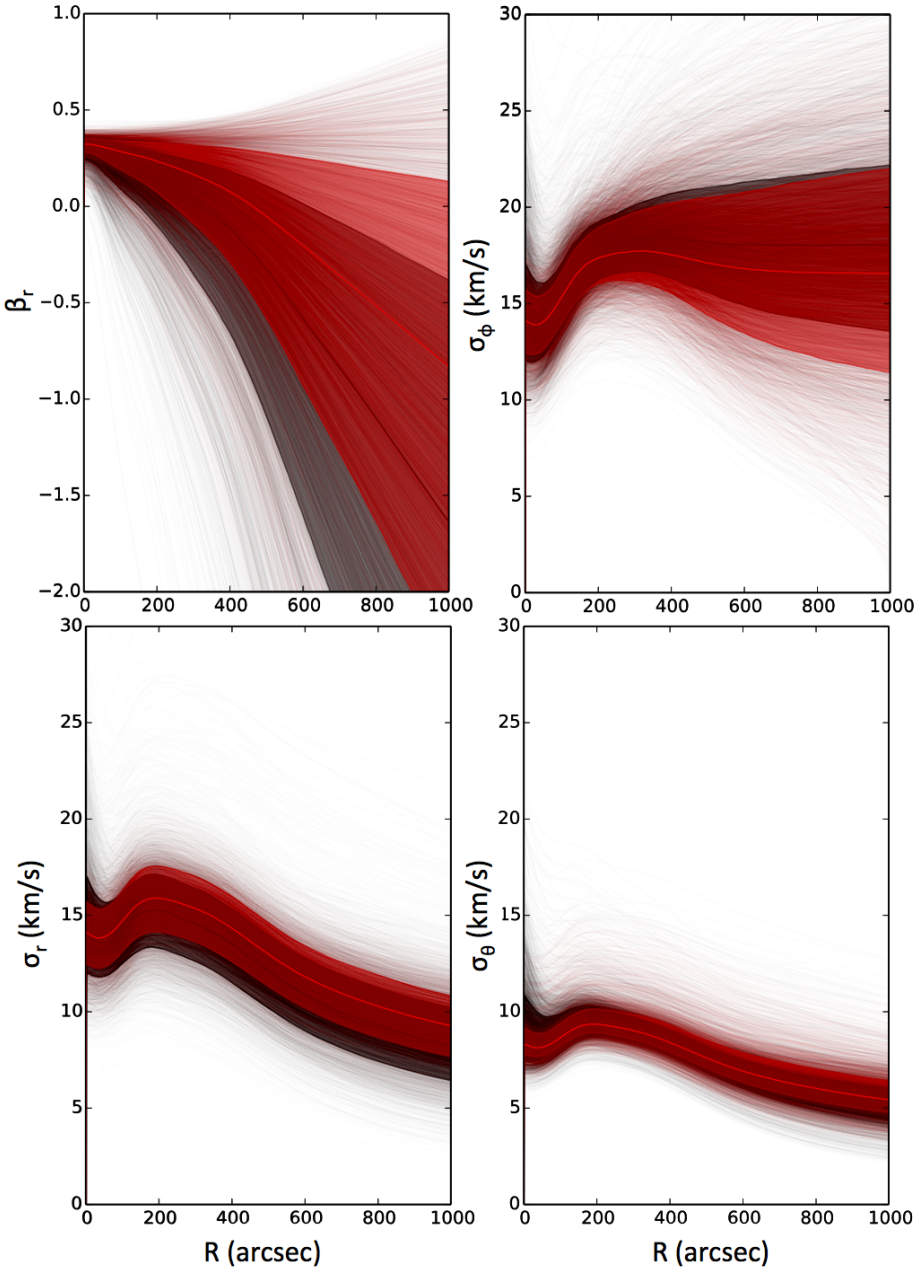

Figure 3.4: The derived $\beta_r(R)$, $\sigma_\phi(R)$, $\sigma_r(R)$ and $\sigma_\theta(R)$ at $z = 0$ from our dynamical models. Thin black and red lines show the profiles of individual MCMC steps for the 'Stars only' and 'Stars + Gas' models respectively. The thick black and red lines show the best fitted profile and the bands show the corresponding $1\,\sigma$ uncertainties.

β_z	κ	$\beta_r(r=0)$	$\beta_r(r=r_{\rm h})$	$\beta_r(r=2r_{\rm h})$	$q_{\rm DM}$	$r_{\rm s}$ (pc)	γ	$\rho_{\rm s}(M_\odot\,{\rm pc}^{-3})$
Stars only, free $q_{\rm DM}$								
$0.61^{+0.07}_{-0.12}$	$0.83^{+0.09}_{-0.11}$	$0.30^{+0.04}_{-0.06}$	$-0.03^{+0.24}_{-0.45}$	$-0.81^{+0.74}_{-1.26}$	$2.9^{+1.3}_{-1.3}$	2544^{+1458}_{-948}	$0.34^{+0.26}_{-0.21}$	$0.039^{+0.028}_{-0.018}$
Stars + Gas, fixed $q_{\rm DM}$								
$0.49^{+0.07}_{-0.11}$	$0.86^{+0.11}_{-0.11}$	$0.24^{+0.4}_{-0.5}$	$0.02^{+0.22}_{-0.34}$	$-0.45^{+0.58}_{-0.89}$	0.5	2442^{+1265}_{-959}	$0.25^{+0.25}_{-0.16}$	$0.032^{+0.031}_{-0.015}$
$0.62^{+0.06}_{-0.09}$	$0.85^{+0.10}_{-0.11}$	$0.31^{+0.03}_{-0.05}$	$0.03^{+0.23}_{-0.37}$	$-0.64^{+0.70}_{-1.07}$	1.0	2142^{+1041}_{-800}	$0.27^{+0.25}_{-0.17}$	$0.036^{+0.031}_{-0.016}$
$0.63^{+0.05}_{-0.09}$	$0.86^{+0.10}_{-0.11}$	$0.32^{+0.03}_{-0.04}$	$0.06^{+0.21}_{-0.36}$	$-0.54^{+0.62}_{-1.15}$	1.5	2342^{+1163}_{-834}	$0.27^{+0.26}_{-0.17}$	$0.038^{+0.030}_{-0.018}$
$0.64^{+0.05}_{-0.07}$	$0.86^{+0.10}_{-0.11}$	$0.31^{+0.03}_{-0.04}$	$0.05^{+0.21}_{-0.39}$	$-0.58^{+0.64}_{-1.14}$	2.0	3148^{+1254}_{-919}	$0.31^{+0.16}_{-0.16}$	$0.028^{+0.019}_{-0.013}$
$0.62^{+0.06}_{-0.10}$	$0.84^{+0.09}_{-0.11}$	$0.31^{+0.03}_{-0.05}$	$0.03^{+0.22}_{-0.38}$	$-0.64^{+0.69}_{-1.13}$	2.5	2453^{+1179}_{-835}	$0.28^{+0.27}_{-0.19}$	$0.041^{+0.027}_{-0.017}$
$0.63^{+0.06}_{-0.07}$	$0.84^{+0.10}_{-0.11}$	$0.32^{+0.03}_{-0.05}$	$0.05^{+0.22}_{-0.36}$	$-0.59^{+0.67}_{-1.05}$	3.0	3136^{+1006}_{-826}	$0.34^{+0.12}_{-0.15}$	$0.027^{+0.016}_{-0.010}$
$0.64^{+0.06}_{-0.08}$	$0.87^{+0.09}_{-0.11}$	$0.32^{+0.03}_{-0.04}$	$0.09^{+0.27}_{-0.33}$	$-0.45^{+0.49}_{-1.01}$	3.5	2900^{+1451}_{-1034}	$0.27^{+0.25}_{-0.17}$	$0.038^{+0.025}_{-0.016}$
$0.63^{0.06}_{-0.09}$	$0.86^{+0.10}_{-0.11}$	$0.31^{+0.03}_{-0.05}$	$0.05^{+0.22}_{-0.37}$	$-0.58^{+0.67}_{-1.10}$	4.0	2741^{+1438}_{-1067}	$0.31^{+0.27}_{-0.20}$	$0.041^{+0.035}_{-0.020}$
Stars + Gas, free $q_{\rm DM}$								
$0.65^{+0.06}_{-0.09}$	$0.88^{+0.10}_{-0.11}$	$0.32^{+0.03}_{-0.04}$	$0.13^{+0.18}_{-0.30}$	$-0.35^{+0.57}_{-0.90}$	$2.1^{+1.3}_{-0.9}$	3331^{+926}_{-778}	$0.34^{+0.12}_{-0.13}$	$0.025^{+0.012}_{-0.009}$
Stars only, fixed $q_{\rm DM}$								
$0.53^{+0.06}_{-0.08}$	$0.92^{+0.11}_{-0.13}$	$0.26^{+0.03}_{-0.04}$	$0.15^{+0.15}_{-0.28}$	$-0.08^{+0.25}_{-0.72}$	0.5	3061^{+1046}_{-759}	$0.27^{+0.14}_{-0.14}$	$0.028^{+0.016}_{-0.012}$
$0.66^{+0.05}_{-0.18}$	$0.89^{+0.09}_{-0.10}$	$0.33^{+0.02}_{-0.04}$	$0.14^{+0.18}_{-0.31}$	$-0.29^{+0.53}_{-0.90}$	1.0	3406^{+1247}_{-1014}	$0.35^{+0.13}_{-0.16}$	$0.023^{+0.017}_{-0.010}$
$0.66^{+0.05}_{-0.06}$	$0.88^{+0.09}_{-0.10}$	$0.33^{+0.02}_{-0.03}$	$0.15^{+0.16}_{-0.15}$	$-0.29^{+0.50}_{-0.74}$	1.5	3118^{+984}_{-855}	$0.31^{+0.14}_{-0.15}$	$0.028^{+0.016}_{-0.011}$
$0.64^{+0.05}_{-0.07}$	$0.86^{+0.10}_{-0.11}$	$0.32^{+0.03}_{-0.03}$	$0.09^{+0.19}_{-0.28}$	$-0.48^{+0.53}_{-0.86}$	2.0	3148^{+1254}_{-919}	$0.31^{+0.16}_{-0.16}$	$0.028^{+0.019}_{-0.013}$
$0.64^{+0.05}_{-0.07}$	$0.86^{+0.09}_{-0.11}$	$0.32^{+0.03}_{-0.04}$	$0.08^{+0.18}_{-0.31}$	$-0.51^{+0.58}_{-0.93}$	2.5	2989^{+818}_{-730}	$0.31^{+0.12}_{-0.14}$	$0.029^{+0.015}_{-0.010}$
$0.63^{+0.06}_{-0.07}$	$0.84^{+0.11}_{-0.11}$	$0.31^{+0.03}_{-0.04}$	$0.03^{+0.22}_{-0.32}$	$-0.68^{+0.70}_{-0.97}$	3.0	3136^{1006}_{-829}	$0.34^{+0.12}_{-0.15}$	$0.027^{+0.016}_{-0.010}$
$0.63^{+0.05}_{-0.07}$	$0.83^{+0.11}_{-0.11}$	$0.31^{+0.03}_{-0.03}$	$0.03^{+0.22}_{-0.32}$	$-0.69^{+0.70}_{-0.95}$	3.5	3113^{+969}_{-844}	$0.33^{+0.12}_{-0.14}$	$0.028^{+0.015}_{-0.010}$
$0.64^{+0.05}_{-0.07}$	$0.86^{+0.10}_{-0.11}$	$0.31^{+0.03}_{-0.04}$	$0.00^{+0.21}_{-0.31}$	$-0.80^{+0.65}_{-0.96}$	4.0	3148^{+1254}_{-919}	$0.32^{+0.16}_{-0.16}$	$0.028^{+0.019}_{-0.013}$

Table 3.5:: Best-fitted Jeans model parameters and 1σ uncertainties for $q_{\rm DM}$ free and $q_{\rm DM}$ models at $0.5 < q_{\rm DM} < 5.0$ at 0.5 intervals.

3.4.3 Dependence on $q_{\rm DM}$

While both the 'Stars only' and the 'Stars + Gas' model prefer a prolate halo, the flattening of the dark matter halo $q_{\rm DM}$ has some of the most important correlations with other parameters. We would therefore like to understand the degeneracies between the choice of halo flattening and other parameters of interest. To asses this we run models where the DM halo flattening is fixed to values over a grid of $q_{\rm DM}$; ($0.25 < q_{\rm DM} < 4.0$, at intervals of 0.25), in order to evaluate the effect of $q_{\rm DM}$ on the stellar dynamical and dark matter properties.

The best-fit parameters for these constrained models are plotted as a function of $q_{\rm DM}$ in Figure 3.5 in solid lines, with the respective 1-σ uncertainties indicated by dashed lines. The free parameters are then reported in intervals of $q_{\rm DM} = 0.5$ in Table 3.5. Black lines show the parameters constraints from the 'Stars only' models and the red lines show the parameters constraints from the 'Stars + Gas' models. The best fit parameters from the models where $q_{\rm DM}$ is free to vary are also shown by the error bars for reference.

In both the 'Stars only' and 'Stars + Gas' cases, $\beta_{\rm z}$ shows a well known degeneracy with $q_{\rm DM}$ at $q_{\rm DM} \lesssim 1$; a flatter dark matter halo gives a lower $\beta_{\rm z}$. Similar degeneracies also exist between $q_{\rm DM}$ and β_r. The derived β_r at $r = 0$, $r = r_{\rm h}$ and $r = 2\,r_{\rm h}$ are listed in Table 3.5. The degeneracies are stronger at large radii ($r \gtrsim r_{\rm h}$), with a higher $q_{\rm DM}$ corresponding to a lower β_r (more tangential anisotropies). Also, the degeneracies between $q_{\rm DM}$ and β_r extend to much higher $q_{\rm DM}$, all the way up to $q_{\rm DM} = 4$. Curiously, such $\beta_r - q_{\rm DM}$ degeneracy is only present in the 'Stars + Gas' models but not in the 'Stars only' models. The other stellar orbital parameter κ also show a degeneracy in the direction of higher $q_{\rm DM}$- lower κ, again such a degeneracy is only present in the 'Stars + Gas' models.

Reassuringly, the inner slope of the DM density profile, γ appears robust to the choice of halo shape. As in the case of the freely varying q_{DM} models, the dark matter parameters, $r_{\rm s}$, γ and $\rho_{\rm s}$, are better constrained on average by 27%, 39% and 46% at all $q_{\rm DM}$ when we include $V_{\rm c,HI}$ as a constraint.

3.5 Discussion

Using discrete Jeans models, together with circular velocity constraints from the HI gas rotation curve, we have derived tight constraints on the DM halo shape and density profile. Additionally, we derive, for the first time, the stellar velocity

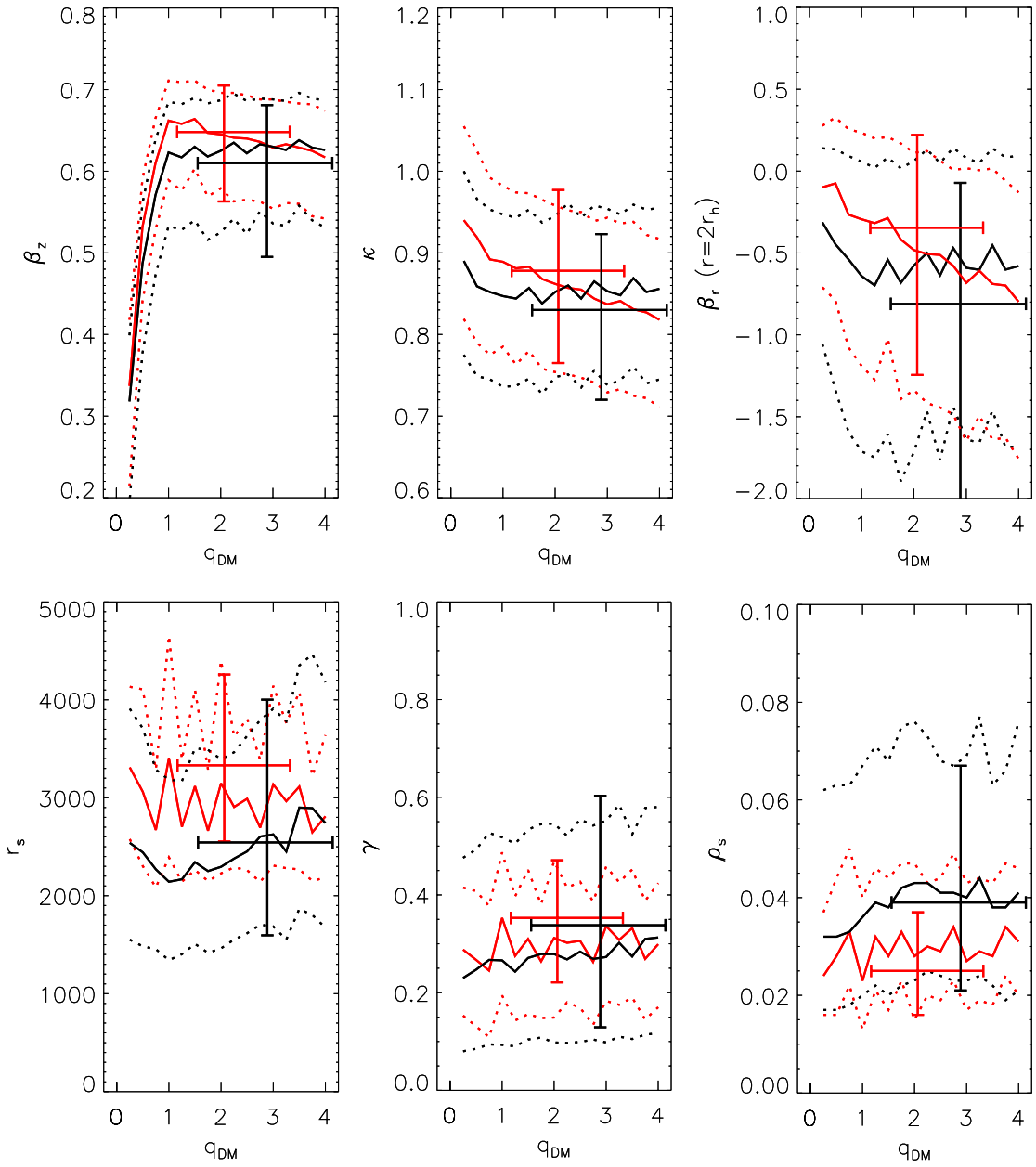

Figure 3.5: The best-fitted (solid line) and 1-σ uncertainties (dashed lines) of the parameters constrained from the MCMC process with $q_{\rm DM}$ fixed between 0.5 and 1.5. Models are ran at intervals of 0.1 in $q_{\rm DM}$. Black lines show the results from the 'Stars only' models and red lines show the results from the 'Stars + Gas' models.

anisotropy profile of a dIrr. Below we discuss the implications of our results for modified gravity and dark matter theories, and formation models of dwarf galaxies.

3.5.1 WLM's dark matter halo properties in the context of ΛCDM cosmology

The halo parameters from our best fit models can be used to reconstruct the three dimensional mass distribution in WLM with high confidence. Here we examine the inner density profile and flattening of the dark matter halo with respect to simulations of galaxy formation in a ΛCDM framework.

Dark matter density profile

Figure 3.6 shows the dark matter and stellar mass profiles derived from our 'Stars + Gas' and $q_{\rm DM}$ free dynamical model in green and purple respectively. The dark matter virial mass, $M_{\rm vir}$, is constrained to within $2.50^{+1.75}_{-1.23} \times 10^{10}\,M_{\odot}$ in the 'Stars + Gas' model and $2.10^{+3.32}_{-1.32} \times 10^{10}\,M_{\odot}$ in the 'Stars only' model - in good agreement with Leaman et al. (2012), who used an SIS and NFW fit to the asymmetric-drift-corrected stellar kinematics.

The derived stellar to halo mass ratio is therefore $\log_{10}(M_{\star}/M_{\rm vir}) = -3.4 \pm 0.3$, which is slightly higher than the stellar-mass-halo-mass (SMHM) relation found by Moster et al. (2010) $\log_{10}(M_{\star}/M_{\rm vir}) = -3.1 \pm 0.1$ using the same $M_{\star}$ value, but consistent within the uncertainties. When we run models with a prior on the stellar mass of $M_{\star} = 4.3{\times}10^{7}\,M_{\odot}(\pm 50\%)$, a larger value favoured from star formation history studies of WLM (Leaman et al. 2017), we derive a higher $\log_{10}(M_{\star}/M_{\rm vir}) = -2.8{\pm}0.2$. In Figure 3.7e we show the $\log_{10}(M_{\star}/M_{\rm vir})$ from the 'Stars only' and 'Stars+Gas' models with a prior $M_{\star} = 1.1 \times 10^{7}\,M_{\star}(\pm 50\%)$ in black and red, and for completeness a 'Stars+Gas' model with prior $M_{\star} = 4.3 \times 10^{7}\,M_{\odot}(\pm 50\%)$ in orange.

The dark matter halo concentration ($c \equiv r_{\rm vir}/r_{-2}$ where $r_{\rm vir}$ is the virial radius and r_{-2} the radius at which the logarithmic slope of the dark matter density is $\mathrm{d}\ln\rho_{\rm DM}/\mathrm{d}\ln r = -2$) for our best fit models is close to the expected mass-concentration ($M_{\rm vir} - c$) relation from dark-matter-only simulations (Dutton & Macciò 2014). Given our derived $M_{\rm vir}$, the $M_{\rm vir} - c$ relation found by Dutton & Macciò (2014) would suggest $c = 12.1^{+0.9}_{-0.6}$. Our dynamical models infer a slightly lower halo concentration of $c = 11.4 \pm 1.6$. Such small discrepancies may be caused by the impact of stellar feedback, and correlated with the change in the inner slope of the DM density profile.

Our analysis suggests that WLM has a relatively cored DM density distribution with a best fit to the inner slope of the density profile $\gamma = 0.34 \pm 0.12$. This value is robust to the recovered DM halo shape (q_{DM}), and has an expected correlation with the scale length and normalisation of the dark matter halo, r_s and ρ_s. The central density profile of low mass dwarfs is an important tracer of internal and external evolutionary processes in dwarf galaxies (e.g., Zolotov et al. 2012; Brooks & Zolotov 2014; Oñorbe et al. 2015). Using hydrodynamical simulations, Di Cintio et al. (2014) found that the feedback process which alters the inner slope of dark matter haloes also modifies the final stellar-to-halo-mass ratio ($M_\star/M_{\rm vir}$), and a relation between the two was parameterised as:

$$\gamma = -0.06 + \log_{10}[(10^{X+2.56})^{-0.68} + (10^{X+2.56})], \tag{3.6}$$

where $X = \log_{10}(M_\star/M_{\rm vir})$.

In the mass range of WLM, a higher $M_\star/M_{\rm vir}$ would translate to a flatter inner slope (smaller γ) - as the stellar feedback is proportionally more effective at causing halo expansion due to rapid gas expulsion in the relatively shallow potential well. For our derived $M_\star/M_{\rm vir}$, the Di Cintio et al. (2014) predicts $\gamma = 0.5 \pm 0.2$, higher than the γ derived from our models ($\gamma = 0.34 \pm 0.12$), but consistent within the errors. If we use the 'Stars + Gas' model ran with $M_\star = 4.3 \times 10^7$, the derived value from Di Cintio et al. (2014): $\gamma = 0.25 \pm 0.16$ is in excellent agreement with our modelled value: $\gamma = 0.23 \pm 0.12$ (as shown in orange contours in the bottom panel of Figure 3.7). To compare to the simulations from Read et al. (2016), we have also fit our derived dark matter density profile with a cored-NFW profile and found a core size of $r_{\rm core} = 1257^{+318}_{-269}$ pc. In those simulations the typical core size was found to scale with the stellar half mass radius as $r_{\rm c} \sim 1.75\, r_{\rm h}$. Our derived core size is slightly smaller than this finding, with the ratio $0.6 \leq r_{\rm c}/r_{\rm h} \leq 1.0$ for our best fit models. However we note that taking the exponential scale length of the disk ($r_{\rm d} = 987$ pc; Leaman et al. 2012) gives $0.98 \leq r_{\rm c}/r_{\rm d} \leq 1.65$.

In the context of ΛCDM galaxy formation, WLM appears to have been able to efficiently convert its presumably primordial NFW dark matter cusp into a shallower density profile over a Hubble time of star formation and feedback. This process has occurred, and yet left the system with: an exponential and smoothly distributed intermediate age population (Leaman et al. 2012), no quenched SFH (Weisz et al. 2014), a metallicity distribution function and age-metallicity relation in agreement with a simple leaky box model (Leaman et al. 2013), and a stellar age-velocity dispersion relation consistent with gradual dynamical cooling of the gas (Leaman et al. 2017). These all suggest that the core-creation process need not always quench the system, nor be catastrophic to the structural, dynamical or chemical properties

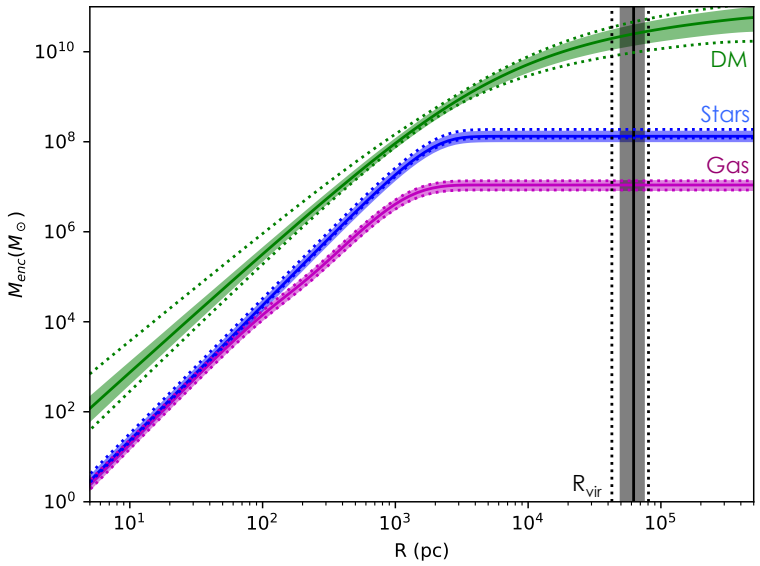

Figure 3.6: Enclosed mass profiles. The stellar, gas and dark matter profile from the best fit 'Stars + Gas' model are plotted in magenta, blue and green respectively. Vertical lines indicate the virial radius. Width of the bands give the $1\,\sigma$ uncertainties. Dotted lines show the corresponding constraints from the 'Stars only' dynamical models.

of the galaxy - at least in this virial mass range. A more detailed joint analysis of the chemical and kinematic properties may help disentangle whether the core creation process was bursty as expected from feedback scenarios (e.g., El-Badry et al. 2017), or more gradual as in the case of self interacting dark matter.

Previous numerical studies have also explained many of WLM's properties in terms of a feedback based alteration to the underlying NFW profile. For example, using a set of hydrodynamical simulations for dwarf galaxies, Teyssier et al. (2013) were able to reproduce the spatial and dynamical structural properties of WLM, while at the same time transforming the dark matter halo from cusped to core by stellar feedback from bursty star formation. Two WLM-like galaxies with exponential stellar disks of $V/\sigma \sim 1$ were also formed in the study by Shen et al. (2014) from a fully cosmological high-resolution ΛCDM simulation, again with baryonic feedback playing an important role. The dwarf galaxies from their simulation lie on the observed mass-metallicity relation observed in the Local Group dwarfs, suggesting that the feedback process can operate in a non-destructive fashion for isolated dwarfs.

This provides a counter example to systems such as Ultra-diffuse Galaxies

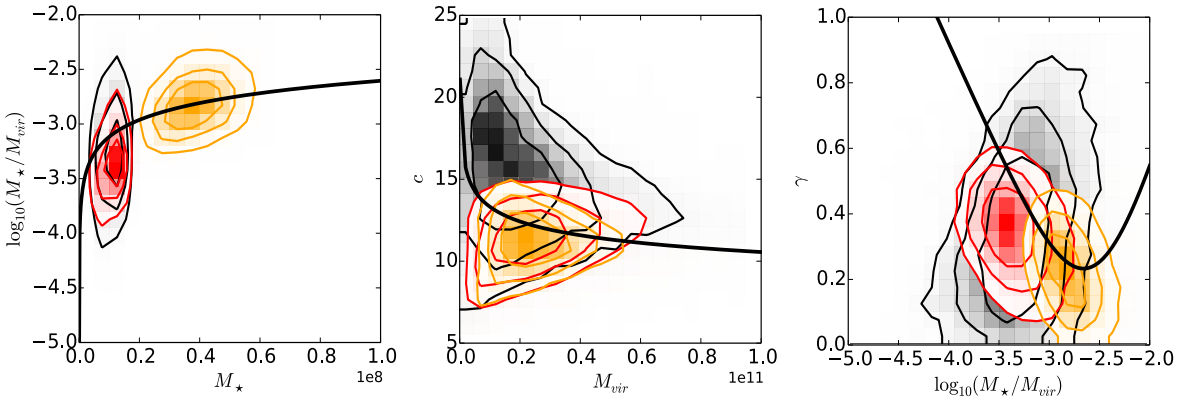

Figure 3.7: Contours showing the constrained values as labeled from models with prior $M_\star = 1.1 \times 10^7\ M_\star(\pm 50\%)$ 'Stars only (black) and 'Stars+Gas' (red), and with prior $M_\star = 4.3 \times 10^7\ M_\star(\pm 50\%)$ 'Stars + Gas' in orange. Overlaid are the $M_\star - M_\star/M_{vtr}$ relation from Moster et al. (2010) *left*, the mass-concentration relation from Dutton & Macciò (2014) *middle* and the $M_\star/M_{vit} - \gamma$ relation from Di Cintio et al. (2014) *right* are shown as thick black lines.

(UDGs), which may acquire their extended structure and old stellar populations partly due to the same feedback processes (Di Cintio et al. 2017), but with more extreme consequences on the system. Given that some UDGs are estimated to be comparable virial mass to WLM (Beasley & Trujillo 2016), understanding what different conditions during the galaxy's lifetime (e.g., star formation density, environment) lead to such disparate final states is an avenue worth further study. For example, the resultant decrease in central density and gas concentration may be extremely important for evolutionary changes of dwarf satellites, as demonstrated by Brooks & Zolotov (2014). Finding present day observational signatures which can trace the rapidity and strength of the potential fluctuations may provide further insight into the timescales, and mechanisms with which the DM core is growing, and can potentially differentiate feedback driven or particle scattering processes (e.g., gas and stellar spatial distributions; Mondal et al. 2018). This will be discussed in the subsequent section, however to first order the DM halo density profile we derive is in excellent agreement with the predictions from simulations which incorporate the effect of feedback driven halo expansion in a CDM framework.

Dark matter halo flattening

We now turn to the shape (axial ratio) of the dark matter halo inferred from our dynamical models. Table 3.5 shows that in the 'Stars + Gas' model, a prolate dark matter halo ($q_{\rm DM} \sim 2$) is preferred, with an uncertainty of $\delta q_{\rm DM} \sim 1$. Pure dark

matter ΛCDM cosmological simulations show that dark matter haloes with our derived $M_{\rm vir}$ for WLM have an average short-to-long axis ratio of ~ 0.7 at the virial radii $r_{\rm vir}$ (Macciò et al. 2008). Butsky et al. (2016) find similar $q_{\rm DM}$ at $r_{\rm vir}$ with high-resolution dark matter only simulations. They however extend the analysis towards the inner region and show that over the radii where our stellar kinematics cover ($< 5\% \, r_{\rm vir}$), dark matter haloes of $M_{\rm vir} \sim 10^{10} \, M_{\odot}$ have an even lower average short-to-long axis ratio of $\sim$0.5 and are predominantly prolate.

Those authors used a suite of high-resolution hydrodynamical simulations and showed that while baryonic feedback does not have noticeable effects on $q_{\rm DM}$ at the virial radii, it may change $q_{\rm DM}$ in the inner region of the halo depending on the $M_{\rm vir}$ of the galaxy. The inner region ($< 0.12 \, r_{\rm vir}$) of DM haloes evidently become more spherical for galaxies with $M_{\rm vir} > 10^{11} \, M_{\odot}$. For galaxies with $M_{\rm vir}$ similar to the one we derived for WLM however, $q_{\rm DM}$ does not significantly differ from dark matter only simulations, meaning that a prolate halo with short-to-long axis ratio of $\sim$0.5 is still expected, corresponding to a $q_{\rm DM}$ of $\sim$2. This is in excellent agreement with the $q_{\rm DM}$ derived from our 'Stars + Gas' model. Although a spherical/oblate halo has been ruled out at the 1-σ level, such geometries are still possible within the 2-σ level. Given the evident $q_{\rm DM} - \beta$ (especially β_r) degeneracies, future proper motion measurements will help us to further constrain the halo geometry.

As we shall see below, the halo shape measurement is a strong prediction of our models, and together with the DM density slope, may offer one of the most powerful lever arms to differentiate baryonic feedback plus CDM scenarios, from self-interacting dark matter models.

3.5.2 WLM as a test of self-interacting dark matter models and modified gravity

The simultaneous recovery of a density core and a prolate DM halo is extremely important in understanding the viability of models of non-standard dark matter, e.g., thermal relic, self-interacting (SIDM), Bose-Einstein condensate (BECDM or "fuzzy") dark matter. We have previously seen the good agreement between our observations and predicted values for the DM inner density profile slope and axial ratios in CDM simulations with baryonic feedback. These models work under the assumption that the DM itself is collisonless and the modifications to the density profile arise indirectly due to stellar feedback rapidly changing the potential well through gas expulsion (c.f., Pontzen & Governato 2012).

Galaxy formation simulations where the dark matter particle may have a

self-interaction cross section, can also produce modifications to the central density profile. In this case the particle self-interactions, which have a higher rate of occurrence in the denser central regions, result in elastic (or inelastic; Vogelsberger et al. 2019) scattering of particles (of order one event per particle per Hubble time) and the formation of a density core in the galaxy dark matter distribution (Vogelsberger et al. 2012; Peter et al. 2013).

To place our results in the context of such SIDM theories, we compute the model DM density at the core radius $\rho(r_c)$ using the best fit 'Stars + Gas' profile parameters, and derive the likely velocity weighted interaction cross section for SIDM models to produce this cored profile:

$$\frac{\langle \sigma v \rangle}{m_X} = \{\rho(r_c) t_{halo}\}^{-1} \tag{3.7}$$

where m_X is the mass of the SIDM particle candidate and t_{halo} is the collapse time of the DM halo, here taken to be 13 Gyr. Figure 3.8 plots the constraints on the cross section using our derived halo properties for WLM. Also shown are the limits on the same quantity for the Fornax dSph (Chapter 4), based on modelling of that dwarf galaxy's GC dynamics. Velocity independent scattering predictions for different SIDM cross sections are shown as the background colour bar and lines. Constraints from high mass galaxy clusters indicate that such velocity independent SIDM models require $\sigma/m_X \lesssim 0.1$ cm^2 g^{-1} (e.g., Kaplinghat et al. 2016) which is the lowest line shown in our figures. Those studies and others suggest that local dwarf galaxies are more consistent with $\sigma/m_X \sim 1 - 2$ cm^2 g^{-1}, and indeed the two dwarfs reported in our studies are consistent with this value.

The mismatch between the required velocity independent cross sections needed for local dwarfs and high mass galaxy clusters has led to velocity *dependent* scattering models to be preferred. We show three examples as the red, green and blue lines in Figure 3.8, all of which pass through the combined constraints of WLM and Fornax, but which only the one with the high peak velocity dependence ($v_{max} = 400$ km s^{-1}) is also consistent with the cluster measurements of Leaman et al. (2012). The constraints posed by WLM do not a priori prefer a velocity dependence to the self-interacting DM models - however as we shall see, the *simultaneous finding of a core and a prolate halo may rule out the velocity independent models*, as these are reported to become thermalised and spherically symmetric in their inner regions for the values needed here (Peter et al. 2013).

The final core sizes generated from DM scattering can be ~ 1 kpc, just as in baryonic feedback + CDM scenarios. Therefore additional signatures may be needed to differentiate whether a detected DM core is a unique consequence of baryonic

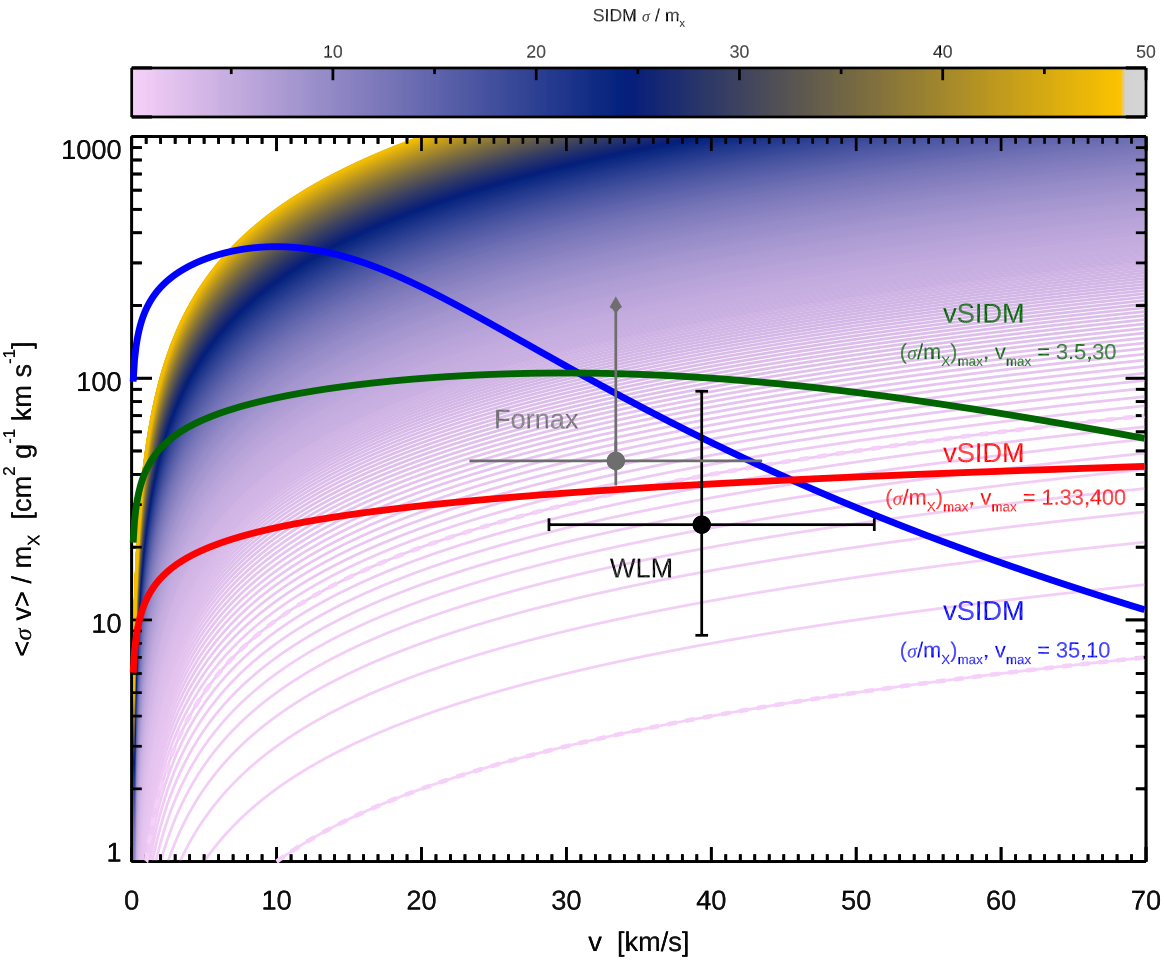

Figure 3.8: Velocity averaged interaction cross sections as a function of characteristic halo velocities. The self-interacting DM particle cross section necessary to reproduce the density profile of WLM is shown as the black data point. Limits for the Fornax dSph from Leung et al. 2019 are shown in grey. Colour bar and background shows the cross section for velocity *independent* SIDM models, with $\sigma/m_X = 0.1$ and 1 cm^2 g^{-1} indicated with dashed lines. The latter value, which is favoured by galaxy clusters is ruled out by the dwarfs, while the former value is excluded as it is unable to simultaneously preserve prolate halo shapes. Velocity *dependent* SIDM models are shown in thick coloured lines, with parameters indicated. While all three vSIDM models are compatible with the dwarf galaxy limits, only the red curve can also reproduce the constraints from galaxy clusters - however whether they also preserve aspherical geometries is not yet quantified in simulations.

feedback, or self-interaction modifications to the DM density profile. The timescale for the core to form may be longer in SIDM, however this depends on the particular baryonic sub-grid prescriptions adopted (e.g., star formation or feedback injection efficiencies). For example, Fry et al. (2015) showed that the growth rate and final size of the DM core in halos with $V_{max} \leq 30$ km s^{-1} may be largely the same in self interacting dark matter with or without baryonic feedback - though this again depends on the mass range and adopted cross section. While there could be chemical and/or phase space signatures which may help understand the precise mechanism(s) better, the sparsity of detailed abundances and numbers of observed stars in low mass galaxies makes this a daunting process. What then may be a potential way to understand whether self-interacting dark matter or feedback scenarios have generated observed cores in dwarf galaxies?

The scattering process that generates a core in self-interaction models may potentially sphericalise the mass distribution, as the interactions are isotropic. This means that the core formation process in pure self-interaction dark matter models could result in spherical mass distributions in the inner regions of the halos. The simultaneous quantification of DM density profile slope and axis ratio has unfortunately only been reported as far as we can tell, in simulations of high mass ($M_{vir} \geq 10^{11}$) halos (Schive et al. 2014b). In these simulations, halos with $\sigma/m_X = 1$ which form increasingly cored density distributions (approaching $\gamma \sim 0.4$) become approximately spherical ($c/a \sim 0.9$). For lower cross sections of $\sigma/m_X = 0.1$, density profiles slopes of $\gamma = 0.8$ still retain axis ratios of $c/a \sim 0.6$, but these values are not nearly as cored as what we find, and are only reported for halos of $M_{vir} \sim 10^{13-14}$. Most importantly, these low values for the cross section are already ruled out on the basis of the WLM DM density profile.

Simulations which explore the halo shape of velocity independent SIDM models in the presence of baryons have found that the core creation process can occur with non-spherical final halo shapes in the inner regions (Sameie et al. 2018). However in that case the inner halo progressed towards the axis ratios of the embedded baryonic distribution, which in the case of WLM would be *oblate* with $c/a = 0.4 - 0.6$ (Leaman et al. 2012). Fitts et al. (2018) simulated dwarf galaxies in our halo mass range with SIDM and baryonic components and found similar behaviour, whereby baryons were the dominant process in altering the DM halo profiles (either indirectly through feedback, or afterwards through contraction) - however there was no reported characterisation of the halo shapes. Velocity dependent SIDM models presented in Zolotov et al. (2012) show indications that high mass halos can preserve their shapes in the presence of central density modifications, however these simulations were again with MW mass halos.

There is clear need for numerical simulations to quantify the simultaneous evolution of the DM density inner slope and halo shape in the presence of baryons for halos of mass $M_{vir} \sim 10^{10}$. *WLM's recovered prolate DM halo with $q_{DM} = 2$, density slope of $\gamma = 0.34$ and core of size $r_c = 1257$ pc may provide a strong constraint which velocity dependent self-interacting dark matter models need to satisfy.*

Axion mixed DM models or BECDM models also predict a relation between the core size and halo mass - however in this case the core is inherent to the structure formation in these models. Following Vogelsberger et al. (2012), in the case of ultra-light BECDM, the soliton core size is related to the halo virial mass and effective particle mass (m_ψ) as:

$$r_{\rm c,} = 1.6{\rm kpc} \left(\frac{M_{350}}{10^9 M_\odot} \right)^{-1/3} \left(\frac{m_\psi}{10^{-22}\,{\rm eV/c^2}} \right)^{-1}, \tag{3.8}$$

where $r_{\rm c,}$ is the DM core radius defined through a soliton and M_{350} is the viral mass calculated as $M_{350} = (4\pi/3 r_{\rm vir}^3)\Delta_{\rm c}\rho_{\rm c}$ with $\rho_{\rm c}$ being the critical density and $\Delta_{\rm c} = 350$. For WLM's constraints on the core size and virial mass we find $1.1^{+0.2}_{-0.1} \times 10^{-22}\,{\rm eV/c^2}$, consistent with constraints from large scale structure studies. Similar to the above SIDM studies more work is needed to quantify the halo axis ratios in low mass halos (with non-negligible baryon fractions), in these or other alternative cosmological models (e.g., ETHOS; Vogelsberger et al. 2016).

Finally, we comment briefly on the implications of our inferred dark mass distribution on theories of modified gravity such as MOND (Milgrom 1983). WLM is an interesting test case in that it has well defined inclination and measurements of a circular velocity curve from HI kinematics (Iorio et al. 2017), stellar velocity dispersion and anisotropy (Leaman et al. 2012 and this work) and an intrinsic thickness (Leaman et al. 2012). Our discrete Jeans model for WLM suggests that there is an extended dark mass distribution around WLM, with a prolate axis ratio of 2:1. MOND will reproduce the contributions to the observed circular velocity field by altering the acceleration field in the outer regions - however this can only mimic a mass distribution with $q = 0.9$. WLM is in the deep MOND regime and its extreme isolation means that an external field effect can not be invoked to alleviate discrepancies with MOND predictions in the outer disk. The prolate dark mass distribution inferred for WLM may represent a significant obstacle for describing the dynamics and structure of this dwarf galaxy with MOND. A more detailed discussion and analysis of WLM's stellar structure, dynamics and enclosed mass profile with respect to MOND is beyond the scope of this work and will be presented in a follow up paper.

3.5.3 Tangential velocity anisotropy in an evolutionary context for dwarf galaxies

Determining velocity anisotropy in systems with a single type of kinematic tracer has long assumed to be difficult due to the mass-anisotropy degeneracy inherent to spherical Jeans equations. For a couple of well studied dSphs, authors have used discrete Jeans models, or orbit based Schwarzschild superposition models to better constrain the velocity anisotropy, and found that the anisotropy becomes increasingly more tangential with radius, for both Sculptor (Zhu et al. 2016) and Fornax (Kowalczyk et al. 2018). Subsequent work using proper motions measured from GAIA, Massari et al. (2018) determined a median radial anisotropy of $\beta_r \sim 0.46$ for Sculptor, but only for the inner region $r \lesssim 0.35\, r_{\rm h}$.

Interestingly, WLM also demonstrates a mild radial anisotropy in the inner region of $r \lesssim 1\, r_{\rm h}$, which turns tangential towards larger radii ($\beta_r \sim -0.5$). To demonstrate the similarities between the β_r profile we obtained from the dIrr WLM and the dSphs, we overlay the β_r profiles obtained by Zhu et al. (2016) for Sculptor (blue) and Kowalczyk et al. (2018) for Fornax (green) on top of the one we obtained from the 'Stars + gas' $q_{\rm DM}$ free model (red) in Figure 3.9. There are clear similarities in all three dwarfs, with the anisotropy profile becoming increasingly tangential in the outer regions.

The interpretation of any anisotropy profile is not straightforward, nor unique. For example, dissipationless gravitational collapse can lead to an isotropic core, surrounded by an envelope of radially anisotropic orbits (van Albada 1982) - however the same configuration is seen to occur in simulations of dwarfs which undergo bar-buckling (Mayer 2010). There, bar formation can be triggered by strongly radial anisotropy, before undergoing a bending instability which erases the radial anisotropy (preferentially increasing the vertical velocity dispersion). In higher mass halos, the reconfiguration of stellar orbits due to minor merging can reproduce the typically radial anisotropic profiles seen for MW mass galaxies, with transient tangential anisotropy appearing due to recent major accretion or flybys of satellites (Loebman et al. 2018).

Alternatively, simulations have shown that tangential anisotropy can be caused by preferential stripping of stars on radial orbits in a tidal field (e.g., Baumgardt & Makino 2003; Hurley & Shara 2012). The tangential anisotropy in some dSphs, found especially at large radii ($r \gtrsim r_{\rm eff}$, the effective radius), has often been used to support the scenario in which dIrrs are transformed into dSphs via tidal processing.

The negative β_r derived at large radii from our dynamical models for WLM puts

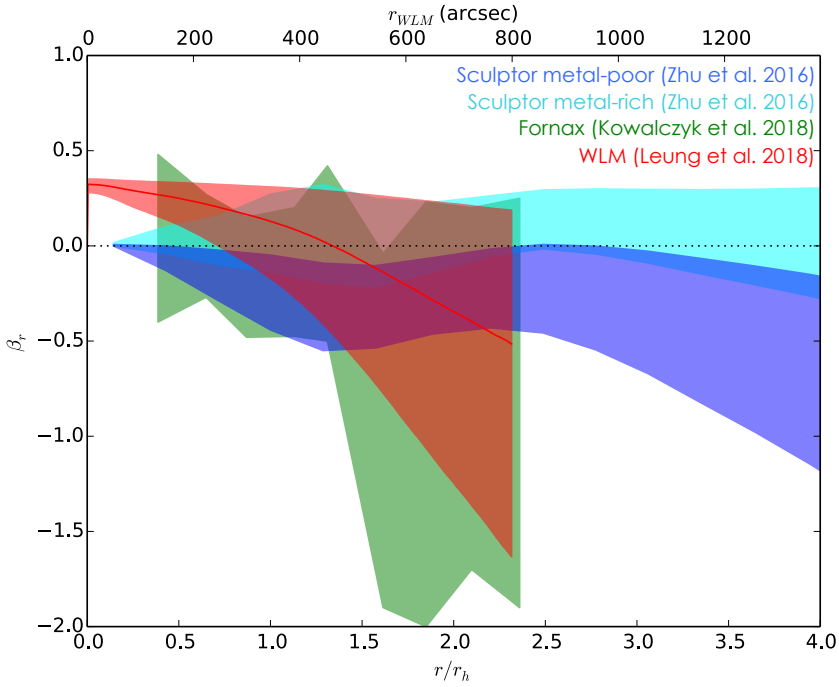

Figure 3.9: Derived WLM β_r profile (in red) overlaid on the β_r profiles of two dSphs, Sulptor in blue (Zhu et al. 2016) and Fornax in green (Kowalczyk et al. 2018), as an illustration of the similarities in their overall trend. The metal-poor population of Sculptor plotted in cyan has more radial anisotropy but is only dominant in the inner $\sim 1.5\,r_{\rm h}$.

such the last scenario into question. The velocity anisotropy profiles we find in the dIrr WLM, being nearly isotropic in the centre and increasingly tangential towards the outskirts of the galaxy (reaching $\beta_r = -0.5^{+0.6}_{-1.0}$ at $r = 2\,r_{\rm h}$), are very similar to those found in the aforementioned dSphs. WLM is an extremely isolated galaxy ($D_{MW,M31}$ ~1 Mpc; see Fig. 1 Leaman et al. (2012)), with Local Group barycentric velocity suggesting it has last been in the proximity of a massive neighbour ~11 Gyrs ago.

WLM's derived β_r profile thus provides an environmentally unprocessed baseline for using stellar kinematics to understand the evolutionary similarities or links between dIrrs and dSphs. First of all, the similarity of β_r between these dSphs and an isolated dIrr implies that the negative β_r seen in dSphs needs not be a result of tidal stripping. The orbital information of both Sculptor and Fornax inferred from proper motion measurements done with GAIA also have weakened the case that they have been tidally stripped (Fritz et al. 2018), as the derived pericentre of these two galaxies are both 50 kpc.

Given the other evidence in its dynamical and chemical evolution for a quiescent existence, it would seem that the tangential anisotropy in this case is either primordial, or imparted through some other mechanism. Whatever the mechanism to form or impart this anisotropy profile, the similarity between the dIrr and dSphs may also suggest that the transformation from dIrr to dSph is not a violent or dynamical one. Indeed the stellar kinematics, chemistry and SFHs of some of the *massive* dSphs are becoming increasingly similar to the dIrrs where studies of both are done to comparable depths (e.g., Kirby et al. 2013; Leaman et al. 2013; Wheeler et al. 2017). In that case the present day differences may only become extreme where there is significantly early infall, for example for more low mass nearby dSphs - and in other cases perhaps the difference is only quenching of the SF due to gentle ram pressure in the outer halo of the MW's CGM.

If extreme tidal processing is not playing a role in determining the anisotropy profile, we might ask if it it something intrinsic to the formation of galaxies of this mass regime? Some studies have looked at the relative role of gas pressure support in the initial gas disk of dwarfs (Kaufmann et al. 2007) or spatial distribution of star formation and stellar populations in dwarf galaxies (Schroyen et al. 2011b). However neither study provided quantification of the newly formed stellar anisotropy profiles. The details of how any aspects of the gas inflow history (e.g Kereš et al. 2005) or turbulence map into 3-D stellar kinematics needs additional study, but may provide help in understanding the similarities in Figure 3.9.

If the anisotropy at formation is not preserved until present day, the similar profiles for two of the bright classical dSphs and WLM indicate that any evolutionary process which generates tangential anisotropy, may need to operate in a generic galaxy of this mass. Such processes could either be connected to dynamical scattering of stars, or the dynamical mixing of gas at the epoch of formation of the surviving stellar populations.

For example, Christensen et al. (2016) showed how the re-accretion of gas in the outskirts of MW mass galaxies could introduce flows which have different angular momentum than the local reservoirs. It is unclear if this would lead to preferential mixing of the newly formed stellar orbits in the tangential direction, or if it could apply in low mass galaxies where there is evidence that a significant amount of the metals in the system may not have been retained or recycled (Kirby et al. 2011).

Latent dynamical heating of the stellar orbits in dwarf galaxies may be another mechanism to impart changes in the orbit distribution. Leaman et al. (2017) showed that the SFHs of Fornax, Sculptor and WLM were largely consistent with the age-velocity dispersion being a result of dynamical cooling of the ISM as the gas

fractions declined over time, however low level scattering of stars was still expected during epochs where the gas and newly formed stellar dispersion was ≤ 5 km s^{-1}. Individual stars can scatter off of over-densities (e.g., GMCs, spiral arms) in the molecular mid-plane of any galaxy.

GMC scattering is largely thought to result in both planar and vertical heating and isotropises the stellar velocity ellipsoid, as the stellar disks are much thicker than the molecular gas layers. Scattering from spiral arms or bars is predominantly planar and so could increase the dispersion in the radial or tangential directions. However dwarfs of this mass are much too thick and dynamically hot to form spiral arms. Bar formation has been invoked as an agent important in dwarf galaxy evolution, however the simulations tend to predict either strongly radial (before bar buckling) or vertical (after bar buckling) anisotropies.

Other processes for which increasing evidence is being assembled are the aforementioned feedback driven DM core creation, and dwarf-dwarf mergers. The non-adiabatic change to the potential induced by the expulsion of gas in the centres of dwarf galaxies, is suggested to result in preferentially larger orbit expansion for stars on circular orbits. If the response of these stars to the largely symmetric change to the potential is a net increase in their orbital radius, then could it be possible that the migrating stars enter final orbits with azimuthal velocities differing from the locally formed stars? Kaplinghat et al. (2016) studied the changes in anisotropy induced by potential fluctuations for dwarf galaxies of this mass, but even though they showed there could be variations, the anisotropy profiles were all significantly radial at all times and locations.

Mergers have been shown to temporarily induce tangential anisotropy in MW mass galaxies, provided the merging satellite remains coherent in the outskirts (Loebman et al. 2018). However, while there is increasing evidence for dwarf-dwarf mergers in the Local Group, and indeed Fornax (though not recent mergers; Leung et al. 2019), there is no concrete evidence presented in literature for mergers in the other two dwarf galaxies showing tangential anisotropy. A final speculative idea may be that the tangential anisotropy is a *consequence* of the prolate shape of the DM halo. This will be discussed in a follow up paper.

While the exact cause of the anisotropy profile in WLM, and its similarities to those seen in the dSphs is yet unclear, it is clear that the disparate environment posed by WLM offers an important constraint that simulations of isolated field dwarfs (and their potential transformation into dSphs) may want to reproduce.

WLM is an optimal candidate for the analysis we have presented here as its mass and isolation are both large enough that a significant dynamically cold

gaseous component exists. It is observationally expensive to get stellar kinematics for such objects, but as we illustrate here, the improvement on the recovered dark matter properties are significant. Amoung other Local Group dwarf irregulars, few have as well defined HI rotation curves or existing stellar kinematic data sets. Irregular dwarfs with gas such as IC1613, NGC 6822, Sextans A/B and Pegasus have more chaotic gas kinematic fields or non-optimal inclinations, however Aquarius, Sagittarius dIrr, VV124 may all be possible targets to repeat this type of joint stellar-gaseous dynamical modelling.

3.6 Conclusions

We performed Jeans Axisymmetric Models (JAM) on a discrete set of stellar kinematics, consisting of 180 stars, of an isolated dwarf irregular galaxy (dIrr) WLM. The discrete stellar kinematics is obtained using FORS2 on VLT and DEIMOS on Keck, as reported by Leaman et al. (2009, 2012). Our models incorporated cold HI gas kinematics from Kepley et al. (2007) by introducing the measured circular velocities from HI, $V_{\rm c,HI}$, as a prior to the total gravitational potential. We model the dark matter halo with the generalised NFW profile (Zhao 1996), characterised by the inner slope γ, the scale radius $r_{\rm s}$ and the characteristic density $\rho_{\rm s}$. We allow the flattening of the dark matter halo, $q_{\rm DM}$, to be a free parameter in our models. The velocity anisotropy is described by $\beta_{\rm z} = 1 - \sigma_{\rm z}^2/\sigma_{\rm R}^2$, which we take to be radially constant for our JAM models. We constrain our model parameters by employing Bayesian statistics. We show that all parameters are better constrained when including $V_{\rm c,HI}$ as a prior in our model; the $1\,\sigma$ uncertainties of the parameters ($\beta_{\rm z}$, $q_{\rm DM}$, $r_{\rm s}$, γ, $\rho_{\rm s}$) improve by 24%, 15%, 29%, 48% and 54% respectively.

The dark matter halo is shown to be cored, with $\gamma = 0.34 \pm 0.12$. Such a cored dark matter halo is robust against variations in the dark matter flattening $q_{\rm DM}$ and different $M_\star$ values from the literature. Our inferred γ is also consistent with predictions by hydrodynamical CDM simulations, which suggest a relationship between the stellar-to-halo-mass ratio $M_\star/M_{\rm halo}$ and the inner slope γ of the dark matter halo (Di Cintio et al. 2014). For our inferred value of, when adopting $M_\star = 4.3 \times 10^7\,M_\odot$, $\log(M_\star/M_{\rm halo}) = -2.8 \pm 0.2$, our derived inner slope of $\gamma = 0.23 \pm 0.12$, in excellent agreement with inner slope inferred by Di Cintio et al. (2014) of $\gamma = 0.25 \pm 0.16$.

We infer the radial anisotropy profile $\beta_r(r) = 1 - (\sigma_\phi^2 + \sigma_\theta^2)/2\sigma_r^2$ from our JAM models and found that the orbital structure of WLM is characterised by a mildly radially anisotropy core with $\beta_r(r = 0) = 0.32^{+0.03}_{-0.04}$ at the centre, which

become increasingly tangential and reaches $\beta_r(r = 2\,r_{\rm h}) = -0.35^{+0.57}_{-0.90}$ at 2 half-light radius. Such β_r profile is very similar to ones obtained from nearby dwarf spheroidal galaxies (dSphs), such as Sculptor and Fornax. While it has been suggested that the tangential anisotropy in dSph were caused by preferential tidal stripping of the radial orbit, the isolated nature of WLM suggests that the tangential anisotropy in dwarf galaxies can be of primordial origin and may not be informative on the evolution between dIrrs to dSphs.

Our model shows that a prolate dark matter halo is preferred in WLM, albeit with relatively high uncertainties: $q_{\rm DM} = 2.1^{+1.3}_{-0.9}$. The best-fit value in good agreement with the dark matter flattening found in ΛCDM cosmological simulations, both from dark matter only or hydrodynamical simulations, both of which suggest a prolate dark matter halo with $q_{\rm DM} \sim 2.0$ over the radii covered by our kinematic tracers ($\lesssim 5\%\, r_{\rm vir}$) (Butsky et al. 2016). The derived prolate halo suggests challenges to MOND and some self-interacting DM models. Such implication however is inconclusive given the large uncertainties inferred for $q_{\rm DM}$. Additionally, we show a $q_{\rm DM} - \beta$ degeneracy that extend from $q_{\rm DM} = 0.5$ to $q_{\rm DM} = 4.0$ in the 'Stars + Gas' models, which provides a window into a better-constrained $q_{\rm DM}$ if β can be constrained by other means such as proper motion measurements in the future.

Acknowledgments

We would like to thank G. Iorio for providing the HI circular velocity profiles. RL acknowledges funding from the Natural Sciences and Engineering Research Council of Canada PDF award and support provided by Sonderforschungsbereich SFB 881 "The MilkyWay System" (subproject A7 and A8) of the German Research Foundation (DFG).

Chapter 4

Dynamical friction as a tool for understanding dark matter and dwarf galaxy evolution

Abstract[1]

The five globular clusters (GCs) of the Fornax dSph are puzzling for two reasons; the mass in GCs is high with respect to the galaxy's old stellar mass, and their survival and large distance ($> 1\,\mathrm{kpc}$) is at odds with naive expectations of dynamical friction. We present here a semi-analytic model, simultaneously addressing both problems in a comprehensive evolutionary framework for Fornax. Key to the model is inclusion of: 1) hydrodynamical constraints on the GC formation locations, 2) self-consistent velocity distribution functions in the dynamical friction calculations and 3) expansion of GC orbits due to a past dwarf-dwarf merger in the orbit integrations. The latter is crucial for reconciling the dynamical survival of the clusters, and their chemical properties with respect to the Fornax field stars. We find that in order for four of the GCs to survive at their observed projected location, a dark matter core of size $r_\mathrm{c} > 1.5\,\mathrm{kpc}$ and a dwarf merger with dynamical mass ratio of 1:5 $\leq \eta \leq$1:2 with Fornax is required. We support the merger scenario by showing that aspects of the field star metallicity distribution function and anomalous chemical properties of GC5, are representative of a merging galaxy which is $\sim$1/3 less massive than Fornax.

---

[1]This chapter has been submitted in similar form to the journal MNRAS and is currently under peer review process. I am the first author of the paper and I hereby affirm that I have conducted all the research presented here myself.

Together the chemical and dynamical models suggest a scenario where three in-situ GCs in proto-Fornax were ejected to the outskirts during the merger, a GC4 formed during the merger at about 10 Gyrs ago, with GC5 being brought in by the merging galaxy to Fornax.

4.1 Introduction

As mentioned in Chapter 1, cosmological and N-body dark matter only simulations, under the standard cold dark matter (CDM) paradigm, have found that the density profiles of dark matter haloes tend to have cuspy profiles in the inner regions (e.g. Navarro et al. 1996). The scale free nature of dark matter suggests that these typically cuspy NFW halos are characteristic of all bound structures in a ΛCDM universe. However, the predicted steep inner slope of the DM density profile is at odds with several observational constraints in low mass galaxies.

There are two possible solutions to this problem. It has been shown that baryonic feedback can remove the central density cusps in CDM haloes of dwarf galaxies to produce central cores (e.g. Peñarrubia et al. 2012; Pontzen & Governato 2012). These simulations indicate that bursty star formation histories can make cores in the DM density distribution comparable in size to the effective radii of the stellar distribution (Read et al. 2016). On the other hand, existing alternative theories such as warm dark matter (WDM), Bose-Einstein condensate dark matter (ψDM) and self-interacting dark matter (SIDM) predict shallow inner density slopes even in pure DM simulations. The inner slope and the size of the dark matter core vary between different species of DM particles, between different DM particle masses within each species (e.g. Lovell et al. 2014; Schive et al. 2014a), and in the case of SIDM, and also between different DM interaction cross-sections (Kaplinghat et al. 2016). Precise observational constraints on the shape and the core size of dark matter haloes can therefore help us understand the impact of baryonic feedback, and the nature of dark matter itself.

The low-mass dwarf spheroidal galaxies (dSph) around the MW and M31 provide excellent test beds for the nature dark matter, as they are highly dark matter dominated objects. Methodologies such as the rotation curve decomposition and dynamical modelling with stellar kinematics are typically used to infer the DM mass distribution, but have limitations such as uncertainties in stellar mass-to-light ratio and mass-anisotropy degeneracies. As an alternative, the survival of globular clusters (GCs) in dwarf galaxies has also been used to understand the dark matter halo shape, as the tidal forces and dynamical friction forces are sensitive to the total

density that the GC sees.

For example, Amorisco (2017) suggested that the survival of low-density star clusters in Eridanus II and Andromeda XXV favours cored dark matter density profiles as a cuspy dark matter halo would exert too large a tidal force and hence disrupt the clusters. Together with considerations of dynamical friction and stellar evolution, Contenta et al. (2018) also found that the size and projected position of the low-density cluster in Eridanus II suggest a cored dark matter halo.

Of the classical dSphs, Fornax contains five GCs, which, together with extensive ancillary data of the host (e.g. stellar velocity, age and metallicity measurements), makes it a unique test case for probing the nature of its dark matter halo. All but one of the five GCs have masses of $> 10^5\,M_\odot$, the massive GCs in Fornax are therefore not subjected to destruction by the tidal field of the host galaxy, unlike the GCs in Eridanus II. The large projected distances of 240 to 1600 pc between the GCs and the center of Fornax, however, pose another challenge. With ages > 10 Gyr, they are naively expected to have already been brought to the center of the galaxy via dynamical friction from the field stars and the dark matter halo to form a nuclear star cluster (e.g. Tremaine 1976; Hernandez & Gilmore 1998). This is known as the 'Fornax timing problem'. This discrepancy poses a challenge to our understanding of not only the N-body problem, but also the nature and structure of dark matter.

N-body simulations have shown that the shape of the density profile of the underlying background particles has a profound impact on the orbital decay trajectory and therefore the time it takes for a massive infalling object to reach the galactic center (e.g. Read et al. 2006; Inoue 2009, 2011; Cole et al. 2011). In particular, cored dark matter halo profiles are found to allow slower decay than cuspy halo profiles. In addition, the orbital decay is found to stall in cored halo profiles, before the massive infalling object reaches the galactic center.

Semi-analytic prescriptions for dynamical friction (e.g. Chandrasekhar 1943) have shown some success at reproducing the orbital decay of a massive object under a background particle distribution. Several works have studied and verified the orbital decay of massive object under background particles of various density profiles. Notably, Petts et al. (2015) and Petts et al. (2016) have successfully reproduced the slower decay and the core-stalling effect of cored halo profile with the inclusion of tidal stalling and by adopting more a radially varying impact parameters. With detailed treatments of dynamical friction, the timing problem can therefore provide a constraint on the dark matter halo profile and hence allow a glimpse into the nature of dark matter.

Several solutions to the Fornax timing problem have been proposed in the

literature. Oh et al. (2000) suggested that the survival of GCs in Fornax can be resolved by invoking massive black holes which scatter the GCs to large radii, or a strong external tidal field from the Milky Way. There is however a lack of evidence for the existence of such black holes in Fornax. More problematic is that the proper motion of Fornax suggests that the dSph had never been closer to the Milky Way than its present location (Lux et al. 2010; Gaia Collaboration et al. 2018), implying that Fornax had never encountered a sufficient tidal field from the Milky Way to expand its GCs' orbit to their observed locations.

With N-body simulations of the Fornax system, it has been shown that the GCs in Fornax would not reach the galactic center within a Hubble time with a cored profile (Goerdt et al. 2006; Read et al. 2006; Cole et al. 2012). Cole et al. (2012) have also reported a 'dynamical buoyancy' in their N-body simulations of the five GCs in Fornax orbiting in a dark matter halo with a core radius $r_{\rm c}$ of 1000 pc. Such dynamical buoyancy would act as a force that pushes the GCs outwards, acting against the dynamical friction. While Cole et al. (2012) have performed the N-body simulations on four different halo profiles, only the profile with a large core shows noticeable dynamical buoyancy. With such a profile, two out of the five GCs can survive outside of the observed galactocentric distance. Interestingly, Sánchez-Salcedo et al. (2006) have also ruled out MOND using the Fornax timing problem, as the GCs would fall into the galactic center too quickly ($\sim$1 Gyr) under MOND. Conversely, Hui et al. (2017) show that dynamical friction would be largely reduced if dark matter is made up of the ψDM superfluid. In addition to the cored density profile of ψDM, the wave nature of ψDM would suppress the over-densities formed behind the infalling GCs, leading to a weaker dynamical friction.

Without a constraint on the starting position of the GC's initial orbit, modelling the orbital decay due to dynamical friction provides an incomplete and unconstrained picture of the GCs history and origin of their present-day location. Previous studies therefore either focus on whether the dynamical friction timescale is larger than the age of the GCs (e.g. Goerdt et al. 2006; Sánchez-Salcedo et al. 2006; Hui et al. 2017), or reproducing the observed distance by forcing the GCs to be formed at $>$1000 pc or even at the current tidal radius ($\sim$2000 pc) (e.g. Angus & Diaferio 2009; Cowsik et al. 2009; Arca-Sedda & Capuzzo-Dolcetta 2016). Given the measured age of the GCs (10-13 Gyrs), it is unclear whether the gas density would have been high enough at those redshifts to support the formation of the GCs at such large galactocentric distance - especially given the more compact size expected for the high-redshift progenitor of Fornax. It is therefore crucial to incorporate gaseous and stellar disk evolution models when estimating the galactocentric distances at which the GCs are formed, when addressing the present day position of the GCs.

For example, Kruijssen (2015) suggested that once formed in a central high (local) gas density environment, the GCs have to be ejected out of their formation environment to avoid disruption due to the strong chaotic tidal field of the gaseous interstellar medium. Such an ejection could be caused by dynamical interactions with gas clumps, stellar feedback or a merger. In particular, past merger events might be expected in dSphs like Fornax as they are found also as a possible pathway for the transformation of gas-poor dSphs from gas-rich dwarf irregulars in cosmological simulations (e.g. Wetzel et al. 2015). Specifically to Fornax, past merger events have been suggested in order to account for its complex metallicity distribution function, multiple stellar populations and differential internal dynamics between the populations (e.g. Walker et al. 2009; Amorisco & Evans 2012). The large total mass of the GCs relative to the mass of metal poor field stars would also be alleviated if one or more of the GCs are accreted via a merger as pointed out by Larsen et al. (2012). It is therefore crucial to incorporate possible influences on the positions of the GCs in Fornax due to the past merger event. Depending on the nature of the merger, the orbit of the GCs can undergo either an expansion or a contraction (e.g. Naab et al. 2009). For a non-dissipative (dry) merger, the GCs' orbits would gain energy from the merger and expand according to the mass ratio between the host and the merging galaxies.

An additional aspect contributing to the orbital evolution which has been neglected in previous semi-analytic models of the GCs' orbital trajectories in Fornax is the aforementioned dynamical buoyancy as reported in Cole et al. (2012). The dynamical buoyancy effect is particularly crucial if the formation location of the GC was at a galactocentric distance less than the current day location. Clearly a holistic approach which takes into account, dynamical buoyancy/friction, along with physical constraints on the formation position and merger history of Fornax is necessary to provide a better understanding of the evolution of this unique galaxy. This would require an exploration of a wide range of halo profiles and merger mass ratios, which can be too computationally expensive to be done with N-body simulations.

The goal of this work is to build the first semi-analytical model that includes the aforementioned ingredients: (1) a physically-motivated formation location of the GCs, (2) the effect of dynamical buoyancy and (3) a past merger, and then infer the underlying dark matter halo profile of Fornax by requiring the modelled current galactocentric distances of the five GCs to be outside of their observed projected distance ($d_{\rm p}$; see Table 4.1). In the following sections, we first present the ingredients of our semi-analytical model in Section 4.2. This includes the estimation of the formation location of the GCs, the density profiles of background dark matter and stellar particles, the dynamical friction treatment with dynamical buoyancy

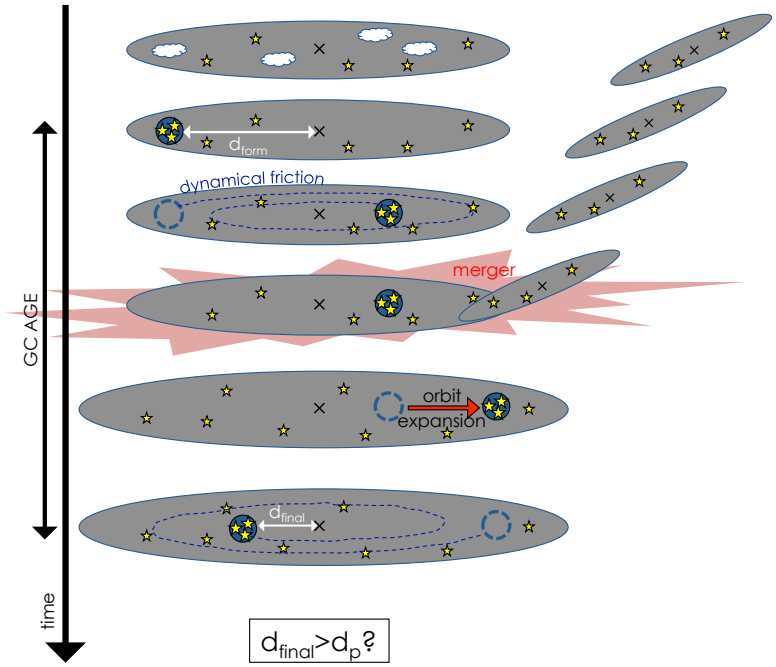

Figure 4.1: Schematic diagram of our semi-analytical model. Our model includes constraints on the formation location of the GCs ($d_{\rm form}$), an analytical prescription for dynamical friction and an orbit expansion caused by a merger. The modelled present-day positions of the GCs ($d_{\rm final}$) are then compared to the observed projected distance ($d_{\rm p}$) to constrain the dark matter halo profile.

implementation, and orbital expansions caused by mergers. We then present the result in Section 4.3, which is followed by a discussion on how the dark matter halo parameters we obtained compare with respect to ΛCDM cosmological simulations and whether the required merger mass ratio in our model is consistent with the observed metallicity distribution function in Section 4.4. We summarise our key findings and conclude in Section 4.5.

4.2 Semi-analytic Model

In the following section we will describe the ingredients that go into building our semi-analytic model of the co-evolution of Fornax and its GCs. The model is unique in that it provides physically motivated expressions for the GC formation distance, an updated dynamical friction/buoyancy prescription and the effect of a dwarf-dwarf

merger on the orbits of the GCs. A schematic representation of all the ingredients of our model can be found in Figure 4.1.

4.2.1 Constructing the host galaxy Fornax

We represent Fornax with two components: a dark matter halo and a spherical stellar distribution. The dark matter halo is parametrised by a 'cored NFW' profile (cNFW), which was found to be a good description of simulated dark matter haloes on dwarf galaxies which were altered by baryonic feedback mechanisms (Read et al. 2016):

$$\begin{aligned}
\rho_{\rm NFW}(r) &= \rho_0 \Big(\frac{r}{r_s}\Big)^{-1} \Big(1+\frac{r}{r_s}\Big)^{-2} \\
\rho_{\rm cNFW}(r) &= f^n \rho_{\rm NFW} + \frac{n f^{n-1}(1-f^2)}{4\pi r^2 r_c} M_{\rm NFW} \\
M_{\rm cNFW} &= M_{\rm NFW} f^n,
\end{aligned} \tag{4.1}$$

where ρ_0 is the characteristic density, r_s is the scale radius, r_c is the core radius, ρ and M represent the density and enclosed mass profile of the respective halo, f^n renders the profile at $r < r_c$ to be shallower than an NFW profile and can be written as:

$$f^n = \Big[\tanh\Big(\frac{r}{r_c}\Big)\Big]^n, \tag{4.2}$$

and n is a parametrisation of how 'cored' a profile is with $n = 0$ representing an NFW profile and $n = 1$ representing a completely cored profile. In this work we test the limiting case of $n = 1$ for all dark matter profiles.

The surface brightness profile of the stellar component, $\Sigma_\star(R)$, is described using a Sersic profile as fitted by Battaglia et al. (2006):

$$\Sigma_\star(R) = \Sigma_{0,\star} \exp\Big[\Big(\frac{R}{R_{\rm s}}\Big)^{1/m}\Big], \tag{4.3}$$

where R is the 2D-projected radius, $R_{\rm s} = 694.5\,{\rm pc}$, $m = 0.71$, and $\Sigma_{0,\star}$ is obtained through a normalisation to the total stellar mass in Fornax of $4.3{\times}10^7\,{\rm M}_\odot$ (de Boer et al. 2012). The surface brightness profile is then deprojected to a density profile $\rho_\star(r)$ using Eq. 17-19 of Lima Neto et al. (1999). The density profile of the stellar component takes the following form throughout this chapter:

$$\rho_\star(r) = \rho_{0,\star}\Big(\frac{r}{R_{\rm s}}\Big)^{-p} \exp\Big[-\Big(\frac{r}{R_{\rm s}}\Big)^{1/m}\Big], \tag{4.4}$$

with $\rho_{0,\star} = 0.015\,\mathrm{M}_\odot\,\mathrm{pc}^{-3}$ and $p = 0.25$[2]. The stellar density and enclosed mass profiles are plotted in the middle and bottom panel of Figure 4.3 respectively.

While the density distribution of the stellar component is fixed in our semi-analytic model, the r_s and r_c of the dark matter halo remain as free parameters. For each (r_s, r_c), the corresponding ρ_0 is obtained through a normalisation to the observed stellar velocity dispersion $\sigma_\star(R)$ from Battaglia et al. (2006). The $\sigma_\star(R)$ for each halo profile is estimated with the Jeans equation under the spherical and isotropic assumption:

$$\sigma^2(r) = \frac{1}{\rho(r)} \int_r^\infty \rho(r) \frac{d\Phi}{dr'} dr', \tag{4.5}$$

where $\sigma(r)$ and $\rho(r)$ in this case is the intrinsic velocity dispersion and density profile of the tracer particle, i.e. $\sigma_\star(r)$ and $\rho_\star(r)$ and Φ is the corresponding gravitational potential computed from the density distribution of the background particles (dark matter and/or stars). The binned stellar velocity dispersion for each of the total potentials is shown in Figure 4.3. As examples we over-plotted the $\sigma_\star(R)$ (obtained through the 2D-projection of $\sigma_\star(r)$)[3] of six different profiles in Figure 4.3. We summarise our steps in normalising the dark matter halo profiles in Figure 4.2. This is not an attempt to get a 'best-fit' dark matter profile from the observed $\sigma_\star(R)$ profile, but rather, to illustrate the degeneracies between various profiles when using just the observed $\sigma_\star(R)$ as a constraint and to show that the normalisation of our dark matter halo profiles are reasonable.

4.2.2 Constraining the formation location of the Globular Clusters

While the detailed formation physics of dense star clusters is currently debated, there are simple analytic estimates for the necessary environment of the gaseous regions which they are expected to form from. In particular, Elmegreen & Efremov (1997) suggested that the star clusters kinematic density may form in pressure equilibrium with the mid-plane pressure of the surrounding molecular gas phase. To constrain the starting location of the GCs, we consider a pressure equilibrium scenario at their formation. In such scenario, the external pressure of the galactic disk (P_ext) should

[2]Here $\rho_{0,\star}$ is obtained again through the normalisation of the total stellar mass and p is given as a function of m (as defined in Eq. 4.3) in Lima Neto et al. (1999).

[3]Once again, r and R here provide the distinction between the 3D and 2D projected radii respectively.

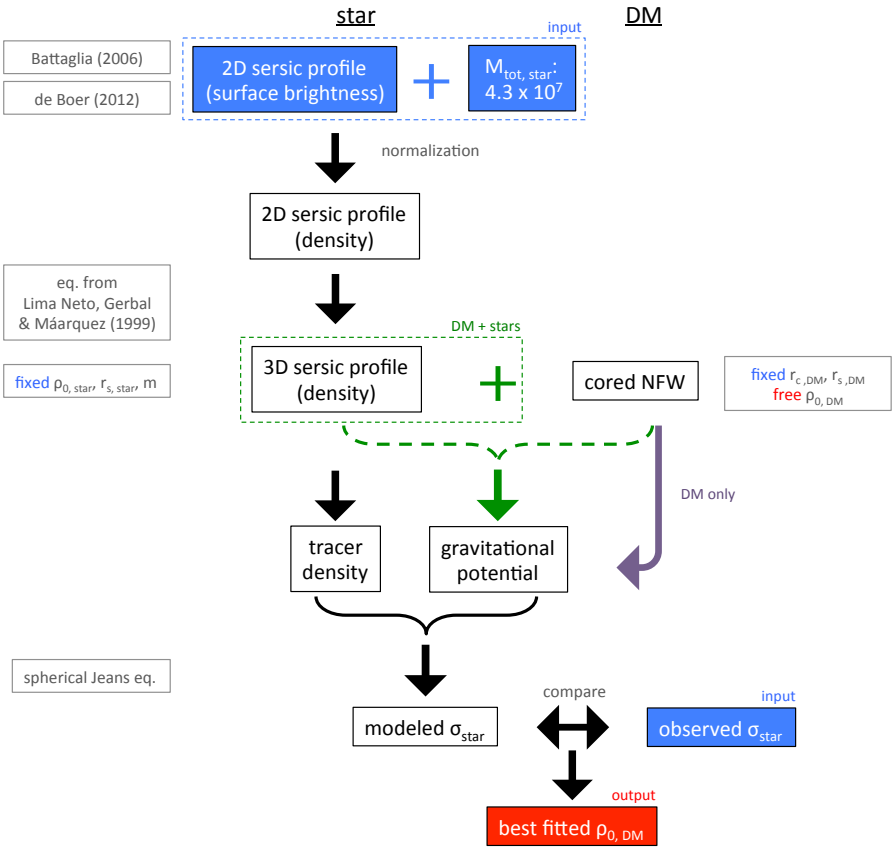

Figure 4.2: A flow chart showing the steps for normalising dark matter halo profiles with various $(r_{\rm s}, r_{\rm c})$. The purple and green paths show how the gravitational potential is obtained in the dark matter only and the dark matter + stars case respectively.

be equal to the internal pressure of the GC ($P_{\rm in}$) itself. $P_{\rm in}$ can be written as:

$$P_{\rm in} = 4\pi G \Sigma_{\rm GC}^2 = 4\pi G (\frac{M_{\rm GC}}{\pi R_{\rm GC}^2})^2, \tag{4.6}$$

where G is the gravitational constant, $\Sigma_{\rm GC}$, $M_{\rm GC}$ and $R_{\rm GC}$ are the surface density, mass and half-mass radius of the GC respectively. $M_{\rm GC}$ and $R_{\rm GC}$ are listed in Table 4.1. $P_{\rm ext}$ is related to the gas surface density ($\Sigma_{\rm gas}$), stellar surface density ($\Sigma_\star$) and the ratio between the velocity dispersion of gas and star ($f_\sigma = \sigma_{gas}/\sigma_\star$) by:

$$P_{\rm ext} = 4\pi G \frac{\pi}{2} \Sigma_{gas} (\Sigma_{gas} + f_\sigma \Sigma_\star). \tag{4.7}$$

To obtain the gas and stellar surface density at the formation epoch of the GCs, we utilise the star formation history of Fornax dSph. We obtained the star formation history from de Boer et al. (2012). We then assume that the star formation rate

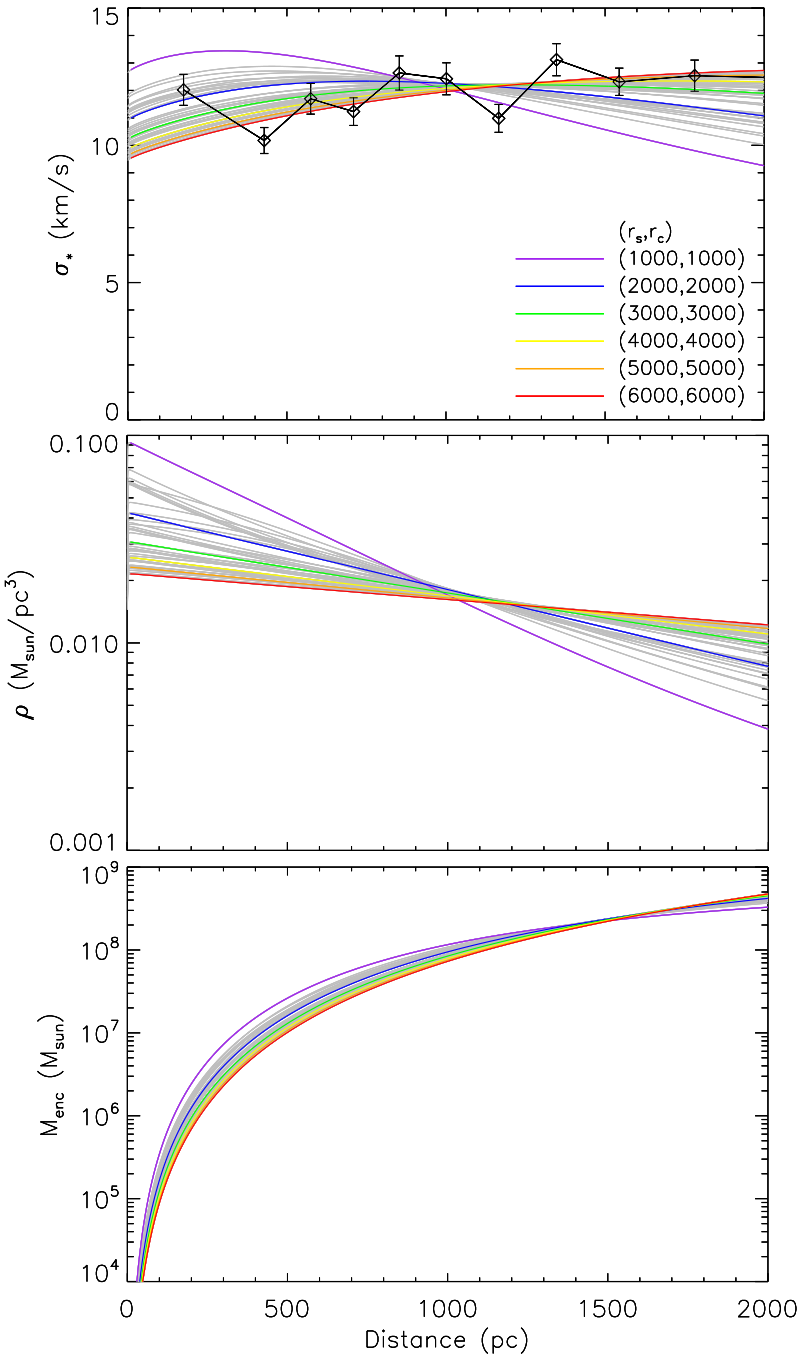

Figure 4.3: *Top:* the observed stellar velocity dispersion radial profile of Fornax (Battaglia et al. 2006) is plotted in black diamonds with error bars. Overlaid in grey are all the dark matter profiles we tested in our $(r_{\rm s}, r_{\rm c})$ grid. We show in colour six examples of the $\sigma_\star$ profiles from our normalised dark matter profiles. *Middle and bottom:* the corresponding density and enclosed mass profiles.

GCs	$M_{\rm GC}$ ($10^5\,M_\odot$)	Age (Gyr)	[Fe/H]	d_p (pc)	$R_{\rm GC}$ (pc)
GC1	0.37	12.1	-2.5	1600	10.03
GC2	1.82	12.2	-2.5	1050	5.81
GC3	3.63	12.3	-2.5	430	1.60
GC4	1.32	10.2	-1.2	240	1.75
GC5	1.78	11.5	-1.7	1430	1.38

Table 4.1:: Properties of the five globular clusters of Fornax dSph. The masses ($M_{\rm GC}$) are taken from Mackey & Gilmore (2003b). The ages are taken from de Boer & Fraser (2016). Metallicities are taken from de Boer & Fraser (2016). The projected distances (d_p) of GC1, 2, 3 and 5 are taken from Mackey & Gilmore (2003a) and that of GC4 taken from Greco et al. (2007). The radii of the GCs ($R_{\rm GC}$) listed here are the fitted core radii of a King model from Mackey & Gilmore (2003a).

has an exponential profile with radius at any time epoch and create star formation rate profiles $\Sigma_{\rm SFR}(R)$ for $t = t_{\rm GC}$, where $t_{\rm GC}$ is the age of the globular cluster. From $\Sigma_{\rm SFR}(R)$ we can obtain the gas surface density of the disk $\Sigma_{\rm gas,disk}(R)$ by adopting a depletion timescale $\tau_{\rm dep}$ such that $\Sigma_{\rm gas,disk}(R) = \tau_{\rm dep}\Sigma_{\rm SFR}(R)$. We adopt the cosmological model from Dutton & van den Bosch (2009) to allow the scale radius of the exponential profile of the gaseous disk to grow with time. To account for the fact that GCs often form in overdense regions of giant molecular clouds, the final $\Sigma_{\rm gas}$ we adopt for Equation 4.7 is (Kruijssen 2015; Krumholz & McKee 2005):

$$\Sigma_{\rm gas} = 3.92\Sigma_{\rm gas,disk}(5 - 4(1. + 0.025(\Sigma_{\rm gas,disk}/100)^{-2})^{-1})^{1/2} \tag{4.8}$$

The stellar surface density profile $\Sigma_\star(R)$ is then obtained by integrating the star formation history from $t = 13.6\,{\rm Gyr}$ to $t = t_{\rm GC}$.

To provide physical constraints to the formation location of the GCs, we then adopt a range of possible $\tau_{\rm dep}$, f_σ and $R_{\rm GC}$. With $0.3\,{\rm Gyr} < \tau_{\rm dep} < 3\,{\rm Gyr}$, $0.2 < f_\sigma < 1.0$ and $2\,{\rm pc} < R_{\rm GC} < 10\,{\rm pc}$ (Leaman et al. 2017), we calculated the range of possible $M_{\rm GC}$ formed at different galactic radii at different time epoch. The results are shown in Figure 4.4, with the red and blue region indicating the possible $M_{\rm GC}$ at different radii for the old GCs (GC1, GC2, GC3, GC5) and young GC4 respectively. We then consider the maximum possible formation location for each GCs, given their observed $M_{\rm GC}$, as the most optimistic formation distance ($d_{\rm form}$) from which to evolve the orbit of the GC. We derive $d_{\rm form} \leq 1144$, 863, 740, 1344 and 866 pc respectively for GC1, GC2, GC3, GC4 and GC5.

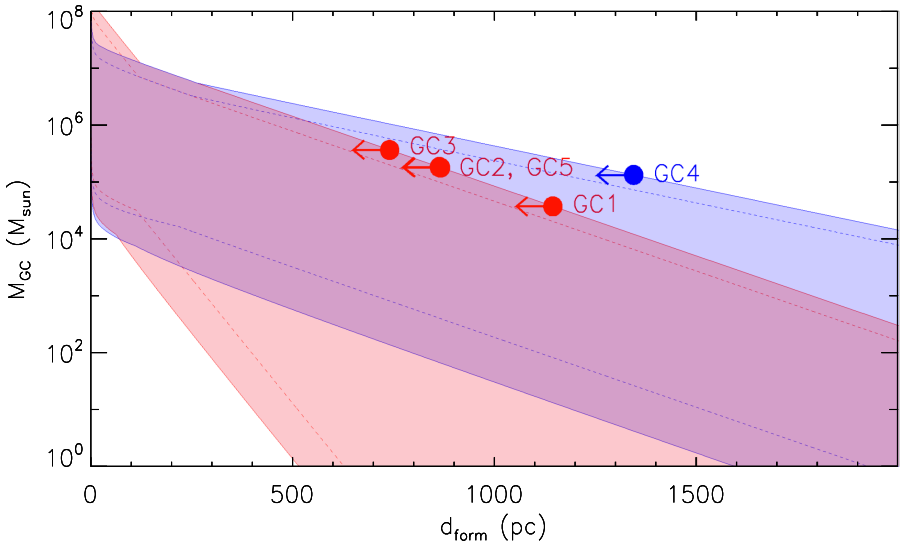

Figure 4.4: Hydrodynamic constraints on the formation location of the GCs in Fornax. The red and blue shaded regions show the allowed mass range of a GC to be formed at each galactic distance, at epochs representative of the formation of the 12 ± 1 Gyr (red) and 10 ± 1 Gyr GCs (blue). The mass of each GC and the maximum galactic distance at which each GCs can be formed are marked with red and blue dots for the co-eval and younger GCs respectively.

4.2.3 GC Orbital Evolution

Dynamical friction implementation

In the seminal paper on dynamical friction by Chandrasekhar (1943), the dynamical effect of an infalling object of mass M_s and velocity v_s through a halo of background particles moving with velocities $v_\bullet$ is described analytically as:

$$a_{\rm df} = \frac{d\vec{v_s}}{dt} = -\frac{\pi}{2} G^2 M_s \rho_\bullet \frac{\vec{v_s}}{v_s^3} \int_0^{v_{\rm esc}} \frac{1}{v_\bullet} J(V) 4\pi v_\bullet^2 f(v_\bullet) dv_\bullet, \tag{4.9}$$

where $\rho_\bullet$ is the density of the background particles (dark matter and/or stars), $v_{\rm esc}$ is the escape velocity, $f(v_\bullet)$ is the velocity distribution function of the background particles and V is the relative velocity between the background particle and the satellite. Due to different directions of encounter, for each $v_\bullet$, V ranges from $|v_s - v_\bullet|$ to $v_s + v_\bullet$. $J(V)$ is an integral characterising the effect that a background particle can exert on the satellite given the different relative velocities and can be written as:

$$J(V) = \int_{|v_s - v_\bullet|}^{v_s + v_\bullet} \left(1 + \frac{v_s^2 - v_\bullet^2}{V}\right) \ln(1 + \frac{b_{max}^2 V^4}{G^2 M_s^2}) dV, \tag{4.10}$$

where b_{max} is the maximum impact parameter. Equations 4.9 and 4.10 can be found as Equations 25 and 26 in Chandrasekhar (1943).

By assuming that the effect of fast-moving background particles (with $v_\bullet > v_\mathrm{s}$) is negligible, Equations 4.9 and 4.10 are often simplified as (e.g. Binney & Tremaine 1987):

$$a_\mathrm{df} = \frac{d\vec{v_s}}{dt} = -4\pi G^2 M_s \rho_\bullet \ln(\Lambda) f(v_\bullet < v_s) \frac{\vec{v_s}}{v_s^3}, \tag{4.11}$$

where $\ln(\Lambda)$ is the Coulomb logarithm, which is given by the ratio between the maximum (b_max) and minimum (b_min) impact parameters as $\ln(\Lambda) = \ln(b_\mathrm{max}/b_\mathrm{min})$ and $f(v_\bullet < v_\mathrm{s})$ is the fraction of background particle that has a velocity slower the v_s. When taking a simple assumption of the Maxwellian velocity distribution function (e.g. Angus & Diaferio 2009; Petts et al. 2015), the fraction $f(v_\bullet < v_s)$ can be expressed as:

$$f(v_\bullet < v_\mathrm{s}) = \mathrm{erf}\Big(\frac{v_\mathrm{s}}{\sqrt{2}\sigma_\bullet}\Big) - \frac{\sqrt{2}v_\mathrm{s}}{\sqrt{\pi}\sigma_\bullet} \exp\Big(-\frac{v_\mathrm{s}^2}{2\sigma_\bullet^2}\Big), \tag{4.12}$$

with $\sigma_\bullet$, the velocity dispersion of the background particles, being estimated by Equation 4.5. While such assumptions are generally sufficient for a cuspy dark matter profile, Petts et al. (2016) have recently pointed out that this is not true for cored dark matter haloes.

To show the effects of fast-moving background particles in different halo profiles, we calculated a_df for GC3 with $M_{GC} = 3.63 \times 10^5\,M_\odot$ for a cuspy and a cored dark matter profile. For demonstration purpose, we adopt here the NFW profile as obtained by Amorisco & Evans (2011) with phase-space modelling, with $r_\mathrm{s} = 1090\,\mathrm{pc}$ and compare the derived a_df with a cNFW profile of the same r_s and $r_\mathrm{c} = 1260\,\mathrm{pc}$, which is equal to 1.75 times the stellar half-mass radius as suggested by Read et al. (2006). The mass of the cNFW profile is normalised to the mass of the NFW profile at $r = r_\mathrm{c}$. These two test profiles are labelled as '`nfw0`' and '`cored0`' from hereon and are shown on the left column of Figure 4.5. We note here that there is a wide range of halo profiles derived for Fornax using various dynamical modelling technique, the `nfw0` and `cored0` profiles are merely adopted here for demonstrating the different effects of our dynamical friction treatment on cuspy and cored profiles.

The a_df are then derived for both profiles under the Maxwellian assumption and plotted with respect to the galactic radii in dashed lines on the left panels in Figure 4.6. a_df calculated with only the effects of slow background particles (SS) are plotted in blue and that calculated with effects from both fast and slow background particles (FS) are plotted in red. In both profiles, a_df is negative at large r, representing a dynamical friction. Where $a_\mathrm{df} = 0$, we shall expect the in-spiral of the GCs due to

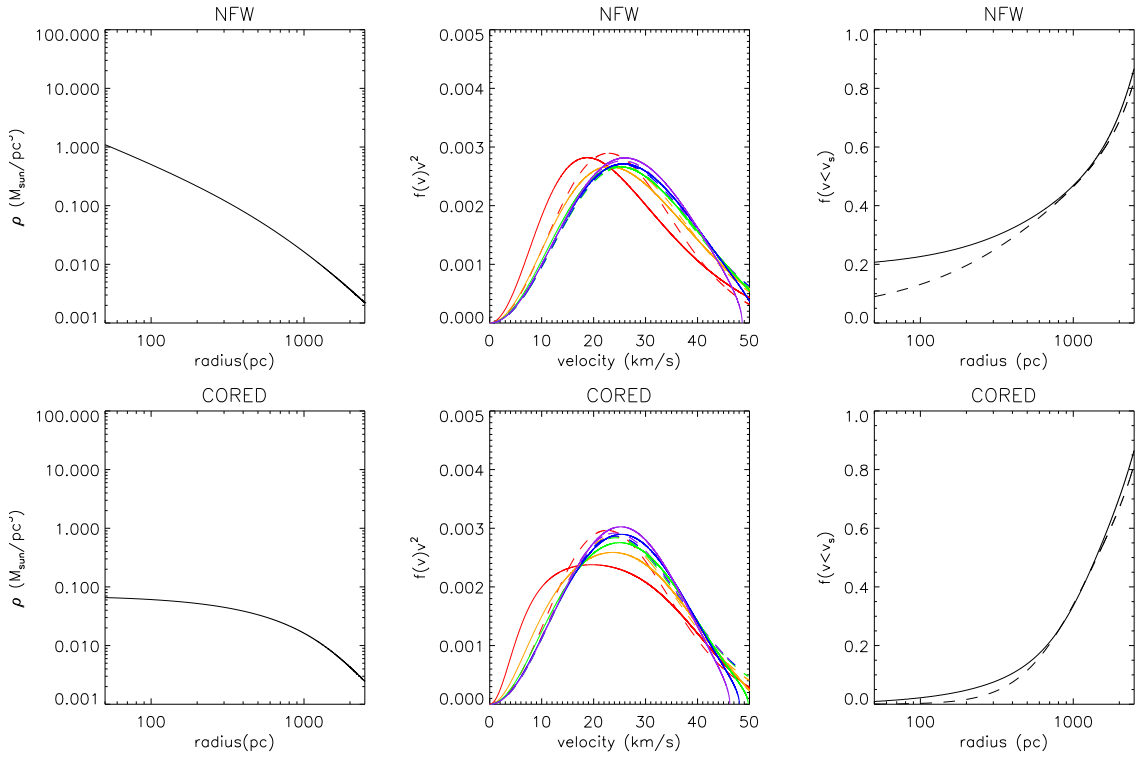

Figure 4.5: *Left and middle columns:* the density profiles $\rho(r)$ and velocity distribution functions $f(v)$ derived from Eddington equation (solid) and assumed as a Maxwellian (dashed) distribution, for the `nfw0` *(top)* and `cored0` *(bottom)* profiles. The different colours in the middle panels represent the velocity distribution functions evaluated at radii of, red: 200 pc, orange: 400 pc, green: 600 pc, blue: 800 pc, and purple: 1000 pc.The velocity distribution function estimated with a Maxwellian assumption is increasingly erroneous towards the small galactic radii. *Right:* the fraction of slow background particles ($f(v < v_s)$). In general, the Maxwellian assumption underestimates the fraction of slow background particles.

dynamical friction to stall. Towards the inner region, $a_{\rm df}$ becomes positive for both haloes, albeit at very different radii. The positive $a_{\rm df}$ means that when starting at these radii, the satellite will be pushed outward to where $a_{\rm df} = 0$. The corresponding orbital decay calculated through orbital integration for GC3 starting with a circular orbit on the right panels. The orbit decays stalled at where $a_{\rm df} = 0$ as expected.

We therefore see here, that the dynamical buoyancy as found by Cole et al. (2012) in a Fornax-like system, can be reproduced analytically by including fast-moving background particles. While it appears at first as an exotic dynamical phenomena, it is more understandable when considering dynamical friction as a manifestation of energy equipartition, where fast-moving background particles are able to transfer kinetic energies to the infalling object. Dynamical buoyancy has a much more prominent effect in the `cored0` halo, as also found by Cole et al. (2012). In contrast to the `cored0` profile, in which dynamical buoyancy exists up to $r \sim 500\,{\rm pc}$, the dynamical buoyancy occurs at a much smaller radius of $r \sim 200\,{\rm pc}$ in the NFW profile. This is because of the higher fraction of fast-moving particles in the inner region of the `cored0` profile, which are calculated using Eq. 4.12 and shown in the right column of Figure 4.5 in dashed lines.

In addition to the stalling effects produced by the fast stars, we also include tidal stalling as shown in N-body simulations by Inoue (2011) and described analytically by Petts et al. (2016). When the GC approaches the galactocentric distance $d_g = r_t$ (where r_t is the tidal radius of the satellite itself) the satellite will become unaffected by dynamical friction and stall. This is implemented by setting $a_{\rm df} = 0$ when $d_g = r_t$. While tidal stalling is not important for the FS cases as $d_g = r_t$ happens within the stalling radii defined by dynamical buoyancy, it is the primary stalling mechanism for the SS cases. As pointed out by Petts et al. (2016), tidal stalling is more prominent in a cored dark matter halo than a cuspy one. The same effect is seen in our models; GC3 in the SS model in the `cored0` profile stalls at $\sim$200 pc in the `cored0` halo but $<$50 pc in the `nfw0` halo.

Velocity distribution function

Both simulations and theoretical analyses have shown that dark matter haloes do not typically have a Maxwellian velocity distribution (e.g. Evans & An 2006; Hansen et al. 2005; Kuhlen et al. 2010). Petts et al. (2016) showed that such an assumption can lead to an error in $f(v_\bullet < v_s)$ by up to $\sim$80% depending on the halo profile. To have a more accurate handle on the velocity distribution function of various dark matter halo profiles at different radii, we therefore compute the distribution function self-consistently for an arbitrary potential by using the Eddington equation (Binney

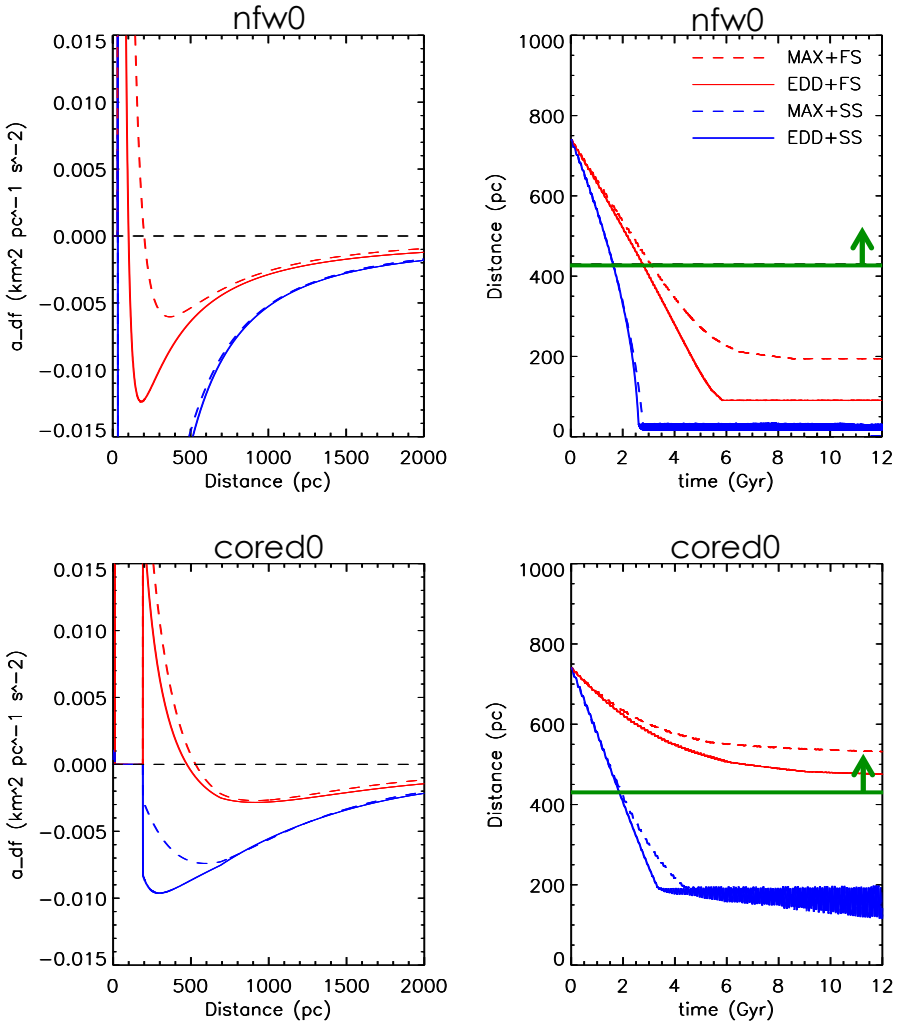

Figure 4.6: *Left:* Acceleration due to dynamical friction, $a_{\rm df}$, experienced by GC3 under different profile shapes and for different velocity distribution functions. Red lines denote dynamical friction treatments including fast stars (FS). Blue lines denote slow stars only (SS). Solid and dashed lines are runs using velocity distribution functions from the Eddington equation 4.13 (EDD) and Maxwellian assumptions (MAX) respectively. *Right:* the orbital decay of GC3 under the same four dynamical friction prescriptions. The green lines mark the observed galactic distance $d_{\rm p}$ of GC3, a lower limit of the galactocentric distance of GC3. Top and bottom row show the corresponding figures for the `nfw0` and the `cored0` profile.

& Tremaine 1987):

$$f(E) = \frac{1}{\sqrt{8}\pi^2} \int_0^E \frac{d^2\rho}{d\Phi^2} \frac{d\Phi}{\sqrt{E-\Phi}}, \tag{4.13}$$

where E is the relative energy, $E = \Phi - mv^2/2$.

As an example, we show in Figure 4.5, the difference in velocity distribution functions derived using the Eddington equation and that calculated by assuming a Maxwellian distribution for two different profiles. We show in the middle column the velocity distribution function for the `nfw0` and `cored0` halo profile at different radii, as labelled with different colours. The solid lines show the velocity distribution function as derived using Equation 4.13 and the dashed line show a Maxwellian distribution. The Maxwellian distribution function tend to under-predict the amount of slow background particles but over-predict the amount of fast background particles.

We than go on to show $f(v_\bullet)$ at different radii on the right column, where v_s is taken as the circular velocity under the particular dark matter halo at each radii. For both the velocity distributions derived using the Maxwellian assumptions and from the Eddington equation, we see a progressively decreasing amount of slow background particles towards the centre of the haloes. Furthermore, within radius of $r < r_c$, the `cored0` profile clearly has a smaller fraction of slow background particles, suggesting already that a GC would undergo less dynamical friction within $r < r_c$ for a `cored0` profile than an `nfw0` profile.

We then show a_df calculated for GC3 in the `nfw0` and `cored0` profiles with the the Eddington velocity distribution function in solid lines. Again, the blue curve shows the results obtained for the SS case and the red curve shows the results obtained for FS case. Notice here that adopting a Maxwellian assumption will lead to an overestimation of the stalling radius by a factor of 2 in the NFW halo. For the rest of the chapter, we shall adopt the improved dynamical friction treatment using velocity distribution function calculated from the Eddington equation and taking into account the effects from fast stars (i.e. case EDD+FS).

Orbit integration

Starting at a galactocentric distance in Fornax determined as described in Section 4.2.2, we then integrate the orbit of each GC, subjecting to dynamical friction/buoyancy as described in Section 4.2.3, as well as the gravitational acceleration given by the underlying potential of Fornax. The orbit integration continues for the respective ages of each of the GCs. The positions, velocities and

accelerations are updated at every time step of 1 kyr, with a precision of 0.01 pc and $0.01\,\mathrm{km\,s^{-1}}$. We assume circular orbits for the GCs to study the most conservative case as GCs on more eccentric orbits would simply be subjected to a severer dynamical friction. The numerical integrations are done with the Python module `odeint` from `scipy`.

Comparing the dynamical buoyancy effect from semi-analytical model to simulations

Dynamical buoyancy was first demonstrated in N-body simulations by Cole et al. (2012). Cole et al. (2012) used these N-body simulations to study the orbital decay of the five GCs in Fornax dSph under four different dark matter halo profiles, which are labelled as strong-cusp (SC), intermediate-cusp (IC), weak-cusp (WC) and large-core (LC), and are progressively less cuspy in the order listed here. The details of these four profiles can be found in Cole et al. (2012). Here we compare the stalling position of the GCs in the two extreme cases: SC and LC profiles, obtained from our analytical dynamical friction implementation with the ones obtained from N-body simulations by Cole et al. (2012), to provide further support to our analytic model for dynamical friction.

Figure 4.8 shows the dynamical effects exerted on GC3 by the background dark matter particles for the SC and LC profiles. Just like Figure 4.6, GC3 experience dynamical friction at radii with $a_{\rm df} < 0$ and dynamical buoyancy at radii with $a_{\rm df} > 0$. The stalling radius is the radius at which $a_{\rm df} = 0$. Cole et al. (2012) showed that the stalling radius of GCs in their LC profile occurs at $\sim$800 pc, inside which the GCs experiences dynamical buoyancy. This result is well-reproduced by our analytical model including the effects of fast-moving background particles and a velocity distribution calculated from the Eddington equation, as shown in the red solid line on the right panel of Figure 4.8. The stalling radius of LC is underestimated by $\sim 25\%$ if we assume Maxwellian velocity distribution (red-dashed curve) and the dynamical buoyancy cannot be reproduced at all if we only consider slow-moving background particles (blue curves). We note that for the SC profile, our analytical model has predicted a stalling radius of ~ 100 pc, while the simulations of Cole et al. (2012) suggest that the GCs can sink below 10 pc. Even without the inclusion of fast-moving particles, tidal stalling alone predicts a stalling radii of ~ 50 pc (blue curves). The discrepancies between analytic description of dynamical friction and the simulations could be caused by the lack of spatial resolution of the simulations, or that the velocity distributions in the innermost part of the halo cannot be captured by our simple assumptions. In either case, since the present-day

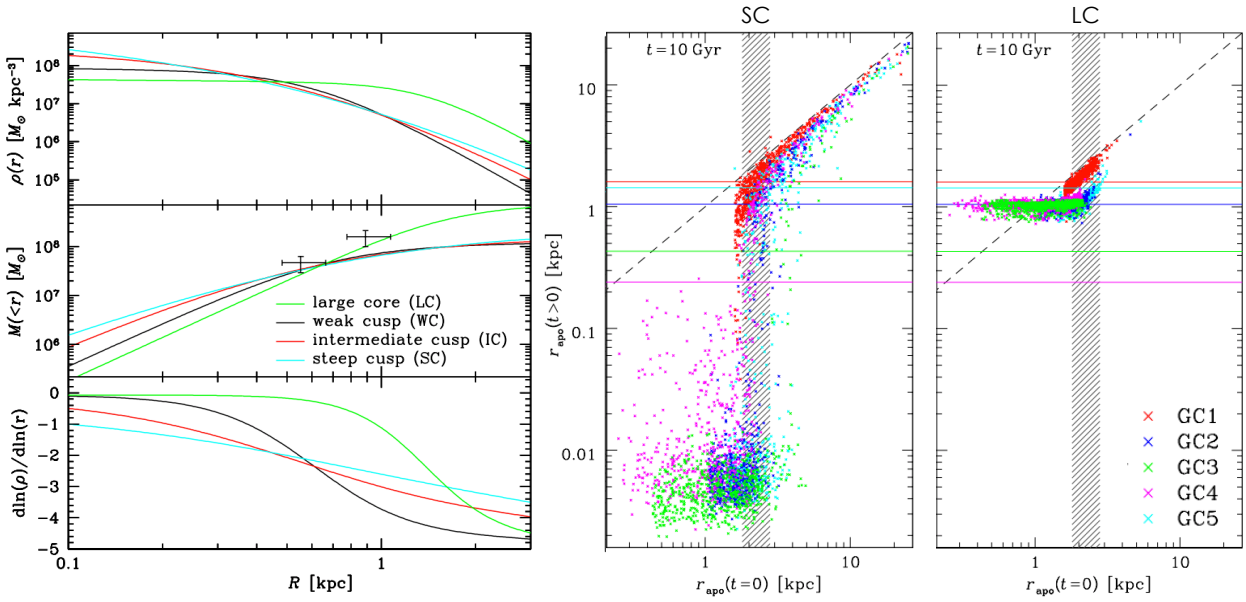

Figure 4.7: *Left:* The four dark matter profiles tested by Cole et al. (2012), from top to bottom are the density profiles, enclosed mass profiles and the slope of the density profiles, with the SC (cuspy) profile plotted in cyan and the LC (cored) profile plotted in green. The error bars in the middle panel show the mass estimates from Walker & Peñarrubia (2011) from using two chemically-distinct stellar populations. *Middle:* The apocentric radii of the five GCs after 10 Gyrs of evolution inside the SC DM halo plotted against their starting radii in dots. The grey band indicates where the current tidal radius of Fornax is. The five coloured horizontal lines are the observed projected distances d_p of the five GCs, with GC1 in red, GC2 in navy, GC3 in green, GC4 in magenta and GC5 in cyan. The dashed line indicate where the starting radii are equal to the radii at 10 Gyrs. The dots lying below the dashed line indicates correspond to the dynamical friction effect exerted by the underlying SC DM halo. *Right:* Same as the middle panel but for the LC profile. Dots that are lying above the dashed line correspond to the dynamical buoyancy effect. The GCs stalls at $\gtrsim$800 pc under the LC DM halo.

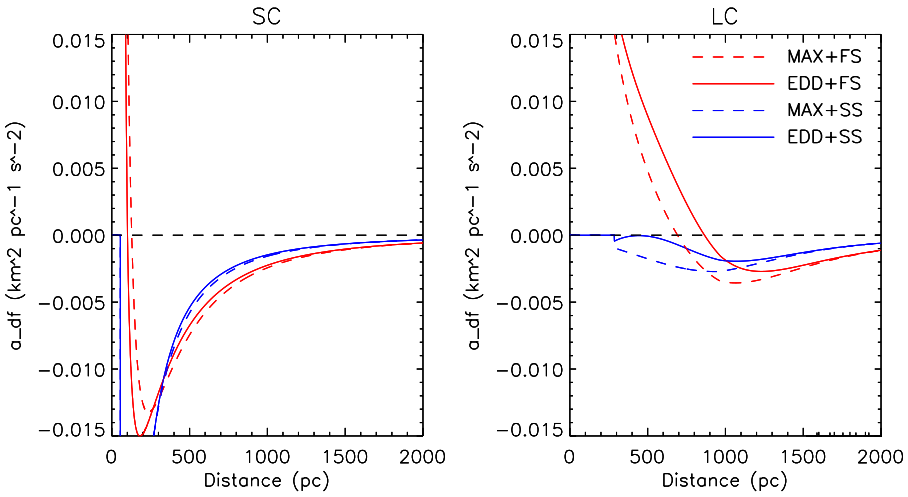

Figure 4.8: Same as the left column of Figure 4.6 but for the SC (*left*) and LC (*right*) profiles used in Cole et al. (2012).

location of the GCs are much greater than 100 pc, especially for GC1, GC2, GC3 and GC5, which provide the strongest constraints on the halo profile and merger history, such discrepancies at small radii would not affect our results.

Figure 4.9 shows the velocity distribution function $f(v_\bullet)$ of the dark matter particles of the SC and LC profiles tested in Cole et al. (2012). Just like when comparing the `nfw0` and `cored0` profiles, the cuspy profile SC has a larger fraction of slow particles (with $v_\bullet < v_s$, here v_s is the velocity of the infalling satellite and is taken to be the circular velocity of the considered dark matter halo) than the cored profiles LC.

4.2.4 A past merger event

The complex stellar morphology, metallicity and age distribution of Fornax suggests the galaxy might have experienced a significant merger event. A dry merger can significantly expand the final system size, given that the dominant stellar and dark matter components are non-dissipative. This could cause the GC (and stellar and DM) orbits to expand. In other words, a non-dissipative merger would have allowed the GCs to acquire a larger present-day galactic distance than the pressure equilibrium criteria allow for. To estimate this effect, we adopt the analytic

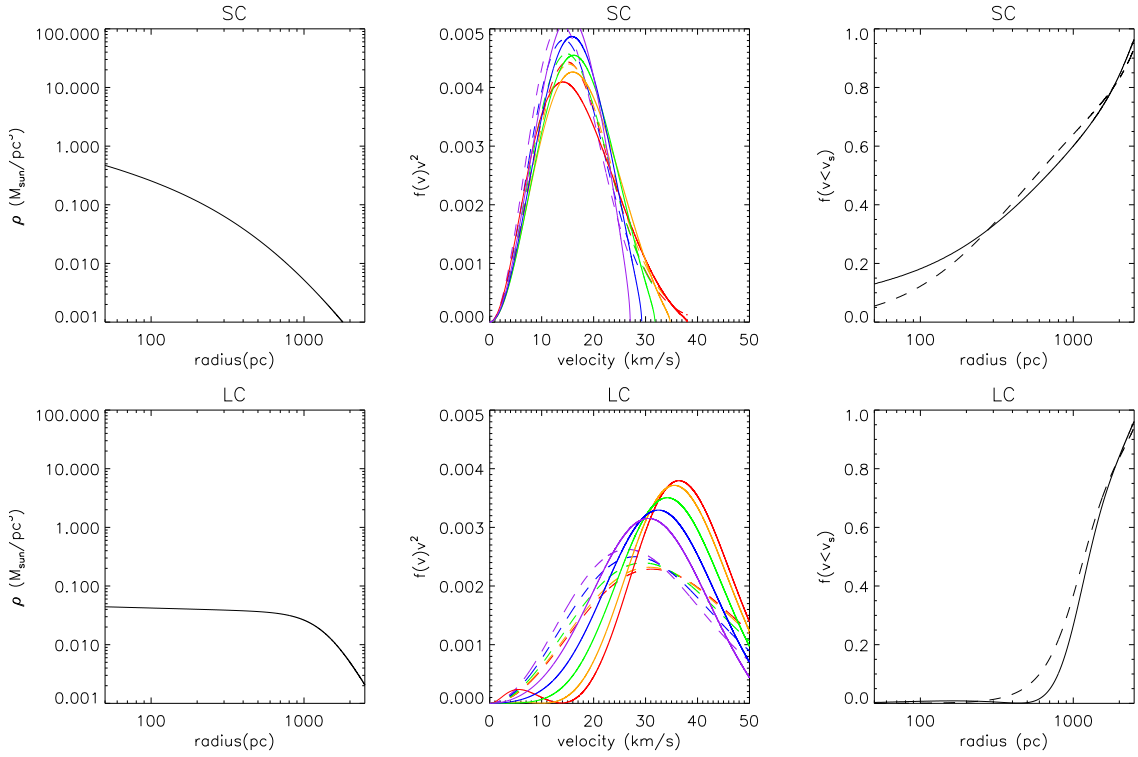

Figure 4.9: Same as Figure 4.5 but for the SC (*top*) and LC (*bottom*) profiles used in Cole et al. (2012).

expansion derived in Naab et al. (2009):

$$\frac{r_{\rm f}}{r_{\rm i}} = \frac{(1+\eta)^2}{(1+\eta\epsilon)}, \tag{4.14}$$

where $r_{\rm i}$ and $r_{\rm f}$ are the position of the GCs before and after the merger, η and ϵ are determined by the merger ratio with:

$$\eta = \frac{M_{\rm acc}}{M_{\rm host}}; \epsilon = \frac{\langle v^2_{\rm acc}\rangle}{\langle v^2_{\rm host}\rangle}, \tag{4.15}$$

where $M_{\rm acc}$, $\langle v^2_{\rm acc}\rangle$, $M_{\rm host}$ and $\langle v^2_{\rm host}\rangle$ are the mass and velocity dispersion of the accreted and host galaxies. We have assumed the Faber-Jackson relation of $M \propto \sigma^4$ (Faber & Jackson 1976) when calculating $\langle v^2_{\rm acc}\rangle$ and $\langle v^2_{\rm host}\rangle$.[4]

[4]It has been suggested that the index of the Faber-Jackson relation α in low-mass galaxies can be as low as $\sim$2 (e.g. Kourkchi et al. 2012). The differences in $r_{\rm f}/r_{\rm i}$ between $\alpha = 4$ and $\alpha = 2$ can be written as $(1+\eta^{1.5})/(1+\eta^2)$. Within our tested range of $0.0 < \eta < 0.5$, it amounts to an 8% change in the final to initial position ratio.

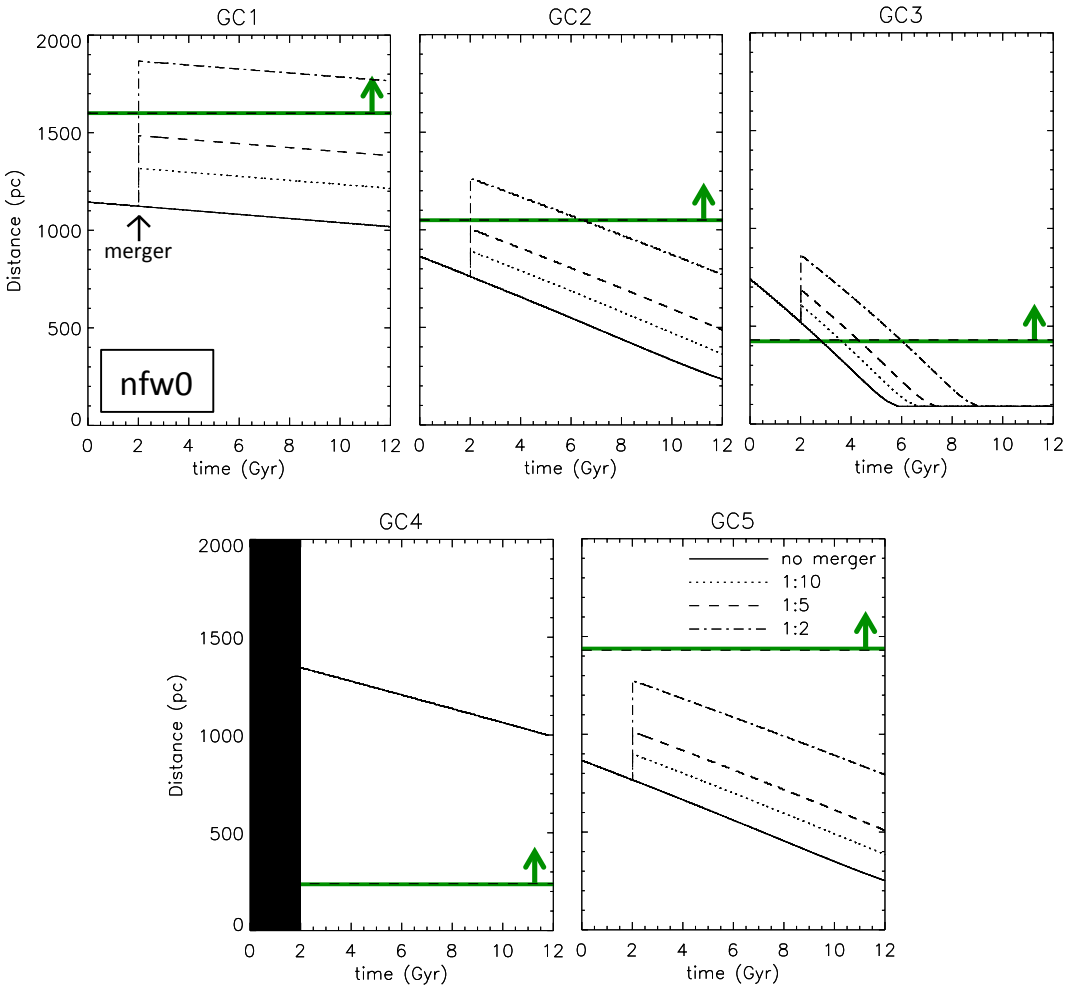

Figure 4.10: Orbital evolution of GCs in the `nfw0` halo with various merger histories. The green lines mark the observed present day distance $d_{\rm p}$ of each GC, a lower limit of the their galactocentric distances.Under this profile, only GC4 can survive outside of its observed distance without a merger, GC1 would need an 1:5 merger and GC2 an 1:2 merger. Both GC3 and GC5 would need a merger with an even more substantial mass ratio than 1:2 to exist outside of its $d_{\rm p}$ under this profile.

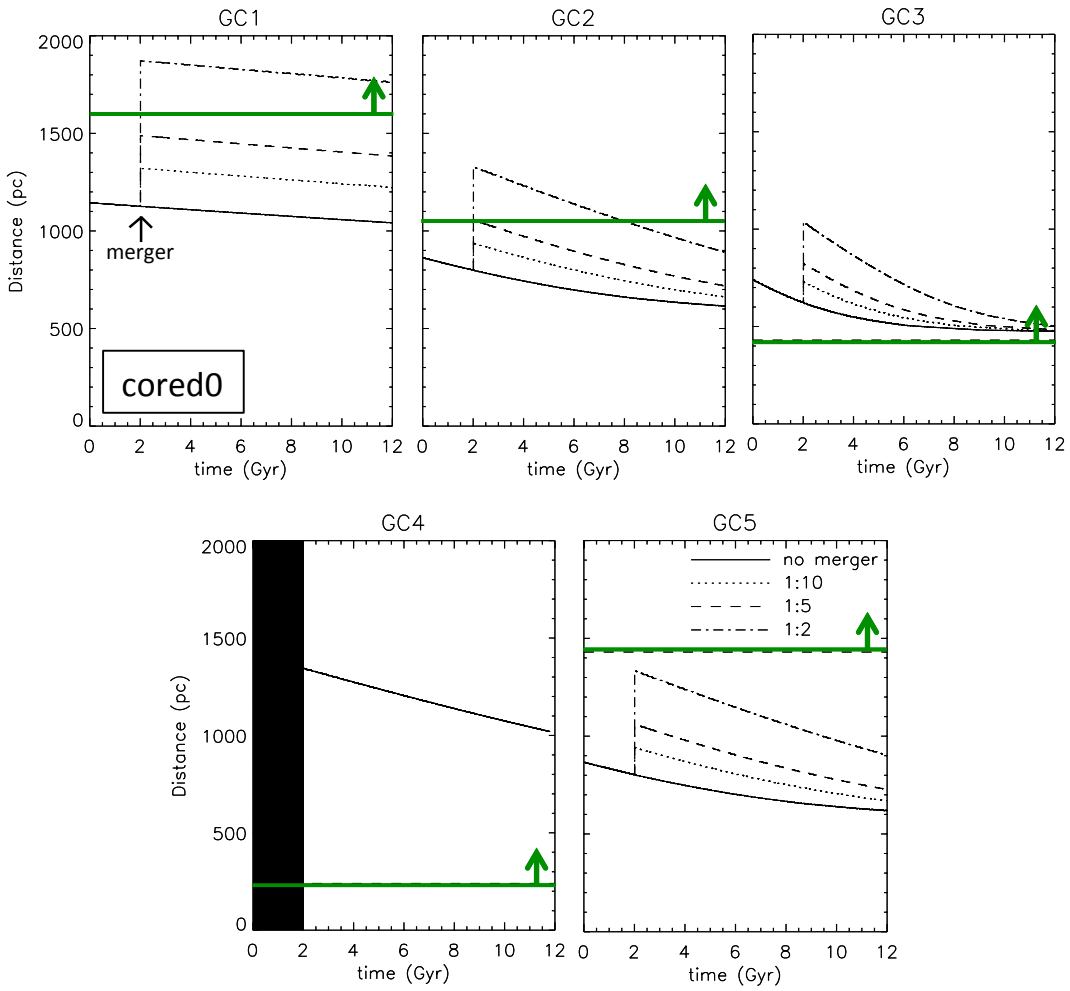

Figure 4.11: Same as Figure 4.10, but for the `cored0` halo profile. Under this profile, both GC3 and GC4 can survive outside of its observed distance without a merger. As with the NFW profile, GC1 would need an 1:5 merger and GC2 an 1:2 merger. GC5 would however still need a merger with a mass ratio smaller than 1:2 to exist outside of its $d_{\rm p}$ under this profile.

Given the younger age and significantly higher metallicity of GC4 (de Boer & Fraser 2016), we consider the case in which a dry merger happened 10 Gyrs ago which triggered the formation of GC4 from small amounts of residual gas in the total system[5]. GC1, GC2, GC3 and GC5 will hence experience an orbital expansion due to the merger while GC4 will not. We demonstrate how our simple analytic expansion from Equation 4.14 would affect the final GCs positions in Figure 4.10 and 4.11 for the `nfw0` and `cored0` profiles respectively. We tested four different scenarios: no merger (solid lines), an 1:10 merger (dotted lines), an 1:5 merger (dashed lines) and an 1:2 merger (dash-dotted lines). GC1, GC2, GC3 and GC5 would hence for the first 2 Gyrs orbit through a dark matter halo with a viral mass $1-\eta$ times the current day virial mass, the $r_{\rm s}$ and $r_{\rm c}$ of the dark matter profile before the merger also scale as Equation 4.14. As shown in Figure 4.10 and 4.11, the expansion experienced by the GCs increases as the mass ratio between the host and accreted galaxy decreases. By comparing the modelled present location of the GCs with the observed projected presented-day position $d_{\rm p}$ (horizontal dashed line), the `nfw0` profile can be ruled out because both GC3 and GC5 end up inside their respective $d_{\rm p}$s even with an 1:2 merger. As for the `cored0` profile, GC3 can survive out of its $d_{\rm p}$ but GC5 still fails to do so even with an 1:2 merger.

4.3 Results

In this section we will show the results of the orbital evolution for the GCs in Fornax. We run our semi-analytic model on a grid of dark matter halo profiles with $r_{\rm s}$ and $r_{\rm c}$ each drawn from $1000-6000$ pc in steps of 1000 pc. For each halo profile we include a 'no merger' case and three merger cases with merger mass ratios of 1:10, 1:5 and 1:2. We then compare the modelled present day galactic distance of each GCs with the observed $d_{\rm p}$.

The results are presented in Figure 4.12. The size of the squares represents the merger ratio. The colour coding represents the difference between the final model galactocentric distance and the current projected distance, $d_{\rm p}$ for each GCs. Blue implies that the modelled distance is outside of the observed $d_{\rm p}$, meaning that the dark matter halo with parameters $(r_{\rm s}, r_{\rm c})$ is plausible given the corresponding merger with mass ratio η had happened.

[5]Naively assuming a star formation efficiency per free-fall time for a molecular cloud of $\epsilon_{ff} = 0.03$, this would require $M_{gas} \geq 5 \times 10^6\, M_\odot$ in Fornax at the time. This is reasonable given that Fornax continued to form another $5 \times 10^6\, M_\odot$ of field stars at a low level for another $\sim$9 Gyrs after this and so clearly retained some gas.

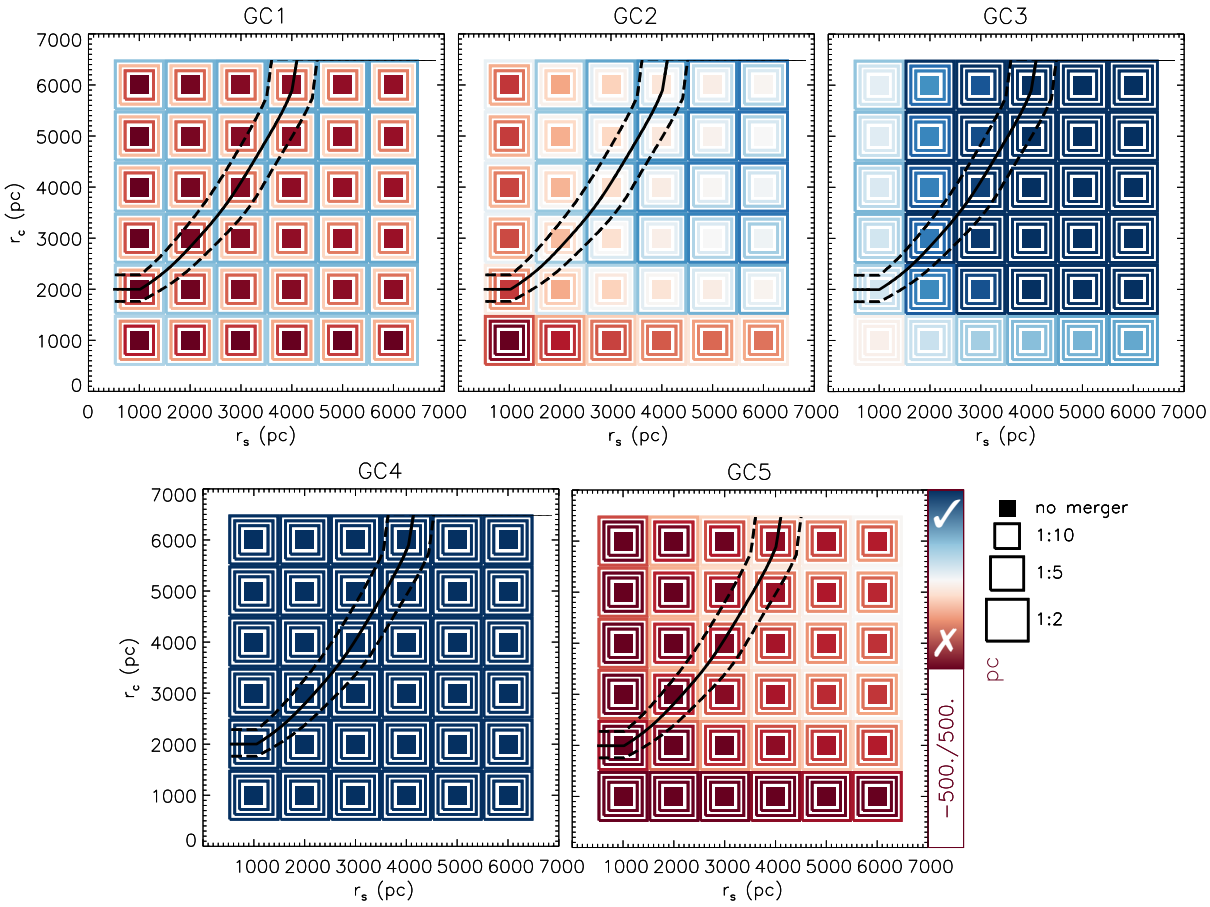

Figure 4.12: Summary of orbit integration for the grid of DM halos and merger mass ratios. Each plot is for a different GC and shows the grid of DM halo scale radii $r_{\rm s}$ and core radii $r_{\rm c}$ for that trial. For each $(r_{\rm s}, r_{\rm c})$ pair, we have run the dynamical friction model under the assumption that Fornax has experienced no merger (filled squares), a 1:10 merger, a 1:5 merger, and a 1:2 merger, with the merger mass ratio indicated by the size of the square. In each trial, the final position oof the GC relative to its observed present day is indicated by the colour of the box. The models marked with blue means that the GC is found to survive outside the $d_{\rm p}$ (as marked by tick on the colour bar) and hence suggesting the particular parameters $(r_{\rm s}, r_{\rm c}, \eta)$ represent a plausible dark matter profile and merger history for Fornax. The halo parameters which follow an $M_{\rm vir}$-concentration relation inferred from cosmological simulations (Dutton & Macciò 2014) are shown in the background marked with black contours, the dashed contours mark the 5-σ values.

The observed galactocentric distance of both GC3 and GC4 can be well reproduced with any of the dark matter halo profile, without the need for any merger. The addition of a past merger event does not significantly change the required (r_s, r_c) for GC3. This is because of the large mass of GC3, which implies that the dynamical friction timescale is relatively short compared to the other GCs. Therefore, GC3 reaches its stalling radius within a Hubble time regardless of the merger. This is also reflected in Figure 4.11, which shows that the final position of GC3 under different merger ratios all converge to the stalling radius of the `cored0` profile. It is different for GC1, GC2 and GC5 because their masses are a half to an order of magnitude smaller than GC3, allowing them to have a much longer dynamical timescale. The orbital expansion given by the merger event therefore has more importance on these final GC positions.

Given a merger with mass ratio 1:2, the observed d_p of GC1 can also be reproduced with any of the dark matter profiles. Without that, none of the tested profile can reproduce the observed d_p for GC1. The minimum (r_s, r_c) required for GC2 is (5000, 3000) pc in the 'no merger' case, (3000, 2000) pc with an 1:10 or an 1:5 merger and (3000, 1000) pc for a 1:2 merger. Finally, the observed d_p of GC5 can only be reproduced with a merger of mass ratio 1:2 at $(r_s, r_c) > (6000, 4000)$ pc. The minimum r_s and r_c as required by each GC is plotted in Figure 4.15, with the case for a 1:1 merger marked as an additional reference in this plot.

While these results are run with only the dark matter halo contributing to the potential, the stellar contribution within the tidal radius of Fornax is expected to be non-negligible. Therefore we repeat the exercise and include the stellar component as described in Section 4.2.1. The dark matter haloes of each (r_s, r_c) are renormalised with the inclusion of the stellar component using the observed $\sigma_\star(R)$ as described also in Section 4.2.1. The corresponding stellar velocity dispersion profiles, density profiles and mass profiles are shown from top to bottom in Figure 4.13. In general, either a larger (r_s, r_c) or a smaller mass ratio in the merger is required due to the fact that the stellar component tends to steepen the overall density profile. This is true in particular for GC2, GC3 and GC5, where the profile shape has a noticeable effect on the final location of the GC. GC4 is still permitted under all halo profiles, due to its small present-day galactocentric distance. As for GC1, the small GC mass leads to a long dynamical friction timescale, which means that the merger ratio has a more prominent effect on the final GC location than the underlying density profile. As in the case of DM only, GC1 requires a merger ratio of 1:2 to allow the final location of the GC to be outside of the present-day observed distance d_p. GC2 requires at least an 1:2 merger, with which a (r_s, r_c) of (2000, 2000) pc is sufficient for the GC to end up outside of d_p. GC3 requires a minimum merger mass ratio of

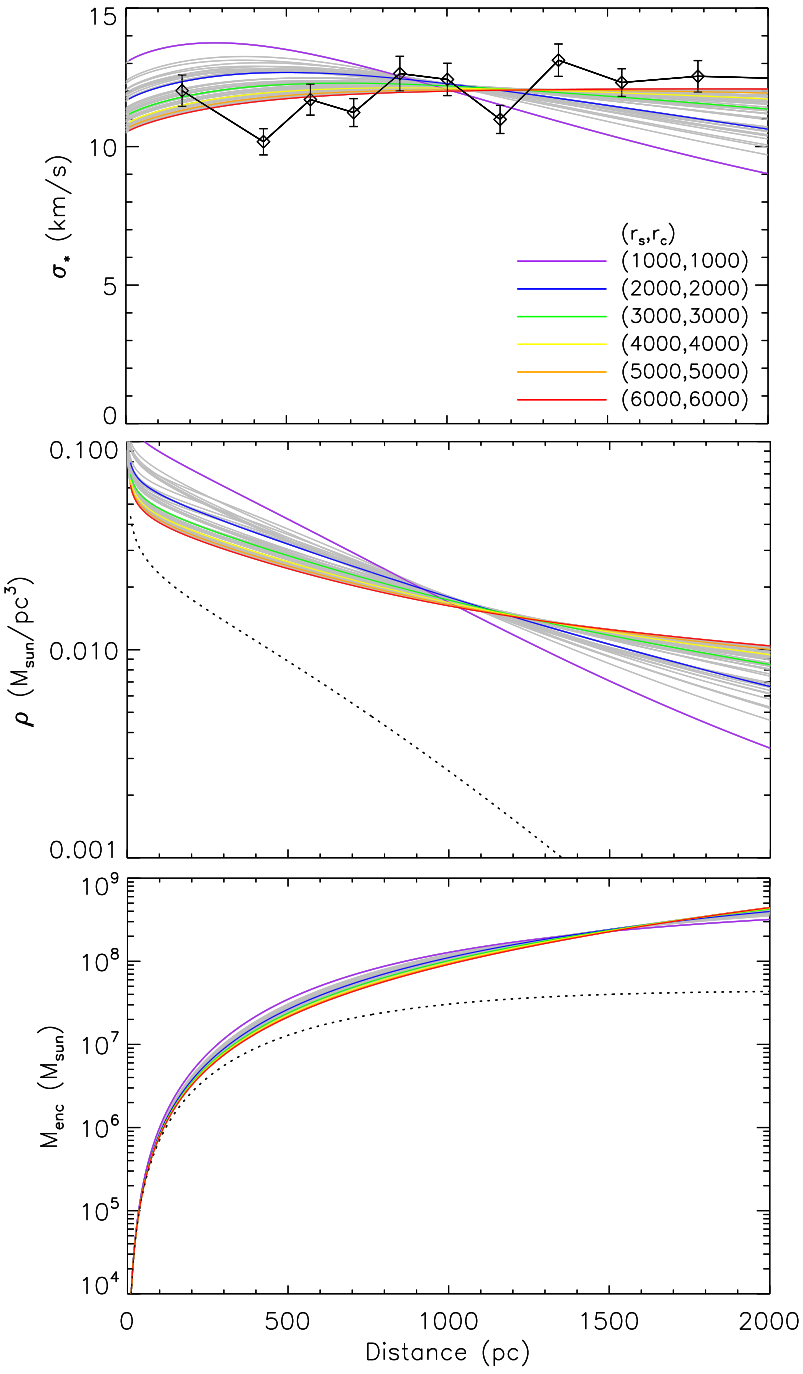

Figure 4.13: Same as Figure 4.3 but the dark matter profiles are normalised together with a stellar component. The dotted black lines in the middle and bottom panel show the stellar density and enclosed mass profiles respectively.

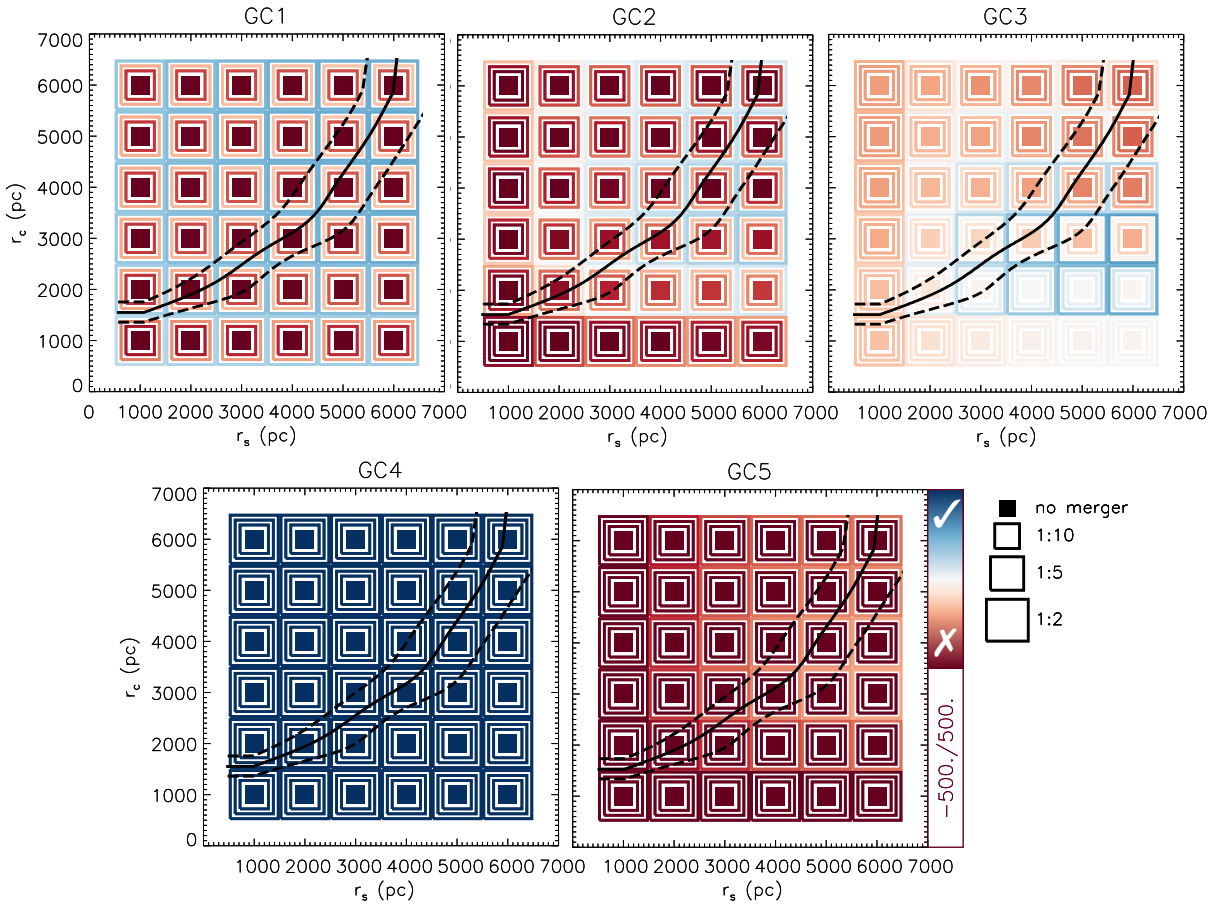

Figure 4.14: Same as Figure 4.12, but with a stellar component included in the background mass profile.

1:10 at (r_s, r_c) of (3000, 2000) pc, a mass ratio of 1:2 allows a (r_s, r_c) of as small as (2000, 1000) pc. GC5 now becomes problematic under all halo profiles and they are not permitted to exist outside of d_p with any merger with mass ratios larger than 1:2.

4.4 Discussion

With constraints from the d_p of the GCs in Fornax, our semi-analytic orbital evolution model suggests that there is a dark matter core of size no smaller than 1000 pc in Fornax, and that the galaxy has experienced a past merger of mass ratio more substantial than 1:5. In this section, we first present a self-consistent picture for

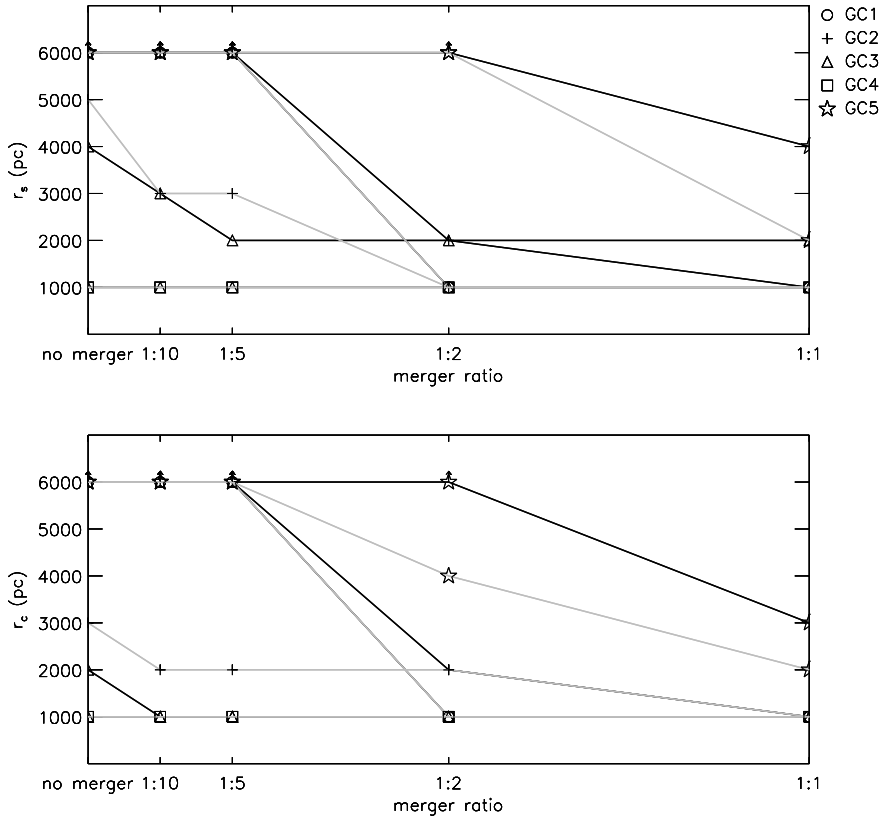

Figure 4.15: Minimum $r_{\rm s}$ (top panel) and $r_{\rm c}$ (bottom panel) of Fornax dark matter halo as constrained by the five GCs under the various merger scenarios. The grey lines correspond to the DM only case while the black lines correspond to the DM+stars case.

the co-evolution of Fornax and its GCs in Section 4.4.1. We then provide additional evidences from the chemistry of Fornax to support the merger scenario in Section 4.4.2 and our proposed origins of the GCs in Section 4.4.3. Section 4.4.4 concerns with evidences of dwarf-dwarf mergers both from cosmological simulations and observed interactions between dwarfs. In Section 4.4.5 we compare our derived dark matter halo profile with cosmological simulation results and discuss the implications of the apparent large dark matter core on the nature of dark matter. We close this section by presenting some caveats of this work.

4.4.1 A self-consistent picture for the co-evolution of Fornax and its GCs

GC5 stands out as the only GC that would require a (r_s, r_c) larger than our explored range of value. The younger age and higher metallicity of GC5 when compared with GC1, GC2 and GC3 also might be hinting at a different origin of this GC (Section 4.4.2). We propose the following scenario for the co-evolution of Fornax and its GCs: (1) GC1, GC2 and GC3 were formed in a proto-Fornax at ∼12 Gyrs ago, (2) GC5 was formed ∼11 Gyrs ago in the lower mass dwarf galaxy that will go on to merge with the proto-Fornax, and (3) the merger which happened ∼10 Gyrs ago triggered the formation of GC4, and at the same time deposits GC5, and scatters GC1,2,3 to larger orbits conducive to their survival.

The existence of a sixth GC has recently been re-discussed by Wang et al. (2019), where they show with deep DECam imaging data that a past association of stars is likely to be a star cluster with stellar mass of $M_* \sim 10^4\, M_\odot$. This object has a projected distance of d_p of 270 pc and its metallicity is inferred through photometry to be similar to GC4 ([Fe/H]~ -1.4). Notably, its low mass but small projected distance is at odds with naive expectations for dynamical friction (especially relative to the higher mass, but further out GCs). While further work on the orbit and ages of this GC will be necessary to fully understand its role in the evolution of Fornax, we note that its central position and relatively high metallicity (compared to other GCs) can be naturally explained with our merger scenario: just like GC4, GC6 would be a product of triggered star formation due to compression of gas in the dwarf-dwarf merger approximately 10 Gyrs ago and reside close to the center of Fornax after that event.

4.4.2 Support for the merger scenario from Fornax's chemical evolution

We consider here whether a merger with mass ratios of 1:5 to 1:2 are supported (or even permitted), given the observed metallically distribution function (MDF) of Fornax's field stars. For this exercise, we take the observed metallicity measurements of individual RGB stars within several local group dwarf galaxies (Leaman et al. 2013, and references therein, as recalibrated by Starkenburg et al. (2010)), perform superpositions of pairs of dwarf galaxies and then compare the combined metallicity distribution with that of Fornax. To avoid possible systematics introduced by binning, we apply this analysis on the cumulative distribution function (CDF) instead of the MDFs themselves.

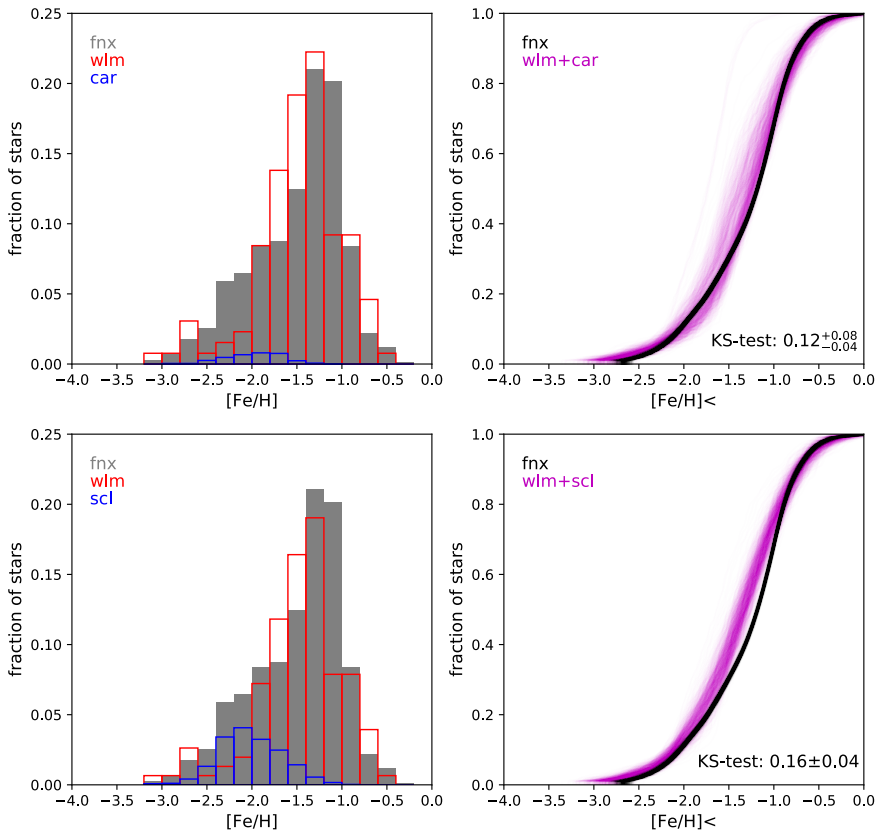

Figure 4.16: *Left:* Normalised MDF of Fornax in grey, the mass-weighted MDFs of WLM+Carina (*top*) and WLM+Sculptor (*bottom*) in red and blue respectively. *Right:* 1000 Monte-Carlo realisations of the CDF of Fornax in black and that of the corresponding combined dwarfs in magenta. The mean and 1-σ KS-test values are show in the bottom right corner.

To demonstrate the feasibility and support the premise of a past merger for Fornax, we show in Figure 4.16 the combined stellar metallicity CDF for two sets of galaxy pairs which satisfy the mass ratio requirements: WLM+Carina and WLM+Sculptor, in the top and bottom rows respectively. With stellar masses of $1.1{\times}10^7\,M_\odot$ (WLM; Jackson et al. 2007), $3.8{\times}10^5\,M_\odot$ (Carina; McConnachie 2012) and $2.3{\times}10^6\,M_\odot$ (Sculptor; McConnachie 2012), a merger between WLM+Carina and WLM+Sculptor would constitute a 1:5 and a 1:2 merger respectively if we consider the stellar-mass-halo-mass (SMHM) relation from Moster et al. (2010) at redshift zero.

We show the observed MDF of Fornax in grey in the left panel of Figure 4.16, and those of WLM and Carina in red and blue respectively. When computing the CDFs of each galaxy, we also take into account the measurement errors of

the metallicities of individual stars. We did a Monte-Carlo sampling with 1000 realisations, each time varying the metallicity of each stars within a gaussian distribution with width equal to the star's measurement error.

We construct the combined CDF of Carina and WLM by drawing N_1 and N_2 stars from the normalised CDFs of the two galaxies, where N_1 and N_2 are determined by the stellar mass ratio between the two galaxies and $N_{\rm tot} = N_1 + N_2$ is constrained by the total number of stars to be equal to the number of stars measured in Fornax. We again do a Monte-Carlo sampling with 1000 realisation, each time varying the total stellar mass within the measurement error, which we take to be 30% of the measured value.

The resultant 1000 realisations of the combined CDF is plotted in magenta and that of Fornax is plotted in black on the top-right panel of Figure 4.16. We next perform a Kolmogorov-Smirnov test between the combined WLM+Carina, and the Fornax metallicity CDFs for each realisation – deriving a KS-test value of $0.12^{+0.08}_{-0.04}$.

As a plausible representation of a dwarf-dwarf merger with mass ratio of 1:2, we compute a similar CDF of Sculptor and WLM as a comparison. We plot the MDF of Sculptor in blue on the bottom-left panel of Figure 4.16. We perform the same exercise as in WLM+Carina to obtain a combined CDF of Sculptor and WLM, with the Monte-Carlo realisations of the combined CDF shown in magenta on the bottom-right panel of Figure 4.16. The analysis of the simulated MDFs of these mergers show comparable K-S statistics within the uncertainties. Our exercise, while simple, gives independent support from empirical chemical properties that a merger with mass ratio anywhere between 1:5 to 1:2 could have happened in the past of Fornax, plausibly giving rise to its field star MDF.

4.4.3 Resolving the tension between the stellar mass in GCs and field stars in Fornax

In addition to a surprisingly large number of GCs, Fornax notably shows an extremely high fraction of mass in star clusters relative to low metallicity field stars (Larsen et al. 2012). This provides strong constraints on the amount of mass loss and initial mass of GCs, which is of extreme importance for the multiple population phenomena in GCs (c.f., Bastian 2017).

The top panel of Figure 14 shows the cumulative mass in the five GCs relative to field stars with metallicities lower than that ($M_{\rm GC}/M_{\star,\rm gal}$ <[Fe/H]). Here we have used the observed SFH of Fornax (corrected for spatial completeness) and the

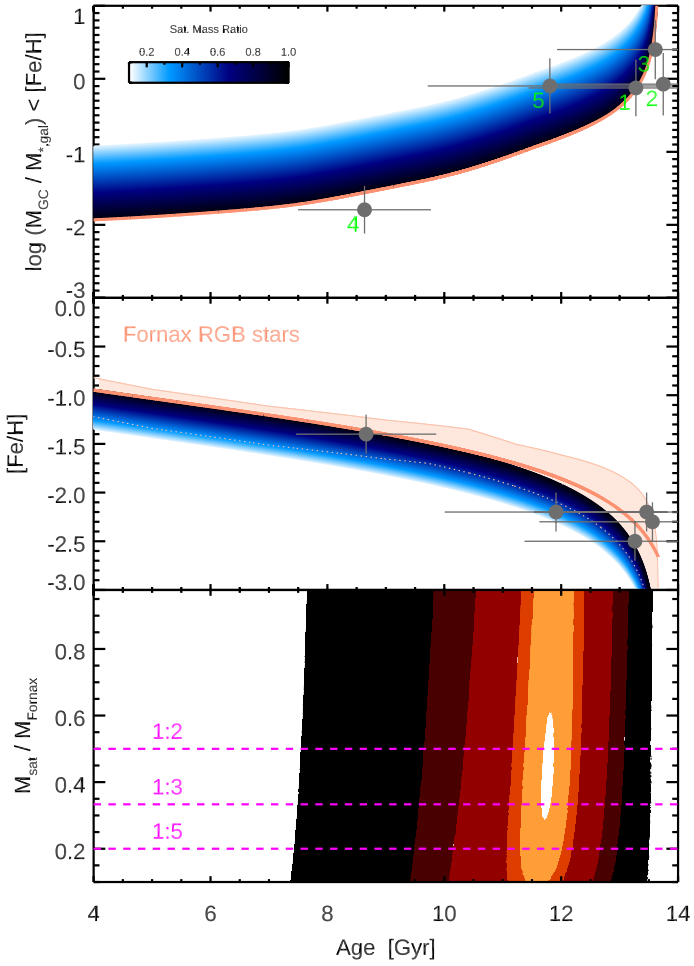

Figure 4.17: *Top:* the cumulative mass in GC stars (grey dots) relative to Fornax fields stars below that [Fe/H] value; Middle: observed age-metallicity relation of the RGB field stars in Fornax (orange). In the top and middle panel, the blue band represents the change in the plotted quantities for a dwarf of mass ratio η, ranging from 0 (light blue) to 1 (dark blue), which had a single GC. *Bottom:* The offset location of GC 5 in the top and middle panels suggests a required mass ratio close to the one derived from our dynamical model. The contours are in fractions of [0.1, 0.5, 0.7, 0.9,0.95,0.99] of the maximum likelihood.

observed mean Age-Metallicity relation (AMR) of the field stars (Battaglia et al. 2006; Leaman et al. 2013) to compute $M_\star$ as function of [Fe/H]. We plot this versus the age of the stellar populations (from the field star AMR) and the age of the GCs from isochrone fitting (de Boer & Fraser 2016). Larsen et al. (2012) computed the mass fraction based in GCs relative to field stars by analysing the MDF of the field stars directly and making corrections for sample selection and stellar evolution effects. Here we find comparable qualitative results when using the stellar mass growth for the galaxy itself derived from the SFH of Fornax and the spectroscopic AMR.

The orange line shows the values for a galaxy with the observed SFH and chemical enrichment who formed a single GC of $M_{GC} = 2 \times 10^5$ at any point in time. The blue lines show what values would be expected if you formed the same mass GC in a dwarf galaxy that was some stellar mass ratio $1:10 \leq \eta_* \leq 1:1$ less than Fornax. This is computed by simply shifting the AMR by an amount based on the observed Local Group mass metallicity relation (e.g. Kirby et al. 2013). It is clear that a dwarf with stellar mass $\sim 1/3$ of that of Fornax and a single GC would have values similar to where GC5 sits on this diagram.

Another way to compare the GC and field stellar population is by looking at their AMRs. In the middle panel of Figure 4.17 we show the observed AMR of the Fornax RGB stars as the orange band. The observed AMR closely follows a leaky box analytic chemical evolution model, and similar to the top panel, we show in blue the implied AMR for dwarf galaxies of smaller total stellar masses using the same shifted empirical mass-metallicity relations. As above, the corresponding observed ages and metallicities for the GCs are plotted in grey dots. Once again GC5 is an outlier with respect to the field stars' AMR, and corresponds more closely to the chemistry of a dwarf galaxy of mass $\sim$1/3 of Fornax.

The bottom panel shows a summary of the implied mass ratios which are more chemically consistent with GC5. Merger ratios of 1:2, 1:3 and 1:5 are marked by magenta dashed lines. The analysis here suggests that not only would a merger of mass ratio 1:2 to 1:5 allow GC5 to survive outside of it observed projected distance, but that it also relieve the tension between the mass and stellar populations in GC5 and those of the field stars in Fornax.

4.4.4 Additional evidence of dwarf-dwarf mergers

It has been shown in cosmological zoom-in simulations that group processing such as mergers of gas-rich dwarf irregulars (dIrrs) is a formation pathway for

gas-poor dSphs like Fornax (e.g. Wetzel et al. 2015). With cosmological simulations, Benítez-Llambay et al. (2016) show that such a process can explain the metallicity gradients found in dSphs, where young and concentrated metal-rich components are surrounded by older and metal-poorer stars, as seen in for example Sextans (Tolstoy et al. 2004; Battaglia et al. 2011), Sculptor (Battaglia et al. 2008), as well as Fornax (Battaglia et al. 2006). This is because the older and more metal-poor stars are dispersed by mergers, leading to a larger spatial distribution and lower central density as compared with the younger metal-rich population.

Observational evidence of dwarf-dwarf mergers is also becoming increasingly common. The TiNy Titans Survey (TNT) found evidence of interactions between isolated pairs of dwarf galaxies, such as disturbed optical and HI morphologies, as well as images of dwarf pairs on the verge of merging (Stierwalt et al. 2015). The Magellanic Clouds have been shown to host a rich satellite system in recent surveys, such as the Dark Energy Survey (DES; Bechtol et al. 2015; Koposov et al. 2015) and the Survey of the MAgellanic Stellar History (SMASH; Martin et al. 2015). These works suggest that dwarf galaxies can have satellites of their own that may later be assimilated. Amorisco et al. (2014) kinematically detected a stellar stream in the dSph Andromeda II (And II) of which the progenitor is possibly a dwarf galaxy with similar mass as And II, indicating a past major merger. Differential rotation between the metal-rich and metal-poor stars in the dSph Sculptor is also possibly a result of a past merger (Zhu et al. 2016). Cicuéndez & Battaglia (2018) also found merger evidences in the dSph Sextans, where a ring-like stellar feature shows higher-than-average line-of-sight velocities and lower-than-average metallicities, while Kacharov et al. (2017) found evidence of prolate rotation in the Phoenix dSph.

Specifically to Fornax, Amorisco & Evans (2012) (AE12 hereafter) suggest signatures of three stellar populations from its complex MDF, and show that there is a 40 difference in the rotation axes between the metal-poor (MP) and the intermediate-metallicity (IM) populations which imply counter-rotation. The authors have attributed such complexities to a merger of a bound pair, with the companion, represented by the MP population, comprising a fraction of 0.31 ± 0.06 of the spectroscopic sample of stars. Given the uncertainties on the complete spectroscopic selection function for Fornax, to compare to our work we bound the possible mass fraction of this population by: 1) multiplying this fraction directly with the total stellar mass of Fornax (likely an upper limit), or by 2) following AE12 and multiplying the observed luminosity of the RGBs in the MP population by 6[6] and then applying a mass-to-light ratio $M_\star/L$ of 2 (McConnachie 2012). This

[6]AE12 assume that 1/3 of the MP giants reside in the metal poorest tail and that the RGB

analysis yields a stellar mass of $3 \times 10^6 - 1.5 \times 10^7\,M_\odot$ for the MP population, which could comprise the lower mass merging fragment. Given the observed age-metallicity relation for Fornax, the pre-merger proto-Fornax is plausibly represented by the IM population, which comprises a fraction of 0.56 ± 0.05 of the spectroscopic sample. A similar computation for this population results in a proto-Fornax stellar mass $1 \times 10^7 - 2.5 \times 10^7\,M_\odot$. Our suggested candidates in Section 4.4.2; with Sculptor as the companion and WLM as proto-Fornax , have stellar masses of $7 \times 10^6\,M_\odot$ (Bermejo-Climent et al. 2018) and $0.9 - 1.8 \times 10^7\,M_\odot$ (Leaman et al. 2017) respectively at $z \sim 2$, falling right into the ranges suggested by the chemodynamical analysis of AE12. With a dynamical mass ratio of ∼1:3 at $z \sim 2$ (Leaman et al. 2017; Bermejo-Climent et al. 2018, and the references therein), the merger mass ratio of 1:2 to 1:5 inferred from our dynamical friction analysis is therefore consistent with the results from AE12. Given that Battaglia et al. (2006) can associate most of the more metal poor component with an old age of >10 Gyrs, it is therefore plausible that the merger fragment stopped forming stars at ∼10 Gyrs ago, indicating an early merger around that time for Fornax. While there is additional evidence for substructures in the central region of Fornax (Coleman et al. 2005), the young ages and high metallicities of these features, as pointed out by Amorisco & Evans (2012), necessitate that it formed from self-enriched gas of Fornax itself at late times, rather than due to an accretion event.

4.4.5 Implication for the nature of dark matter from the derived halo profile

The conditions for GC survival in Fornax require a particular form of the dark matter halo. Here we briefly discuss how this may place constraints on the self-interacting nature of dark matter. To provide a comparison of the required $(r_\mathrm{s}, r_\mathrm{c})$ with respect to dark matter halo parameters in ΛCDM cosmological simulations, we show the mass-concentration $(M - c)$ relation as seen in such simulations as a black contour in Figure 4.12 and 4.14. We adopt here the $M - c$ relation from Dutton & Macciò (2014). The concentration of our dark matter haloes are calculated as $c = r_{200}/r_{-2}$, where r_{-2} is the radius at which the logarithmic slope of the density profile equals -2. With a merger mass ratio of 1:2, GC1, GC2, GC3 and GC4 can all survive outside their respective d_p with a dark matter profile that lies on the $M - c$ relation, of $(r_\mathrm{s}, r_\mathrm{c})$∼(2000, 2000) pc.

We next check whether the required core size is compatible with dark matter

luminosities is 1/2 of the total luminosity.

cores created by baryonic feedback processes, such as those seen in ΛCDM hydrodynamical simulations of dwarf galaxies. As Read et al. (2016) have shown, the dark matter core size in their simulations is approximately 1.75 times of the half-light radius. In the case of Fornax, that would mean a $r_{\rm c}$ of 1260 pc. To check whether such core size would allow the GCs to survive outside of their $d_{\rm p}$, we rerun our orbital evolution model on a finer grid of $r_{\rm s}$, $r_{\rm c}$ in between 1000 pc and 2000 pc, in steps of 100 pc, with the inclusion of a stellar disk. We find that the minimum required ($r_{\rm s}$, $r_{\rm c}$) is (1600, 1500) pc in order for all GC1 to GC4 to survive outside of their $d_{\rm p}$. Such a core size is larger than expected from the coring of the dark matter halo due to baryonic feedback alone in the CDM scenario, given the feedback recipe in Read et al. (2016). Observationally, Bermejo-Climent et al. (2018) have shown that given the star-formation history of Fornax derived by de Boer et al. (2012), to produce such a large DM core from stellar feedback alone would imply that $\gtrsim 30\%$ of that energy is used in the coring of the DM halo, which is $\gtrsim$ two times the maximum fraction of energy from stellar feedback that can be coupled to the retained gas.[7] However given that the merger required for Fornax may also cause some expansion of the DM profile such DM core size might still be possible in the CDM scenario, and should be tested with simulations.

The halo profile constraints may have implications for non-standard DM particle theories as well. With respect to the ultra-light Bose-Einstein condensate dark matter (ψDM), our result can provide constraints on the dark matter particle mass. With cosmological simulations, Schive et al. (2014b) found that the core size of a ψDM halo ($r_{\rm c,\psi DM}$) should obey a scaling with the total halo mass $M_{\rm vir}$:

$$r_{\rm c,\psi DM} = 1.6\,{\rm kpc}\Big(\frac{M_{\rm vir}}{10^9 M_\odot}\Big)^{-1/3} m_{22}^{-1}, \tag{4.16}$$

where m_{22} is related to the dark matter particle mass $m_{\psi\rm DM}$ as:

$$m_{22} \equiv \frac{m_{\psi\rm DM}}{10^{-22}\,{\rm eV}/c^2}. \tag{4.17}$$

From the fitting to the observed $\sigma_\star(R)$, the derived $\rho_{\rm c}$ for a dark matter halo of ($r_{\rm s}$, $r_{\rm c}$) = (1700, 1500) pc is $0.03\,M_\odot\,{\rm pc}^{-3}$. The $M_{\rm vir}$ of such a profile is $2.93\times10^9\,M_\odot$[8].

[7]Note that when using the star-formation history (SFH) obtained by del Pino et al. (2013), Bermejo-Climent et al. (2018) derived a lower required energy fraction of $\sim 10\%$ for the creation of a DM core of size $\sim$1.5 kpc. Although this SFH comes from a deeper photometric data obtained using VLT/FORS (as compared to the CTIO/Mosaic II data used to derive the SFH in de Boer et al. (2012)), the spatial coverage is tiny.

[8]While the M_{200} of our dark matter halo is $3.24\times10^9\,M_\odot$, here we calculate the virial mass as $M_{\rm vir} = (4\pi/3r_{\rm vir}^3)\Delta_{\rm c}\rho_{\rm c}$ with $\rho_{\rm c}$ being the critical density and $\Delta_{\rm c} = 350$ following Schive et al. (2014b)

We have also fitted the derived cNFW density profile with that characterised for ψDM by Schive et al. (2014a) and obtained $r_{\mathrm{c},\psi\mathrm{DM}} \sim 1006\,\mathrm{pc}$[9]. Using Eq.4.16, we derive a m_{22} of ~ 1.1, which is within the constraint of $m_{22} = 0.26 - 2.5$ obtained from large-scale structures (e.g. Bozek et al. 2015; Sarkar et al. 2016). We note that, however, in the ψDM case, dynamical friction is suppressed by the wave nature of the dark matter particles (Hui et al. 2017) and hence our analysis is not directly applicable. With the suppressed dynamical friction, the required r_{c} is likely smaller and hence allows for a larger m_{22}. Our work hence still refines the complementary constraints from large-scale structures on m_{22}.

In the case of self-interacting dark matter (SIDM), the dark matter halo core size is correlated with the scattering cross-section σ as:

$$\frac{\langle \sigma v \rangle}{m_{\mathrm{SIDM}}} \rho(r_1) t_{\mathrm{age}} \sim 1, \tag{4.18}$$

where v and m_{SIDM} is the velocity between the DM particles and the mass of the DM particles, t_{age} is the age of the halo, and r_1 is the characteristic radius beyond which, the DM particles are scattered less than once per particle on average over t_{age} (Kaplinghat et al. 2016). The dark matter halo can be described by an NFW profile beyond r_1 and hence this characteristic radius would correspond to the core radius r_{c} in the cNFW profiles that we adopted. $\rho(r_{\mathrm{c}})$ of the profile with the minimum required (r_{s}, r_{c}) of (1600, 1500) pc is $0.0095\,M_{\odot}\,\mathrm{pc}^{-3}$, corresponding to a $\frac{\langle \sigma v \rangle}{m_{\mathrm{SIDM}}}$ of $\sim 36\,(\mathrm{cm}^2/\mathrm{g} \times \mathrm{km/s})$. Our derived value for Fornax is comparable to other dwarfs or low-surface brightness galaxies in Kaplinghat et al. (2016).

4.4.6 Caveats

In attempting to incorporate several evolutionary aspects of Fornax in one model, there will necessarily be caveats and simplifications. We outline these here, and hope this work motivates future studies to produce idealised numerical simulations which can test this scenario. When estimating the d_{form} of the GCs, we assume a well ordered, exponential disk, while the current structure is much more of a thick oblate blob of stars. Although such a structure could have resulted from the past merger event, in the case where the structure of the stellar component was

[9]The ψDM density profile is characterised by an inner soliton that transit abruptly to an outer NFW halo. When fitting our derived DM density profile with that of ψDM, we have fixed the transition radius to be $3\,r_{\mathrm{c},\psi\mathrm{DM}}$, a cosmic average found by Schive et al. (2014a). Our derived $r_{\mathrm{c},\psi\mathrm{DM}}$ is comparable with their derived value of $r_{\mathrm{c},\psi\mathrm{DM}} = 920^{+150}_{-110}\,\mathrm{pc}$, found by using the velocity dispersion from three different stellar population in Fornax.

already puffy when the GCs are formed, we would have overestimated the maximum galactocentric distance at which the GCs can be formed. This is because given the same scale radius and mass, a thicker disc would render a lower density at each specific location. A smaller $d_{\rm form}$ would only increase the required $(r_{\rm s}, r_{\rm c})$ in order for the GCs to survive outside of its present-day $d_{\rm p}$ and hence our derived dark matter parameters would still serve as a lower-bound as intended.

Although the underlying dark matter profile is expected to vary due to cosmological halo growth, within the timescales (after the first Gyr since the beginning of the universe) and radial range ($d_{\rm form} < 2000\,{\rm pc}$) relevant for the orbital decay of the GCs, the change of dark matter profile under cosmological halo growth has a negligible impact for our orbit calculations when we tested orbit integration in a growing potential.

Baryonic feedback can additionally cause the coring of the dark matter profile, and lead to the expansion of the GCs' orbit in additional ways. Just like dark matter particles, the GCs gain energy indirectly from stellar feedback ejecting gas in the inner regions of the galaxy and rapidly altering the potential. The repetitive deposition of such energy and subsequent ejection of gas leads to an irreversible non-adiabatic heating of the orbits of the particle in the potential (Pontzen & Governato 2012). While Pontzen & Governato (2012) provide analytic expressions for how the overall spatial scale of a system of (e.g. dark matter) particles would be altered given an amount of energy, the effect on an individual particle (e.g. a GC) by such deposition of energy is not well understood and hence not included in our model. Secondly, the GCs would move outwards due to the gradual (rather than instantaneous) shallowing of the gravitational potential. The resultant position of GCs in a coring profile would still lie between the final position under an NFW and a cored profile of the same $r_{\rm s}$ and $r_{\rm c}$, with that from the cored profile giving an upper bound. The exact position would depend on the timescale for core creation. Since we do not possess information on the timescale at which the dark matter halo change from a cuspy to a cored profile, we only consider the completely cored ($n = 1$) cases to obtain an upper limit of the final GCs positions for each set of dark matter parameters $(r_{\rm s}, r_{\rm c})$.

Lastly, we have also considered a spherical system where both the geometry of the gravitational potential as well as the velocity anisotropy is isotropic. How axisymmetric or triaxial potentials with anisotropic velocity dispersions would affect our result is beyond the scope of this work.

4.5 Conclusions

We present an analysis on how the present day location of the five globular clusters in the dwarf spheroidal galaxy Fornax provides constraints on its dark matter halo profile. In particular, we incorporate a careful consideration on the formation location of the GCs based on pressure equilibrium arguments, and allow for orbital expansion due to a past merger. We also consider the effect of dynamical buoyancy by including the effect of fast-moving background particles in our dynamical friction treatment, and adopt a velocity distribution function computed self-consistently from each gravitational potential using the Eddington equation (instead of the commonly adopted assumption of a Maxwellian distribution). With these ingredients we study the orbital decay of Fornax's five GCs in a self-consistent framework with their co-evolution of the dynamics and chemistry of the host galaxy. Our main findings from this joint analysis are as follows:

1. Our joint analysis shows that survival of three of the GCs (1, 2, 3) in Fornax is possible for halo profiles with minimum scale and core radii of 1700 and 1500 pc respectively - provided that Fornax has had a merger of mass ratio ($1{:}5 \leq \eta \leq 1{:}2$) in its past. The younger GC4 can survive in any halo profile provided the same merger occurs, we suggest it may have been triggered during the merger ($\sim$10 Gyrs ago).

2. GC5 can not survive in a halo unless there is a core radii larger than 6 kpc (3 times the tidal radius). As stellar feedback based mechanisms for core creation can not produce a change outside the tidal radius, we posit that GC5 could have been brought in with the merging galaxy to the Fornax host.

3. Consistent with this, we show that GC5 is unique among the five GCs in that it lies off the Fornax field star age-metallicity relation, with a lower metallicity at fixed age, suggestive of being born in a galaxy with 1/3 the mass of Fornax.

4. This is also supported by empirical chemical evolution arguments. The MDF of Fornax's fields stars are shown to be consistently reproduced by a weighted super-position of pairs of Local Group dwarfs with the necessary mass ratio.

5. This merger origin for the evolution and survival of Fornax and its GCs reconciles the large number of GCs within Fornax, and alleviates the problem of Fornax having an extremely high mass in GC stars relative to metal poor field stars, as well as its high specific globular cluster frequency of $S_N = 29$ (van den Bergh 1998).

6. We have compared the required dark matter core size with several dark matter models and find that a dark matter core of 1600 pc is larger than that expected from baryonic feedback alone in the CDM paradigm. Even though we did not incorporate the wave nature of ψDM in our dynamical friction model, our derived particle mass of m_{22} $\sim$0.7 is still marginally consistent with the lower limit from large-scale structure constraints. Lastly, we find a scattering cross-section of $\frac{\langle\sigma v\rangle}{m_{\rm SIDM}}$ of $\sim 55\,({\rm cm}^2/{\rm g}\times{\rm km/s})$ for SIDM, consistent with values obtained for other dwarf and low-surface brightness galaxies in the literature.

This scenario, whereby Fornax and its GC populations were assembled by merging dwarfs (with 1 GC coming in through the merger, 1 formed during the merger and three pre-exisiting in the proto-Fornax) can be tested with high resolution idealised simulations, and may provide constraints on how common this mechanism is for dwarfs in a cosmological framework.

Acknowledgments

We would like to thank Else Starkenburg, Chris Brook, Arianna di Cintio for useful discussions which helped improve this manuscript. RL was supported by funding from the Natural Sciences and Engineering Research Council of Canada PDF award, and this work was supported by Sonderforschungsbereich SFB 881 "The Milky Way System" (subproject A7 and A8) of the Deutsche Forschungsgemeinschaft (DFG), and DAAD PPP project number 57316058 "Finding and exploiting accreted star clusters in the Milky Way". GL and GvdV acknowledge support from the German Academic Exchange Service (DAAD) under PPP project ID 57319730. GvdV acknowledges funding from the European Research Council (ERC) under the European Union's Horizon 2020 research and innovation programme under grant agreement No 724857 (Consolidator Grant ArcheoDyn). G.B. gratefully acknowledges financial support from the Spanish Ministry of Economy and Competitiveness (MINECO) under the Ramon y Cajal Programme (RYC-2012-11537) and the grant AYA2017-89076-P.

Chapter 5

Understanding the sources of ionised gas velocity dispersion

5.1 Introduction

Hα gas in galaxies, both locally and at high redshift, can show velocity dispersions of the order of $\sim 30 - 200\,\mathrm{km\,s^{-1}}$ (e.g. Weijmans et al. 2008; Kassin et al. 2012). This velocity dispersion is driven by a combination of thermal, turbulent (including for example, shocks from supernova and stellar winds) and gravitational effects, such that $\sigma^2_{\mathrm{tot}} = \sigma^2_{\mathrm{thermal}} + \sigma^2_{\mathrm{turb}} + \sigma^2_{\mathrm{grav}}$. The thermal contribution can be estimated trivially given the ionised gas temperature with $\sigma^2_{\mathrm{thermal}} = kT/m$ (where k is the Boltzmann constant, T the gas temperature and m the gas particle mass) and are typically only $\sim 10\,\mathrm{km\,s^{-1}}$. It is currently unknown whether the observed large σ_{tot} is dominated by σ_{turb} or σ_{grav}, as it is not a priori possible to decompose the ratio of these two sources from ionised gas observations. Understanding this balance of $\sigma_{\mathrm{grav}}/\sigma_{\mathrm{turb}}$ as a function of star formation rate (SFR), gas fraction (f_{gas}) or stellar mass ($M_\star$) is of the utmost importance for interpreting the growth of galaxy disks at high redshift (e.g. Wisnioski et al. 2015).

In addition, galaxy formation simulations typically require energetic feedback from stellar winds and supernovae to produce realistic galaxies (e.g. Dalla Vecchia & Schaye 2012; Zolotov et al. 2012; Di Cintio et al. 2014). However, the coupling of the feedback energy to the gas is typically implemented in an ad hoc sub-grid manner (e.g., various prescriptions for thermal or kinetic energy, how they are distributed and over what timescales from a star particle). Therefore characterising the fraction of σ_{tot} that is due to σ_{turb} would represent a crucial constraint for simulations of

galaxy formation and evolution.

Understanding the source of velocity dispersion in ionised gas is also important for galaxy dynamics. For example, when deriving a galaxy's enclosed mass from its Hα kinematics, we need to compute the circular velocity, defined as $V_{\rm c} \equiv -R(d\Phi/dR)$, where Φ is the gravitational potential. When the ratio of rotation velocity to gravitational velocity dispersion ($V_\phi/\sigma_{\rm grav}$) is small, a correction must be made (using $\sigma_{\rm grav}$) to infer the $V_{\rm c}$ value it would have if the orbital energy were purely rotational. Understanding how much of the observed velocity dispersion is due to gravitational perturbations, is therefore crucial in getting an accurate measure of the enclosed mass using Hα kinematics. Hα is typically used for high-z galaxies due to the lack of alternative/better observations from kinematic tracers such as cold gas and/or stars. As $V_\phi/\sigma_{\rm grav}$ is expected to be smaller for galaxies of higher redshifts, such correction becomes especially important. The common approach of assuming $\sigma_{\rm grav,H\alpha} = \sigma_{\rm tot,H\alpha}$ or $\sigma_{\rm grav,H\alpha} = 0$ in the derivation of $V_{\rm c,H\alpha}$ respectively over- and underestimates the enclosed mass.

These incomplete assumptions can both lead to significant changes in the implied astrophysical interpretation. Understanding the balance of $\sigma_{\rm grav}/\sigma_{\rm turb}$ using nearby galaxies is therefore an essential calibration for obtaining accurate mass profiles for high-z galaxies. In particular, accessing how the intrinsic ratio of $\sigma_{\rm grav}/\sigma_{\rm turb}$ systematically varies with global parameters such as the star formation rate (SFR), disk scale height (h_z), or gas fraction (f_{gas}), would provide an extremely useful set of prescriptions to analyse other galaxies where detailed observations are not possible.

The decomposition of Hα velocity dispersion ($\sigma_{\rm H\alpha}$) into its contributing sources can be done if one has circular velocity measurements from other independent kinematic tracers such as stars and molecular gas. Such calibration is possible for nearby galaxies which can be observed kinematically through multiple tracers. Stellar kinematics are not affected by turbulent or thermal effects, meaning that its velocity dispersion is solely contributed by the gravitational component, and so one can recover $V_{\rm c,*}$ by directly applying stellar dynamical models such as the asymmetric drift correction (ADC, Weijmans et al. 2008), axisymmetric Jeans dynamical models (JAM, Cappellari 2008), and Schwarzschild models (Schwarzschild 1979) onto the observed velocity moments (see Chapter 2). Since the stars and the Hα gas of each galaxy are moving through the same gravitational potential, the derived circular velocities obtained using stellar or Hα kinematics should agree. Therefore once the circular velocity is determined from the stellar or molecular data, the Hα velocity dispersion can be decomposed as follows: First, from the observed Hα dispersion, subtract off the contribution from the thermal contribution ($\sigma_{\rm thermal} \sim 10\,{\rm km\,s^{-1}}$).

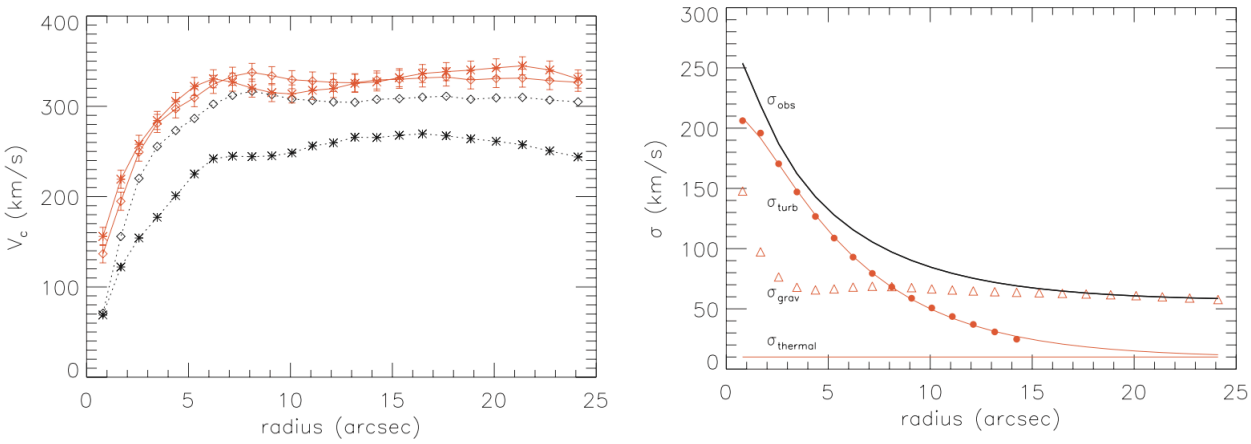

Figure 5.1: The panel on the left shows the rotational velocities in black and the asymmetric drift corrected V_c in orange. The asymmetric drift correction is assumed to be constant for Hα with the value taken to be $\sim 120\,\mathrm{km\,s^{-1}}$ (asymptotic value at large radius). The panel on the right shows the decomposition of $_{\mathrm{H}\alpha}$. (Figure from Weijmans et al. (2008))

The remaining velocity dispersion is some mixture of the turbulent and gravitational components. Only the gravitational component goes into the asymmetric drift correction to the Hα rotation velocity. Thus one can ask what fraction of the remaining Hα dispersion is needed in order for the ADC to produce the V_c given by the independent stellar tracer. This exercise of using an external kinematic tracer to set V_c, allows one to decompose the sources of the Hα dispersion into turbulent and gravitational.

Such a decomposition has been done on only one galaxy so far. Using both the SAURON stellar and Hα observations, Weijmans et al. (2008) decomposed the Hα dispersion of NGC2974. As shown in Figure 5.1 left panel, the Hα rotation curve ($V_{\phi,\mathrm{H}\alpha}$, black open diamonds) is below the circular velocity derived from stellar kinematics ($V_{c,\star}$, orange crosses). This difference can only be due to random non-circular motions providing additional support to the gas in the gravitational potential, and is proportional to $\sigma_{\mathrm{grav,H}\alpha}$. By subtracting this best fitting $\sigma_{\mathrm{grav,H}\alpha}$ contribution,which recovers the circular velocity, and $\sigma_{\mathrm{thermal}}$ in quadrature from $\sigma_{\mathrm{tot,H}\alpha}$, they could obtain the contribution to the total velocity dispersion from turbulent sources, $\sigma_{\mathrm{turb,H}\alpha}$ – which turned out to follow an exponential profile (Figure 5.1, right panel). Although for NGC 2947 the ADC is radially constant and $\sigma_{\mathrm{turb,H}\alpha}$ shows a neat exponential profile, this result of a single galaxy can not be extended to the generic galaxy population.

Motivated by this, we identified galaxies within our EDGE-CALIFA dataset

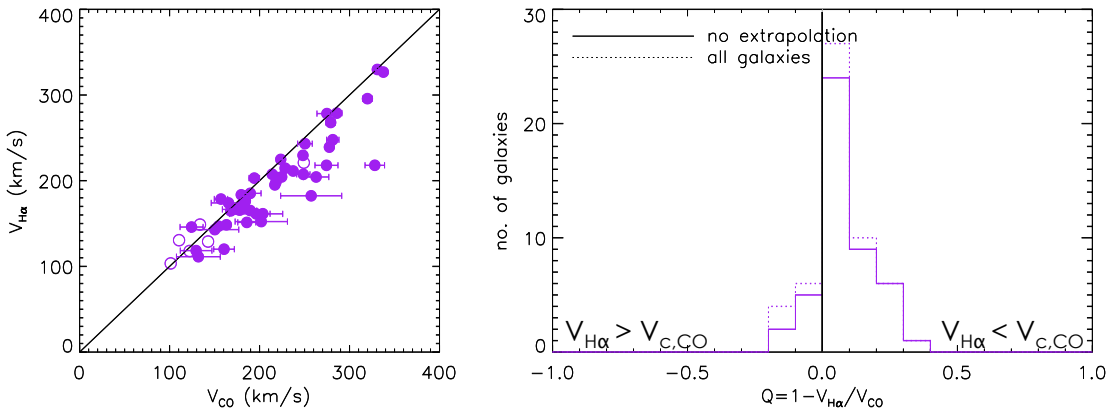

Figure 5.2: Comparison between the $V_{\phi,\mathrm{H}\alpha}$ and $V_{\mathrm{c,CO}}$ at $1\,R_{\mathrm{e}}$ similar to Figure 2.9. *Left:* $V_{\phi,\mathrm{H}\alpha}$ plotted against $V_{\mathrm{c,CO}}$, with the black line indicating the one-to-one line. *Right:* The relative difference, $Q_{H\alpha}$. The black vertical lines indicate $Q = 0$, to which most of the galaxies lie on the right, meaning that there is a bias towards $V_{\mathrm{H}\alpha} < V_{\mathrm{c,CO}}$.

which might have high velocity dispersions in their ionised gas components. From the sample of 54 EDGE-CALIFA galaxies we examined in Chapter 2, we find similarly that $V_{\phi,\mathrm{H}\alpha}$ (derived in the same way as with $V_{\mathrm{c,CO}}$ through harmonic decomposition as described in §2.3) tend to lie below the circular velocities derived from both CO ($V_{\mathrm{c,CO}}$) and stellar kinematics ($V_{\star}$). When compared at $1\,R_e$, $V_{\phi,\mathrm{H}\alpha}$ is systematically lower than $V_{\mathrm{c,CO}}$ on average by $\sim 10\%$. In Figure 5.2, we show comparison plots between $V_{\phi,\mathrm{H}\alpha}$ and $V_{\mathrm{c,CO}}$ at $R = R_e$, similar to the ones between $V_{\mathrm{c},\star}$ and $V_{\mathrm{c,CO}}$ as shown in Figure 2.9. Such a bias towards $V_{\mathrm{H}\alpha} < V_{\mathrm{c,CO}}$ is evidence of the contribution of $\sigma_{\mathrm{grav,H}\alpha}$ in providing orbital support. Given the morphology, SFR and mass diversity in the CALIFA parent sample, our data set provides a large sample of galaxies to study the physical origin of the ionised gas velocity dispersion.

Unfortunately a similar exercise as done for NGC2947 is not possible with the CALIFA data alone in our galaxies. Although CALIFA also provide kinematic measurements in Hα, the spectral resolution of the instrument of R$\sim$850 ($\sim 140\,\mathrm{km\,s^{-1}}$) is too low for decomposing the Hα velocity dispersion.

Instead, Hα kinematics of a selected subset of the CALIFA galaxies may be analysed with a higher spectral resolution instrument – for example a Fabry-Perot spectro-imager. With a spectral resolution of R=250,000 (a few $\mathrm{km\,s^{-1}}$), Fabry-Perot instruments can provide sufficient precision in measurements of both the mean velocity and velocity dispersion that are seeing-limited, and cover a wide field of

view. The large sample of CALIFA galaxies, when complimented by the Fabry-Perot Hα measurements, will provide the optimal data set to understand the relative contribution of turbulent support in ionised gas, and how it depends on the star forming and gas content of the host galaxies.

We have, as a pilot project, obtained Hα kinematics for four galaxies from the CALIFA sample using the Fabry-Perot instrument GHαFas from the William Herschel Telescope. In this work, we present the decomposition of $\sigma_{\mathrm{H}\alpha}$ of four of the observed galaxies and is laid out as the following: in §5.2 we explain how a Fabry-Perot spectrometer works, the details of the observations, as well as show the data we obtained. In §5.3, we explain in details how we decompose $\sigma_{\mathrm{H}\alpha}$. We present the results and limitation to our current methodologies in §5.4. We summarise and present possible ways forward in §5.5.

5.2 Data and Observations

Our selected galaxies are drawn from a sample of 300 CALIFA galaxies across the Hubble sequence. These galaxies have high-quality stellar kinematics from which we have already derived $V_{\mathrm{c},\star}$ (using methods as described in §2). We then select galaxies by their expected relative contribution of turbulent and gravitational dispersion to the total ionised gas velocity dispersion budget. This was done following analytic arguments which suggest $\sigma_{\mathrm{grav}} \sim V_c \times f_{\mathrm{gas}}$ and $\sigma_{\mathrm{SN}} \sim \mathrm{SFR}^{1/3}$ (c.f. Krumholz & Burkert 2010; Wisnioski et al. 2015). In order to get enough signal to noise from the observations, we had to consider only galaxies with an Hα flux $\mathrm{F}_{\mathrm{H}\alpha} > 7 \times 10^{-13}\,\mathrm{erg\,s^{-1}\,cm^{-2}}$. This gave a sample of 12 galaxies which we planned to observe and submitted an observing proposal for. While six nights were granted, the bad weather on a few of the nights reduced our sample to six galaxies. The observed galaxies cover stellar masses of $10^{9.8} \leq M_\star/M_\odot \leq 10^{10.2}$, star formation rates of $-0.2 \leq \log \mathrm{SFR}\ (M_\odot\,\mathrm{yr}^{-1}) \leq 0.6$ and gas fractions of $0.01 \leq f_{gas} \leq 0.08$. We list in Table 5.1 the four observed galaxies which had sufficient observed Hα flux to analyse, with their relevant parameters.

5.2.1 Fabry-Perot Spectrometer

The observations were carried out on the William Herschel 4.2m Telescope (WHT) at Observatorio del Roque de los Muchachos on La Palma in March 6-9, 13-16 2017. To achieve the required velocity resolution in order to observe $\sigma_{\mathrm{H}\alpha}$, we utilised the Fabry-Perot Instrument at the Nasmyth focus of WHT: the Galaxy Hα Fabry-Perot

galaxy	$\log M_\star/M_\odot$	$\log \mathrm{SFR}\ (M_\odot\,\mathrm{yr}^{-1})$	f_{gas}	Type
IC11151	9.82±0.10	-0.20±0.06	0.01	Scd
NGC3811	10.44±0.11	0.35±0.07	0.07	Sbc
NGC5056	10.64±0.09	0.57±0.06	0.06	Sc
UGC09476	10.23±0.11	0.05±0.06	0.08	Sbc

Table 5.1:: The galaxy sample. Stellar mass ($\log M_\star/M_\odot$), star formation rate (SFR) and gas fraction (f_{gas}) are taken from Bolatto et al. (2017).

Spectrometer (GHαFas). GHαFas provides a FOV of $3.4' \times 3.4'$, with seeing limited spatial resolution. This is one of the only instruments in the world with the large enough field of view and spectral resolution to do this kind of analysis.

A Fabry-Perot etalon consists of two parallel reflecting surfaces, the distance between which (Δd) can be controlled through the supplied voltage. As parallel light shines through, the Fabry-Perot etalon produces ring-like spatial interference pattern such that at each particular Δd, each ring on the sky correspond to a particular wavelength. The correspondence between Δd and the observed wavelength at each ring can be calibrated through emission of known wavelength. At GHαFas, this is done with a neon lamp with Ne [6598] emission.

The etalon at GHαFas operates at the interference order of 765, which gives a Free Spectral Range (FSR) of ~ 8 Å, depending on the central wavelength of the particular observation session. Filters are applied according to each galaxy's redshift to allow measurements of the Hα emission in galaxies with high spectral resolution across their entire extent. We list the FSR for observations of each galaxy in Table 5.2. Throughout an observation, the etalon then steps through different Δd, allowing each ring to be observed at different wavelengths throughout the FSR. In our observations, the etalon steps through 64 different Δd at each cycle, allowing a velocity resolution Δv of ≥ 6.2 km/s. Each step has an exposure time of 10 seconds and we observed our galaxies at a minimum of 16 cycles (∼3 hours). The photons are then collected by an image photon-counting system (IPCS) camera with $0.2''$/pixel resolution. This yields a set of channel maps showing the flux across the field of view at each wavelength interval. The advantage of the Fabry-Perot spectro-imager is much higher spectral resolution, over a large field of view compared to optical spectrographs. The total exposure time and the velocity resolution of each of the observed galaxies are listed also in Table 5.2.

galaxy	$t_{\rm exp}$(hh:mm:ss)	seeing ($''$)	FSR (Å)	Δv (km/s)
IC11151	02:50:40	$2.0''$	8.69	6.20
NGC3811	03:12:00	$2.0''$	8.73	6.24
NGC5056	03:01:20	$1.3''$	8.88	6.34
UGC09476	03:22:40	$1.5''$	8.75	6.24

Table 5.2:: Details of the observation of each galaxy. *From left to right:* Integrated exposure time, seeing, full spectral range (FSR) in wavelengths and channel width in velocities.

5.2.2 Data reduction

Before each observation session, we measure the spatial-spectral correlation of the GHαFas instrument using a neon lamp. The corresponding calibration map is then input into the data reduction pipeline to assign each of the 64 steps into a wavelength at a particular spatial location. Since no de-rotator is available for GHαFas, the whole image cube needs to be de-rotated after the observations. This spatial de-rotation needs to be done simultaneously with the wavelength calibration due to the interlinked nature between the spatial and spectral dimensions of a Fabry-Perot Spectrometer. The de-rotation is done through tracking the position of bright stars or compact Hα regions in the FOV. The wavelength calibration and the de-rotation together then allow us to transfer the raw data into a cube with two spatial dimension and one velocity dimension.

We then apply smoothing both spatially and spectrally. The spatial smoothing is done with a two-dimensional Gaussian with a width of 3 pixels and the spectral smoothing is done with a Gaussian with a width of 1 channel. To obtain the moment maps, we then fit a Gaussian to the line-of-sight velocity distribution (LOSVD) at each pixel. The fitted continuum is taken as the sky emission and its square-root is taken as the root-mean-square noise. From the Gaussian fit to the LOSVD at each pixel, we obtain the (sky-subtracted) amplitude, mean velocity and velocity dispersion of the Hα emission at each pixel. We clip away pixels from the moment maps which have a fitted-amplitude-to-noise ratio <5. The resultant maps are shown in Figure 5.3.

5.3 Decomposing the ionised gas velocity dispersion

As described in §5.1, the ionised gas velocity dispersion we measure ($\sigma_{H\alpha}$) can be decomposed through comparison between Hα rotation curve $V_{\phi,\mathrm{H}\alpha}$, and an independent measurement of the circular velocity, V_c. Since not all the galaxies in our sample have well-observed CO kinematics (which provide a useful proxy for the circular velocity), we employ the circular velocities derived from stellar kinematics using Schwarzschild models of the CALIFA galaxies (Zhu et al. 2018b,a). The V_c of each galaxies is plotted in dashed lines in the bottom right panels of Figure 5.3. $V_{\phi,\mathrm{H}\alpha}$ is derived from the GHαFas mean velocity maps using the ellipse fitting and harmonic decomposition procedure as described in §2.3.2. When fitting for the rotation curves, we adopt the same inclination and position angle as adopted in the Schwarzschild models. The modelled velocity maps and the derived $V_{\phi,\mathrm{H}\alpha}$ (grey diamonds) are shown in the bottom panels in Figure 5.3. In purple diamonds we overlay the $V_{\phi,\mathrm{H}\alpha}$ derived from the CALIFA data. Except for NGC3811, the $V_{\phi,\mathrm{H}\alpha}$ derived from GHαFas and CALIFA agree well with one another, indicating that no biases in our measured Hα kinematic maps on large scales. The differences between the two in NGC3811 may be caused by the patchy nature of the emission, which has been smoothed over to fill the whole FOV in the CALIFA data (a similar discrepancy is see also in the inner region of NGC5056, where there is an inner hole to the Hα emission).

Next, we derive the contribution to the velocity dispersion from gravitational perturbations (σ_grav), using the asymmetric drift correction (Weijmans et al. 2008):

$$V_\mathrm{c}^2(R) = \overline{V_\phi}^2 - \sigma_\mathrm{grav,R}^2\Big[\frac{\partial \ln \nu}{\partial \ln R} + \frac{\partial \ln \sigma_\mathrm{grav,R}^2}{\partial \ln R} + 1 - \frac{\sigma_\mathrm{grav,\phi}^2}{\sigma_\mathrm{grav,R}^2} + \frac{R}{\sigma_\mathrm{grav,R}^2}\frac{\partial \overline{V_R V_\mathrm{z}}}{\partial z}\Big], \quad (5.1)$$

where ν is the surface density of the Hα emission, V_ϕ is the Hα rotation curve and $\sigma_\mathrm{grav,R}$ and $\sigma_\mathrm{grav,\phi}$ are the radial and azimuthal components of the gravitational velocity dispersion of Hα in the cylindrical coordinates. For the tracer flux density ν, we take the integrated Hα flux and compute a radial profile of this along the galaxy's major axis, sampled at each ellipse (from which we fitted for $V_{\phi,\mathrm{H}\alpha}$). The integrated flux map and the derived ν profiles (in grey diamonds) are shown on the top panels of Figure 5.3. To avoid numerical effects due to the data stochasticity, we parameterise the profiles with an exponential and a power-law profile to ν and $V_{\phi,\mathrm{H}\alpha}$ respectively, such that:

$$\nu = \nu_0 \exp\Big(-\frac{R}{R_0}\Big) + \nu_\infty \quad (5.2)$$

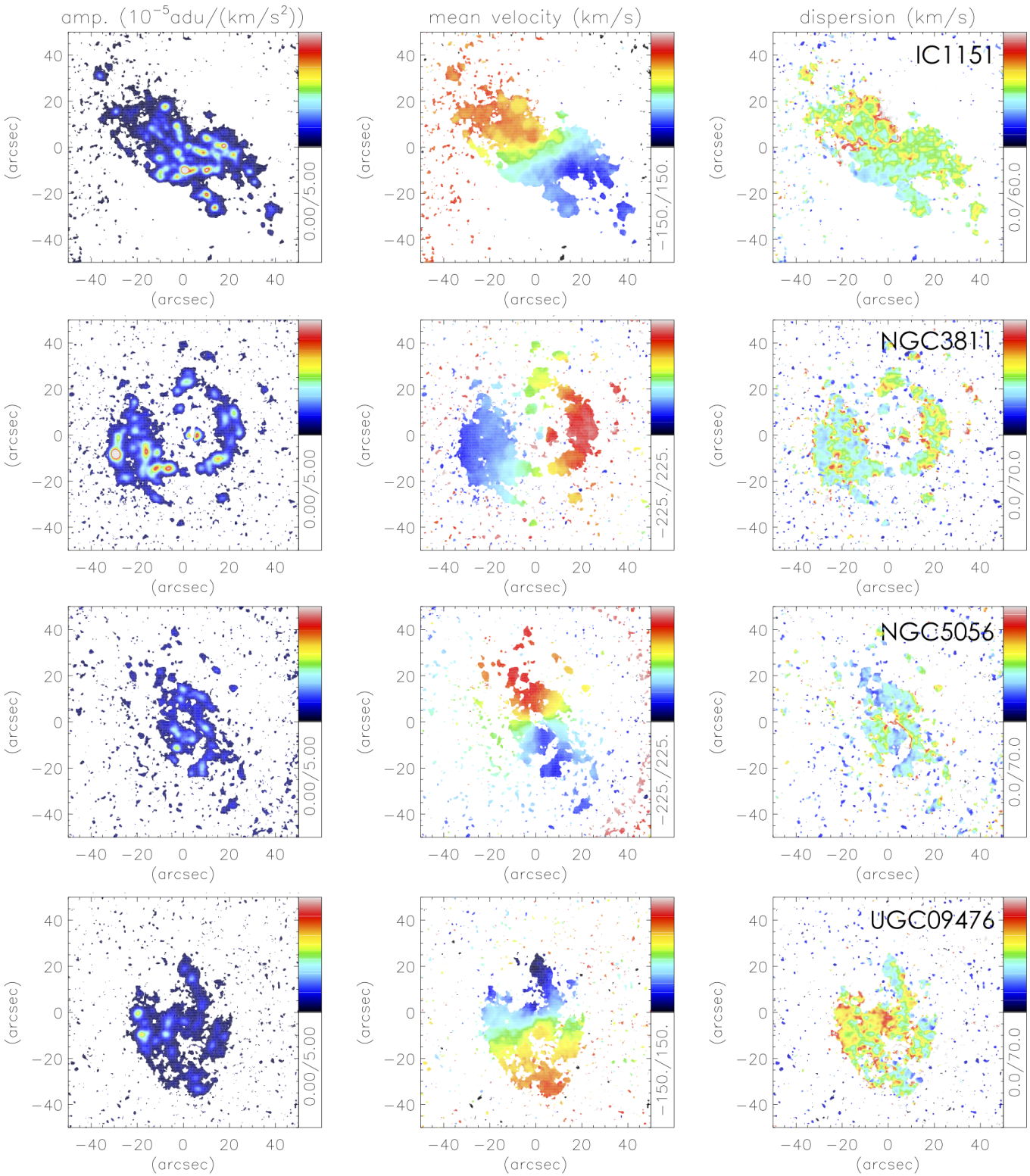

Figure 5.3: Ionised gas moment maps. *From left to right:* amplitude, mean velocity and velocity dispersion of the four galaxies in our sample. The scale of the colour-coding is shown on the right of each image.

and

$$V_{\phi,\mathrm{H}\alpha} = V_0 \frac{R}{(R_c^2 + R^2)^{0.5+0.25\alpha}}, \tag{5.3}$$

with ν_0, R_0, ν_∞, V_0, R_c and α being the free parameters. The fitted profiles are shown in black curves in the right panels of Figure 5.3. We exclude some of the inner ellipses from NGC3811 and NGC5056 due to their patchiness in the center. NGC5056 is furthermore problematic, as the derived $V_{\phi,\mathrm{H}\alpha}$ is very eratic with some of the ellipses having $V_{\phi,\mathrm{H}\alpha}$ even higher than V_c. We still include it here as a reference, using only ellipses that have $V_{\phi,\mathrm{H}\alpha} < V_\mathrm{c}$. We note that there is no physical reason why the turbulent component could not inject enough energy to make $V_{\phi,\mathrm{H}\alpha} > V_\mathrm{c}$ prior to the decomposition. In such cases (perhaps relevant for low mass dwarf galaxies) this exercise would only provide a limit on the ratio of $\sigma_\mathrm{grav}/\sigma_\mathrm{turb}$.The ellipses that are used for fitting are marked with black diamonds. The fits to the the CALIFA $V_{\phi,\mathrm{H}\alpha}$, using the form in Equation 5.3, are shown with purple curves.

With these parametrisation of ν and $V_{\phi,\mathrm{H}\alpha}$, Eq. 5.1 can then be inverted and solved analytically to obtain the contribution to the observed ionised gas dispersion from gravitational sources (along the radial axis R) $\sigma_\mathrm{grav,R}$:

$$\begin{aligned} u(R) &= \int \Big(\frac{1}{R}\frac{\mathrm{d}\ln\nu}{\mathrm{d}\ln R} + \beta_\phi + \kappa\beta_z\Big)\mathrm{d}R, \\ \sigma^2_\mathrm{grav,R} &= -\frac{1}{\exp(u(R))}\int \frac{1}{R}\exp(u(R))(V_\mathrm{c}^2 - V^2_{\phi,\mathrm{H}\alpha})\mathrm{d}R, \end{aligned} \tag{5.4}$$

where β_ϕ, β_z and κ are free parameters that describe the velocity anisotropy of the ionised gas ($\beta_\phi = 1 - \sigma^2_{\mathrm{grav},\phi}/\sigma^2_\mathrm{grav,R}$, $\beta_z = 1 - \sigma^2_\mathrm{grav,z}/\sigma^2_\mathrm{grav,R}$) and the alignment with respect to the cylindrical coordinates such that (Eq. A4 of Weijmans et al. 2008):

$$\overline{V_R V_\mathrm{z}} = \kappa(\sigma^2_\mathrm{grav,R} - \sigma^2_\mathrm{grav,z})\frac{z/R}{1-(z/R)^2}. \tag{5.5}$$

$\kappa = 0$ describes a cylindrically aligned system and $\kappa = 1$ describes a spherically aligned system and $0 \leq \kappa \leq 1$. The integrals are then closed by requiring $\sigma_\mathrm{grav,R}$ to vanish at infinity. The total velocity dispersion σ_tot can be obtained by deprojecting the observed σ_Ha (when deprojecting we assumed that the velocity anisotropy is the same for the gravitational dispersion and the total dispersion), which then gives us the ratio of gravitational to total velocity dispersion $\sigma_\mathrm{grav}/\sigma_\mathrm{tot}$.

5.4 Results

We perform the $\sigma_{\mathrm{H}\alpha}$ decomposition as described above in a grid of $-1.0 \leq \beta_\phi \leq 1.0$, $-1.0 \leq \beta_z \leq 1.0$ and $0 \leq \kappa \leq 1$, all in steps of 0.5. We show in Figure 5.4, 5.5

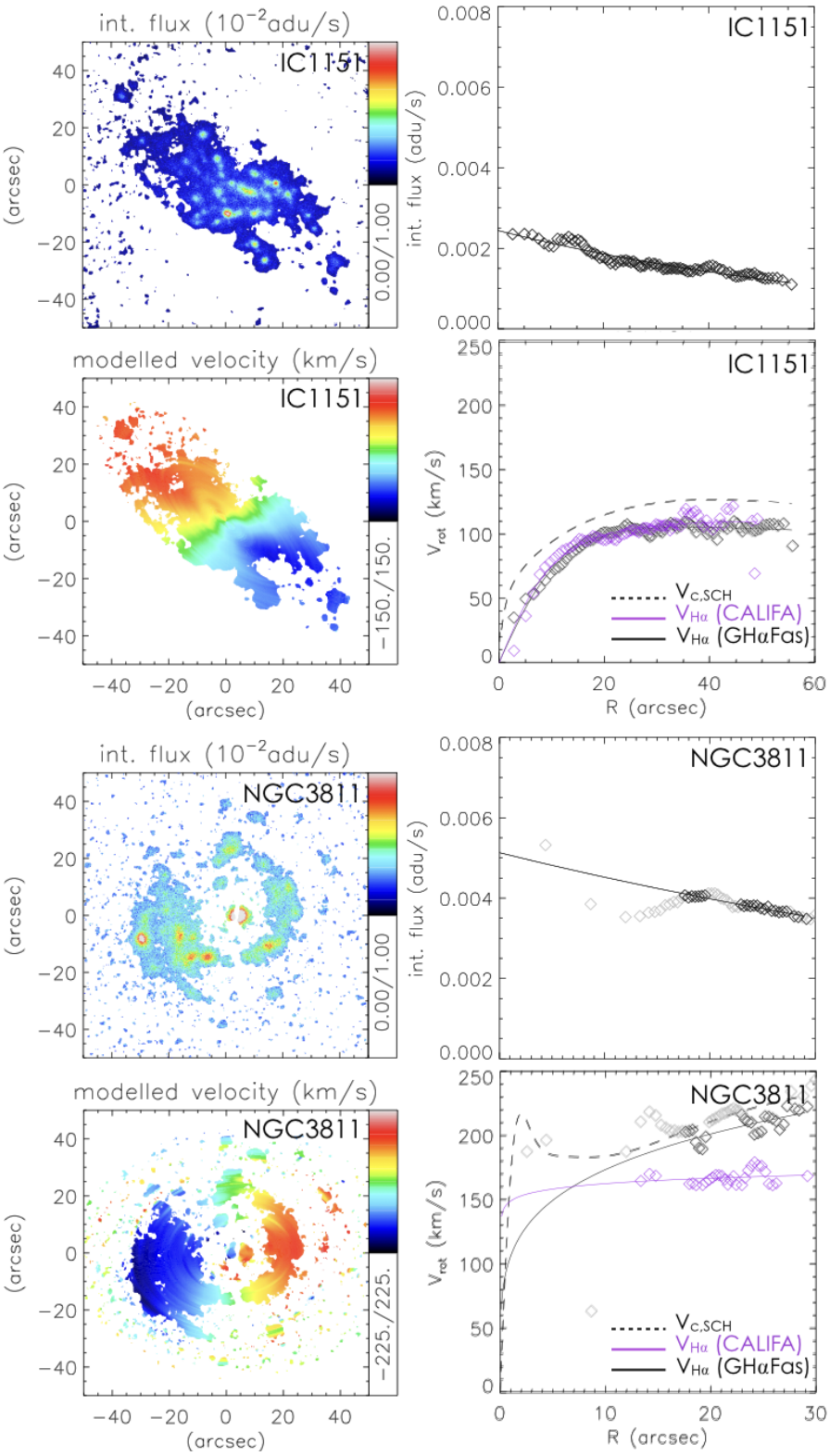
int. flux (10^{-2}adu/s)
IC1151
0.00/1.00
modelled velocity (km/s)
IC1151
−150./150.
(arcsec)
int. flux (adu/s)
IC1151
V_{rot} (km/s)
R (arcsec)
$V_{c,SCH}$
$V_{H\alpha}$ (CALIFA)
$V_{H\alpha}$ (GHαFas)
int. flux (10^{-2}adu/s)
NGC3811
0.00/1.00
modelled velocity (km/s)
NGC3811
−225./225.
(arcsec)
int. flux (adu/s)
NGC3811
V_{rot} (km/s)
R (arcsec)
$V_{c,SCH}$
$V_{H\alpha}$ (CALIFA)
$V_{H\alpha}$ (GHαFas)

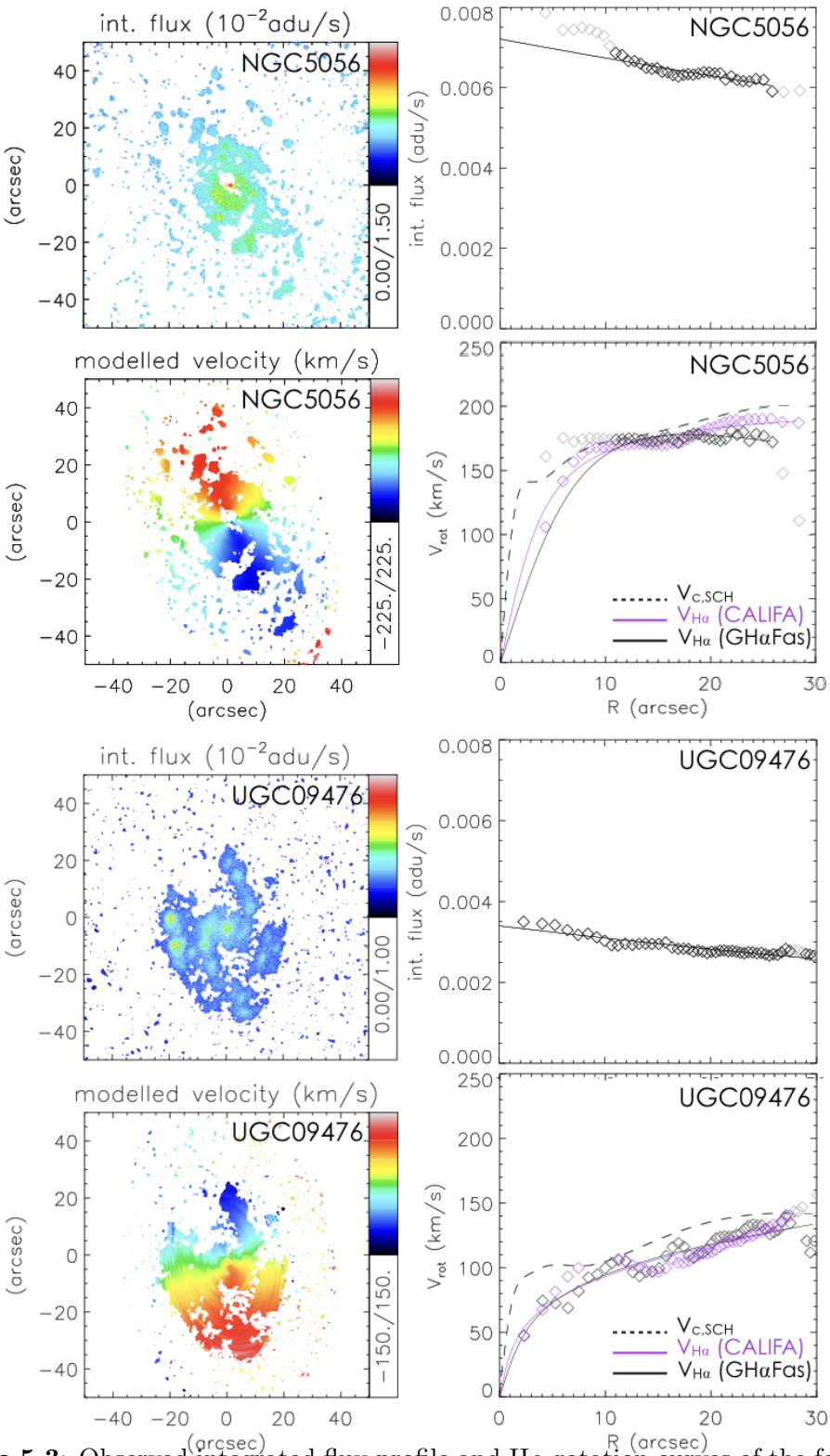

Figure 5.3: Observed integrated flux profile and Hα rotation curves of the four galaxies in our sample. *Top left:* Integrated flux map. *Top right:* Integrated flux profile at each ellipse plotted in grey opened diamonds. Black line shows the fitted exponential profile and black diamonds show the ellipses used for the fitting. *Bottom left:* Modelled velocity map from harmonic decomposition. *Bottom right:* derived $V_{\phi,\mathrm{H}\alpha}$ from the GHαFas observations shown in grey diamonds, fitted power-law profile shown with black curve and black diamonds show again the ellipses used for the fitting. Purple diamonds and curve show the $V_{\phi,\mathrm{H}\alpha}$ derived from the CALIFA observations and the corresponding fitted power-law profile. Dashed black line is V_c derived from stellar kinematics using Schwarzschild models.

and 5.6 the results from $\kappa = 0.0$, $\kappa = 0.5$ and $\kappa = 1.0$ respectively. The rows show the results of IC1151, NGC3811, NGC5056 and UGC09476 from top to bottom. The obtained $\sigma_{\rm grav,R}$ are shown in coloured solid curves in the left panels and the deprojected $\sigma_{\rm tot,R}$ are shown in coloured dashed curves. The observed $\sigma_{\rm obs}$ derived along the major axis of each ellipse extracted through harmonic decomposition is shown in grey diamonds, with the employed ellipses marked with black diamonds (as described in §5.3). Curves in different colours indicate the different (β_ϕ, β_z) assumed and the corresponding (β_ϕ, β_z) of each colour is shown on the right panels. The corresponding decomposition of the ionised gas velocity dispersion $\sigma_{\rm grav}/\sigma_{\rm tot}$, are shown in the middle panels in solid coloured lines. The vertical dashed lines in the middle panels show the radii of the innermost ellipses where we have a derived $V_{\phi,\rm H\alpha}$. Beyond these radii, we require $\sigma_{\rm grav}/\sigma_{\rm tot} < 1$ (as marked by the horizontal dashed lines). The (β_ϕ, β_z) pairs that satisfy this requirement for each galaxy are marked with white dots on the right panel.

5.4.1 Dependence on velocity anisotropy

While varying κ does not significantly alter the derived $\sigma_{\rm grav}/\sigma_{\rm tot}$ ratios, varying (β_ϕ, β_z) varies the ratio significantly. In general, the higher the assumed velocity anisotropies (β_ϕ, β_z), the lower $\sigma_{\rm grav}/\sigma_{\rm tot}$. This degeneracy between the assumed velocity anisotropy and the required $\sigma_{\rm grav,R}$ to recover $V_{\rm c}$ from $V_{\phi,\rm H\alpha}$, together with our requirement of $\sigma_{\rm grav}/\sigma_{\rm tot} < 1$, constrain the β_ϕ and β_z to be always ≥ 0 and in some cases even > 0.5, as shown by the position of the white dots in the right panels of Figure 5.4, 5.5 and 5.6. We note here however, if the velocity anisotropy varies with radius, then negative β_ϕ and β_z are still possible at the outer region of the galaxies.

While this degeneracy does not allow us currently to pinpoint the $\sigma_{\rm grav}/\sigma_{\rm tot}$, our results show that even with the highest β_ϕ and β_z (=1), $\sigma_{\rm grav}/\sigma_{\rm tot} \gtrsim 0.5$ in the inner region and decreases towards larger radii. Even though such a result is robust with respect to the velocity anisotropy, an uncertainty of $\delta\sigma_{\rm grav}/\sigma_{\rm tot} \gtrsim 0.5$ still prevails due to the lack of knowledge in (β_ϕ, β_z).

The constraint on having $(\beta_\phi, \beta_z) \geq 0$ can be understood as the result of the relative higher differences between the $V_{\rm c}$ derived from Schwarzschild models and the Hα rotation curves $V_{\phi,\rm H\alpha}$ in comparison to the observed Hα velocity dispersion. One may ask if this can be caused by the Schwarzschild models overestimating $V_{\rm c}$, as is indeed shown in Chapter 2 that while on average Schwarzschild models can well recover $V_{\rm c}$, there is still a scatter of $\sim 10\%$ and given our small number statistics, it is possible that all four galaxies lie in the regime where the Schwarzschild models

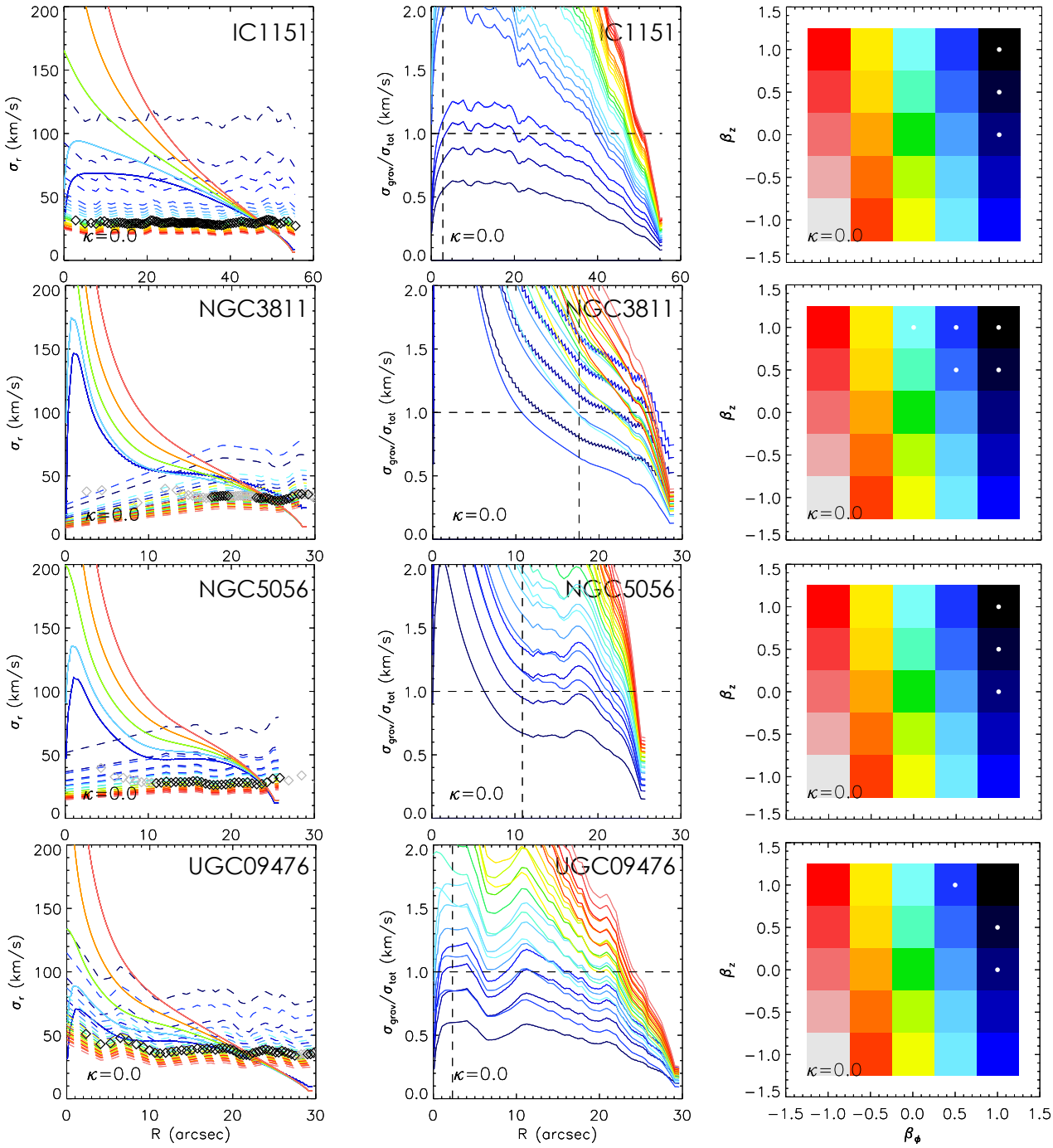

Figure 5.4: Results for $\kappa = 0.0$. Left: Required $\sigma_{\rm grav,R}$ derived from the difference between $V_{\rm c}$ and $V_{\phi,{\rm H}\alpha}$ by using ADC shown in solid curves. The deprojected $\sigma_{\rm tot,R}$ shown in dashed curves. The colour-coding denotes different (β_ϕ, β_z) assumed and the correspondence is shown on the right panel. Grey and black diamonds show the extracted and employed $\sigma_{\rm obs}$ from ellipse fitting. *Middle:* The derived $\sigma_{\rm grav}/\sigma_{\rm tot}$ ratios. Vertical dashed lines show the location of the innermost employed ellipse. *Right:* White dots indicate the (β_ϕ, β_z) pairs that satisfy the requirement $\sigma_{\rm grav} < \sigma_{\rm tot}$ (as shown with horizontal dashed line in the middle panel).

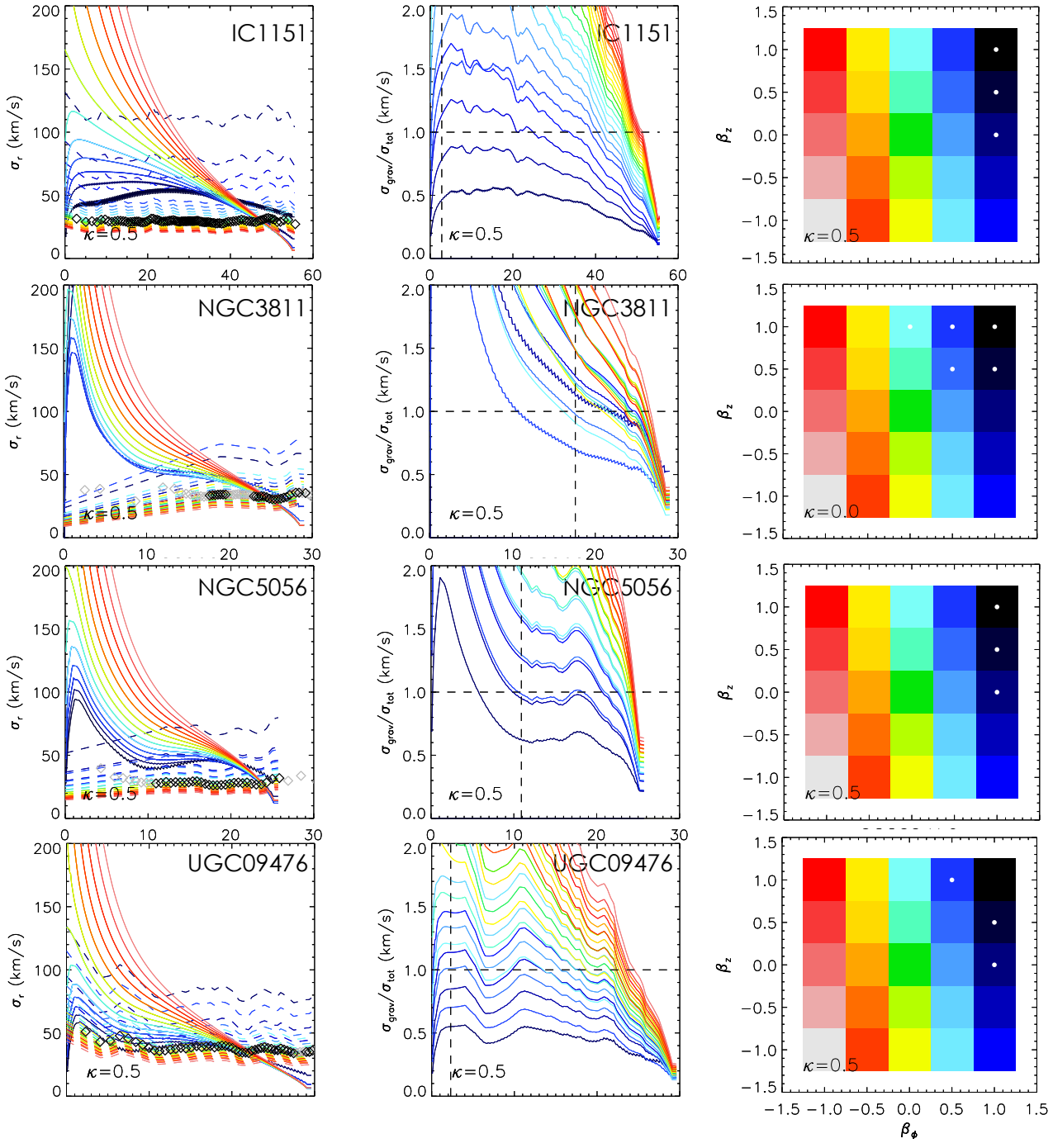

Figure 5.5: Same as Figure 5.4 but for $\kappa = 0.5$.

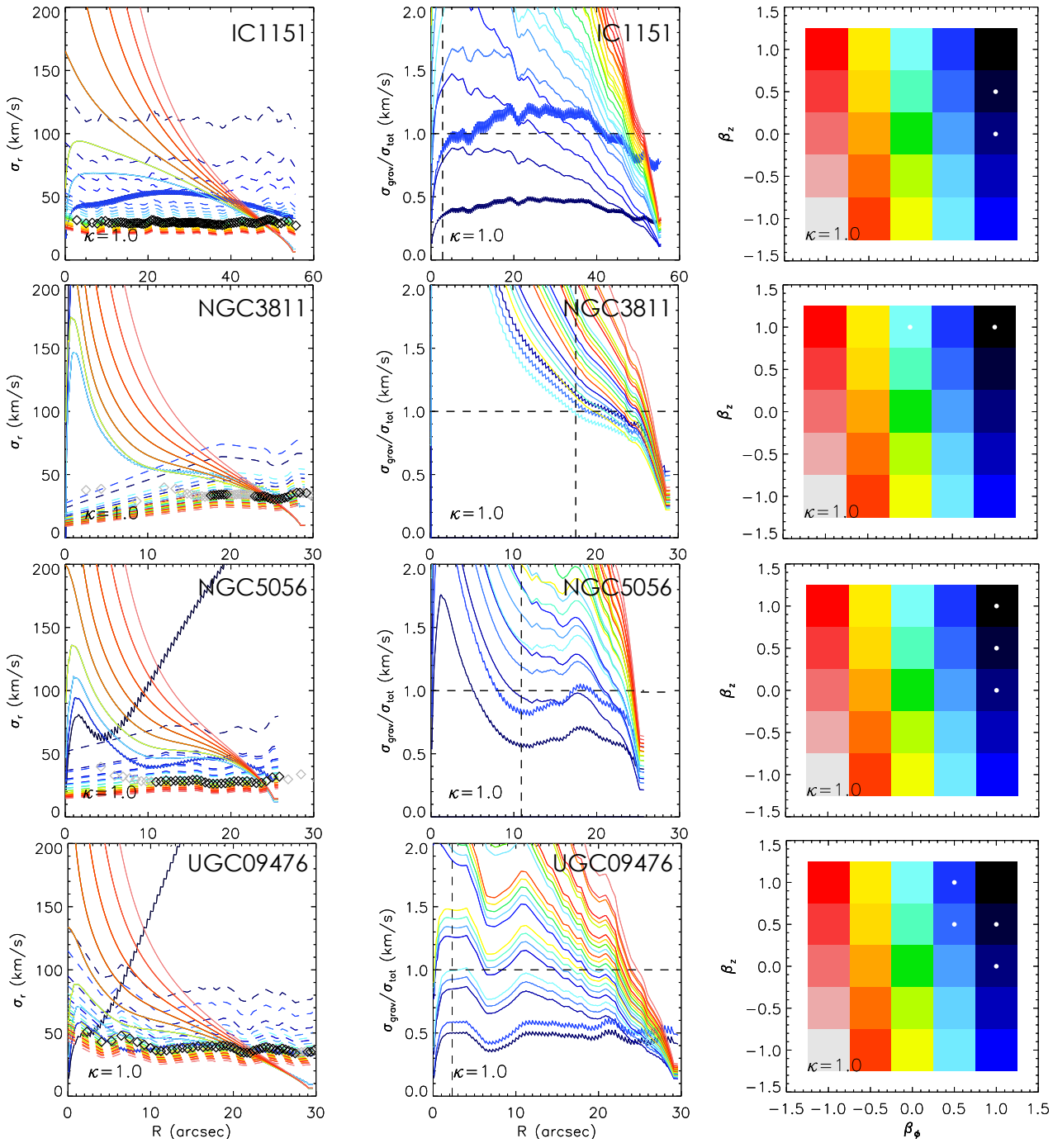

Figure 5.6: Same as Figure 5.4 but for $\kappa = 1.0$.

overestimate V_c. While this is a possibility to ponder upon, we can check from Figure 2.8 that at least for the galaxy NGC50506, for which we have also derived V_c from cold gas CO kinematics, that such a doubt can be eliminated. The derived V_c from CO and Schwarzschild agree well with one another for NGC5056, at least at the radii where we applied $\sigma_{H\alpha}$ decomposition (beyond the central $\sim 5''$ where beam-smearing factor can come into play for the $V_{c,CO}$ and where there is also a central hole in our Hα map). We would need a larger sample of galaxies to determine whether or not a radial anisotropy ($\beta_\phi > 0$) is generally true for disk galaxies.

It remains unclear what is the source of anisotropic dispersions in ionised gas kinematic fields - and if they are merely transient descriptions of the gas which should shock if orbits cross. Added complications could arise if the gas motions are confined by denser regions of the ISM, and interactions with cosmic rays and magnetic fields. It would be interesting to characterise the three-dimensional deviations from non-circular motions within high resolution simulations of isolated regions of galaxy disks.

5.5 Summary and future work

In order to better understand the source of velocity dispersion in the ionised gas phase of star forming galaxies (e.g, due to stellar feedback or gravitational perturbations) we have obtained Hα kinematics with both high spatial and spectral resolution (<6.5 km/s) using the Fabry-Perot instrument on GHαFas for four nearby disk galaxies. By comparing the derived Hα rotation curve $V_{\phi,H\alpha}$ with the circular velocity (V_c) derived independently using Schwarzschild models from stellar kinematics obtained as part of the CALIFA survey, we attempt to measure the contribution of the Hα velocity dispersion from non-turbulent (i.e. gravitational) sources, σ_{grav}. This measure can then be used to study the relative contribution of gravitational and turbulent velocity dispersion (σ_{turb}) by comparing σ_{grav} with the observed total velocity dispersion (σ_{tot}), and to asses how it varies with galaxy properties.

While the ratio $\sigma_{grav}/\sigma_{tot}$ is found to be degenerate with the assumed velocity anisotropies (β_ϕ, β_z), $\sigma_{grav}/\sigma_{tot} \gtrsim 0.5$ in the inner region of all four galaxies and decreases towards larger radii, independent of (β_ϕ, β_z). Also, by simply requiring that $\sigma_{grav} \leq \sigma_{tot}$, we are able to rule out the (β_ϕ, β_z) values being negative. In some cases, β_ϕ and β_z are even required to be > 0.5. While we have shown that such results is conclusive for NGC5056, as the circular velocities derived from the Schwarzschild model and CO agree well with one another, a larger sample of galaxies

with well measured CO V_c is needed to conclude whether the unilateral radial anisotropy ($\beta_\phi > 0$) constraints we find is robust for disk galaxies in general.

The derived anisotropic nature of ionised gas velocity dispersion can be a puzzle given their expected collisional nature. One might imagine the velocity anisotropy being maintained through non-circular orbits of confined ionised gas clumps, and indeed the anisotropic nature of ionised gas might provide a glimpse on how clumpy the gas needs to be in order to maintain the anisotropy. We will however still need advices from simulations to answer questions such as: where does the anisotropy arise from, is it related to stellar velocity anisotropy and if so how, and to constraint the required phase-space distribution of ionised gas/timescale for orbit crossing such that a velocity anisotropy can be maintained.

Simulations may also provide the better handle on the velocity anisotropy we need, in order to further pinpoint the relative composition of $\sigma_{\rm grav}$ and $\sigma_{\rm turb}$. From the analytical side, one possible way forward is to obtain higher order velocity moments from Gaussian-Hermite fitting to the data cube. As has already been demonstrated in the literature for stellar Jeans modelling, having the higher order velocity moments will allow us to use also the higher order Jeans Equations to break the degeneracy between the total mass and velocity anisotropy.

Similarly, we can, instead of just using the radial profiles of ν, $V_{\phi,{\rm H}\alpha}$ and $\sigma_{\rm obs}$, move on to two-dimensional modelling using the whole maps. Just like moving from one-dimensional to two-dimensional Jeans Modelling, the relative distribution of $\sigma_{{\rm H}\alpha}$ along the azimuthal direction would advise us on the Hα velocity anisotropies.

Chapter 6

Conclusion and Outlook

To contribute to our continued understanding of galaxy evolution and the nature of dark matter, this thesis has undertaken an exploration based on galaxy dynamics. Out of the wealth of dynamical tracers, four have been touched upon: cold molecular gas, ionised gas, stars and globular clusters (GCs). The different nature of these tracers implies that different modelling techniques are required. Also, while the kinematics of the different tracers could be affected by effects that are specific to those components (e.g. ionised gas by gas turbulence, stars by stellar orbital structure, and GCs by dynamical friction), they all in the end are moving in the same gravitational potential. Thus, while these effects can sometimes cloud our recovery of the enclosed mass distribution in the galaxy, incorporating kinematic information from multiple tracers would allow us to disentangle them; to derive tighter constraints on the dark matter halo, and simultaneously recover much more information on the host galaxy evolution and orbital structure.

By developing innovative modelling techniques and leveraging data products from multiple kinematic tracers, we are able to 1) provide a homogenous test of stellar dynamical models on the largest sample of galaxies in the literature, 2) explain the curious abundance and location of GCs in the dSph Fornax, 3) derive for the first time the velocity anisotropy profile of a dIrr and 4) unprecedented constraints on the inner slope and the geometry of the DM halo of a dwarf galaxy. The last point in particular has helped us learn about the impact of stellar feedback in modifying galaxy dark matter profiles and constraints on the type of interacting DM particles which may be consistent with high resolution dwarf galaxy observations.

6.1 Summary of results

Validity of stellar dynamical mass models

As mentioned in the introduction, cold gas provides the most straight-forward and potentially most accurate tracer of the underlying gravitational potential, as it is nearly entirely rotationally supported and in a thin disk configuration. On the other hand, when modelling stellar kinematics, considerations must be taken to account for the stellar velocity dispersion and anisotropy (i.e. non-circular motions). In addition, assumptions on spatial or kinematic geometries are made due to the incomplete knowledge of the full 6D velocity phase space. To demonstrate the validity of these stellar dynamical models, we therefore first tested three commonly used models: Asymmetric Drift Correction (ADC), Jeans Model (JAM) and Schwarzschild Model (SCH), by comparing their derived mass distribution to the ones derived from CO (cold gas) kinematics in the same galaxies. This analysis was done on 54 galaxies from the EDGE-CALIFA survey, and was one of the first comparisons of gas and stellar dynamical models on such a large and homogeneous sample. We found that for all of the dynamical models we considered, the CO and stellar circular velocities exhibit excellent agreement (to within $\sim$10%) at large radii ($\gtrsim 1\,R_e$). Larger discrepancies in the inner region ($\gtrsim 50\%$), on the other hand, suggest that when deriving the inner DM density profiles, these stellar dynamical models may suffer from degeneracies (such as the mass-anisotropy degeneracy) and/or over-simplistic assumptions on the geometry or mass to light ratio variations. With the inclusion of gaseous kinematics, one may fare better in both the derivation of the underlying gravitational potential and the stellar orbital structure.

Constraining the orbital structure and testing dark matter theories with multi-tracer dynamical models of an isolated dwarf galaxy

After demonstrating that Jeans stellar dynamical models are performing well for galaxies of a wide range of masses, we next attempted to combine multiple kinematic tracers in the same galaxy. When combining the stellar and gaseous kinematics, not only is the stellar dynamical model benefiting from the knowledge of the circular velocities from the cold gas, the overall model also benefits from the three dimensional nature of stars, allowing us to probe the geometry of the DM halo shape at the same time. As dwarf galaxies provide the best test beds for understanding the nature of dark matter and impact of baryonic feedback, we have focused on a low mass dwarf for the first application of this novel method. The isolated dIrr WLM is one of the few candidates that is both close enough for obtaining stellar kinematics

and of the right mass and distance to retain a rotationally supported gas disk.

Interestingly, we find a prolate, cored DM halo with a short-to-long-axis ratio of $\sim$0.5 and a density profile of inner slope $\gamma \sim 0.3$, both in excellent agreement with that of haloes of the $M_\star/M_{\rm halo}$ of WLM in ΛCDM cosmological and hydrodynamical simulations. The simultaneous finding of a prolate DM halo geometry and a central density core, is potentially problematic or constraining for theories of self-interacting dark matter. This result illustrates the power and leverage that multi-tracer dynamical models have in studying DM physics when applied to isolated dwarf galaxies.

Additionally, for the first time in a dIrr galaxy, we derived a stellar velocity anisotropy profile. We found that the velocity anisotropy transitions from mildly radial in the inner region ($\lesssim 1\,R_e$) towards increasingly tangential at larger radii. Such a shape in the velocity anisotropy profile has been seen in dSphs and was typically interpreted as signatures of tidal stripping. By showing that the velocity anisotropy of the isolated dwarf WLM also has a similar profile, we have demonstrated that external interaction is not necessary in creating such tangential anisotropy. Instead, the tangential anisotropy in WLM might be intrinsic to its formation process, or might have been imparted by other internal mechanisms. Reproducing this orbital structure in an isolated dwarf will be a critical test for future simulations, and will shed further light on the dominant mechanisms for dwarf galaxy evolution.

Using star clusters to trace the merger history and DM halo of a dwarf galaxy

The Fornax dSph galaxy has long posed an interesting problem for star cluster and dwarf galaxy evolutionary pictures, due to its large number of globular clusters (GCs). Understanding how they have survived until present allows a better understanding on the underlying gravitational potential. Here we incorporated a novel treatment of dynamical friction, with the first self-consistent treatment of the effect of mergers on the co-evolution of Fornax and its GCs. Together with a more realistic estimates of their formation location, we came to the conclusion that the DM halo of Fornax contains a large core, with core size $r_{\rm c} \geq 1.5\,{\rm kpc}$. We further showed how this DM density profile exceeds that predicted from baryonic feedback alone, but is consistent with the expectations for the galaxy structure after it has undergone a merger with another dwarf galaxy. This merger plays a crucial role in helping the GCs survive orbital decay, by kicking them out to further distances, thus solving a long-standing problem with the Fornax dSph.

Our dynamical friction model suggests that the past merger in Fornax likely occurred with another dwarf galaxy with mass ratio of 1:5 to 1:2. We show that this is supported by the metallicity distribution function (MDF) of the field stars and their metal contribution relative to the GC stars in Fornax. In particular we suggest that, GC1, GC2 and GC3 have similar ages and metallicities and are likely to be inherent to proto-Fornax before the merger. GC5 is slightly younger and more metal rich and could have come from the merging fragment. The formation of youngest GC4 could have been triggered by the merger itself if the merger happened around the time when GC4 was formed ($\sim$10 Gyrs ago). This work is one of the first to place the GC formation and survival in the context of a larger picture of the evolution of its host galaxy, and its dark matter halo.

Understanding the contribution of baryonic feedback to gas kinematics

Finally, we undertook an observational campaign to constrain the energetics of baryonic feedback in galaxies through high resolution observations of the kinematic structure of the ionised gas component. The aim was to decompose the velocity dispersion of the ionised gas $\sigma_{\mathrm{H}\alpha}$ into its turbulent component $\sigma_{\mathrm{turb,H}\alpha}$ and gravitational component, σ_{grav}. Understanding the relative contribution of the two is crucial to improve the accuracy of dynamical models at high redshift, and understand how stellar feedback impacts gas in galaxies.

We proposed for and observed the ionised gas velocity dispersion $\sigma_{\mathrm{H}\alpha}$, for four galaxies in the EDGE-CALIFA survey, with the high spectral resolution ($\sim$6 km s^{-1}) Fabry-Perot spectrometer (GHαFas), mounted on the William Herschel 4.2m Telescope. As these galaxies span a range of star formation rates and gas fractions, understanding their $\sigma_{\mathrm{turb,H}\alpha}$ provides important constraints to the feedback recipes used in hydrodynamical simulations (a key factor in controlling the DM inner slope and core size produced by baryonic feedback in a CDM halo).

The ionised gas velocity dispersion decomposition was done by constraining the enclosed mass profile with independent circular velocity estimates from stellar dynamical models. This then lets us derive the required gravitational component of velocity dispersion $\sigma_{\mathrm{grav,H}\alpha}$ that reproduces the total potential in combination with the rotation curves of Hα. $\sigma_{\mathrm{turb,H}\alpha}$ is then estimated from the remaining/excess velocity dispersion seen in the gas.

We found that the contribution of the gravitational component to the total velocity dispersion, $\sigma_{\mathrm{grav,H}\alpha}/\sigma_{\mathrm{tot,H}\alpha}$, is dependent on the assumed velocity anisotropy of the ionised gas. And for all four galaxies, except for the very outer regions.

radial anisotropies are required such that the needed gravitational components do not exceed the total observed dispersion. However, given the lack of insights on the parametrisation of velocity anisotropies of Hα, more sophisticated modelling techniques are required to further pinpoint $\sigma_{\mathrm{grav,H}\alpha}/\sigma_{\mathrm{tot,H}\alpha}$.

6.2 Implications

6.2.1 Evolution of dwarf galaxies

The similarity between the velocity anisotropy profiles of the dIrr WLM and other dSphs: a mildly radially anisotropic central region that becomes increasingly tangential towards larger radii, suggests that such signatures could be imprints from the formation of the dwarfs or secular processes, instead of a result of environmentally driven morphological transformation. Possible internal processes that can impart velocity dispersions in a galaxy include scattering from spiral arms, bars and GMCs. However, as already discussed in Chapter 3, spiral arms are not likely to be formed in dwarfs while GMCs tend to isotropise the velocity anisotropies and bars tend to impart radial anisotropies. On the other hand, the effects of feedback and gas accretion on the velocity anisotropies of dwarfs is still unknown and could be a possible source of tangential anisotropies.

This also means that the transformation process either (i) does not impart significant dynamical influence on the stellar structure or (ii) is a three dimensional agent that imparts equal amount of heating in all direction and hence keeping the anisotropy intact (if it was tangential at formation). Possible gentle processes belonging to the first case include for example gas expulsion through stellar feedback and/or gradual ram pressure stripping. Star formation are found to be more efficient in some of the dwarfs than in others (Bermejo-Climent et al. 2018), leading to increased periods of feedback and quicker exhaustion of gas to form dSphs.

The results we obtained from the modelling of dynamical friction and chemistry of GCs in the dSph Fornax, would suggest that dwarf-dwarf interactions may also play a role in the evolution of dwarf galaxies. These mergers can help alter the DM and stellar orbital structure, and in principle could modify the anisotropy as well. A more complete census of observational signatures of dwarf-dwarf mergers, and quantification of the frequency in all environments from simulations would help better understand their role.

Another possibility is that a prolate dark matter halo naturally leads to

tangential velocity anisotropies. An aspherical potential imparts gravitational torque which causes orbital precession (Erkal et al. 2016), and a radial variation in the net potential geometry may possibly increase the tangential velocity dispersion. If velocity anisotropy in dwarfs is indeed linked intimately with the geometry of the potential, the general shape of the velocity anisotropy profiles can also be explained as a natural consequence of the radial variation of the relative contribution to the overall geometry from the oblate stellar component to the prolate DM halo. In this case, since dwarf galaxies are expected to have prolate DM haloes in ΛCDM, the tangential velocity anisotropy might after all not provide meaningful constraint on the evolution of dwarfs, except acting as a baseline from which stellar velocity anisotropies evolve from.

6.2.2 Nature of Dark Matter

Both our WLM and Fornax results show that their DM haloes are not cusped as predicted by pure ΛCDM cosmological simulations. It has been shown that under the CDM paradigm, such shallow inner density slopes in DM haloes can be caused by baryonic feedback. Indeed, in the case of WLM, our derived inner slope of its DM halo, as well as the prolate halo geometry, are in excellent agreement with that shown by ΛCDM cosmological simulations that incorporate baryonic feedback (Di Cintio et al. 2014; Butsky et al. 2016). On the other hand, the core size we derived for the DM halo of Fornax is beyond the prediction of simulations of baryonic feedbacks in CDM haloes.

The large core in Fornax might be indicating an alternative nature of DM. From the core size, we were able to constrain the DM particle mass in the Fuzzy Dark Matter (ψDM) model to be $m_{\psi\mathrm{DM}} \sim 1.1 \times 10^{-22}\,\mathrm{eV/c^2}$. For the Self-Interacting Dark Matter (SIDM) model, we constrained the scattering cross section to be $\langle\sigma v\rangle/m_{\mathrm{SIDM}} \sim 36\,(\mathrm{cm^2/g{\times}km/s})$.

Similar constraints can be obtained using the result from WLM. The good agreement between our derived DM halo parameters with that predicted from hydrodynamical simulations under the CDM paradigm of course does not immediately rule out the possibility of alternative DM models. For the case of SIDM however, it is known that a large scattering cross section could thermalise and isotropise the DM halo, leading to a more spherical DM halo. From the derived DM halo parameters of WLM, we constrained the SIDM scattering cross section to be $\langle\sigma v\rangle/m_{\mathrm{SIDM}} \sim 22\,(\mathrm{cm^2/g{\times}km/s})$. Whether such a scattering cross section can simultaneously allow a prolate DM halo of $q_{\mathrm{DM}} \sim 2$ is to be tested with future SIDM simulations.

6.3 Outlook

A few open questions remain. One of which is the source of tangential anisotropies in dwarfs. Applying our joint gas-and-star dynamical models on more nearby dwarfs will allow us to consolidate whether a prolate dark matter halo and a tangential velocity anisotropy are indeed correlated. Possible candidates include Aquarius, Sagittarius dIrr and VV124, which just like WLM these dwarfs lie in the sweet spots of being close enough for us to obtain stellar kinematics but still contain enough cold gas for deriving the circular velocities. Further analytical models can be done to address quantitatively how the prolateness of DM haloes can impart tangential velocity anisotropies.

Similarly, the joint gas-and-star dynamical model can be applied onto the 54 CALIFA-EDGE galaxies, of which we have already derived the circular velocities from CO kinematics. This would allow us to investigate the geometry of DM haloes across a wider range of galaxy mass. In particular questions such as, if DM haloes become more spherical towards larger mass as predicted by CDM simulations, or if there is one particular SIDM model that fits through the $q_{\rm DM}$ variation through galaxy masses, might allow us to better distinguish between the DM models. To answer the latter, one would also need the predicted dependence of $q_{\rm DM}$ with galaxy mass to be provided by SIDM cosmological simulations.

And in the case of Fornax, questions such as: what orbital parameters of a merger can preserve a tangential velocity anisotropy, if the tangential anisotropy is removed by a merger, what is the timescale for the prolate DM halo to restore the tangential anisotropy, should be answered through simulations.

Another issue that can be addressed simultaneously is whether the large DM core in Fornax can be induced by a merger of our derived mass ratio, and if possible, whether such a large core is stable in the CDM paradigm. In general, understanding the correlation between the merger mass ratio and the radial expansion of DM halo core can provide orthogonal constraint to our semi-analytic model. From our current model, there is a degeneracy between the constrained DM core size and the merger mass ratio: the positions of the GCs can be reproduced by a smaller DM core if amore massive merger has occurred. However such a larger mass merger event, may actually cause a larger expansion of the DM core in Fornax. Hence by characterising the core expansion at each merger mass ratio with simulations, we could break the current degeneracy between the merger mass ratio and the DM core size.

Further work on decomposing ionised gas velocity dispersion will provide a better handle on feedback energetics, which is closely related to the process of

creating density cores in CDM haloes. Proposed ways to break the aforementioned degeneracy with gas velocity anisotropies include: incorporating higher order velocity moments and utilising the azimuthal variation of the observed $\sigma_{\mathrm{H}\alpha}$ in our model. To have a better understanding of the source of anisotropy in ionised gas and/or better parametrisation of the gas dispersion would also require help from future high resolution simulations.

Finally, we have demonstrated that dynamical models are superb tools for studying the tiny 'clouds' that we see in the night sky – allowing us to recover signatures of a galaxy's evolutionary history from the present day motions of its gas, stars and star clusters. When these techniques are applied to the tiniest 'clouds' of all – dwarf galaxies, we are able to glimpse the unseen – dark matter, unveiling one of the biggest mysteries of the universe.

Appendix A

Chapter 2 Appendix

A.1 Possible effects of $m = 2$ perturbation on $V_{\rm CO}$

We extracted $V_{\rm CO}$ with harmonic decomposition:

$$\begin{aligned} V_{\rm mod} &= V_{\rm sys} + c_1 \cos(\phi) + s_1 \sin(\phi) + c_2 \cos(2\phi) \\ &+ s_2 \sin(2\phi) + c_3 \cos(3\phi) + s_3 \sin(2\phi), \end{aligned} \tag{A.1}$$

From here, we take $c_1/\sin(i)$ as $V_\phi = V_{\rm CO}$. In fact, although most of the high-order perturbation can be removed using this method, perturbation of $m = 2$ mode can still have an effect on on c_1. As described in Spekkens & Sellwood (2007), the effect on m=2 mode perturbation on c_1 can be estimated as $c_1 = V_\phi + c_3(s_1 - V_{\rm rad})/s_3$, where $V_{\rm rad}$ is the first order radial flow. All the galaxies in our sample have average s_1, c_3 and s_3 terms of $\lesssim$10% of c_1. While we do not have independent handle on $V_{\rm rad}$, s_1 in general should be dominated by radial flow such that $s_1 \sim V_{\rm rad}$. To put an upper limit on how much $c_1/\sin(i)$ deviate from V_ϕ, we assume that s_1 is completely dominated by $m = 2$ perturbation, i.e. $V_{\rm rad} = 0$. In Figure A.1, we plot for each stellar dynamical model, $\Delta V/V$ versus $V/\sigma_\star$ (as in Figure 2.11), colour coded with the corresponding $|(c_3 s_1/s_3)/c_1|$ value for each galaxy in the specific $V/\sigma_\star$ bin. $|c_3 s_1/s_3|$ gives an upper limit to how much $c_1/\sin(i)$ deviate from the true V_ϕ. We show here the high $\Delta V/V$ points for each models in the low $V/\sigma_\star$ regime are not caused by possible contribution of higher order perturbation in $V_{\rm CO}$ as the corresponding points have low $|(c_3 s_1/s_3)/c_1|$ values. The large scatters in $\Delta V/V$ in the low $V/\sigma_\star$ regime are also not caused by higher order perturbations as there are no trends seen with respect to $|(c_3 s_1/s_3)/c_1|$.

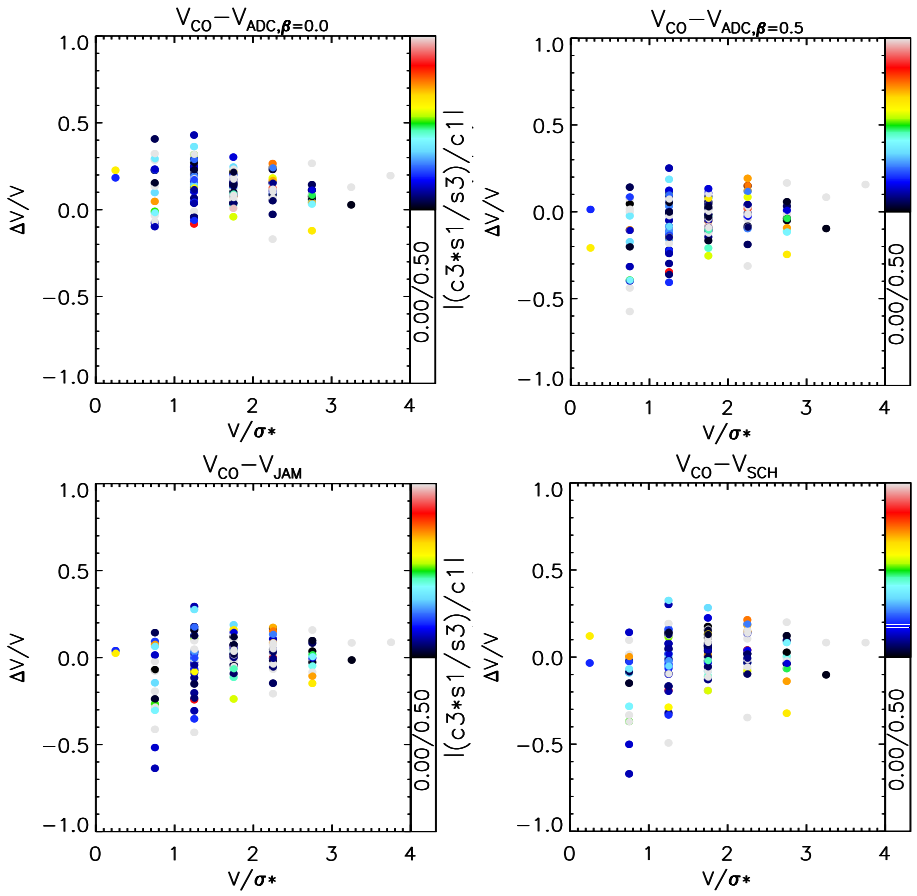

Figure A.1: $\Delta V/V$ plotted against $V/\sigma_\star$, colour coded with the corresponding $|(c_3 s_1/s_3)/c_1|$ value for each galaxy in the specific $V/\sigma_\star$ bin. No trends in $\Delta V/V$ are seen with respect to $|(c_3 s_1/s_3)/c_1|$.

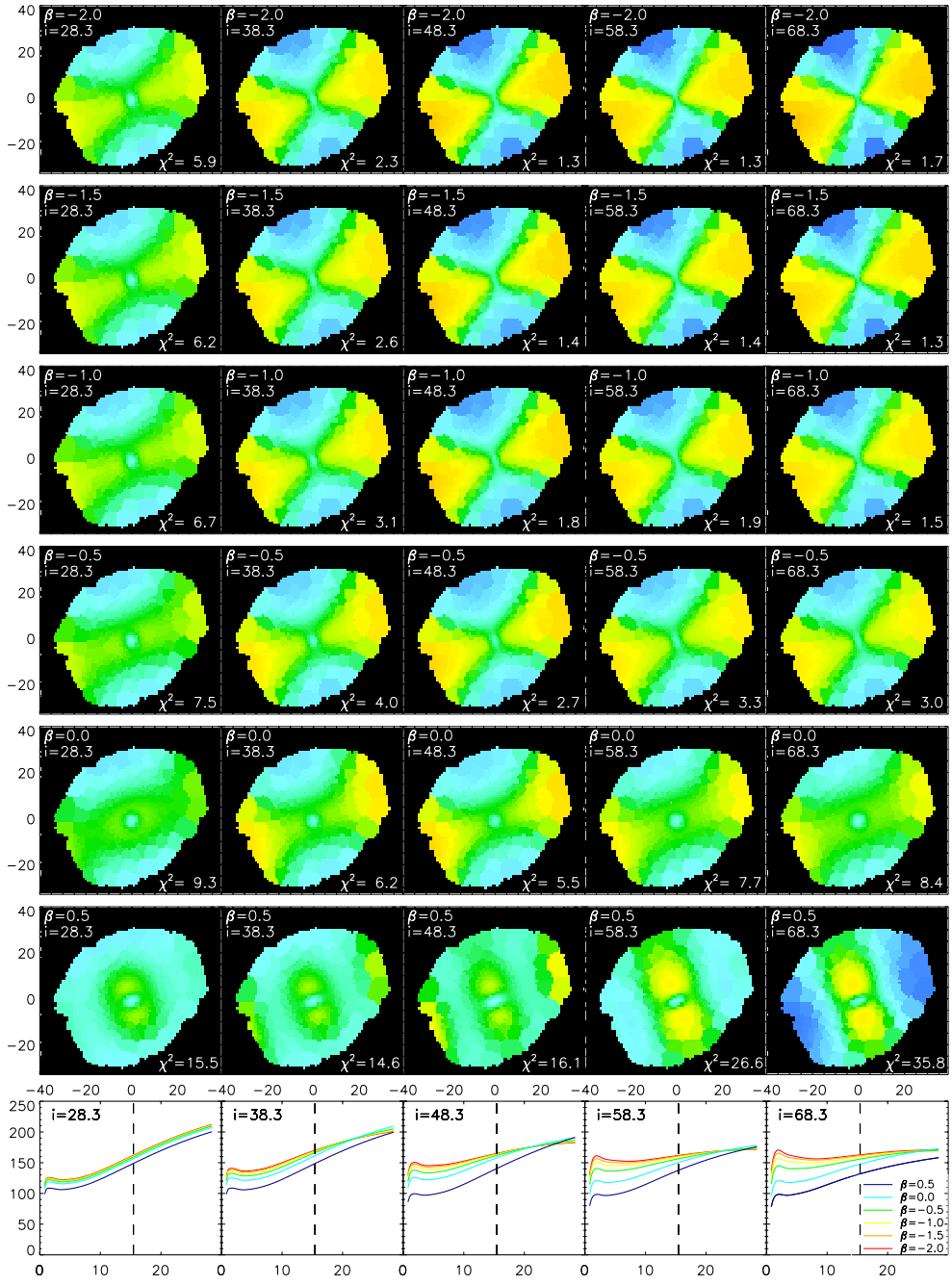

Figure A.2: Best-fitted kinematic maps with fixed β_z and inclination i. Individual panels in the bottom row shows the derived V_c for different fixed inclinations, as marked on the top left corner of each panel. At the bottom right corner, we show the reduced χ^2 of each model. Within each panel, V_c derived with different fixed β_z are plotted with different colours. Vertical dashed lines mark the effective radius.

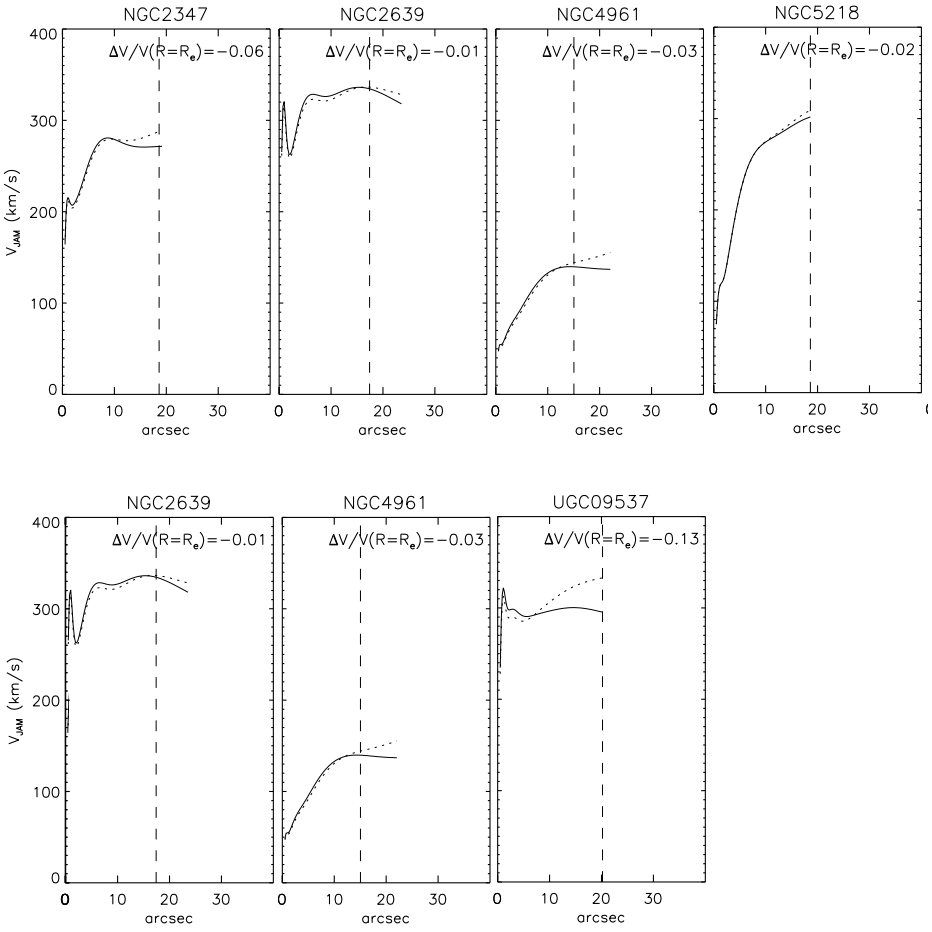

Figure A.3: $V_{\rm JAM}$ for the seven galaxies marked with ‡ in Table 2.3 between when we impose the stellar-mass-halo-mass relation (solid lines) and when we impose an uniform prior of $0-400\,{\rm km\,s^{-1}}$ to $V_{\rm vir}$ (dotted lines). On the top right corner of each panel, we show the relative difference between the two $V_{\rm JAM}$ at $1\,R_{\rm e}$.

A.2 Issues with unphysical parameters with JAM

As discussed in Section 2.4.2, seven galaxies in our sample converge towards the boundary condition of $\beta_{\rm z}=-2$ and 7 other galaxies converge towards the boundary condition of $V_{\rm vir}=400\,{\rm km\,s^{-1}}$ when a stellar vs. halo mass condition is not applied. We quantify here how such unphysical solutions affect our results.

We first show that the $\beta_{\rm z}<-1.5$ cases (i.e. the seven galaxies marked with † in Table 2.3) are not merely caused by an incorrect inclination estimate. As an example we show in Figure A.2, the best-fitted $V_{\rm rms}$ maps at fixed $\beta_{\rm z}$ of $[-2.0,\,-1.5,\,-1.0,\,-0.5,\,0.0,\,0.5]$ and vary the inclination with respective to $i=48.3$

(as derived from the ellipticity of the outer isophotes of r-band photometry) with Δi of [−20, −10, 0, 10, 20]. In every point of the grid (β_z, i) are fixed, but ($\Upsilon_\star$, V_{vir}) are free parameters. The value of the best-fit (β_z, i) of individual galaxies are determined by the shape of the V_{rms} map. There are degeneracies between (β_z, i), in the sense that a more negative β_z and a higher i have similar effects on the shape of the V_{rms} field. We find that for the seven galaxies marked with † however, even with a Δi of 20, the best fitted model still have $\beta_z \leq -1.5$. This suggest that the low β_z values we find are not just an effect of an incorrectly estimated inclinations, but are intrinsic to the JAM models.

We also show how different β_z and i value affect the derived V_{JAM} on the bottom row of Figure A.2. For $\beta_z < -0.5$, V_{JAM} agree to within ∼1% at $1\,R_e$ for any inclinations, suggesting that a highly negative β_z has only negligible effect on the derived V_c. The V_{JAM} derived also provide good agreement with V_{CO}. We therefore do not impose further constrain on β_z. Restricting $\beta_z > 0$ for example, on the other hand, would change the shape of the derived V_c to deviate from V_{CO} and therefore we do not suggest such practice.

We show in Figure A.3 V_{JAM} for the 7 galaxies which has V_{vir} driven to the upper boundary of $400\,km\,s^{-1}$ (marked with ‡ in Table 2.3). The best fit V_c when we impose a uniform prior of $0 < V_{vir} < 400\,km\,s^{-1}$ is shown in dotted lines. The V_c in models where we impose an additional stellar-mass-halo-mass relation (Eq. 2.9) are plotted in solid lines. In 4 of the galaxies, NGC2639, NGC4961, NGC5218 and NGC5784, the differences between the two V_c are only ≤3%. For the other 3 galaxies, NGC2347, NGC5908, and UGC09537, however, V_{JAM} shows a steep rise towards large radii. Such steep rises suggest that an unphysically high V_{vir} can have an effect on the derived V_c and therefore it is necessary to impose Eq. 2.9 to galaxies which do not have V_{vir} converging within the imposed prior.

A.3 Observed and modelled stellar photometry and kinematics

A.4 Observed and modelled CO kinematics

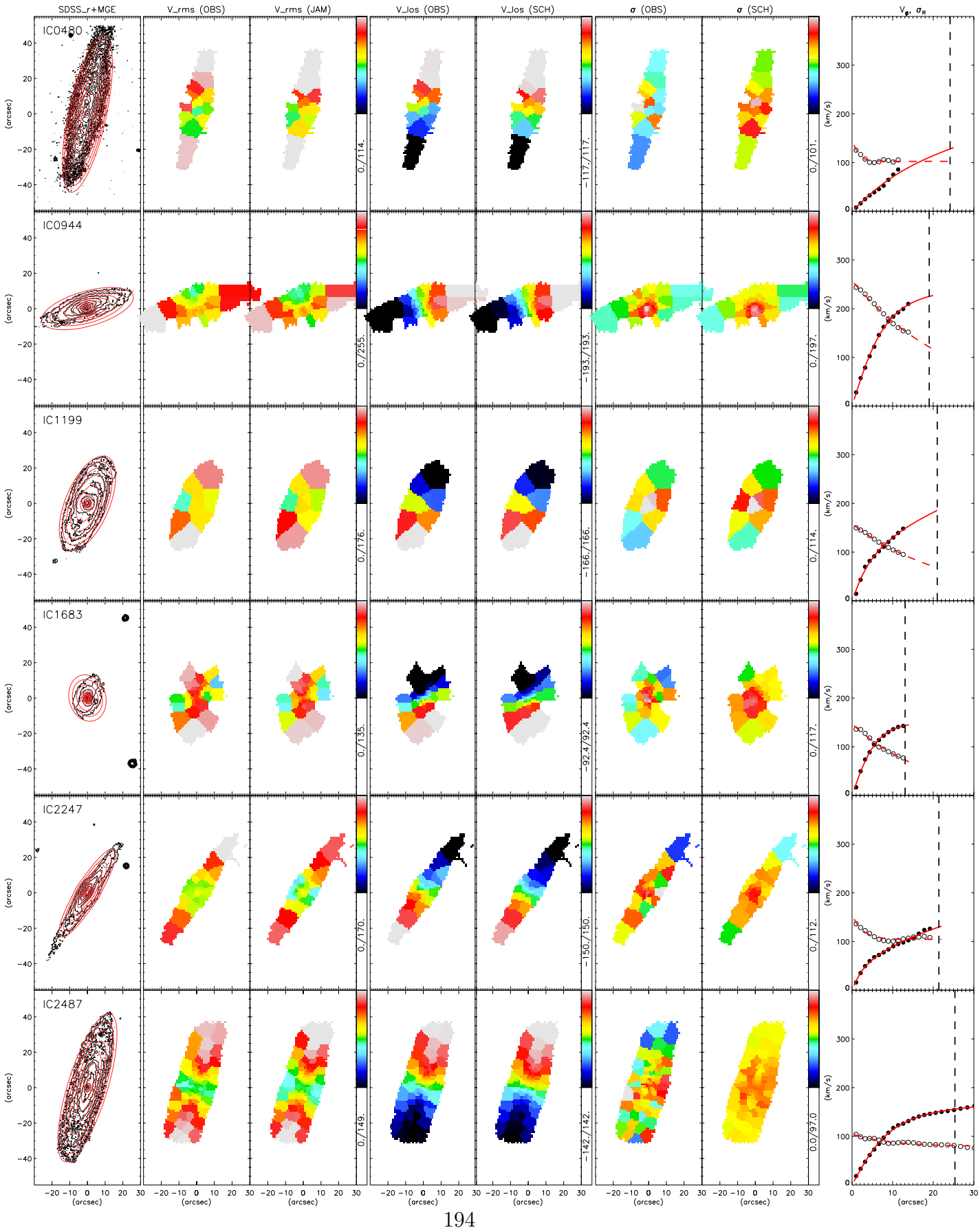
SDSS_r+MGE
V_rms (OBS)
V_rms (JAM)
V_los (OBS)
V_los (SCH)
σ (OBS)
σ (SCH)
V_φ, σ_R
IC0480
IC0944
IC1199
IC1683
IC2247
IC2487
(arcsec)
(km/s)
0./114.
−117./117.
0./101.
0./255.
−193./193.
0./197.
0./176.
−166./166.
0./114.
0./135.
−92.4/92.4
0./117.
0./170.
−150./150.
0./112.
0./149.
−142./142.
0.0/97.0

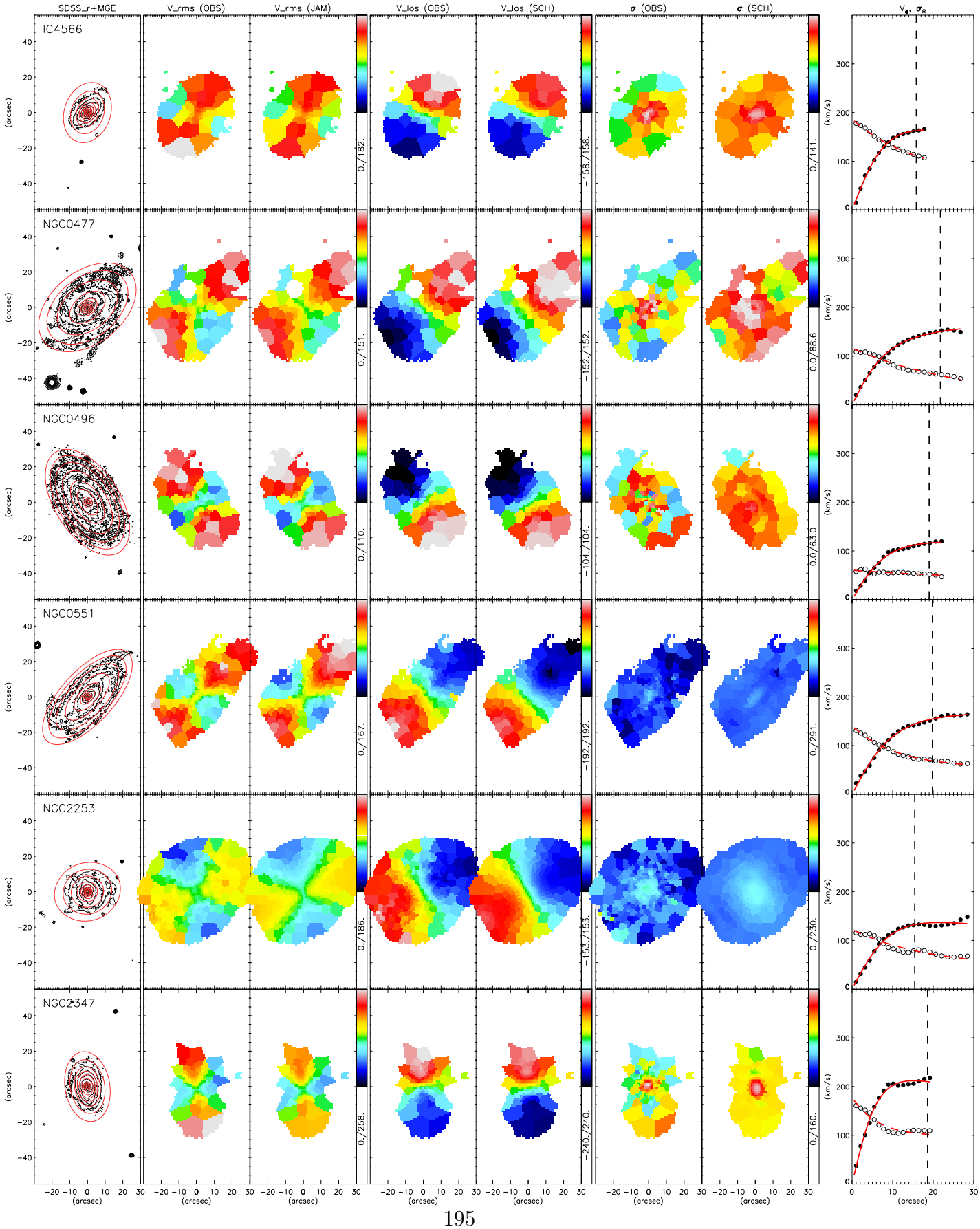
SDSS_r+MGE
V_rms (OBS)
V_rms (JAM)
V_los (OBS)
V_los (SCH)
σ (OBS)
σ (SCH)
V_φ, σ_R
IC4566
NGC0477
NGC0496
NGC0551
NGC2253
NGC2347
(arcsec)
(km/s)
0./182.
−158./158.
0./141.
0./151.
−152./152.
0.0/88.6
0./110.
−104./104.
0.0/63.0
0./167.
−192./192.
0./291.
0./186.
−153./153.
0./230.
0./258.
−240./240.
0./160.

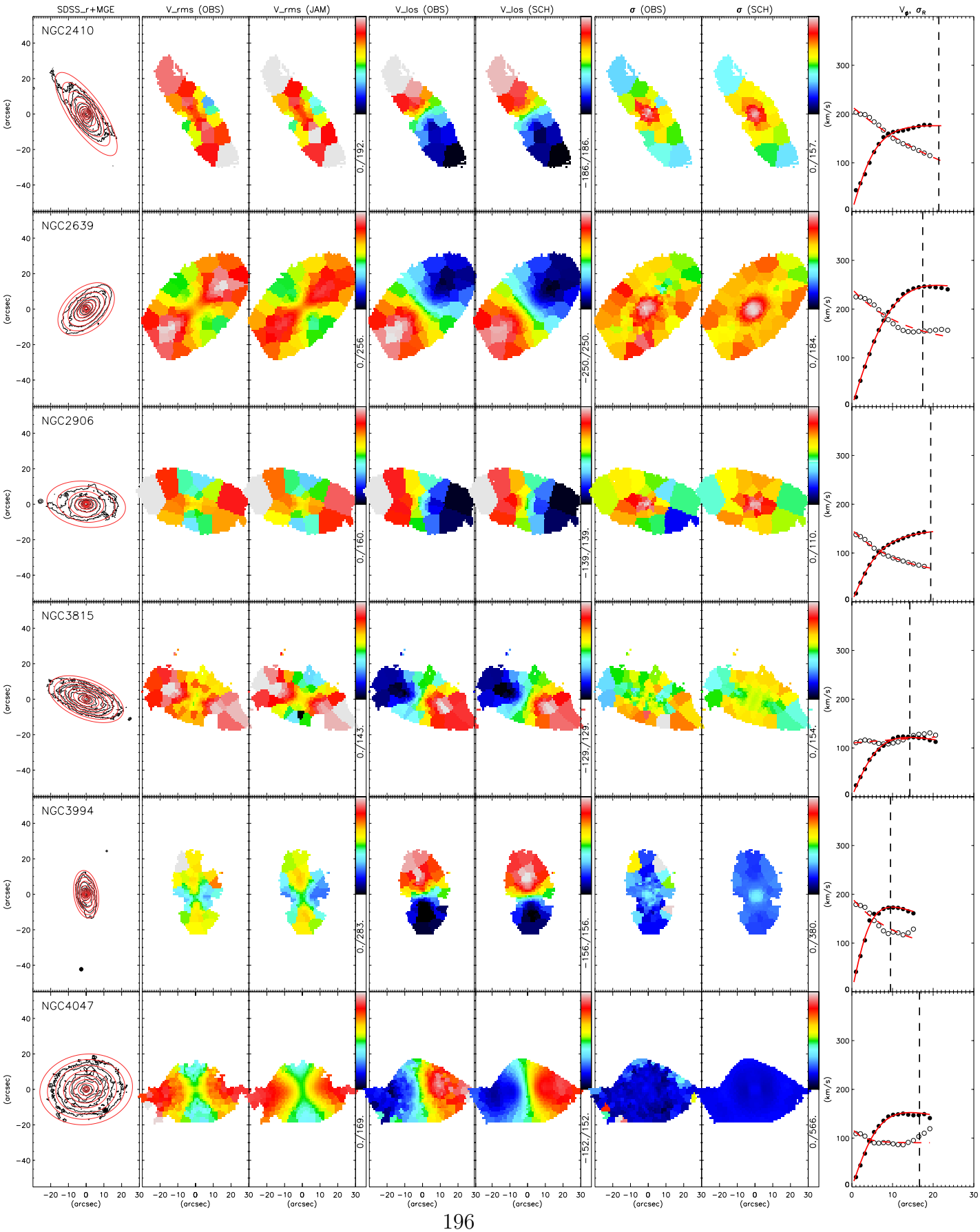
SDSS_r+MGE
V_rms (OBS)
V_rms (JAM)
V_los (OBS)
V_los (SCH)
σ (OBS)
σ (SCH)
V_φ, σ_R
NGC2410
NGC2639
NGC2906
NGC3815
NGC3994
NGC4047
(arcsec)
(km/s)
0./192.
−186./186.
0./157.
0./256.
−250./250.
0./184.
0./160.
−139./139.
0./110.
0./143.
−129./129.
0./154.
0./283.
−156./156.
0./380.
0./169.
−152./152.
0./566.

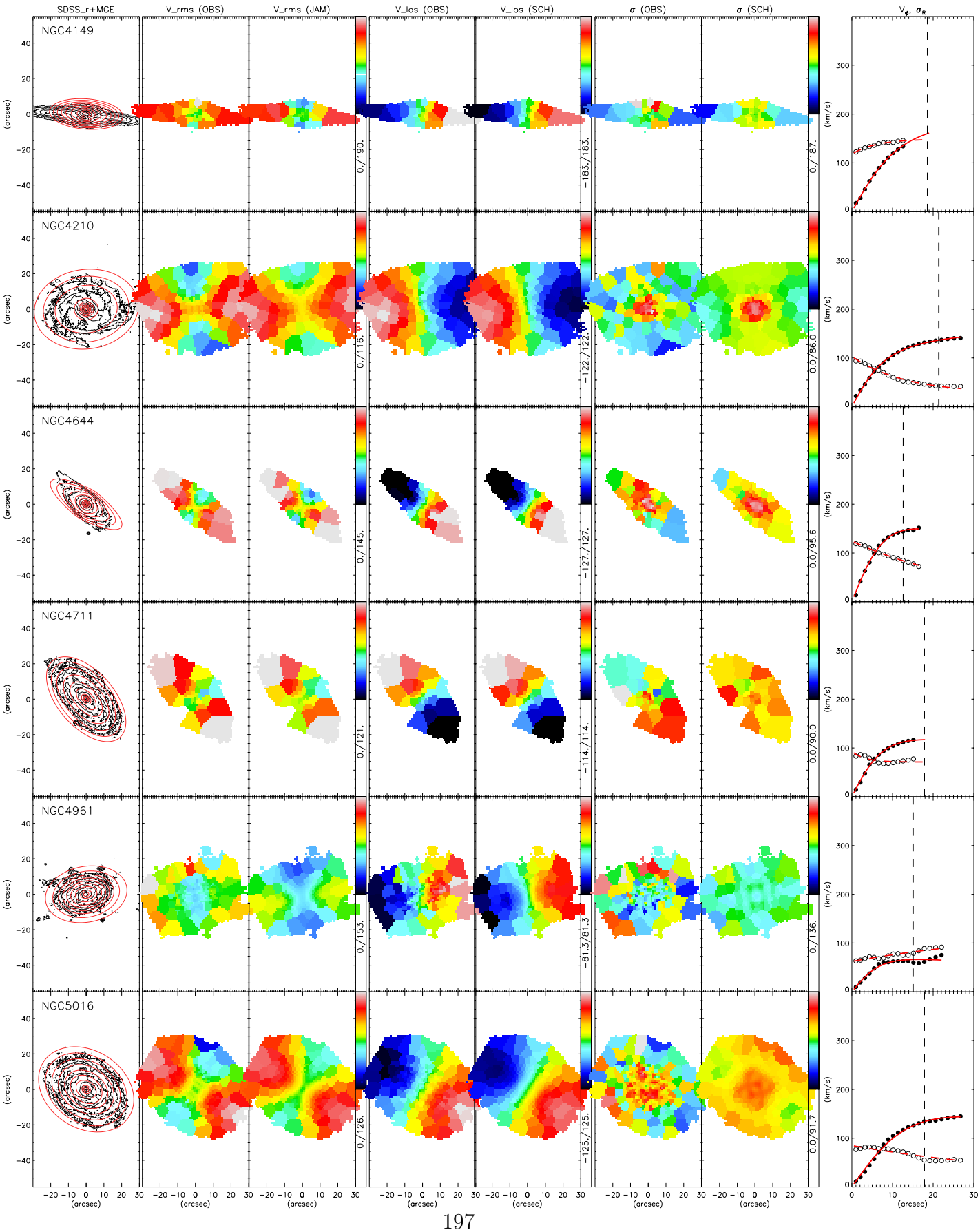
SDSS_r+MGE
V_rms (OBS)
V_rms (JAM)
V_los (OBS)
V_los (SCH)
σ (OBS)
σ (SCH)
V_φ, σ_R
NGC4149
NGC4210
NGC4644
NGC4711
NGC4961
NGC5016
(arcsec)
(km/s)
0./190.
−183./183.
0./187.
0./116.
−122./122.
0.0/86.0
0./145.
−127./127.
0.0/95.6
0./121.
−114./114.
0.0/90.0
0./153.
−81.3/81.3
0./136.
0./126.
−125./125.
0.0/91.7

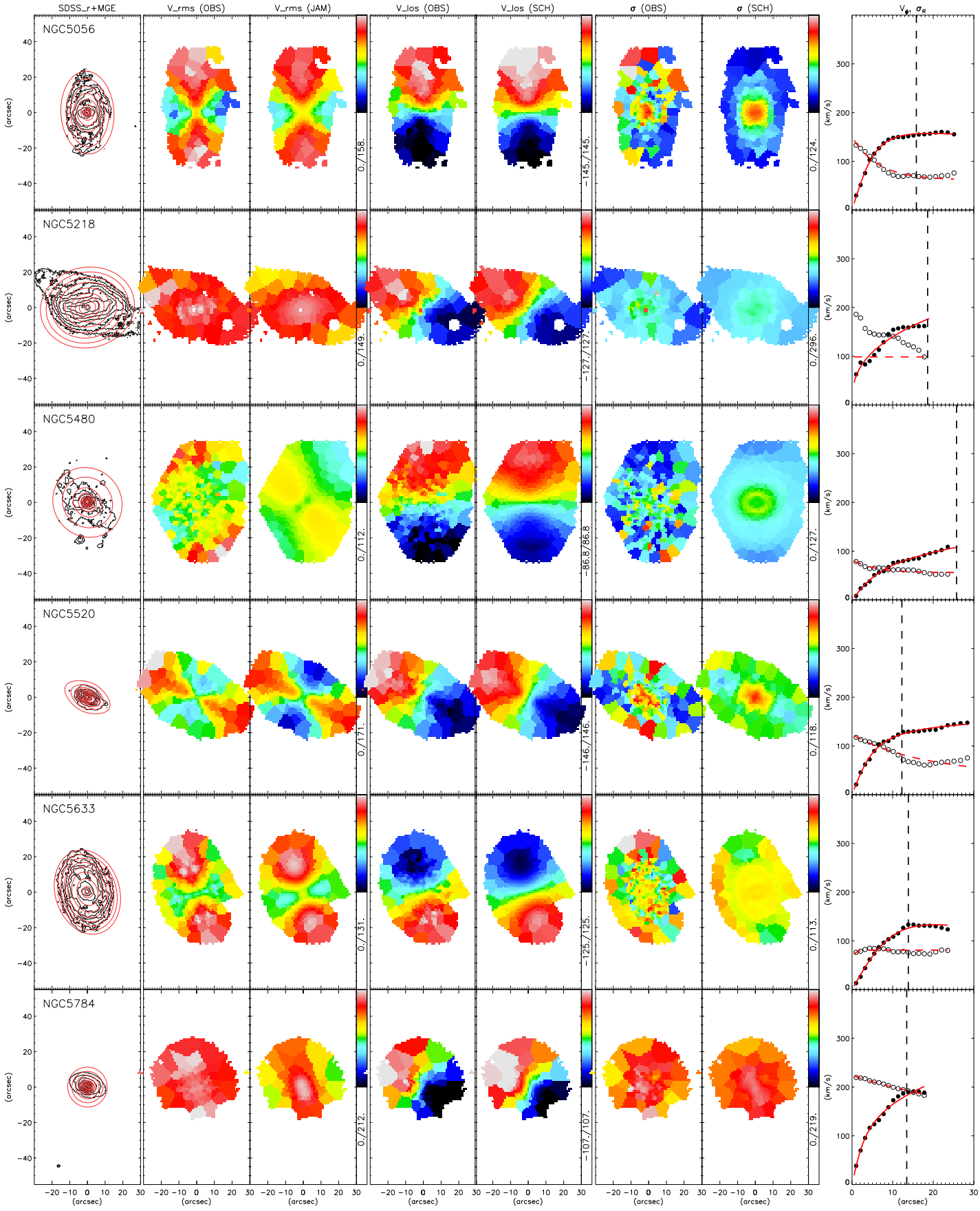
SDSS_r+MGE
V_rms (OBS)
V_rms (JAM)
V_los (OBS)
V_los (SCH)
σ (OBS)
σ (SCH)
V_φ, σ_R
NGC5056
NGC5218
NGC5480
NGC5520
NGC5633
NGC5784
(arcsec)
(km/s)
0./158.
−145./145.
0./124.
0./149.
−127./127.
0./296.
0./112.
−86.8/86.8
0./127.
0./171.
−146./146.
0./118.
0./131.
−125./125.
0./113.
0./212.
−107./107.
0./219.

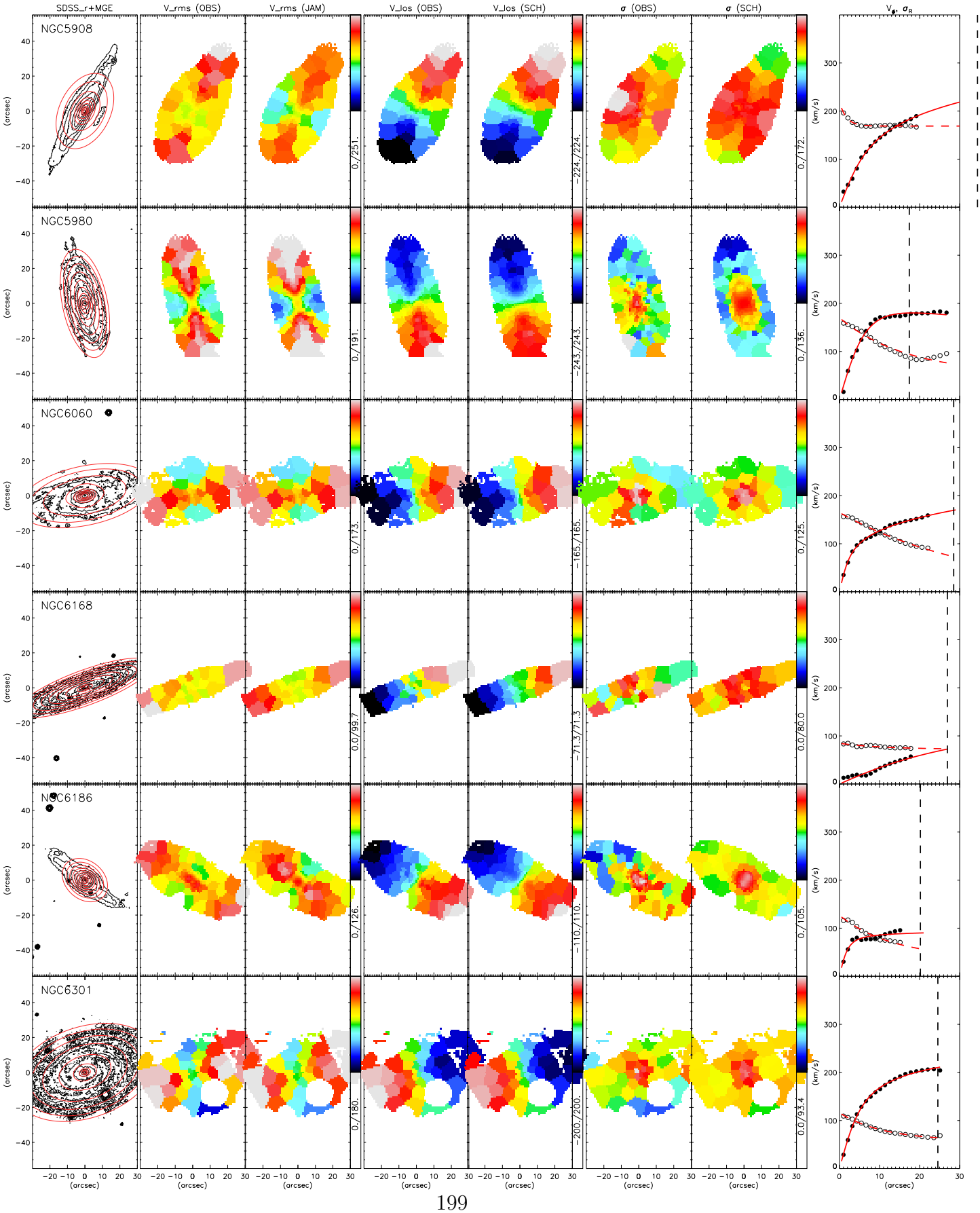
SDSS_r+MGE
V_rms (OBS)
V_rms (JAM)
V_los (OBS)
V_los (SCH)
σ (OBS)
σ (SCH)
V_φ, σ_R
NGC5908
NGC5980
NGC6060
NGC6168
NGC6186
NGC6301
(arcsec)
(km/s)
0./251.
−224./224.
0./172.
0./191.
−243./243.
0./136.
0./173.
−165./165.
0./125.
0.0/99.7
−71.3/71.3
0.0/80.0
0./126.
−110./110.
0./105.
0./180.
−200./200.
0.0/93.4

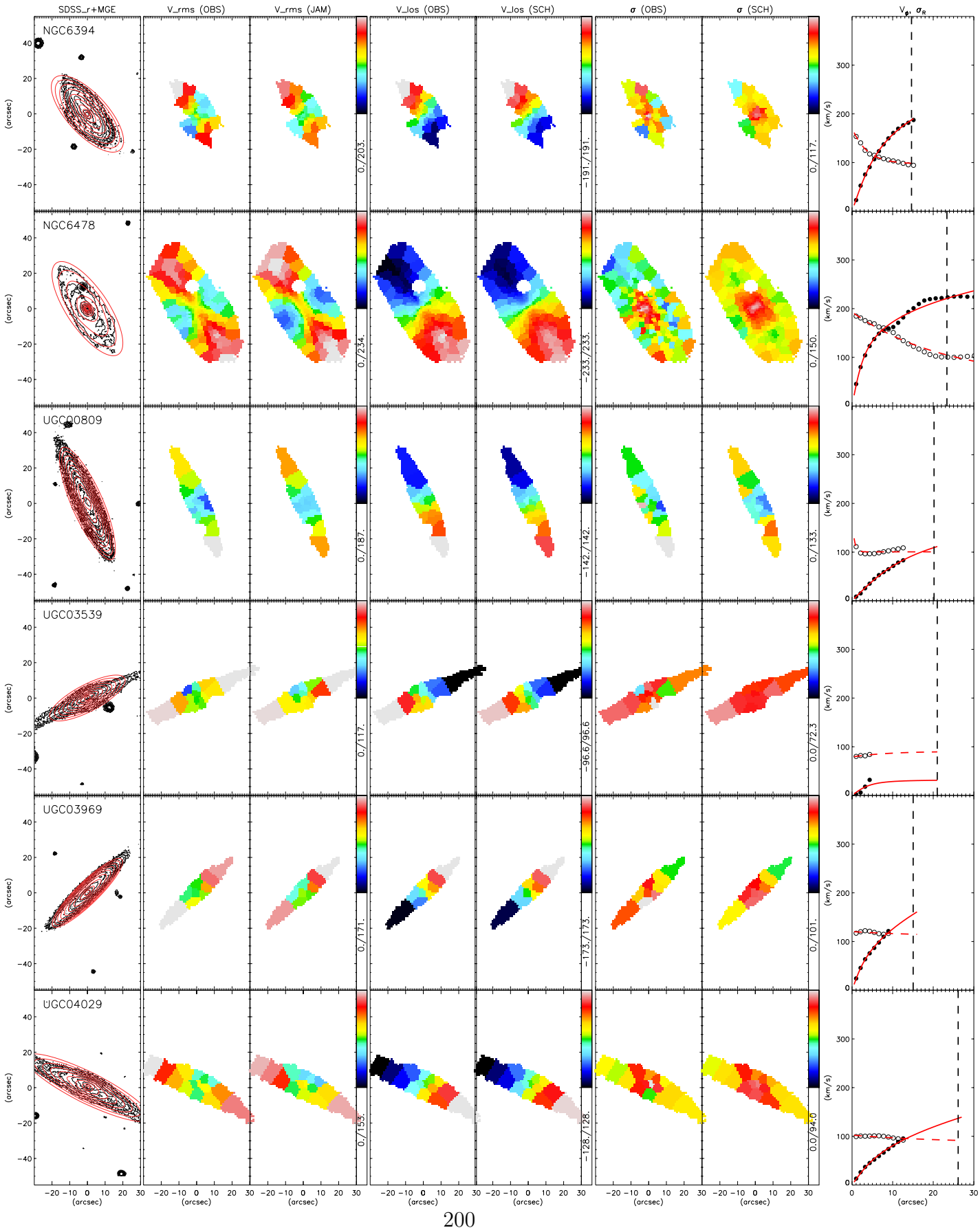
SDSS_r+MGE
V_rms (OBS)
V_rms (JAM)
V_los (OBS)
V_los (SCH)
σ (OBS)
σ (SCH)
V_φ, σ_R
NGC6394
NGC6478
UGC00809
UGC03539
UGC03969
UGC04029
(arcsec)
(km/s)
0./203.
-191./191.
0./117.
0./234.
-233./233.
0./150.
0./187.
-142./142.
0./133.
0./117.
-96.6/96.6
0.0/72.3
0./171.
-173./173.
0./101.
0./153.
-128./128.
0.0/94.0

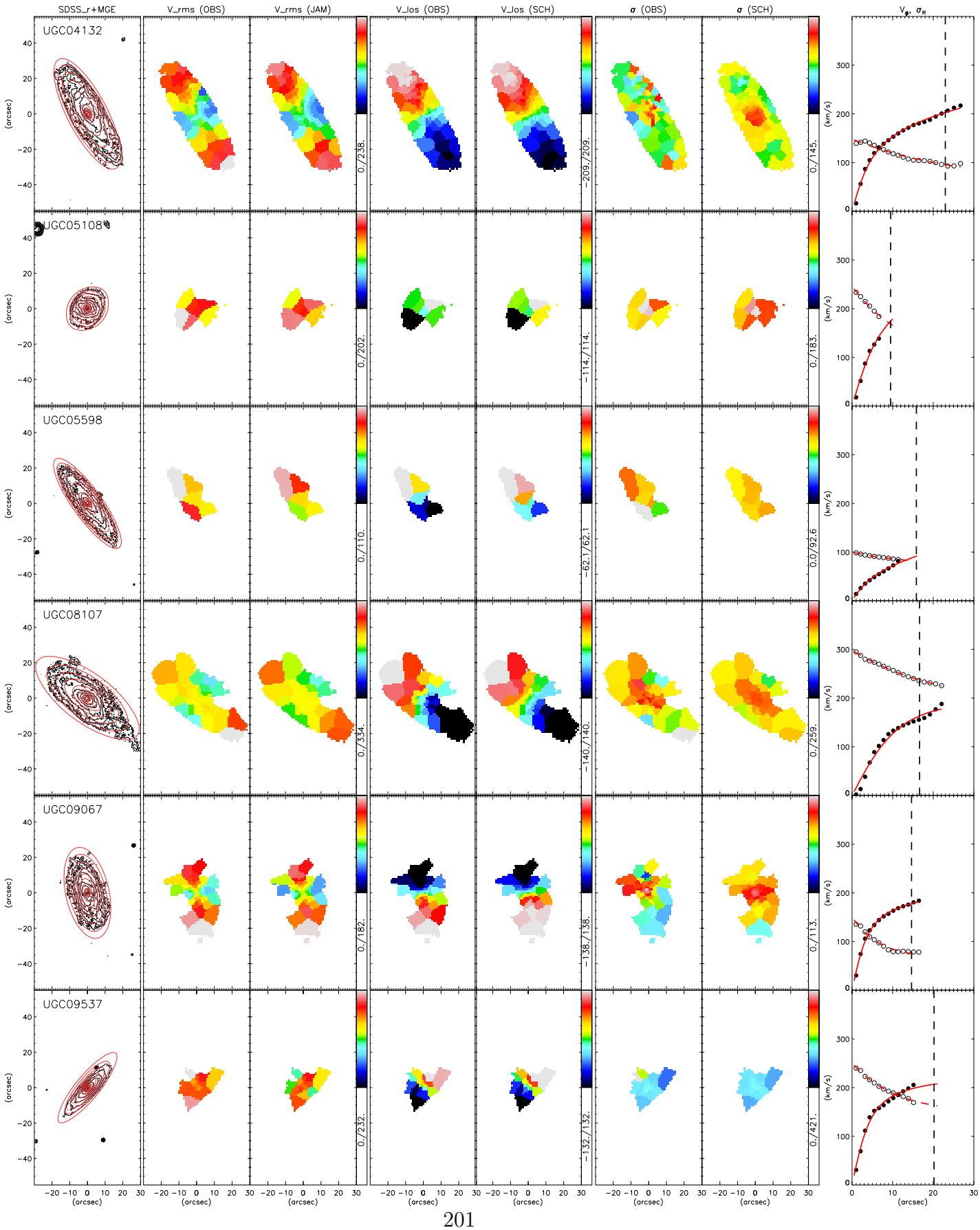
SDSS_r+MGE
V_rms (OBS)
V_rms (JAM)
V_los (OBS)
V_los (SCH)
σ (OBS)
σ (SCH)
V_φ, σ_R
UGC04132
UGC05108
UGC05598
UGC08107
UGC09067
UGC09537
(arcsec)
(km/s)
0./238.
−209./209.
0./145.
0./202.
−114./114.
0./183.
0./110.
−62.1/62.1
0.0/92.6
0./334.
−140./140.
0./259.
0./182.
−138./138.
0./113.
0./232.
−132./132.
0./421.

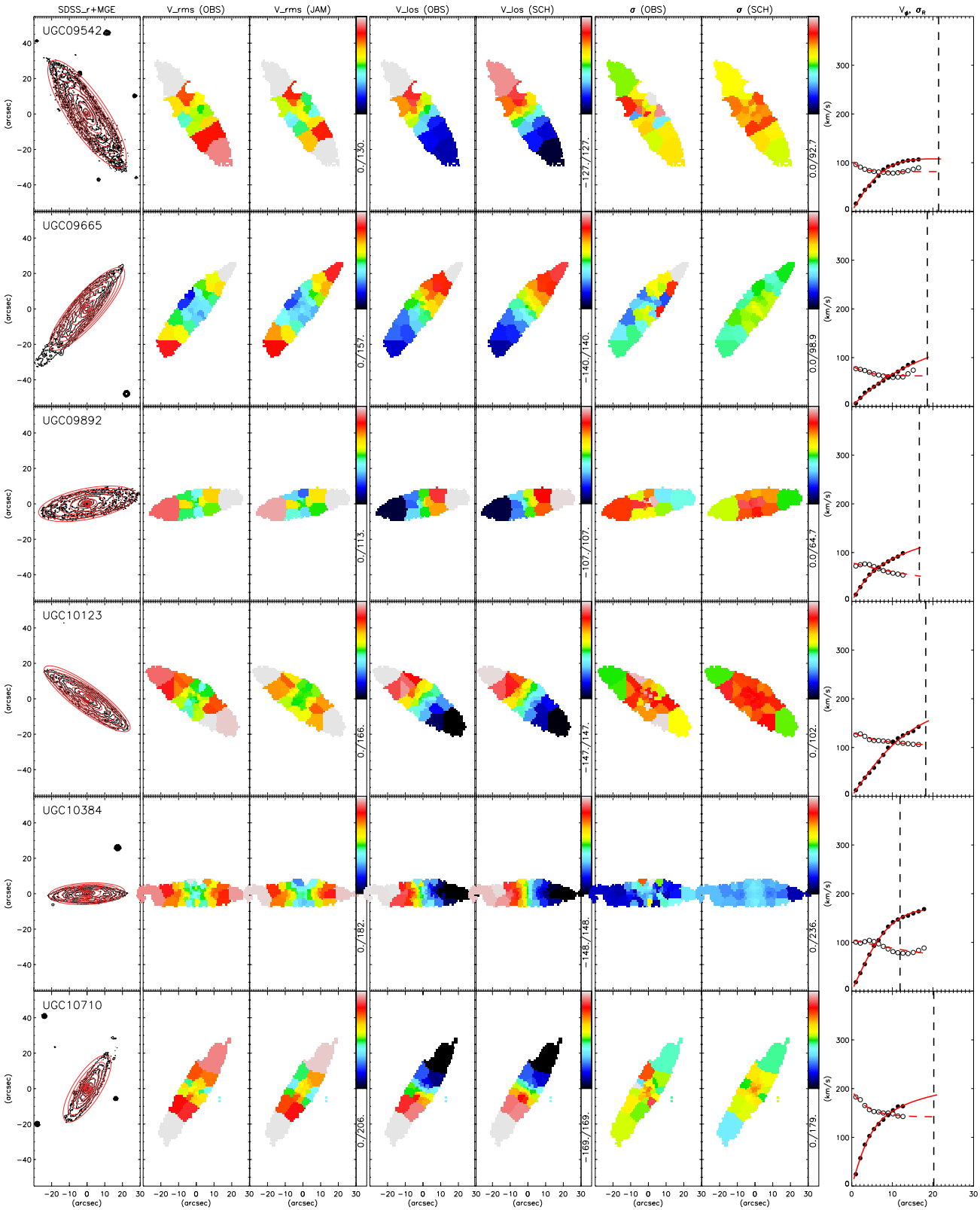

Figure A.4: The eight figures for each galaxy from left to right are: (1) observed SDSS r-band image in black and the fitted MGEs over-plotted in red contours, (2) observed $V_{\rm rms}$, (3) best-fitted JAM $V_{\rm rms}$, (4) observed $V_{\rm los}$, (5) best-fitted Schwarzschild modelled $V_{\rm los}$, (6) observed σ, (7) best-fitted Schwarzschild modelled σ, all colour coded in scales of $\rm km\,s^{-1}$ as denoted by the colour bars; (8) the extracted observed kinematics: V_ϕ and σ_R plotted in filled and open circles respectively. The fitted form used in ADC as mentioned in the main text are over-plotted in solid red lines for V_ϕ and red dashed lines for σ_R (for $\beta = 0.5$). The vertical dashed line represent $1\,R_e$.

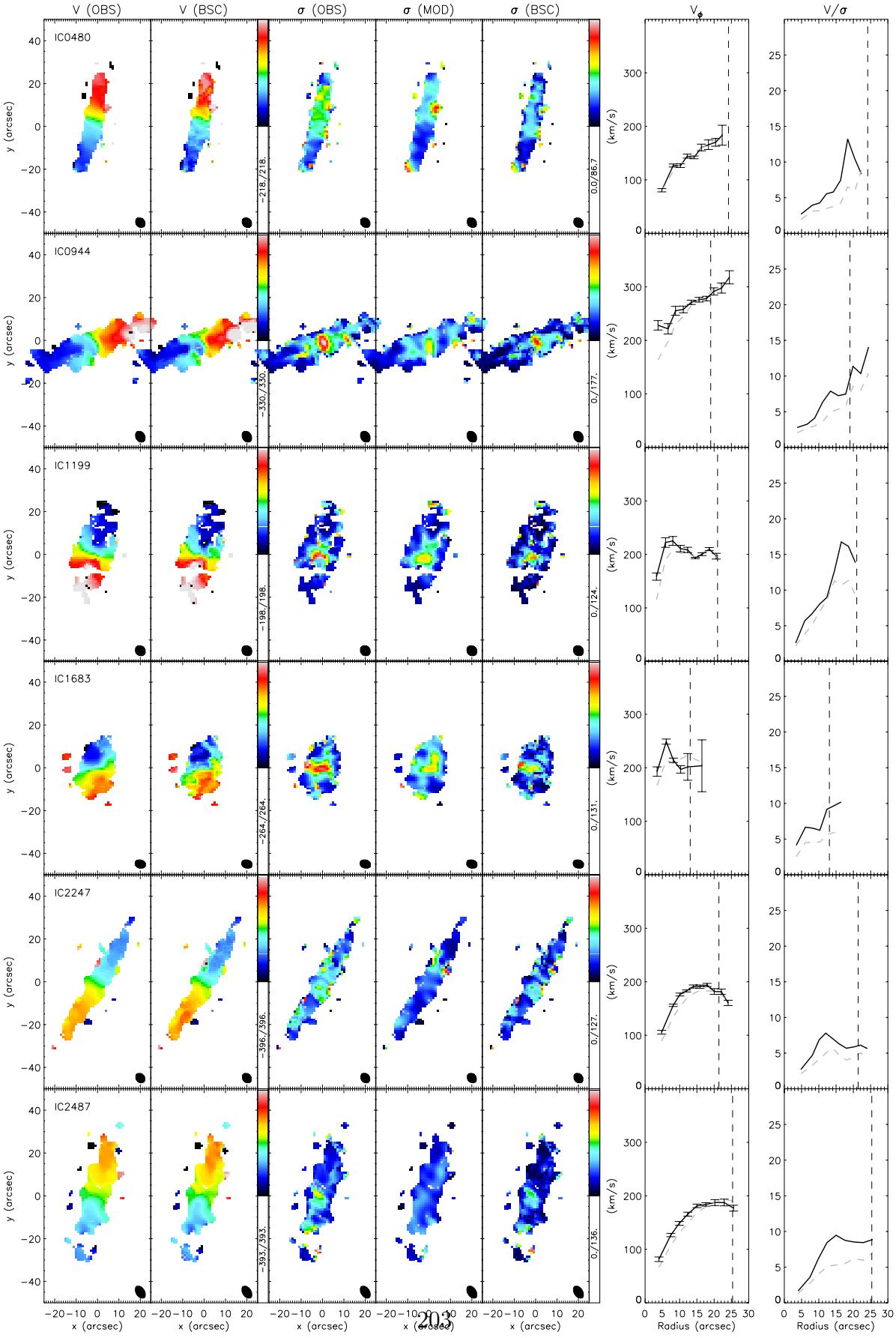
V (OBS)
V (BSC)
σ (OBS)
σ (MOD)
σ (BSC)
V_φ
V/σ
IC0480
IC0944
IC1199
IC1683
IC2247
IC2487
y (arcsec)
x (arcsec)
(km/s)
Radius (arcsec)
−218./218.
0.0/86.7
−330./330.
0./177.
−198./198.
0./124.
−264./264.
0./131.
−396./396.
0./127.
−393./393.
0./136.

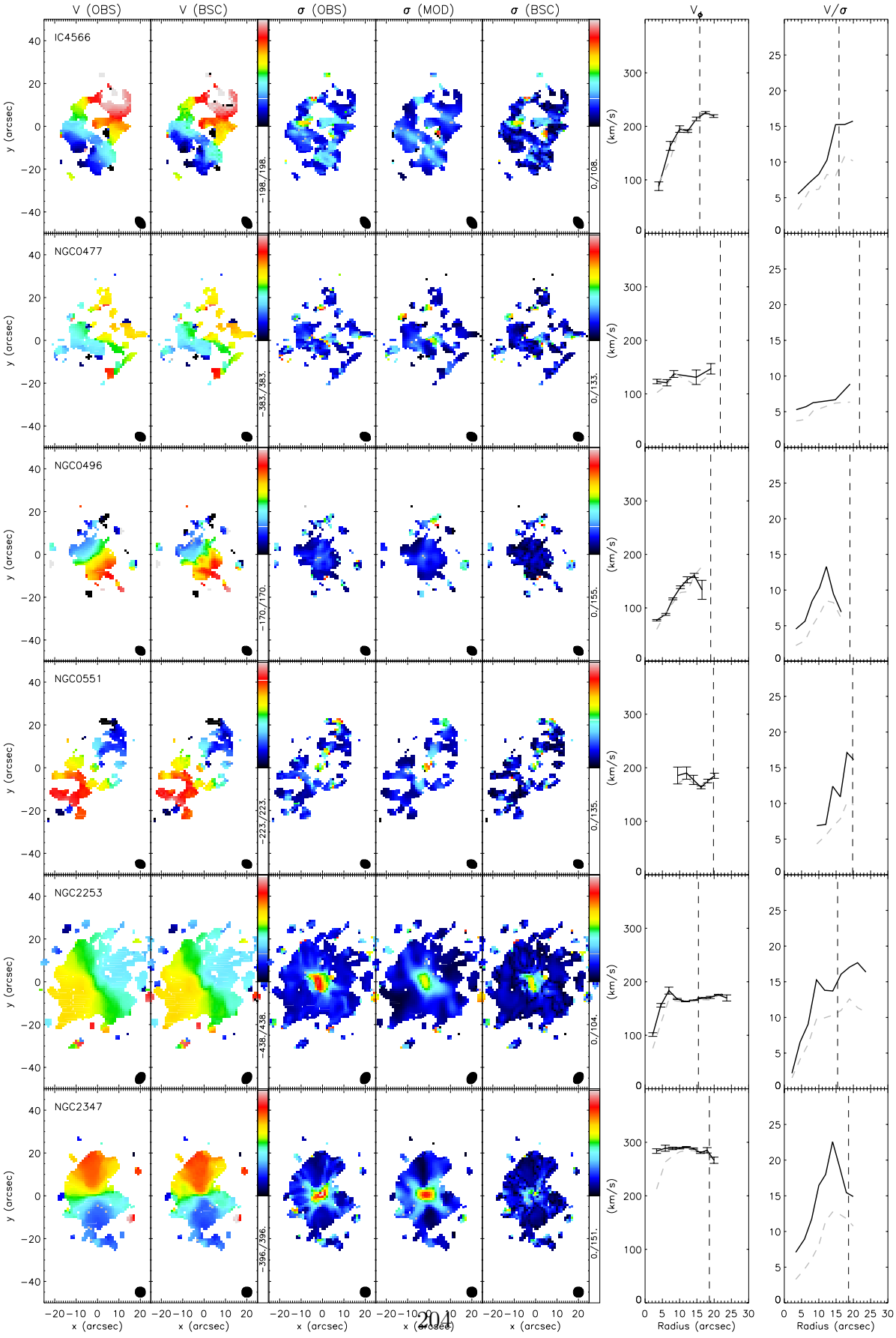
V (OBS)
V (BSC)
σ (OBS)
σ (MOD)
σ (BSC)
V_φ
V/σ
IC4566
NGC0477
NGC0496
NGC0551
NGC2253
NGC2347
y (arcsec)
x (arcsec)
(km/s)
Radius (arcsec)
−198./198.
0./108.
−383./383.
0./133.
−170./170.
0./155.
−223./223.
0./135.
−438./438.
0./104.
−396./396.
0./151.

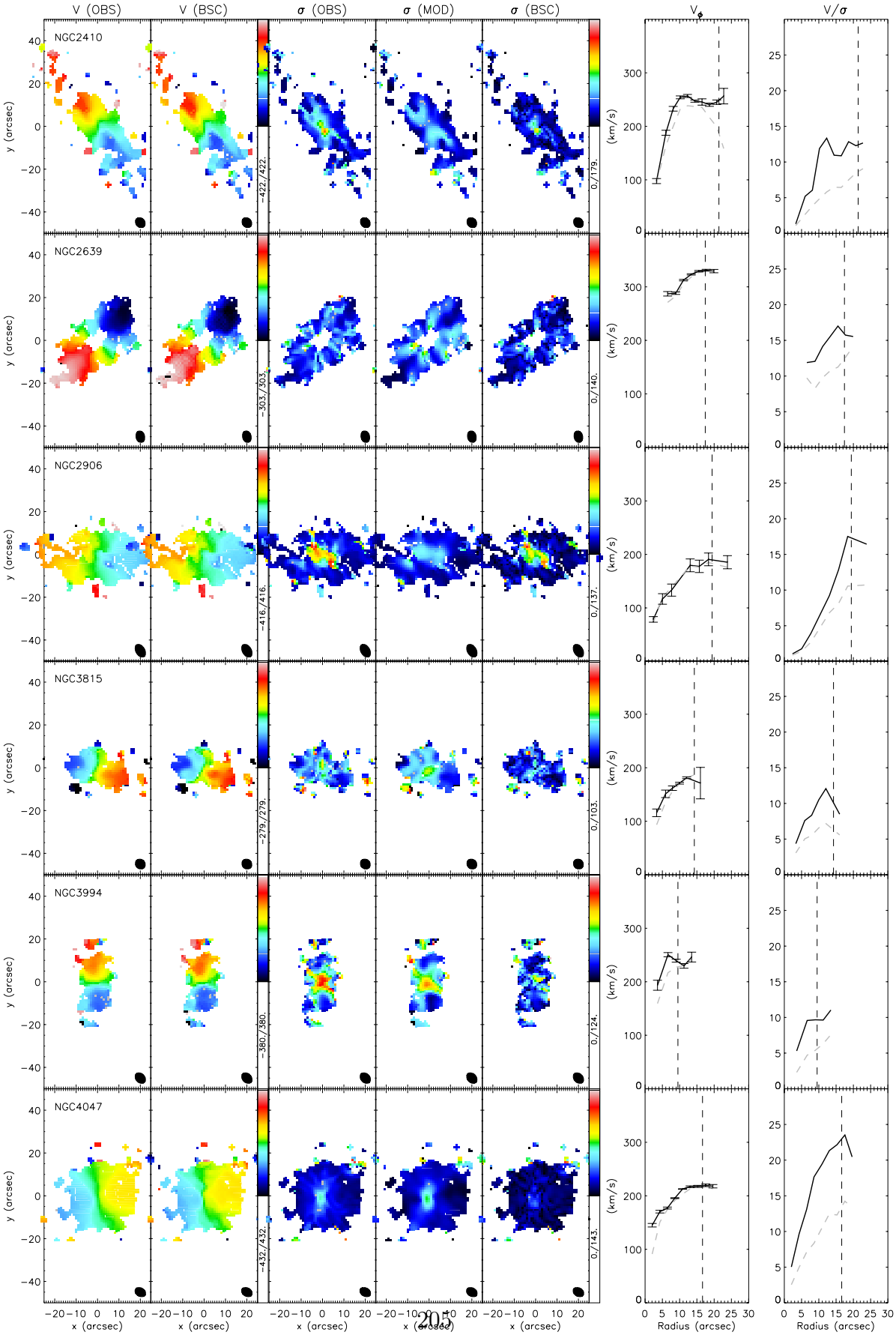
V (OBS)
V (BSC)
σ (OBS)
σ (MOD)
σ (BSC)
V_φ
V/σ
NGC2410
NGC2639
NGC2906
NGC3815
NGC3994
NGC4047
y (arcsec)
x (arcsec)
(km/s)
Radius (arcsec)
−422./422.
0./179.
−303./303.
0./140.
−416./416.
0./137.
−279./279.
0./103.
−380./380.
0./124.
−432./432.
0./143.

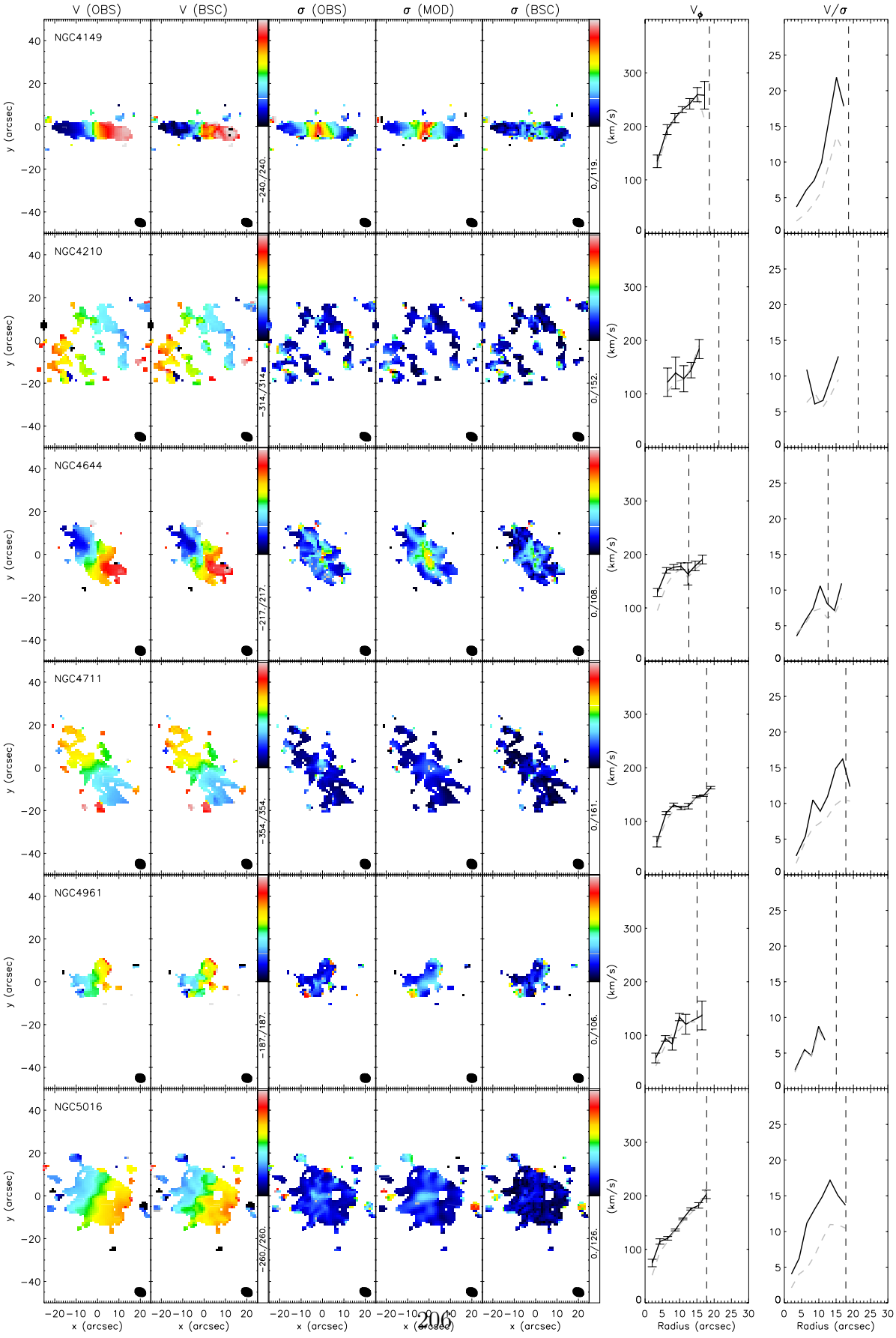
V (OBS)
V (BSC)
σ (OBS)
σ (MOD)
σ (BSC)
V_φ
V/σ
NGC4149
NGC4210
NGC4644
NGC4711
NGC4961
NGC5016
y (arcsec)
x (arcsec)
(km/s)
Radius (arcsec)
−240./240.
0./119.
−314./314.
0./152.
−217./217.
0./108.
−354./354.
0./161.
−187./187.
0./106.
−260./260.
0./126.

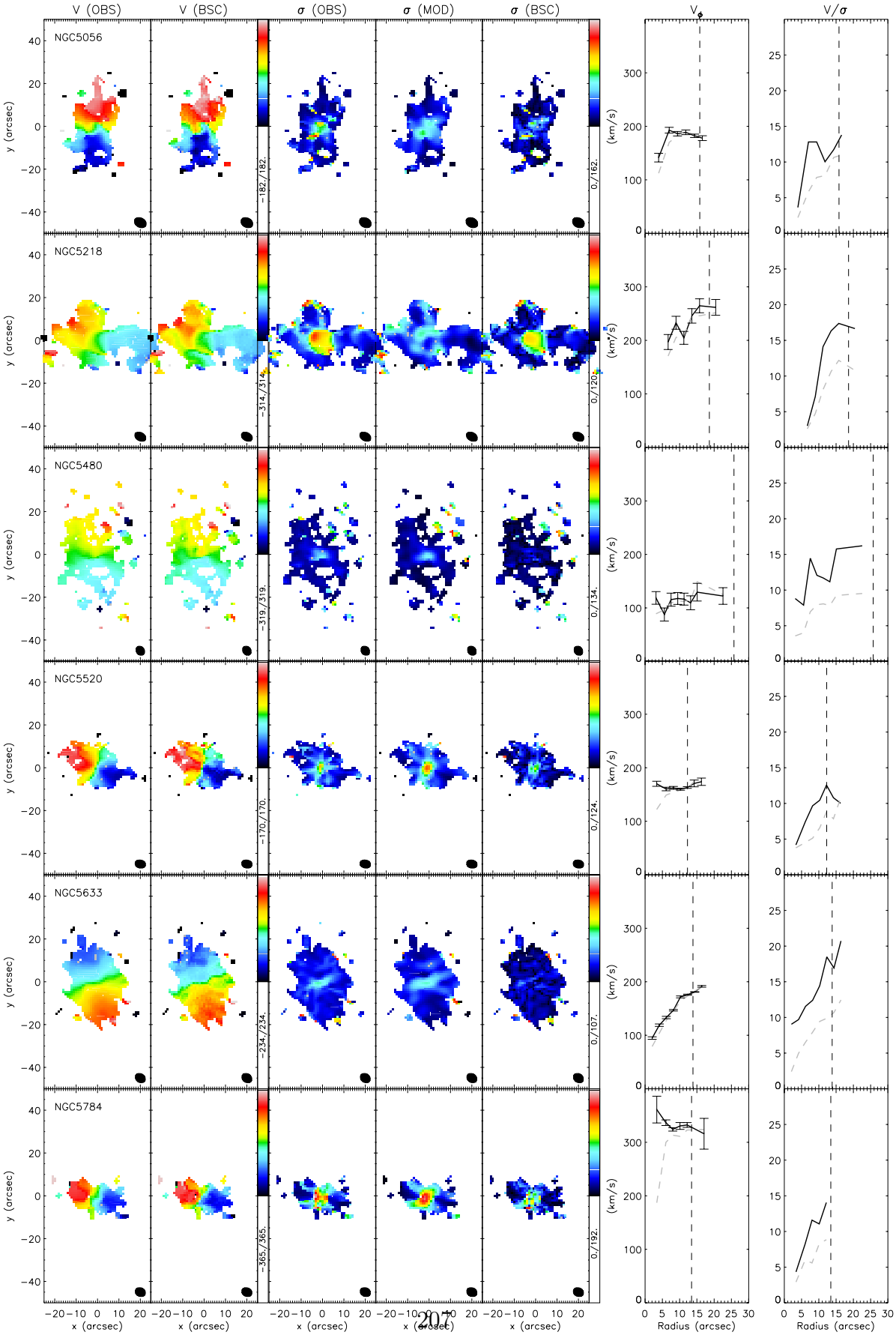
V (OBS)
V (BSC)
σ (OBS)
σ (MOD)
σ (BSC)
V_φ
V/σ
NGC5056
NGC5218
NGC5480
NGC5520
NGC5633
NGC5784
y (arcsec)
x (arcsec)
(km/s)
Radius (arcsec)
−182./182.
0./162.
−314./314.
0./120.
−319./319.
0./134.
−170./170.
0./124.
−234./234.
0./107.
−365./365.
0./192.

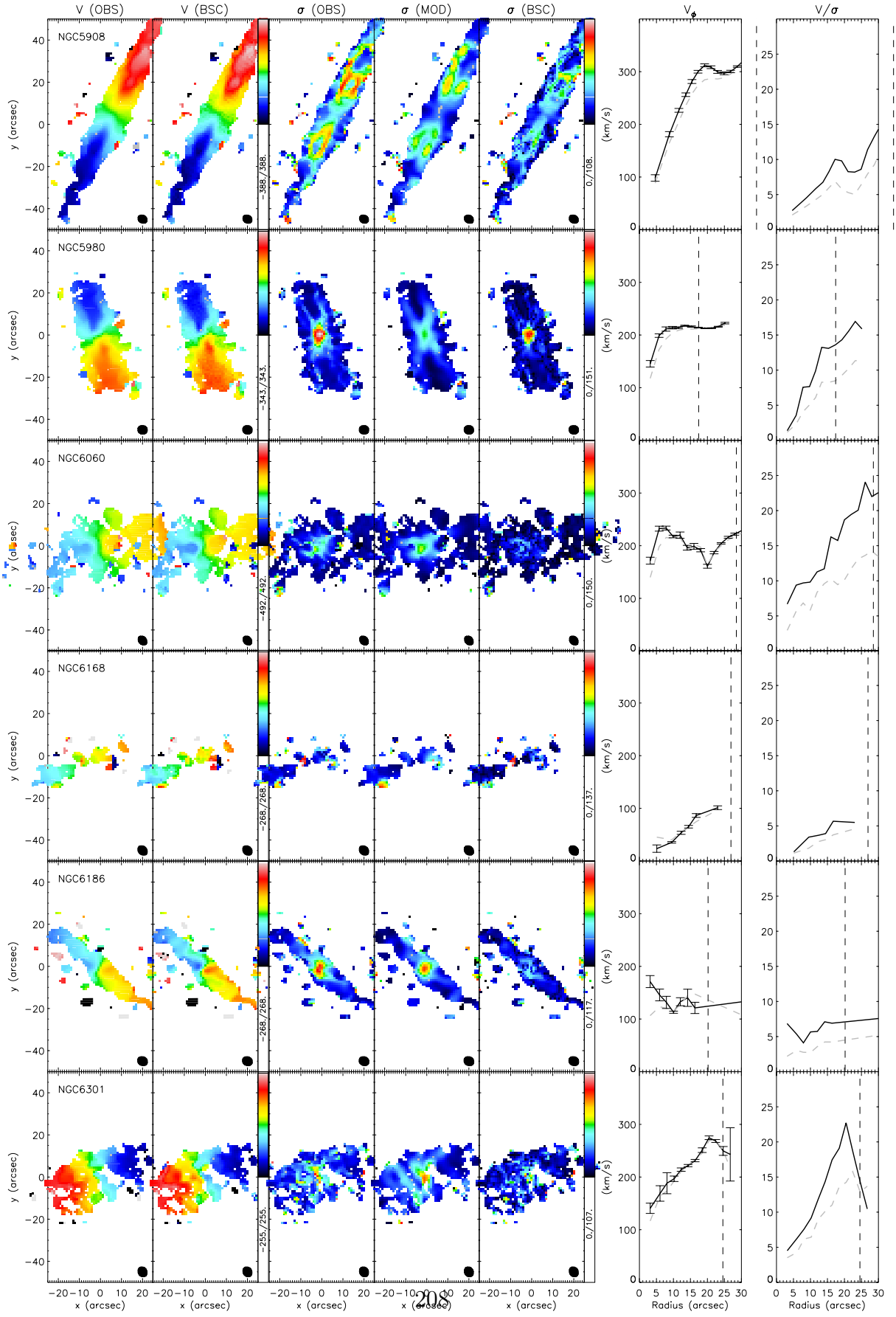
V (OBS)
V (BSC)
σ (OBS)
σ (MOD)
σ (BSC)
V_φ
V/σ
NGC5908
NGC5980
NGC6060
NGC6168
NGC6186
NGC6301
y (arcsec)
x (arcsec)
(km/s)
Radius (arcsec)
−388./388.
0./108.
−343./343.
0./151.
−492./492.
0./150.
−268./268.
0./137.
−268./268.
0./117.
−255./255.
0./107.

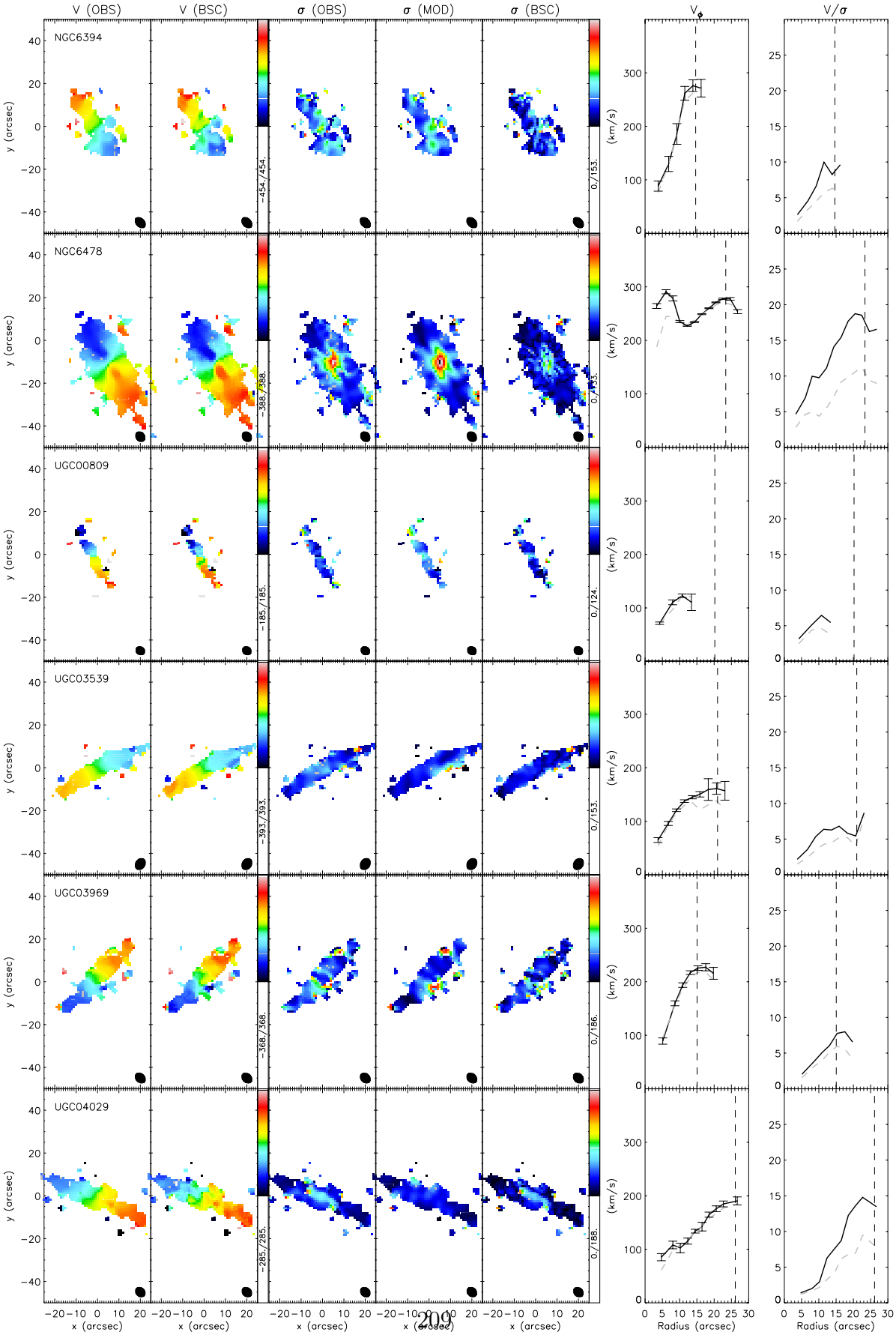
V (OBS)
V (BSC)
σ (OBS)
σ (MOD)
σ (BSC)
V_φ
V/σ
NGC6394
NGC6478
UGC00809
UGC03539
UGC03969
UGC04029
y (arcsec)
x (arcsec)
(km/s)
Radius (arcsec)
−454./454.
0./153.
−388./388.
0./183.
−185./185.
0./124.
−393./393.
0./153.
−368./368.
0./186.
−285./285.
0./188.

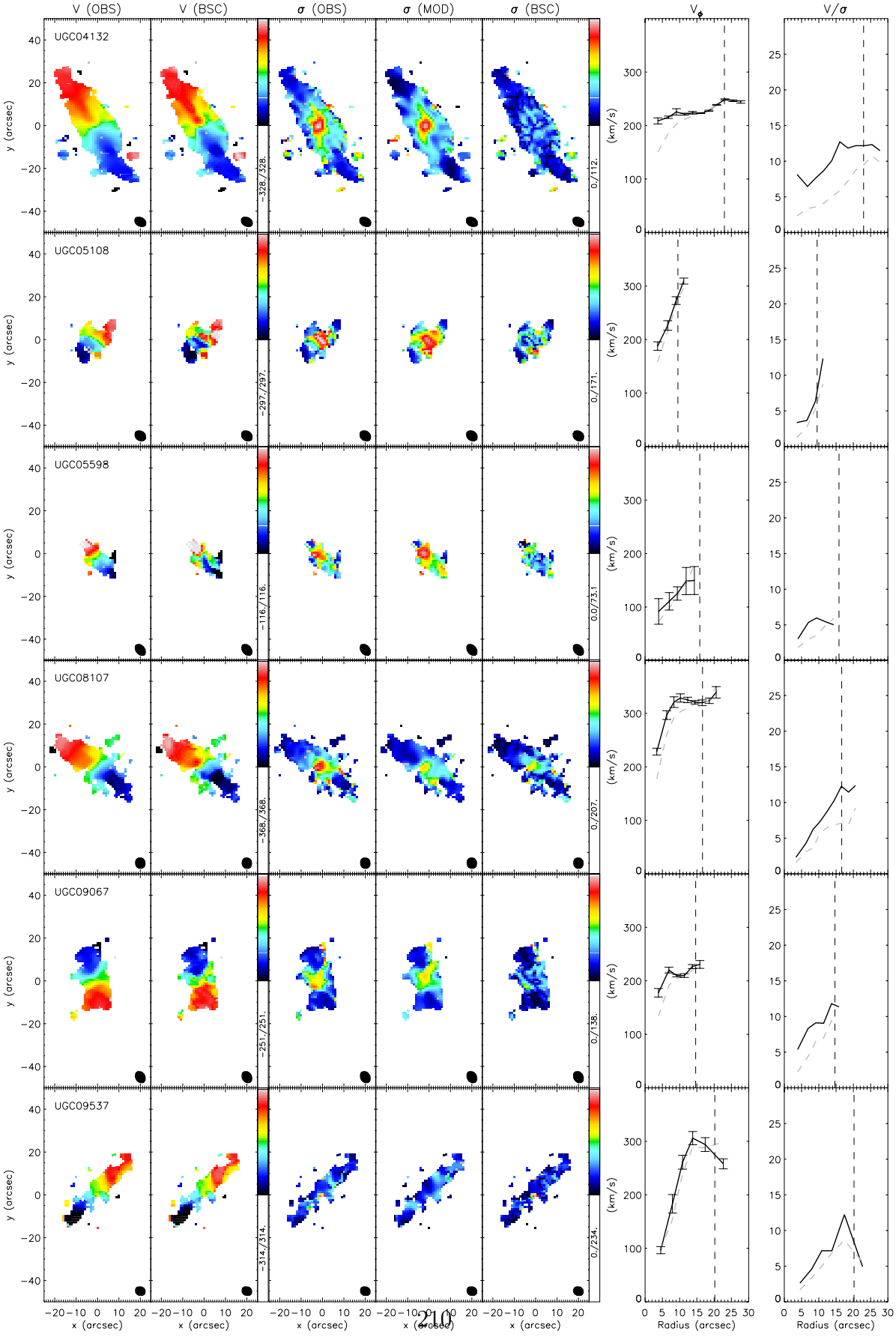
V (OBS)
V (BSC)
σ (OBS)
σ (MOD)
σ (BSC)
V_φ
V/σ
UGC04132
UGC05108
UGC05598
UGC08107
UGC09067
UGC09537
y (arcsec)
x (arcsec)
(km/s)
Radius (arcsec)
−328./328.
0./112.
−297./297.
0./171.
−116./116.
0.0/73.1
−368./368.
0./207.
−251./251.
0./138.
−314./314.
0./234.

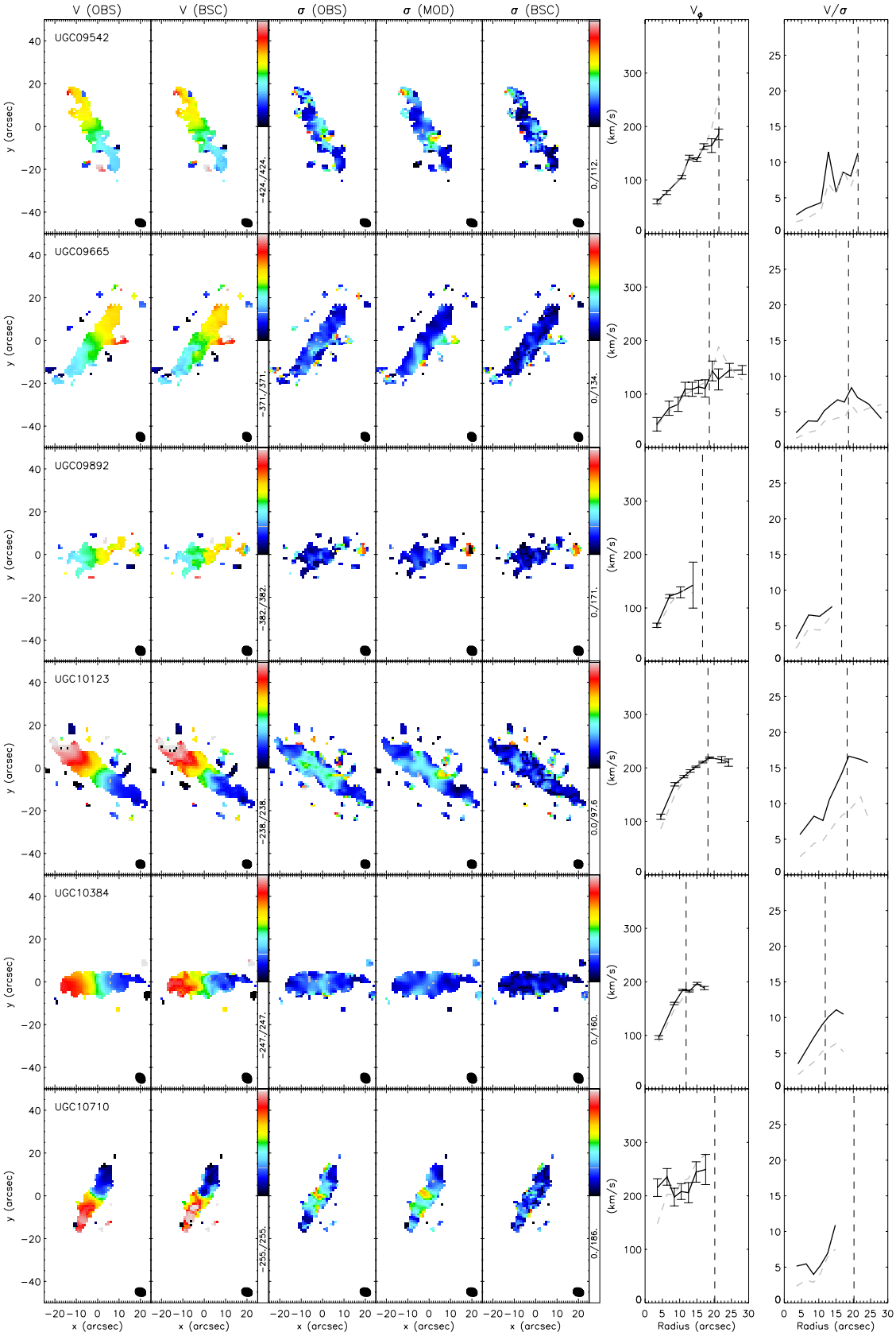

Figure A.5: The seven figures for each galaxy from left to right are: (1) observed velocity field, (2), beam-smearing corrected velocity field, (3) observed dispersion field, (4) modelled dispersion field, (5) beam-smeared corrected dispersion field, all colour-coded in units of $\mathrm{km\,s^{-1}}$; (6) CO rotation curve and (7) V/σ_{CO} plot, where the grey line represent the observed value and the solid black line represent the corrected value, and the vertical dashed line marks the effective radius.

Appendix B

Chapter 3 Appendix

B.1 Dependence on the chosen density profile of kinematic tracer

Here we investigate the effects of the chosen input surface density profile of the kinematic tracer. In the main text we have chosen the RGB star counts, fitted with an exponential profile excluding the inner region ($\sim 5'$) of the galaxy that might be affected by crowding, to represent the density profile of the kinematic tracer, as shown in Figure 3.2 and the corresponding MGEs listed in Table 3.3. We label this profile as 'Rexp'. We then rerun the discrete Jeans models on four other density profiles: (1) the uncorrected RGB star counts 'R', (2) total star counts with again exponentially corrected profile 'Aexp', (3) uncorrected total star counts 'A' and (4) I-band photometry, 'I'; the fitted MGE parameters of (1)-(3) are shown in Tables B.1 to B.3, and (4) in Table 3.2 in the main text. The fitting of the MGEs to the star-count profiles (1) to (3) are shown in Figure B.1. The best-fitted and 1-σ uncertainties of the MCMC parameters constrained from the discrete Jeans model made with each of the profiles are shown in Figure B.2 in black for the 'Stars only' case and in red for the 'Stars + Gas' case.

Under all the tested density profiles, a cored dark matter halo with $\gamma < 0.5$ is recovered. Furthermore, except for the models ran with I-band photometry as the kinematic tracer's density, a prolate dark matter halo with $q_{\rm DM} \gtrsim 2$ is preferred. Such a discrepancy is likely caused by the spatial scale at which the density profiles drop off. Its integrated-light nature causes the I-band photometry to drop off at a smaller scale than the other density profiles, which are by nature discrete. The I-band photometry is also shown to have a much smaller spatial coverage than our

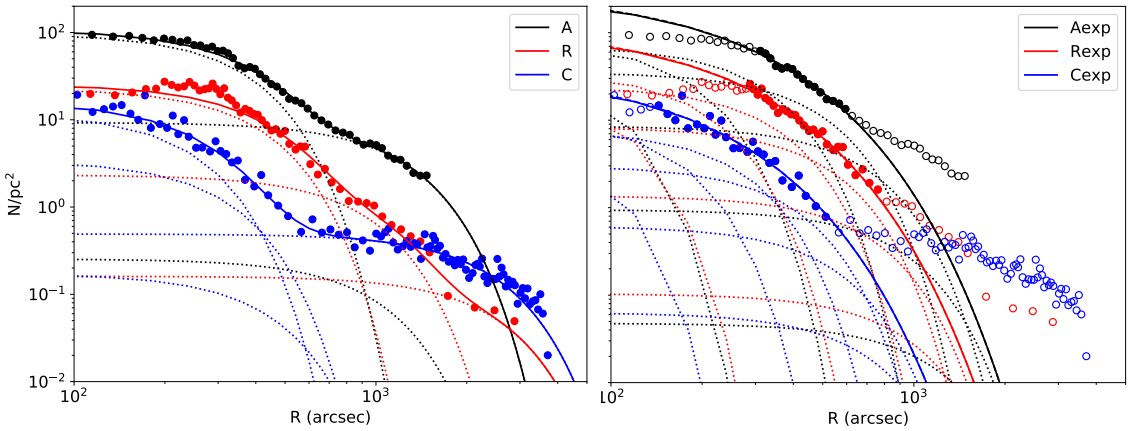

Figure B.1: Fitted MGEs to RGB stars (red) and C stars (blue), *left:* when all measurements are used and *right:* the inner measurements are disregarded to avoid bias from overcrowding, an exponential profile is fitted instead to extrapolate to the inner region. Solid circles show the observed radial profile of the number density of the respective star type. The solids line show the best fitted MGEs and the dotted lines show the individual MGEs. The MGEs fitted from RGB stars are used for both the middle-aged and old populations and the ones from C stars are used for the young population.

kinematic tracers (see Figure 3.1(c) and (d)). The derived β_z from the model using 'I' as the tracer density profile is also slightly higher than those derived using the other profiles.

B.2 Comparison to spherical Jeans Model

Here we compare the dynamical and dark matter parameters as constrained from our JAM model with spherical Jeans model that are commonly used for dwarf galaxies.

$I_{0,\star}$ $(M_\odot\,\mathrm{pc}^{-2})$	$\sigma_\star$ $(''$)	$q_\star$
1.318	278.772	0.422
0.134	622.446	0.422
9.280×10^{-3}	1660.687	0.422

Table B.1:: Multi-Gaussian Expansion of the RGB star counts ('R'), normalised to a total stellar mass of $M_\star = 1.1 \times 10^7\,M_\odot$.

$I_{0,\star}$ ($M_\odot\,pc^{-2}$)	$\sigma_\star$ ($''$)	$q_\star$
1.035	58.378	0.422
1.389	120.767	0.422
1.218	211.198	0.422
0.603	326.504	0.422
0.147	460.855	0.422
1.621×10^{-2}	607.298	0.422
8.153×10^{-4}	759.947	0.422
1.838×10^{-5}	918.728	0.422
1.156×10^{-7}	1100.052	0.422

Table B.2:: Multi-Gaussian Expansion of the exponentially corrected total star counts ('Aexp'), normalised to a total stellar mass of $M_\star = 1.1 \times 10^7\,M_\odot$.

$I_{0,\star}$ ($M_\odot\,pc^{-2}$)	$\sigma_\star$ ($''$)	$q_\star$
1.372	249.495	0.422
3.581×10^{-2}	668.103	0.422
0.131	842.278	0.422

Table B.3:: Multi-Gaussian Expansion of the total star counts ('A'), normalised to a total stellar mass of $M_\star = 1.1 \times 10^7\,M_\odot$.

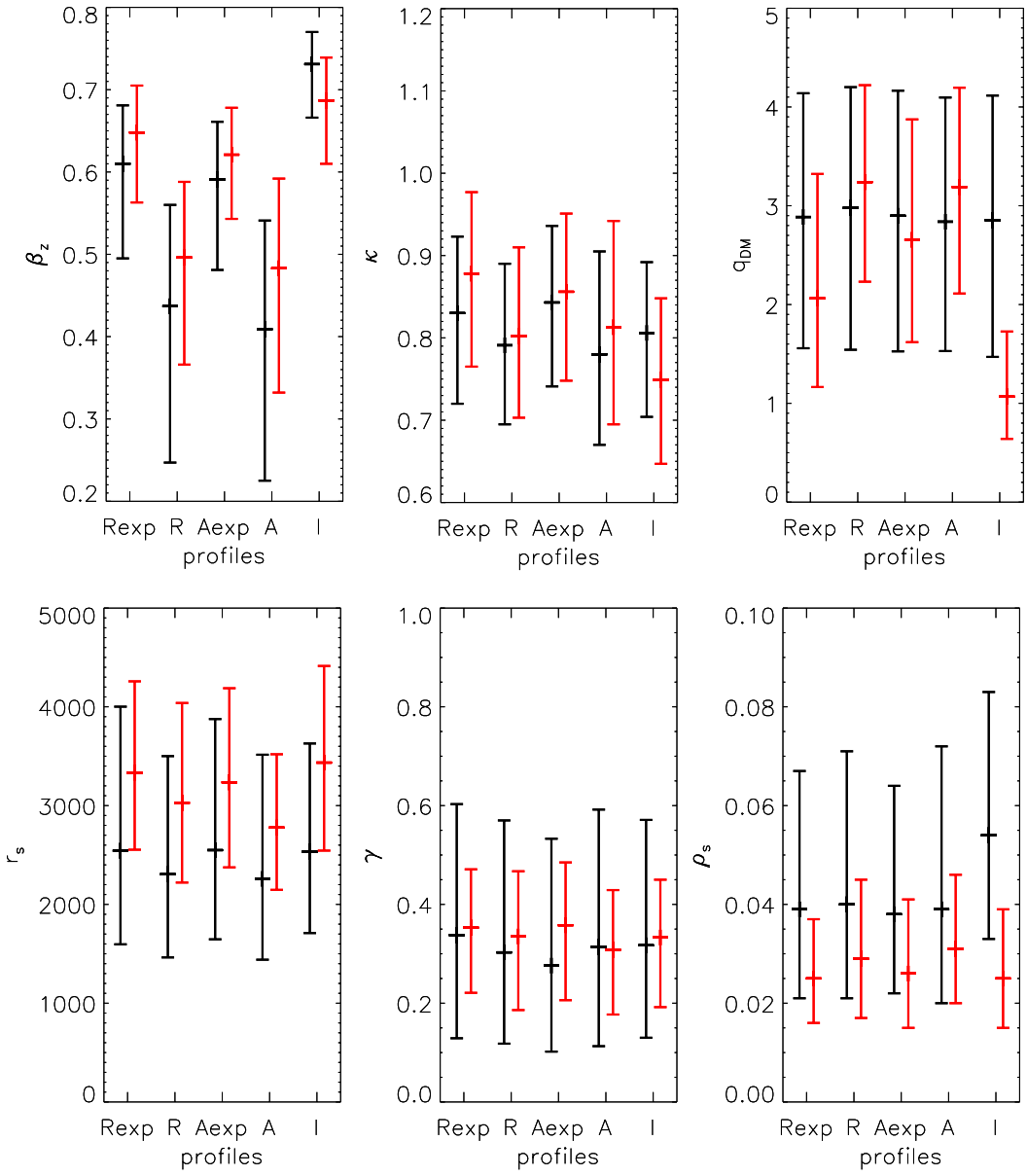

Figure B.2: Constrained parameters from discrete Jeans models using different density profiles as representation of the kinematic tracer's density profile, with black representing the results from the 'Stars only' and red representing the results from the 'Stars + Gas' models. The y-axis of each panel shows the constraints of a free parameter in the model, from left to right: velocity anisotropy β_z, κ, dark matter halo flattening $q_{\rm DM}$, dark matter halo scale radius $r_{\rm s}$, inner slope of the dark matter density profile γ and the characteristic density $\rho_{\rm s}$. The x-axis correspond to the five density profiles that we tested; 'Rexp': RGB star counts fitted with an exponential profile excluding the inner region that might be affected by crowding; 'R': RGB star counts; 'Aexp': total star counts fitted with an exponential profile excluding the inner region; 'A': total star counts; and 'I': I-band photometry.

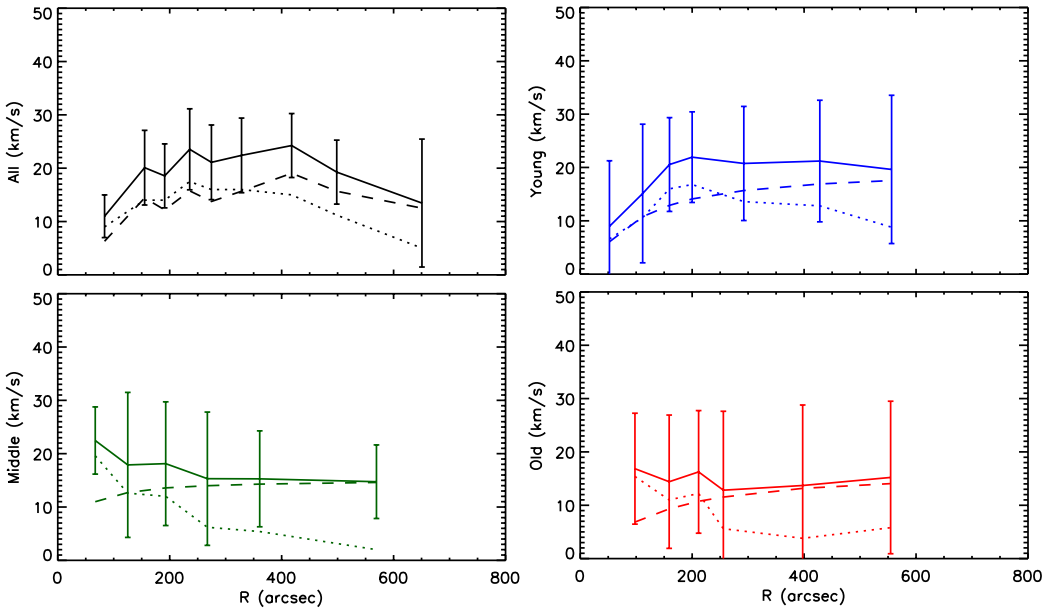

Figure B.3: Binned stellar mean velocity and velocity dispersion. *Top left*: The binned mean velocity $V_{\rm mean}$(dashed line) and velocity dispersion σ (dotted line) of all the stars in our discrete sample. The solid line show the second velocity moment $V_{\rm RMS} = \sqrt{V_{\rm mean}^2 + \sigma^2}$ as an input to the Jeans model. The binned $V_{\rm mean}$, σ and $V_{\rm RMS}$ profiles of the young *(top right)*, middle *(bottom left)* and old *(bottom right)* populations are shown in blue, green and red respectively.

We use radially binned mean velocity ($V_{\rm mean}$) and velocity dispersion (σ)of our discrete kinematics and the spherical Jeans equation, implemented using the publicly available code by Cappellari (2008). The $V_{\rm mean}$ and σ profiles are shown in dashed and dotted lines respectively on the top left panel of Figure B.3, the corresponding observed second moment $V_{\rm RMS} = \sqrt{V_{\rm mean}^2 + \sigma^2}$ and the error bars are plotted in solid lines. The gaseous and stellar MGEs used are the same as the ones listed in Table 3.1 and Table 3.2, but with $q = 1$ and renormalised to the total stellar and gaseous masses respectively. The dark matter haloes are parametrised with a gNFW profile.

We again use MCMC to fit the spherical Jeans models to the data, adopting the 'Rexp' as the density profile of the kinematic tracer with $q = 1$ for all MGEs. The number of walkers, steps and burn-in are the same as the ones we adopt in the axisymmetric case. theSince we are using binned data, there is no need to specify κ.

$I_{0,\star}$ ($M_\odot\,pc^{-2}$)	$\sigma_\star$ ($''$)	$q_\star$
2.426	54.426	0.422
2.801	107.155	0.422
1.980	178.505	0.422
0.774	263.719	0.422
0.157	358.019	0.422
1.611×10^{-1}	458.012	0.422
8.175×10^{-4}	561.771	0.422
1.982×10^{-5}	668.999	0.422
1.986×10^{-7}	782.365	0.422
4.608×10^{-10}	912.600	0.422

Table B.4:: Multi-Gaussian Expansion of the exponentially corrected C star counts ('Cexp'), normalised to a total stellar mass of $M_\star = 1.1 \times 10^7\,M_\odot$.

The relevant velocity anisotropy in the Jeans model is $\beta_\phi = \beta_\theta = 1 - \sigma_\phi^2/\sigma_R^2$.[1] The free parameters are therefore $M_\star$, β_ϕ, r_s, γ and ρ_s, we assume β_ϕ to be constant. We again perform two sets of models, one with constrains from $V_{c,HI}$ and one without. The constrained parameters are plotted in Figure B.4, in black are the models from the 'Stars only' runs and in red the models from the 'Stars + Gas' runs.

Just like in the axisymmetric models, the dark matter parameters are much better constrained when we include $V_{c,HI}$ as a constraint on the total gravitational potential. The result from the axisymmetric model of a cored dark matter halo remains robust under the spherical Jeans model, which derives a γ of $0.37^{+0.11}_{-0.14}$ in the 'Stars + Gas' case. Although β_ϕ is poorly constrained in both the 'Stars only' and the 'Stars + Gas' cases, it is confirmed here that the stars have a tangential velocity anisotropy, with $\beta_\phi(=\beta_r)$ being highly negative ($-1.67^{+1.03}_{-1.66}$ in the 'Stars + Gas' case), just as we find from our discrete JAM models. There is no significant improvement in the constraint on stellar velocity anisotropy by including $V_{c,HI}$, reaffirming our interpretation that the improvement of the constraint of β_z in the axisymmetric models when including $V_{c,HI}$ comes mainly from breaking the $q_{DM} - \beta$ degeneracy.

[1]Under spherical symmetry, this would correspond to the radial anisotropy parameter defined in Section 3.4.2: $\beta_r = \beta_\phi = \beta_\theta$.

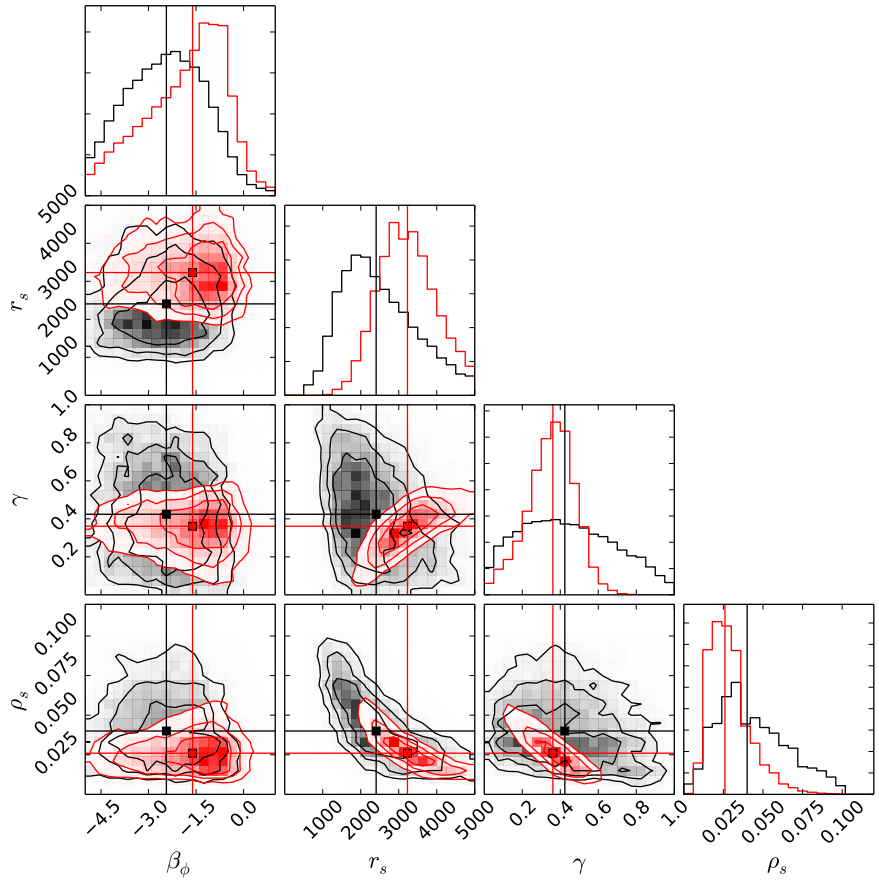

Figure B.4: Marginalised parameters from the spherical Jeans models, adopting the 'Rexp' profile as the surface density profile of the kinematic tracer: the dynamical parameters β_ϕ, and the dark matter parametersr_s, γ and ρ_s. Black contours show the marginalised parameter values with Jeans models performed on stellar kinematics only. Red contours show the ones constrained by using V_c derived from HI kinematics as a prior.

B.2.1 Multi-population spherical Jeans models

It has been shown that the stellar velocity anisotropy depends on their metallicity, and by separating the stars into a metal-rich and a metal-poor population one can obtain a better constrain on the velocity anisotropy (e.g. Battaglia et al. 2006, 2011). We test here whether we can obtain an even better constrain by adding the $V_{\rm c,HI}$ constrain to the multi-population models.

Leaman et al. (2009) have shown that the metal-rich and metal-poor populations in WLM share similar spatial distributions. Here we instead separate the stars into three populations by their ages and characterise their spatial distributions with density profiles from C and RGB stars. The C stars profile is used for the young population (<2 Gyr), the RGB stars profile used for the middle (2-10 Gyr) and old populations (>10 Gyr). We adopt here the 'Rexp' and 'Cexp' (an exponential fit to the C stars profile neglecting the inner $2'$ for which the fitted MGE parameters are listed in Table B.4) profiles which avoid issues with over-crowding of stars at the center of the galaxy. We then fit MGEs to the derived exponential profiles. The MGE fittings are shown in Figure B.1 in red for the RGB stars and blue for the C stars. The $V_{\rm mean}$, σ and $V_{\rm RMS}$ for the young, middle and old populations are shown in Figure B.3 in blue, green and red respectively. The free parameters here are the velocity anisotropies for the young, middle and old age populations: $\beta_{\phi,y}$, $\beta_{\phi,m}$ and $\beta_{\phi,o}$, and the dark matter parameters γ, $r_{\rm s}$ and $\rho_{\rm s}$.

The constrained parameters are plotted in Figure B.5, again with black showing the 'Stars only' case and red the 'Stars + Gas' case. Compared to the single-population models, only the middle-aged population shows a better constrained $\beta_{\phi,m}$ of $0.13^{+0.48}_{-1.19}$, while both the young- and old-aged populations show similar β_ϕ of $\beta_{\phi,y} = -1.16^{+1.06}_{-1.82}$ and $\beta_{\phi,o} = -1.15^{+1.34}_{-1.81}$. The derived inner slope of the DM halo in the 'Stars + Gas' case is 0.29 ± 0.12, again reaffirming the cored density profile.

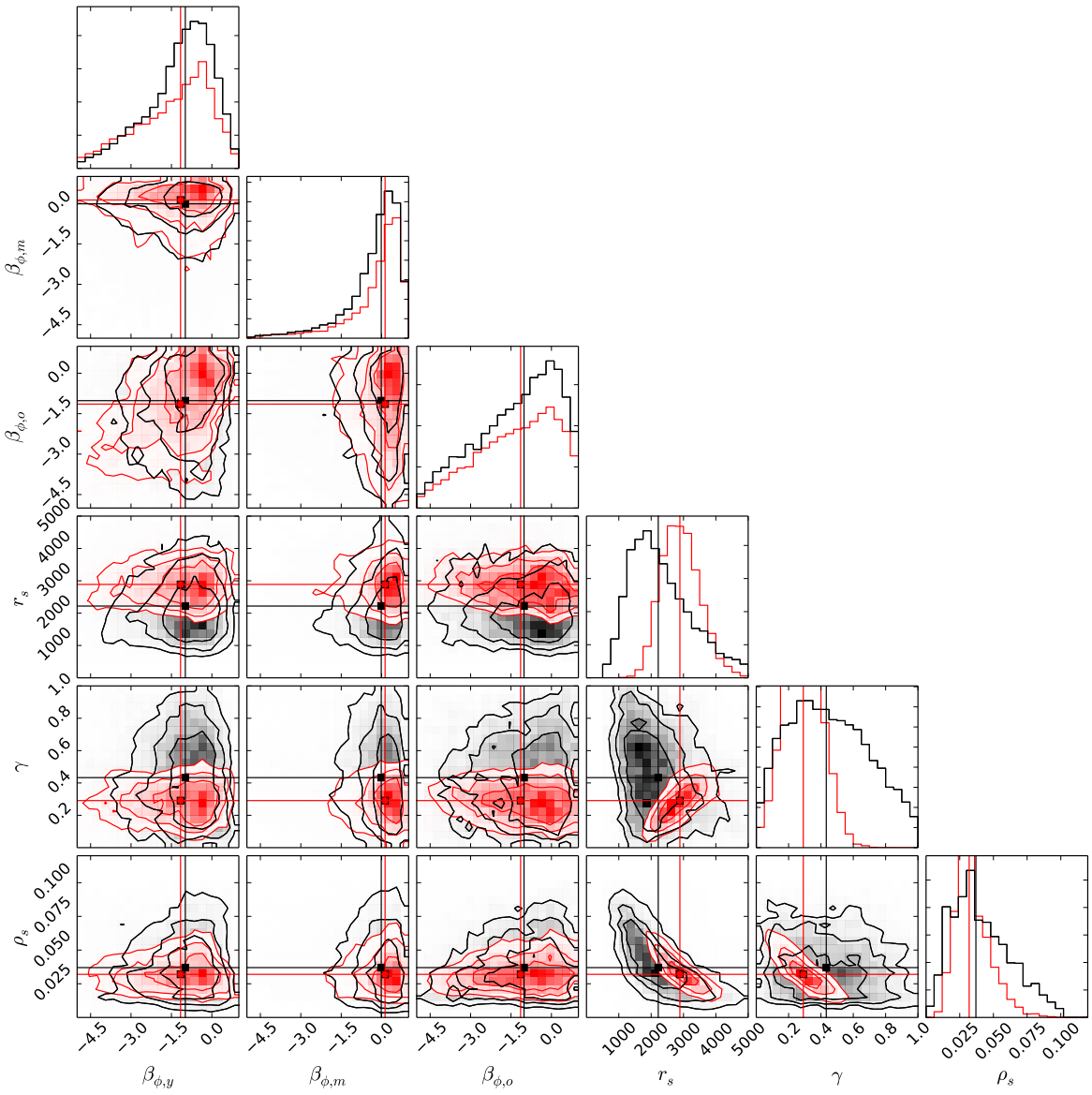

Figure B.5: Marginalised parameters from the spherical Jeans models: the velocity anisotropy for the young ($\beta_{\phi,y}$), middle-aged ($\beta_{\phi,m}$) and old population ($\beta_{\phi,o}$), and the dark matter parameters$r_{\rm s}$, γ and $\rho_{\rm s}$. Black contours show the marginalised parameter values with Jeans models performed on stellar kinematics only. Red contours show the ones constrained by using $V_{\rm c}$ derived from HI kinematics as a prior.

References

Abadi, M. G., Navarro, J. F., Steinmetz, M., & Eke, V. R. 2003, ApJ, 591, 499

Adams, J. J., Simon, J. D., Fabricius, M. H., et al. 2014, ApJ, 789, 63

Allgood, B., Flores, R. A., Primack, J. R., et al. 2006, MNRAS, 367, 1781

Amorisco, N. C. 2017, ApJ, 844, 64

Amorisco, N. C., & Evans, N. W. 2011, MNRAS, 411, 2118

—. 2012, ApJ, 756, L2

Amorisco, N. C., Evans, N. W., & van de Ven, G. 2014, Nature, 507, 335

Angulo, R. E., Lacey, C. G., Baugh, C. M., & Frenk, C. S. 2009, MNRAS, 399, 983

Angus, G. W., & Diaferio, A. 2009, MNRAS, 396, 887

Arca-Sedda, M., & Capuzzo-Dolcetta, R. 2016, MNRAS, 461, 4335

Banerjee, A., & Jog, C. J. 2008, ApJ, 685, 254

Bardeen, J. M., Bond, J. R., Kaiser, N., & Szalay, A. S. 1986, ApJ, 304, 15

Barrera-Ballesteros, J. K., García-Lorenzo, B., Falcón-Barroso, J., et al. 2015, A&A, 582, A21

Bassett, R., Glazebrook, K., Fisher, D. B., et al. 2014, MNRAS, 442, 3206

Bastian, N. 2017, in IAU Symposium, Vol. 316, Formation, Evolution, and Survival of Massive Star Clusters, ed. C. Charbonnel & A. Nota, 302–309

Battaglia, G., Helmi, A., Tolstoy, E., et al. 2008, ApJ, 681, L13

Battaglia, G., Tolstoy, E., Helmi, A., et al. 2011, MNRAS, 411, 1013

—. 2006, A&A, 459, 423

Baumgardt, H., & Makino, J. 2003, MNRAS, 340, 227

Beasley, M. A., & Trujillo, I. 2016, ApJ, 830, 23

Bechtol, K., Drlica-Wagner, A., Balbinot, E., et al. 2015, ApJ, 807, 50

Begeman, K. G. 1987, PhD thesis, , Kapteyn Institute, (1987)

Bender, R., Burstein, D., & Faber, S. M. 1992, ApJ, 399, 462

Benítez-Llambay, A., Navarro, J. F., Abadi, M. G., et al. 2016, MNRAS, 456, 1185

Bermejo-Climent, J. R., Battaglia, G., Gallart, C., et al. 2018, MNRAS, 479, 1514

Binney, J., & Tremaine, S. 1987, Galactic dynamics

Binney, J. J., Davies, R. L., & Illingworth, G. D. 1990, ApJ, 361, 78

Bolatto, A. D., Wong, T., Utomo, D., et al. 2017, ApJ, 846, 159

Bond, J. R., Cole, S., Efstathiou, G., & Kaiser, N. 1991, ApJ, 379, 440

Boylan-Kolchin, M., Ma, C.-P., & Quataert, E. 2008, MNRAS, 383, 93

Bozek, B., Marsh, D. J. E., Silk, J., & Wyse, R. F. G. 2015, MNRAS, 450, 209

Bozek, B., Fitts, A., Boylan-Kolchin, M., et al. 2019, MNRAS, 483, 4086

Breddels, M. A., Helmi, A., van den Bosch, R. C. E., van de Ven, G., & Battaglia, G. 2013, MNRAS, 433, 3173

Brook, C. B. 2015, MNRAS, 454, 1719

Brooks, A. M., Governato, F., Quinn, T., Brook, C. B., & Wadsley, J. 2009, ApJ, 694, 396

Brooks, A. M., & Zolotov, A. 2014, ApJ, 786, 87

Bullock, J. S., Dekel, A., Kolatt, T. S., et al. 2001, ApJ, 555, 240

Butsky, I., Macciò, A. V., Dutton, A. A., et al. 2016, MNRAS, 462, 663

Cappellari, M. 2008, MNRAS, 390, 71

—. 2016, ARA&A, 54, 597

Chandrasekhar, S. 1943, ApJ, 97, 255

Christensen, C. R., Davé, R., Governato, F., et al. 2016, ApJ, 824, 57

Cicuéndez, L., & Battaglia, G. 2018, MNRAS, 480, 251

Cole, D. R., Dehnen, W., Read, J. I., & Wilkinson, M. I. 2012, MNRAS, 426, 601

Cole, D. R., Dehnen, W., & Wilkinson, M. I. 2011, MNRAS, 416, 1118

Coleman, M. G., Da Costa, G. S., Bland-Hawthorn, J., & Freeman, K. C. 2005, AJ, 129, 1443

Contenta, F., Balbinot, E., Petts, J. A., et al. 2018, MNRAS, 476, 3124

Courteau, S., Dutton, A. A., van den Bosch, F. C., et al. 2007, ApJ, 671, 203

Courteau, S., Cappellari, M., de Jong, R. S., et al. 2014, Reviews of Modern Physics, 86, 47

Cowsik, R., Wagoner, K., Berti, E., & Sircar, A. 2009, ApJ, 699, 1389

Cresci, G., Hicks, E. K. S., Genzel, R., et al. 2009, ApJ, 697, 115

Dalla Vecchia, C., & Schaye, J. 2012, MNRAS, 426, 140

Davis, T. A., Alatalo, K., Bureau, M., et al. 2013, MNRAS, 429, 534

de Boer, T. J. L., & Fraser, M. 2016, A&A, 590, A35

de Boer, T. J. L., Tolstoy, E., Hill, V., et al. 2012, A&A, 544, A73

de Lorenzi, F., Debattista, V. P., Gerhard, O., & Sambhus, N. 2007, MNRAS, 376, 71

del Pino, A., Hidalgo, S. L., Aparicio, A., et al. 2013, MNRAS, 433, 1505

Di Cintio, A., Brook, C. B., Dutton, A. A., et al. 2017, MNRAS, 466, L1

—. 2014, MNRAS, 441, 2986

Doroshkevich, A. G. 1970, Astrofizika, 6, 581

Dubinski, J. 1994, ApJ, 431, 617

Dutton, A. A., & Macciò, A. V. 2014, MNRAS, 441, 3359

Dutton, A. A., & van den Bosch, F. C. 2009, MNRAS, 396, 141

—. 2012, MNRAS, 421, 608

El-Badry, K., Wetzel, A. R., Geha, M., et al. 2017, ApJ, 835, 193

Elmegreen, B. G., & Efremov, Y. N. 1997, ApJ, 480, 235

Emsellem, E., Monnet, G., & Bacon, R. 1994, A&A, 285

Erkal, D., Sanders, J. L., & Belokurov, V. 2016, MNRAS, 461, 1590

Evans, N. W., & An, J. H. 2006, Phys. Rev. D, 73, 023524

Faber, S. M., & Jackson, R. E. 1976, ApJ, 204, 668

Falcón-Barroso, J., Lyubenova, M., van de Ven, G., et al. 2017, A&A, 597, A48

Fall, S. M. 1983, in IAU Symposium, Vol. 100, Internal Kinematics and Dynamics of Galaxies, ed. E. Athanassoula, 391–398

Fitts, A., Boylan-Kolchin, M., Bozek, B., et al. 2018, arXiv e-prints, arXiv:1811.11791

Foreman-Mackey, D., Hogg, D. W., Lang, D., & Goodman, J. 2013, PASP, 125, 306

Fritz, T. K., Battaglia, G., Pawlowski, M. S., et al. 2018, ArXiv e-prints, arXiv:1805.00908

Fry, A. B., Governato, F., Pontzen, A., et al. 2015, MNRAS, 452, 1468

Gaia Collaboration, Helmi, A., van Leeuwen, F., et al. 2018, ArXiv e-prints, arXiv:1804.09381

Gallazzi, A., Charlot, S., Brinchmann, J., White, S. D. M., & Tremonti, C. A. 2005, MNRAS, 362, 41

Gatto, A., Fraternali, F., Read, J. I., et al. 2013, MNRAS, 433, 2749

Geha, M., Blanton, M. R., Yan, R., & Tinker, J. L. 2012, ApJ, 757, 85

Goerdt, T., Moore, B., Read, J. I., Stadel, J., & Zemp, M. 2006, MNRAS, 368, 1073

González Delgado, R. M., Cid Fernandes, R., García-Benito, R., et al. 2014, ApJ, 791, L16

Governato, F., Brook, C., Mayer, L., et al. 2010, Nature, 463, 203

Governato, F., Zolotov, A., Pontzen, A., et al. 2012, MNRAS, 422, 1231

Greco, C., Clementini, G., Catelan, M., et al. 2007, ApJ, 670, 332

Hansen, S. H., Egli, D., Hollenstein, L., & Salzmann, C. 2005, , 10, 379

Harris, J., & Zaritsky, D. 2006, AJ, 131, 2514

Hasselquist, S., Carlin, J. L., Holtzman, J. A., et al. 2019, ApJ, 872, 58

Hernandez, X., & Gilmore, G. 1998, MNRAS, 297, 517

Hetznecker, H., & Burkert, A. 2006, MNRAS, 370, 1905

Hidalgo, S. L. 2011, in EAS Publications Series, Vol. 48, EAS Publications Series, ed. M. Koleva, P. Prugniel, & I. Vauglin, 37–42

Hinz, J. L., Rix, H.-W., & Bernstein, G. M. 2001, AJ, 121, 683

Hubble, E. 1923, PASP, 35, 261

—. 1926a, Contributions from the Mount Wilson Observatory / Carnegie Institution of Washington, 310, 1

—. 1926b, Contributions from the Mount Wilson Observatory / Carnegie Institution of Washington, 324, 1

Hubble, E. P. 1929, ApJ, 69, doi:10.1086/143167

Hui, L., Ostriker, J. P., Tremaine, S., & Witten, E. 2017, Phys. Rev. D, 95, 043541

Hunter, D. A., Rubin, V. C., Swaters, R. A., Sparke, L. S., & Levine, S. E. 2002, ApJ, 580, 194

Hunter, D. A., Zahedy, F., Bowsher, E. C., et al. 2011, AJ, 142, 173

Hurley, J. R., & Shara, M. M. 2012, MNRAS, 425, 2872

Inoue, S. 2009, MNRAS, 397, 709

—. 2011, MNRAS, 416, 1181

Iorio, G., Fraternali, F., Nipoti, C., et al. 2017, MNRAS, 466, 4159

Jackson, D. C., Skillman, E. D., Gehrz, R. D., Polomski, E., & Woodward, C. E. 2007, ApJ, 656, 818

Jeans, J. H. 1922, MNRAS, 82, 122

Jenkins, A., Frenk, C. S., White, S. D. M., et al. 2001, MNRAS, 321, 372

Johnson, M., Hunter, D. A., Oh, S.-H., et al. 2012, AJ, 144, 152

Kacharov, N., Battaglia, G., Rejkuba, M., et al. 2017, MNRAS, 466, 2006

Kalinova, V., van de Ven, G., Lyubenova, M., et al. 2017, MNRAS, 464, 1903

Kamada, A., Kaplinghat, M., Pace, A. B., & Yu, H.-B. 2017, Physical Review Letters, 119, 111102

Kaplinghat, M., Tulin, S., & Yu, H.-B. 2016, Physical Review Letters, 116, 041302

Kassin, S. A., Weiner, B. J., Faber, S. M., et al. 2012, ApJ, 758, 106

Katz, H., Lelli, F., McGaugh, S. S., et al. 2017, MNRAS, 466, 1648

Kaufmann, T., Wheeler, C., & Bullock, J. S. 2007, MNRAS, 382, 1187

Kent, S. M., & de Zeeuw, T. 1991, AJ, 102, 1994

Kepley, A. A., Wilcots, E. M., Hunter, D. A., & Nordgren, T. 2007, AJ, 133, 2242

Kereš, D., Katz, N., Weinberg, D. H., & Davé, R. 2005, MNRAS, 363, 2

King, I. 1962, AJ, 67, 471

Kirby, E. N., Bullock, J. S., Boylan-Kolchin, M., Kaplinghat, M., & Cohen, J. G. 2014, MNRAS, 439, 1015

Kirby, E. N., Cohen, J. G., Guhathakurta, P., et al. 2013, ApJ, 779, 102

Kirby, E. N., Martin, C. L., & Finlator, K. 2011, ApJ, 742, L25

Klimentowski, J., Łokas, E. L., Kazantzidis, S., Mayer, L., & Mamon, G. A. 2009, MNRAS, 397, 2015

Klypin, A., Kravtsov, A. V., Valenzuela, O., & Prada, F. 1999, ApJ, 522, 82

Koposov, S. E., Belokurov, V., Torrealba, G., & Evans, N. W. 2015, ApJ, 805, 130

Kormendy, J., & Bender, R. 1996, ApJ, 464, L119

Kourkchi, E., Khosroshahi, H. G., Carter, D., et al. 2012, MNRAS, 420, 2819

Kowalczyk, K., del Pino, A., Lokas, E. L., & Valluri, M. 2018, ArXiv e-prints, arXiv:1807.07852

Krajnović, D., Cappellari, M., de Zeeuw, P. T., & Copin, Y. 2006, MNRAS, 366, 787

Kruijssen, J. M. D. 2015, MNRAS, 454, 1658

Krumholz, M., & Burkert, A. 2010, ApJ, 724, 895

Krumholz, M. R., & McKee, C. F. 2005, ApJ, 630, 250

Kuhlen, M., Weiner, N., Diemand, J., et al. 2010, , 2, 030

Lacey, C., & Cole, S. 1993, MNRAS, 262, 627

Lacey, C. G. 1984, MNRAS, 208, 687

Laine, S., Kenney, J. D. P., Yun, M. S., & Gottesman, S. T. 1999, ApJ, 511, 709

Larsen, S. S., Strader, J., & Brodie, J. P. 2012, A&A, 544, L14

Leaman, R., Cole, A. A., Venn, K. A., et al. 2009, ApJ, 699, 1

Leaman, R., Venn, K. A., Brooks, A. M., et al. 2012, ApJ, 750, 33

—. 2013, ApJ, 767, 131

Leaman, R., Mendel, J. T., Wisnioski, E., et al. 2017, MNRAS, 472, 1879

Leauthaud, A., Tinker, J., Bundy, K., et al. 2012, ApJ, 744, 159

Lelli, F., Fraternali, F., & Sancisi, R. 2010, A&A, 516, A11

Lelli, F., McGaugh, S. S., Schombert, J. M., Desmond, H., & Katz, H. 2019, MNRAS, 484, 3267

Leung, G. Y. C., Leaman, R., van de Ven, G., et al. 2018, MNRAS, 477, 254

Levy, R. C., Bolatto, A. D., Teuben, P., et al. 2018, ApJ, 860, 92

Lima Neto, G. B., Gerbal, D., & Márquez, I. 1999, MNRAS, 309, 481

Loebman, S. R., Valluri, M., Hattori, K., et al. 2018, ApJ, 853, 196

Łokas, E. L. 2009, MNRAS, 394, L102

Łokas, E. L., Kazantzidis, S., Klimentowski, J., Mayer, L., & Callegari, S. 2010, ApJ, 708, 1032

Long, R. J., & Mao, S. 2010, MNRAS, 405, 301

Lovell, M. R., Frenk, C. S., Eke, V. R., et al. 2014, MNRAS, 439, 300

Lux, H., Read, J. I., & Lake, G. 2010, MNRAS, 406, 2312

Macciò, A. V., Dutton, A. A., & van den Bosch, F. C. 2008, MNRAS, 391, 1940

Mackey, A. D., & Gilmore, G. F. 2003a, MNRAS, 345, 747

—. 2003b, MNRAS, 340, 175

Majewski, S. R., Kunkel, W. E., Law, D. R., et al. 2004, AJ, 128, 245

Martig, M., Minchev, I., & Flynn, C. 2014, MNRAS, 443, 2452

Martin, N. F., Nidever, D. L., Besla, G., et al. 2015, ApJ, 804, L5

Massari, D., Breddels, M. A., Helmi, A., et al. 2018, Nature Astronomy, 2, 156

Mayer, L. 2010, Advances in Astronomy, 2010, 278434

Mayer, L., Mastropietro, C., Wadsley, J., Stadel, J., & Moore, B. 2006, MNRAS, 369, 1021

McConnachie, A. W. 2012, AJ, 144, 4

McConnachie, A. W., Irwin, M. J., Ferguson, A. M. N., et al. 2005, MNRAS, 356, 979

McConnachie, A. W., Venn, K. A., Irwin, M. J., Young, L. M., & Geehan, J. J. 2007, ApJ, 671, L33

McGaugh, S., & Milgrom, M. 2013, ApJ, 775, 139

Melotte, P. J. 1926, MNRAS, 86, 636

Merrifield, M. R., & Kent, S. M. 1990, AJ, 99, 1548

Merritt, D., & Hernquist, L. 1991, ApJ, 376, 439

Milgrom, M. 1983, ApJ, 270, 365

Miller, S. H., Bundy, K., Sullivan, M., Ellis, R. S., & Treu, T. 2011, ApJ, 741, 115

Miralda-Escudé, J. 2002, ApJ, 564, 60

Mo, H. J., Mao, S., & White, S. D. M. 1998, MNRAS, 295, 319

Mogotsi, K. M., de Blok, W. J. G., Caldú-Primo, A., et al. 2016, AJ, 151, 15

Molina, J., Ibar, E., Swinbank, A. M., et al. 2017, MNRAS, 466, 892

Mondal, C., Subramaniam, A., & George, K. 2018, AJ, 156, 109

Moore, B., Ghigna, S., Governato, F., et al. 1999, ApJ, 524, L19

Moster, B. P., Somerville, R. S., Maulbetsch, C., et al. 2010, ApJ, 710, 903

Muñoz, R. R., Frinchaboy, P. M., Majewski, S. R., et al. 2005, ApJ, 631, L137

Naab, T., Johansson, P. H., & Ostriker, J. P. 2009, ApJ, 699, L178

Navarro, J. F., Frenk, C. S., & White, S. D. M. 1996, ApJ, 462, 563

Oñorbe, J., Boylan-Kolchin, M., Bullock, J. S., et al. 2015, MNRAS, 454, 2092

Obreja, A., Stinson, G. S., Dutton, A. A., et al. 2016, MNRAS, 459, 467

Oh, K. S., Lin, D. N. C., & Richer, H. B. 2000, ApJ, 531, 727

Oh, S.-H., Brook, C., Governato, F., et al. 2011, AJ, 142, 24

Olling, R. P. 1995, AJ, 110, 591

—. 1996, AJ, 112, 481

Oman, K. A., Navarro, J. F., Fattahi, A., et al. 2015, MNRAS, 452, 3650

Opik, E. 1922, ApJ, 55, doi:10.1086/142680

Panter, B., Jimenez, R., Heavens, A. F., & Charlot, S. 2007, MNRAS, 378, 1550

Peñarrubia, J., Pontzen, A., Walker, M. G., & Koposov, S. E. 2012, ApJ, 759, L42

Peebles, P. J. E. 1969, ApJ, 155, 393

Pelliccia, D., Tresse, L., Epinat, B., et al. 2017, A&A, 599, A25

Peter, A. H. G., Rocha, M., Bullock, J. S., & Kaplinghat, M. 2013, MNRAS, 430, 105

Petts, J. A., Gualandris, A., & Read, J. I. 2015, MNRAS, 454, 3778

Petts, J. A., Read, J. I., & Gualandris, A. 2016, MNRAS, 463, 858

Pizzella, A., Corsini, E. M., Vega Beltrán, J. C., & Bertola, F. 2004, A&A, 424, 447

Planck Collaboration, Aghanim, N., Akrami, Y., et al. 2018, arXiv e-prints, arXiv:1807.06209

Ponomareva, A. A., Verheijen, M. A. W., & Bosma, A. 2016, MNRAS, 463, 4052

Pontzen, A., & Governato, F. 2012, MNRAS, 421, 3464

Press, W. H., & Schechter, P. 1974, ApJ, 187, 425

Price, S. H., Kriek, M., Shapley, A. E., et al. 2016, ApJ, 819, 80

Raha, N., Sellwood, J. A., James, R. A., & Kahn, F. D. 1991, Nature, 352, 411

Read, J. I., Agertz, O., & Collins, M. L. M. 2016, MNRAS, 459, 2573

Read, J. I., Goerdt, T., Moore, B., et al. 2006, MNRAS, 373, 1451

Richstone, D. O., & Tremaine, S. 1984, ApJ, 286, 27

Rix, H.-W., de Zeeuw, P. T., Cretton, N., van der Marel, R. P., & Carollo, C. M. 1997, ApJ, 488, 702

Robles, V. H., Bullock, J. S., Elbert, O. D., et al. 2017, MNRAS, 472, 2945

Romanowsky, A. J., & Fall, S. M. 2012, ApJS, 203, 17

Sameie, O., Creasey, P., Yu, H.-B., et al. 2018, MNRAS, 479, 359

Sánchez, S. F., García-Benito, R., Zibetti, S., et al. 2016, A&A, 594, A36

Sánchez-Salcedo, F. J., Reyes-Iturbide, J., & Hernandez, X. 2006, MNRAS, 370, 1829

Santos-Santos, I. M., Di Cintio, A., Brook, C. B., et al. 2018, MNRAS, 473, 4392

Sarkar, A., Mondal, R., Das, S., et al. 2016, , 4, 012

Satoh, C. 1980, PASJ, 32, 41

Sawala, T., Frenk, C. S., Crain, R. A., et al. 2013, MNRAS, 431, 1366

Schawinski, K., Urry, C. M., Simmons, B. D., et al. 2014, MNRAS, 440, 889

Schive, H.-Y., Chiueh, T., & Broadhurst, T. 2014a, Nature Physics, 10, 496

Schive, H.-Y., Liao, M.-H., Woo, T.-P., et al. 2014b, Physical Review Letters, 113, 261302

Schroyen, J., de Rijcke, S., Valcke, S., Cloet-Osselaer, A., & Dejonghe, H. 2011a, MNRAS, 416, 601

—. 2011b, MNRAS, 416, 601

Schwarzschild, M. 1979, ApJ, 232, 236

—. 1993, ApJ, 409, 563

Shen, S., Madau, P., Conroy, C., Governato, F., & Mayer, L. 2014, ApJ, 792, 99

Shetty, R., Vogel, S. N., Ostriker, E. C., & Teuben, P. J. 2007, ApJ, 665, 1138

Simpson, C. M., Grand, R. J. J., Gómez, F. A., et al. 2018, MNRAS, 478, 548

Soubiran, C., Bienaymé, O., & Siebert, A. 2003, A&A, 398, 141

Spekkens, K., & Sellwood, J. A. 2007, ApJ, 664, 204

Starkenburg, E., Hill, V., Tolstoy, E., et al. 2010, A&A, 513, A34

Stierwalt, S., Besla, G., Patton, D., et al. 2015, ApJ, 805, 2

Strömberg, G. 1946, ApJ, 104, 12

Swaters, R. A., Sancisi, R., van Albada, T. S., & van der Hulst, J. M. 2009, A&A, 493, 871

—. 2011, ApJ, 729, 118

Syer, D., & Tremaine, S. 1996, MNRAS, 282, 223

Takahashi, K., & Lee, H. M. 2000, MNRAS, 316, 671

Tatton, B., Cioni, M. R., & Irwin, M. 2011, in Astronomical Society of the Pacific Conference Series, Vol. 445, Why Galaxies Care about AGB Stars II: Shining Examples and Common Inhabitants, ed. F. Kerschbaum, T. Lebzelter, & R. F. Wing, 547

Teyssier, R., Pontzen, A., Dubois, Y., & Read, J. I. 2013, MNRAS, 429, 3068

Thomas, J., Saglia, R. P., Bender, R., et al. 2004, MNRAS, 353, 391

Tiley, A. L., Stott, J. P., Swinbank, A. M., et al. 2016, MNRAS, 460, 103

Tolstoy, E., Irwin, M. J., Helmi, A., et al. 2004, ApJ, 617, L119

Tormen, G. 1997, MNRAS, 290, 411

Tremaine, S. D. 1976, ApJ, 203, 345

Tully, R. B., & Fisher, J. R. 1977, A&A, 54, 661

Übler, H., Förster Schreiber, N. M., Genzel, R., et al. 2017, ApJ, 842, 121

Valluri, M., Merritt, D., & Emsellem, E. 2004, ApJ, 602, 66

van Albada, T. S. 1982, MNRAS, 201, 939

van de Sande, J., Scott, N., Bland-Hawthorn, J., et al. 2018, Nature Astronomy, 2, 483

van de Ven, G., & Fathi, K. 2010, ApJ, 723, 767

van den Bergh, S. 1998, ApJ, 505, L127

van den Bosch, R. C. E., van de Ven, G., Verolme, E. K., Cappellari, M., & de Zeeuw, P. T. 2008, MNRAS, 385, 647

van der Marel, R. P., Cretton, N., de Zeeuw, P. T., & Rix, H.-W. 1998, ApJ, 493, 613

Viel, M., Becker, G. D., Bolton, J. S., & Haehnelt, M. G. 2013, Phys. Rev. D, 88, 043502

Villaescusa-Navarro, F., & Dalal, N. 2011, , 3, 024

Vogelsberger, M., & Zavala, J. 2013, MNRAS, 430, 1722

Vogelsberger, M., Zavala, J., Cyr-Racine, F.-Y., et al. 2016, MNRAS, 460, 1399

Vogelsberger, M., Zavala, J., & Loeb, A. 2012, MNRAS, 423, 3740

Vogelsberger, M., Zavala, J., Schutz, K., & Slatyer, T. R. 2019, MNRAS, 484, 5437

Vogelsberger, M., Zavala, J., Simpson, C., & Jenkins, A. 2014, MNRAS, 444, 3684

Walker, M. G., Mateo, M., & Olszewski, E. W. 2009, AJ, 137, 3100

Walker, M. G., Mateo, M., Olszewski, E. W., et al. 2007, ApJ, 667, L53

Walker, M. G., & Peñarrubia, J. 2011, ApJ, 742, 20

Wang, M.-Y., Koposov, S., Drlica-Wagner, A., et al. 2019, arXiv e-prints, arXiv:1902.04589

Warren, M. S., Quinn, P. J., Salmon, J. K., & Zurek, W. H. 1992, ApJ, 399, 405

Weijmans, A.-M., Krajnović, D., van de Ven, G., et al. 2008, MNRAS, 383, 1343

Weiner, B. J., Willmer, C. N. A., Faber, S. M., et al. 2006, ApJ, 653, 1027

Weisz, D. R., Dolphin, A. E., Skillman, E. D., et al. 2014, ApJ, 789, 147

Wetzel, A. R., Cohn, J. D., & White, M. 2009, MNRAS, 395, 1376

Wetzel, A. R., Deason, A. J., & Garrison-Kimmel, S. 2015, ApJ, 807, 49

Wheeler, C., Pace, A. B., Bullock, J. S., et al. 2017, MNRAS, 465, 2420

White, S. D. M. 1984, ApJ, 286, 38

Whiting, A. B., Hau, G. K. T., & Irwin, M. 1999, AJ, 118, 2767

Wielen, R. 1977, A&A, 60, 263

Wisnioski, E., Förster Schreiber, N. M., Wuyts, S., et al. 2015, ApJ, 799, 209

Wolf, J. 2010, Highlights of Astronomy, 15, 79

Wolf, M. 1910, Astronomische Nachrichten, 183, 137

Wong, T., Blitz, L., & Bosma, A. 2004, ApJ, 605, 183

Yu, J., & Liu, C. 2018, MNRAS, 475, 1093

Zavala, J., Jing, Y. P., Faltenbacher, A., et al. 2009, ApJ, 700, 1779

Zhao, H. 1996, MNRAS, 278, 488

Zhu, L., van de Ven, G., Watkins, L. L., & Posti, L. 2016, MNRAS, 463, 1117

Zhu, L., Long, R. J., Mao, S., et al. 2014, ApJ, 792, 59

Zhu, L., van den Bosch, R., van de Ven, G., et al. 2018a, MNRAS, 473, 3000

Zhu, L., van de Ven, G., Bosch, R. v. d., et al. 2018b, Nature Astronomy, 2, 233

Zhuang, Y., Leaman, R., van de Ven, G., et al. 2019, MNRAS, 483, 1862

Zolotov, A., Brooks, A. M., Willman, B., et al. 2012, ApJ, 761, 71

Zwaan, M. A., Meyer, M. J., & Staveley-Smith, L. 2010, MNRAS, 403, 1969